

Contents

3	0.1 Introduction	1
4	0.1.1 Historical retrospective	1
5	0.1.2 Actual challenges	2
6	0.1.3 Thesis composition	3
7	1 The Standard Model	5
8	1.1 General composition and key parameters	5
9	1.2 Classical fields and gauge invariance principle	9
10	1.3 Quantum electrodynamics	10
11	1.4 Electroweak theory and the Higgs mechanism	12
12	1.4.1 Electroweak gauge fields	12
13	1.4.2 Fermion sector	13
14	1.4.3 Higgs fields breaking the symmetry	14
15	1.4.4 Physical interpretation of gauge fields and parameters	15
16	1.5 Chromodynamics	15
17	Bibliography	19
18	2 The W boson	21
19	2.1 The motivation for the W mass measurement	21
20	2.2 Massive boson production at hadron colliders	22
21	2.2.1 Deep Inelastic scattering	23
22	2.2.2 The Drell-Yan process	25
23	2.3 Transverse momentum of massive vector bosons	27
24	3 The Large Hadron Collider	31
25	3.1 Introduction	31
26	3.2 The LHC running sequence	31
27	3.3 Special low pile-up run during LHC Run 2	35
28	4 The ATLAS detector	37
29	4.1 General description and layout	37

30	4.2 Coordinate system	37
31	4.3 Magnet system and magnetic field	38
32	4.4 Inner detector	38
33	4.5 Calorimeter system	40
34	4.5.1 Electromagnetic calorimeter	41
35	4.5.2 Hadronic calorimeter	44
36	4.6 Muon detectors	45
37	4.7 Forward detectors	47
38	4.8 Trigger system	49
39	5 Electromagnetic shower shapes correction in the electromagnetic calorimeter	51
40	5.1 Introduction	51
41	5.2 Shower shapes measurement and correction	54
42	5.2.1 Event selection	54
43	5.2.2 Data/MC discrepancies	54
44	5.2.3 The correction procedure	56
45	5.3 Results	57
46	5.4 Appendix: control plots	58
47	6 Event reconstruction	69
48	6.1 Charged particles track reconstruction	69
49	6.2 Determining the primary vertex of the event	70
50	6.3 Muon reconstruction and identification	72
51	6.3.1 Muon reconstruction	72
52	6.3.2 Muon identification	74
53	6.3.3 Muon isolation	75
54	6.4 Electron reconstruction and identification	75
55	6.4.1 Electron reconstruction	75
56	6.4.2 Electron identification	79
57	6.4.3 Electron isolation	80
58	6.5 Particle flow objects	81
59	7 Calibrations and corrections	83
60	7.1 Electron corrections	83
61	7.1.1 Energy scale and resolution correction	83
62	7.1.2 Electron selection efficiency	88
63	7.1.3 SF uncertainties propagation	92
64	7.2 Muon corrections	99
65	7.2.1 Muon momentum calibration	99
66	7.2.2 Correction for charge-dependent momentum bias	100

67	7.2.3 Muon efficiency measurements	106
68	7.3 Hadronic recoil calibration	111
69	7.3.1 SET and u_T reweighting	112
70	7.3.2 u_X and u_Y correction	115
71	7.3.3 Resolution and response corrections	116
72	7.4 Angular coefficients correction	118
73	8 MC samples and selection	119
74	8.1 Data and MC samples	119
75	8.1.1 MC samples and cross-sections	119
76	8.2 Z vertex reweighting	121
77	8.2.1 Multijet background	126
78	8.3 W analysis event selection and control plots	126
79	8.3.1 Event selection	127
80	8.3.2 $\sqrt{s} = 13$ TeV dataset control plots	127
81	8.3.3 $\sqrt{s} = 5$ TeV dataset control plots	137
82	9 W boson pT spectrum	145
83	9.1 Unfolding	145
84	9.2 Uncertainties propagation	146
85	9.2.1 Statistical uncertainty propagation using Bootstrap method	146
86	9.2.2 Systematic uncertainty propagation	147
87	9.2.3 Unfolded uncertainty breakdown	148
88	9.3 Unfolding bias	152
89	9.4 Results	154
90	10 Hadronic recoil regression with deep neural networks	157
91	10.1 Deep neural networks	157
92	10.1.1 Gradient descent optimization	157
93	10.1.2 DNN structure and training	159
94	10.1.3 Batch normalization	161
95	10.2 HR regression	162
96	10.2.1 Input features and model	162
97	10.2.2 Kinematic distributions	163
98	10.3 Technical details	164
99	11 Appendix A	165
100	11.1 Experimental uncertainties of main observables	165

101

List of Figures

102	11	The list of particles that enters the Standard Model (SM)[sm_wiki].	7
103	12	The evolution of the SM running coupling constants [coupl_wiki].	8
104	13	The QEQ diagrams: Compton scattering, electron self-energy, photon self-energy.	11
105	14	Electroweak sector and the Weinberg rotation [coupl_wiki].	16
106	15	The formation of a jet [conf_wiki].	17
107	21	Next-to-leading order diagrams for W boson propagator containing contributions from heavy quarks and the Higgs boson.	21
109	22	W mass measurements and predictions	22
110	23	Examples of hard QCD scatterings.	23
111	24	The evolution of a PDF4LHC15 NNLO Hessian set from $Q^2 = 10^2$ GeV to $Q^2 = 10^4$ GeV using the DokshitzerGribovLipatovAltarelliParisi (DGLAP). Notice the increase in the sea quark density. The PDFs include one standard deviation uncertainty band.	25
114	25	Rapidity distribution for the vector bosons using MSTW2008 and CTEQ6.6 PDF sets for the centre-of-mass energies of 7 and 14 TeV [Halzen:2013bqa].	26
116	26	W and Z boson cross sections LHC at 7 TeV. ATLAS and CMS results, compared to NNLO predictions for various PDF sets [Mangano:2015ejw].	27
118	27	Parton contributions to the cross-sections of W^+ and W^- bosons for LHC and Tevatron cases [Martin:392675].	28
120	28	Kinematic distributions for W^\pm with corrections.	29
121	31	A Toroidal LHC ApparatuS (ATLAS) A hydrogen tank supplies LHC with protons [hydro].	32
122	32	Schematic depiction of the LHC ring.	33
123	33	Bunching at RF cavities	33
124	34	The crossing	34
125	35	Number of Interactions per bunch crossing in ATLAS Run 2 [run2lumi]. A little bump around $\mu \approx 2$ corresponds to special low pile-up runs.	36
127	41	ATLAS detector general layout	38
128	42	Geometry of ATLAS magnet windings	39
129	43	Fichier Gerber des modèles d CFR-34 et CFR-35.	40

130	44	ATLAS calorimeter general layout	41
131	45	ATLAS EM calorimeter layers	43
132	46	Accordion absorbers of the electromagnetic calorimeter (EMC)	44
133	47	ATLAS muon system	45
134	48	Cut views of the muon systems	47
135	49	ATLAS forward detectors	49
136	410	The scheme of ATLAS trigger systems	50
137	51	The schematic portrayal of EM shower development	51
138	52	Visualisations of the 7x11 calorimeter cluster	52
139	53	Shower shapes in the second layer of the electromagnetic calorimeter	52
140	54	Distribution of R_η in simulation (GEANT4) for electrons and jets [sshapes_simulation].	53
141	55	Data/MC Comparison for Calorimeter Shower Shapes of High Et Electrons [geant_corr].	54
142	56	R_η in the barrel and in the end-cap, Data vs MC	55
143	57	R_ϕ in the barrel and in the end-cap, Data vs MC	55
144	58	W_η^2 in the barrel and in the end-cap, Data vs MC	56
145	59	R_ϕ in the barrel and in the end-cap, Data vs MC	57
146	510	Schematic energy profile in ϕ dimension. Bremsstrahlung tails subtraction based on e^+ and e^- energy profiles.	57
148	511	R_η in the barrel and in the end-cap	58
149	512	R_ϕ in the barrel and in the end-cap, Data, MC, reweighted MC	59
150	513	W_η^2 in the barrel and in the end-cap, Data, MC, reweighted MC	59
151	514	Distributions integrated over pT (a) R_ϕ ; (b) R_η ; (c) $W_{\eta 2}$	60
152	515	Electron identification efficiency as a function of the electron pseudo-rapidity	60
153	516	Reta 2	61
154	517	Rphi in all eta slices	62
155	518	Reta 2	63
156	519	Reta 2	64
157	520	Reta 2	65
158	521	Reta 2	66
159	522	Reta 2	67
160	61	Impact parameters	69
161	62	Ambiguity solving.	71
162	63	Vertices	72
163	64	sagitta	73
164	65	muon combined	74
165	66	Electron path	76
166	67	topocluster	77
167	68	Supercluster	78

168	69	Isolation plot	80
169	610	pflow	82
170	71	Schematic overview of energy response calibration procedure for electrons and photons.	83
171	72	Energy scale factors α for low pile-up runs of 2017 (left), 2018 (right) and 2017 at 5TeV (bottom) using 68, 48 and 24 η bins. It can be seen, that the extraction is unstable in case of 68 bins, resulting in α factors with very large uncertainties.	85
174	73	Additional constant term c'_i for low pile-up runs of 2017 (13 TeV), 2018 (13 TeV) and 2017 at 5 TeV using 24 bins. The lower panel shows the difference of c'_i to the 2017 5 TeV run.	86
176	74	The invariant mass distribution around the Z-mass for low pile-up Data for 2017 (13 TeV)	86
177	75	The invariant mass distribution around the Z-mass for low-pileup data for the $\sqrt{s} = 5$ TeV data taken in 2017 (a) and the $\sqrt{s} = 13$ TeV 2018 data (b).	87
179	76	Comparison of the uncertainties due to electron reconstruction, contrasting the high- μ -extrapolated and in-situ-measured SF uncertainties in a $W^+ \rightarrow e^+ \nu$ selection at 13 TeV as function of typical kinematic variables.	90
182	77	Isolation $E_T^{\text{cone}0.3}/25\text{GeV}$ distribution of probe electrons in the ZIso-method using 13 TeV 339 pb $^{-1}$ low-pileup data. Left the denominator and right the numerator distributions are shown, with the data as crosses, the signal $Z \rightarrow ee$ expectation as open line and the background estimate as cyan area (template normalised at high values).	91
186	78	Comparison of electron reconstruction SFs with 5 TeV and 13 TeV data as well as the 5+13 TeV combination in nine η ranges as written in the plot legend, from most central $\eta = 0 - 0.1$ (top left) to most forward $\eta = 2.37 - 2.47$ (bottom right). The bottom panel shows the ratio of 5 TeV and 13 TeV SFs. The total uncertainties are shown.	93
190	79	Electron isolation efficiencies (top panels) and scale factors (lower panels) for the $ptvarcone20/p_T^e < 0.1$ working point using 13 TeV 339 pb $^{-1}$ low-pileup data as function of η in bins of p_T	94
193	710	Electron trigger efficiencies (top panels) and scale factors (lower panels) for <code>HLT_e15_1hloose_nod0_L1EM12</code> using 13 TeV 339 pb $^{-1}$ low-pileup data as function of η in bins of p_T	95
195	711	Total relative uncertainties of electron scale factors at 13 TeV measured with tag-and-probe method	96
197	712	Contributions to the electron uncertainties related to efficiency SF (reconstruction, identification, isolation and trigger) in a $W^+ \rightarrow e^+ \nu$ selection at 13 TeV as function of typical kinematic variables.	97
200	713	Contributions to the electron uncertainties related to efficiency SF (reconstruction, identification, isolation and trigger) in a $W^+ \rightarrow e^+ \nu$ selection at 5 TeV as function of typical kinematic variables.	98
203	714	Example fits to $J/\psi \rightarrow \mu\mu$ (left) and $Z \rightarrow \mu\mu$ (right) mass peaks for pairs with leading muon pseudorapidity in the range $-0.62 < \eta < -0.52$ in low-pile-up 2017 13 TeV data.	99

205	715	Mean (left) and width (right) of the $J/\psi \rightarrow \mu\mu$ mass peak as a function of the leading muon η in 5.02 TeV data and MC. The mean and width are extracted from Crystal Ball components of the fits. In case of the simulation, both the uncorrected (dashed histogram) and corrected parameters (solid histogram) are shown. The fit results are presented for mass peaks constructed using kinematics of the muon ID tracks (top), ME tracks (middle) or CB tracks (bottom). The bottom panels in each plot show the data/MC ratio for uncorrected (dashed histogram) and corrected simulation (points).	101
212	716	Mean (left) and width (right) of the $J/\psi \rightarrow \mu\mu$ mass peak as a function of the leading muon η in 2017 13 TeV data and MC at low pile-up. The mean and width are extracted from Crystal Ball components of the fits. In case of the simulation, both the uncorrected (dashed histogram) and corrected parameters (solid histogram) are shown. The fit results are presented for mass peaks constructed using kinematics of the muon ID tracks (top), ME tracks (middle) or CB tracks (bottom). The bottom panels in each plot show the data/MC ratio for uncorrected (dashed histogram) and corrected simulation (points).	102
219	717	Mean (left) and width (right) of the $Z \rightarrow \mu\mu$ mass peak as a function of the leading muon η in 5.02 TeV data and MC. The mean and width are extracted from Crystal Ball components of the fits. In case of the simulation, both the uncorrected (dashed histogram) and corrected parameters (solid histogram) are shown. The fit results are presented for mass peaks constructed using kinematics of the muon ID tracks (top), ME tracks (middle) or CB tracks (bottom). The bottom panels in each plot show the data/MC ratio for uncorrected (dashed histogram) and corrected simulation (points).	103
226	718	Mean (left) and width (right) of the $Z \rightarrow \mu\mu$ mass peak as a function of the leading muon η in 2017 13 TeV data and MC at low pile-up. The mean and width are extracted from Crystal Ball components of the fits. In case of the simulation, both the uncorrected (dashed histogram) and corrected parameters (solid histogram) are shown. The fit results are presented for mass peaks constructed using kinematics of the muon ID tracks (top), ME tracks (middle) or CB tracks (bottom). The bottom panels in each plot show the data/MC ratio for uncorrected (dashed histogram) and corrected simulation (points).	104
233	719	Sagitta bias corrections derived for 2017 low-pile-up data (left) and simulation (right) at $\sqrt{s} = 13$ TeV. The corrections are evaluated with two Z -mass methods (“ $M_{\mu\mu_MCP}$ ” and “ $M_{\mu\mu_Align}$ ”), the E/p method applied to $W \rightarrow e\nu$ (“ $W_{env_E/p}$ ”) and $Z \rightarrow ee$ (“ $Z_{ee_E/p}$ ”) events, and the $p_T(\mu)$ method, all of which are discussed in the text. The top plot shows the data results, where clear η -dependent and overall biases are observed. The bottom plot shows MC, where a bias smaller by a factor of at least 10, with the exception of the electron E/p method.	105
240	720	Sagitta bias correction based on 2017 low-pile-up data at $\sqrt{s} = 13$ TeV. The statistical uncertainty (combined from uncertainties of the η -dependent correction and the global offset correction) is represented by error bars.	105

243	721 Comparison of reconstruction efficiencies for Medium muons using the low- μ runs of 2017 244 and 2018 at a centre-of-mass energy of $\sqrt{s} = 13$ TeV and $\sqrt{s} = 5$ TeV. Efficiencies are shown 245 as a function of muon η, p_T . Red (orange) points correspond to low- μ data (MC), while the 246 black (blue) points are high- μ data (MC). The bottom panels show the data/MC ratio for the 247 low- μ (orange) and high- μ (blue) sets with statistical and total uncertainties.	107
248	722 Comparison of TTVA efficiencies for Medium muons using the low- μ runs of 2017+18 at 249 $\sqrt{s} = 13$ TeV (top row) and low- μ runs of 2017 at $\sqrt{s} = 5$ TeV (lower row). The low- μ results 250 compared to a high- μ data set as specified in the plot legend. Efficiencies are shown as 251 function of muon η (left) and p_T (middle) and the mean number of interactions $\langle \mu \rangle$ (right). 252 Red (orange) points correspond to low- μ data (MC), while the black (blue) points are high- μ 253 data (MC). The bottom panels show the data/MC ratio for the low- μ (orange) and high- μ 254 (blue) sets with statistical and total uncertainties.	108
255	723 1D trigger efficiency and systematic uncertainty in data and MC, 5 and 13 TeV from 2017 256 and 2018 for probes from the eta barrel region and inclusive ϕ, p_T distributions. Trigger 257 sectors in the barrel and endcap regions are different, only the barrel trigger is shown here. 258 The bin edges correspond to physical edges of the trigger sectors.	109
259	724 Efficiencies for Ptvarcone20 isolation selections measured in 2017 and 2018 data and MC 260 13 TeV and 5 TeV as a function of muon η (left) and p_T (right). The bottom panels show the 261 data/MC scale factors with statistical uncertainties represented by blue boxes, while a sum 262 in quadrature of statistical and systematic uncertainties is represented by orange boxes. . .	110
263	725 Hadronic recoil	112
264	726 Comparison of the $\Sigma E_T - p_T^{\ell\ell}$ description in data of the two MC samples PowHEG and SHERPA 265 at 13 TeV, showing $\Sigma E_T - p_T^{\ell\ell}$ inclusively (left). Figure on the right shows the comparison of 266 SHERPA to the data after a dedicated pileup reweighting.	113
267	727 Ratio of data to predictions in $W \rightarrow \mu\nu$ events at 13 TeV for the $\Sigma \bar{E}_T$ distribution, before 268 and after each $\Sigma \bar{E}_T$ modeling reweighting step. The color band is the data statistical 269 uncertainty. The prediction uncertainty only includes the statistical uncertainty. 'Powheg' 270 uses the baseline MC for the signal. 'Powheg+Z2D' has the 2D ($\Sigma \bar{E}_T, p_T^{true,V}$), Z-based 271 reweighting applied. 'Powheg+Z2D+SETUT' adds the $\Sigma \bar{E}_T$ reweighting in bins of u_T . 272 'Powheg+Z2D+SETUT+1DPT' adds the 1D reweighting to recover the initial $p_T^{true,V}$ spectrum.	114
273	728 Ratio of data to predictions in $W \rightarrow \mu\nu$ events at 5 TeV for the $\Sigma \bar{E}_T$ distribution, before 274 and after each $\Sigma \bar{E}_T$ modeling reweighting step. The color band is the data statistical 275 uncertainty. The prediction uncertainty only includes the statistical uncertainty. 'Powheg' 276 uses the baseline MC for the signal. 'Powheg+Z2D' has the 2D ($\Sigma \bar{E}_T, p_T^{true,V}$), Z-based 277 reweighting applied. 'Powheg+Z2D+SETUT' adds the $\Sigma \bar{E}_T$ reweighting in bins of u_T . 278 'Powheg+Z2D+SETUT+1DPT' adds the 1D reweighting to recover the initial $p_T^{true,V}$ spectrum.	115
279	729 $\phi(u_T)$ at 5 and 13 TeV, for the data and the simulation before and after u_X and u_Y correction, 280 in Z events. The band in the ratio panel is the data statistical uncertainty.	117

281	81	Distributions for the 5 TeV low- μ dataset in a $Z/\gamma^* \rightarrow \mu\mu$ (top row) and a $Z/\gamma^* \rightarrow ee$ (bottom row) selection. The data (points) is compared to $Z/\gamma^* \rightarrow \mu\mu$ or $Z/\gamma^* \rightarrow ee$ signal MC, respectively. The left and middle plots show the actual μ in a coarsely-binned and a finely-binned version. The right plot shows the number of reconstructed primary vertices N_{PV}	120
286	82	Distributions for the 13 TeV low- μ datasets taken in 2017 and 2018 in a $Z/\gamma^* \rightarrow \mu\mu$ (top row) and a $Z/\gamma^* \rightarrow ee$ (bottom row) selection. The data (points) is compared to $Z/\gamma^* \rightarrow \mu\mu$ or $Z/\gamma^* \rightarrow ee$ signal MC, respectively. All distributions are (roughly) normalised to the same number of selected events in the 2017 dataset. The left and middle plots show the actual μ in a coarsely-binned and a finely-binned version. The right plot shows the number of reconstructed primary vertices N_{PV}	120
292	83	Distributions for the 5 TeV (left) and 13 TeV (right) low- μ dataset(s) in a $Z/\gamma^* \rightarrow \mu\mu$ (top row) and a $Z/\gamma^* \rightarrow ee$ (bottom row) selection. The data (points) is compared to $Z/\gamma^* \rightarrow \mu\mu$ or $Z/\gamma^* \rightarrow ee$ signal MC, respectively. The distributions of the z -position of the primary vertex selected as the hard interaction are compared for the dataset(s) and the MC simulation before (“no z_{vtx} rwgt”, blue, only 13 TeV) and after reweighting (black). For the 13 TeV data the 2017 and 2018 data are shown separately and all distributions are (roughly) normalised to the same number of selected events in the 2017 dataset.	126
299	84	ΣE_T^- distribution in the muon and electron channel for the $\sqrt{s} = 13$ TeV dataset.	130
300	85	ΣE_T distribution in the muon and electron channel for the $\sqrt{s} = 13$ TeV dataset.	131
301	86	\vec{E}_T^{miss} distribution in the muon and electron channel for the $\sqrt{s} = 13$ TeV dataset.	132
302	87	Transverse mass distribution of the W boson in the muon and electron channel for the $\sqrt{s} = 13$ TeV dataset.	133
304	88	Lepton pseudorapidity distribution in the muon and electron channel for the $\sqrt{s} = 13$ TeV dataset.	134
306	89	Lepton transverse momentum distribution in the muon and electron channel for the $\sqrt{s} = 13$ TeV dataset.	135
308	810	W transverse momentum distribution in the muon and electron channel for the $\sqrt{s} = 13$ TeV dataset.	136
310	811	ΣE_T^- distribution in the muon and electron channel for the $\sqrt{s} = 5$ TeV dataset.	137
311	812	ΣE_T distribution in the muon and electron channel for the $\sqrt{s} = 5$ TeV dataset.	138
312	813	\vec{E}_T^{miss} distribution in the muon and electron channel for the $\sqrt{s} = 5$ TeV dataset.	139
313	814	Transverse mass distribution of the W boson in the muon and electron channel for the $\sqrt{s} = 5$ TeV dataset.	140
315	815	Lepton pseudorapidity distribution in the muon and electron channel for the $\sqrt{s} = 5$ TeV dataset.	141
317	816	Lepton transverse momentum distribution in the muon and electron channel for the $\sqrt{s} = 5$ TeV dataset.	142

319	817	W transverse momentum distribution in the muon and electron channel for the $\sqrt{s} = 5$ TeV dataset.	143
320			
321	91	Unfolding	146
322	92	Breakdown of systematic uncertainties for 5 (a,b) and 13 (c,d) TeV in the electron channel at the reconstructed level	148
323			
324	93	Breakdown of systematic uncertainties for 5 (a,b) and 13 TeV (c,d) in the electron channel at the unfolded level	149
325			
326	94	Breakdown of systematic uncertainties for 5 (a,b) and 13 (c,d) TeV in the muon channel at the reconstructed level	150
327			
328	95	Breakdown of systematic uncertainties for 5 (a,b) and 13 TeV (c,d) in the muon channel at the unfolded level	151
329			
330	96	Unfolding bias on p_T^W in the electron channel after 3 iterations, for W^- (left) and W^+ (right), at 5 TeV (top) and 13 TeV (bottom).	153
331			
332	97	Unfolded measurement results in the W^- (left) and W^+ (right) electron channels, at 5 TeV (top) and 13 TeV (bottom).	154
333			
334	98	Unfolded measurement results in the W^- (left) and W^+ (right) muon channels, at 5 TeV (top) and 13 TeV (bottom).	155
335			
336	101	A: The nodes perform a linear transformation of the inputs, then apply a non-linear activation function. B: The architecture of a deep neural network: neurons are arranged into layers [dnn1].	160
337			
338			
339	102	A model of the Deep Neural Network (DNN) used in the analysis.	163
340			
341	111	$\Sigma \vec{E}_T$ systematic error breakdown in the muon and electron channel for the $\sqrt{s} = 5$ TeV and $\sqrt{s} = 13$ TeV datasets.	166
342			
343	112	ΣE_T systematic error breakdown in the muon and electron channel for the $\sqrt{s} = 5$ TeV and $\sqrt{s} = 13$ TeV datasets.	167
344			
345	113	\vec{E}_T^{miss} systematic error breakdown in the muon and electron channel for the $\sqrt{s} = 5$ TeV and $\sqrt{s} = 13$ TeV datasets.	168
346			
347	114	Transverse mass systematic error breakdown of the W boson in the muon and electron channel for the $\sqrt{s} = 5$ TeV and $\sqrt{s} = 13$ TeV datasets.	169
348			
349	115	Lepton pseudorapidity systematic error breakdown in the muon and electron channel for the $\sqrt{s} = 5$ TeV and $\sqrt{s} = 13$ TeV datasets.	170
350			
351	116	Lepton transverse systematic error breakdown distribution in the muon and electron channel for the $\sqrt{s} = 5$ TeV and $\sqrt{s} = 13$ TeV datasets.	171

352	117	W transverse momentum systematic error breakdown in the muon and electron channel for the $\sqrt{s} = 5$ TeV and $\sqrt{s} = 13$ TeV datasets.	172
-----	-----	--	-----

354

List of Tables

355	31	Energy and luminosity of the special low-mu runs.	35
356	41	ATLAS calorimeter in numbers	42
357	42	ATLAS muon spectrometer subsystems coverage and parameters	48
358	71	Values of η_{calo} bin frontiers for energy scale factors for low pile-up runs.	84
359	81	Monte Carlo samples at $\sqrt{s} = 13$ TeV. Given is a short description of the process, the ATLAS MC data set number (DSID), the names and version numbers of the MC generator(s), the used value of the higher order cross section times any branching and filter efficiencies ($\sigma \cdot \text{BR} \cdot \epsilon_{\text{filter}}$) with the theoretical uncertainty in percent (“th. unc.”), and finally the number of events analysed after skimming at derivation production ($N_{\text{evt}}^{\text{skim}}$) as well as the number of events originally processed and simulated ($N_{\text{evt}}^{\text{unskim}}$). In the case of $Z \rightarrow \ell\ell$ samples, the given $\epsilon_{\text{filter}} > 1$ is related to the fact, that the cross sections were calculated for $66 < m_{\ell\ell} < 116$ GeV, but the generated mass range is larger. The last section of $t\bar{t}$ samples refers to variation samples for systematics studies. The MC equivalent luminosity $N_{\text{evt}}^{\text{unskim}} / (\sigma \cdot \text{BR} \cdot \epsilon_{\text{filter}})$ is generally above 3fb^{-1} for signal and significant backgrounds, the exception are Powheg $W \rightarrow \tau\nu$ and $Z \rightarrow \tau\tau$ samples, that have about 0.45fb^{-1} only.	122
370	82	Alternative signal $Z \rightarrow \ell\ell$ Monte Carlo samples at $\sqrt{s} = 13$ TeV produced with SHERPA. General description of the table see Table 81. The samples are split into a long list of orthogonal slices based on “max(pTV,HT)” and filtered further into “b/c/light-jet” subcomponents. For the purpose of this analysis, the number of events in each slice is such that the samples are about 2fb^{-1} each (after application of a penalty factor for negative weight events) and an “inclusive sample” is restored after merging the slices.	123
376	83	Alternative signal $W \rightarrow \ell\nu$ Monte Carlo samples at $\sqrt{s} = 13$ TeV produced with SHERPA. See Table 82 for a description of the table. The samples are split into a long list of orthogonal slices based on “max(pTV,HT)” and filtered further into “b/c/light-jet” subcomponents. For the purpose of this analysis, the number of events in each slice is such that the samples are about 1fb^{-1} each (after application of a penalty factor for negative weight events) and an “inclusive sample” is restored after merging the slices.	124

382	84	Monte Carlo samples at $\sqrt{s} = 5\text{TeV}$. The table follows the same format as Table 81. The MC equivalent luminosity $N_{\text{evt}}^{\text{unskim}}/(\sigma \cdot \text{BR} \cdot \epsilon_{\text{filter}})$ is generally above 2.5fb^{-1} for signal and significant backgrounds, the exception are Powheg $W \rightarrow \tau\nu$ and $Z \rightarrow \tau\tau$ samples, that have about 0.20fb^{-1} and 0.45fb^{-1} only.	125
383	85	Analysis cut flow for $W^+ \rightarrow e^+\nu$ 5 TeV signal selection. Lepton p_T is required to be over 18 GeV before the final cut.	127
384	86	Analysis cut flow for $W^+ \rightarrow e^+\nu$ 13 TeV signal selection. Lepton p_T is required to be over 18 GeV before the final cut.	128
385	87	Analysis cut flow for $W^+ \rightarrow \mu^+\nu$ 5 TeV signal selection. Lepton p_T is required to be over 18 GeV before the final cut.	128
386	88	Analysis cut flow for $W^+ \rightarrow \mu^+\nu$ 13 TeV signal selection. Lepton p_T is required to be over 18 GeV before the final cut.	128
387	89	Analysis cut flow for $W^- \rightarrow e^-\nu$ 5 TeV signal selection. Lepton p_T is required to be over 18 GeV before the final cut.	129
388	90	Analysis cut flow for $W^- \rightarrow e^-\nu$ 13 TeV signal selection. Lepton p_T is required to be over 18 GeV before the final cut.	129
389	91	Analysis cut flow for $W^- \rightarrow \mu^-\nu$ 5 TeV signal selection. Lepton p_T is required to be over 18 GeV before the final cut.	129
390	92	Analysis cut flow for $W^- \rightarrow \mu^-\nu$ 13 TeV signal selection. Lepton p_T is required to be over 18 GeV before the final cut.	129
391	93	Observed and Expected yield comparison for all signal selections.	130

403 **0.1 Introduction**

404 **0.1.1 Historical retrospective**

405 The reductionistic idea that all the countless variety of matter types that surrounds us could be in fact
406 brought to a combination of much fewer substances has been around at least since the time of Ancient
407 Greece. A thought that you can construct everything you see around out of one or few (e.g. fire, earth,
408 water and air) indivisible elements ($\alpha\tauομοζ$ in Greek) is simple, logical and therefore conceptually
409 attractive. Knowing all about these elements could potentially grant us profound understanding
410 of nature. But it wasn't before the XIX century when this idea has become something more than a
411 philosophical concept and obtained solid scientific evidence.

412 The composition of the periodic table of elements in 1860s [1] was a tremendous step forward, reducing
413 the number of elements to O(100). The elements of the periodic table resembled the ancient Greek
414 concept so much, that they were christened atoms. But the periodic character of the table and strong
415 correlation of atom position in the table with its chemical properties was insinuating on a certain inner
416 structure of the atoms, a possibility for them to be composed out of even smaller objects. The discovery
417 of isotopes in 1913 [2] left little room for other explanation.

418 Further evidences in favour of atomistic views kept coming in late XIX and early XX centuries from
419 theoretical and experimental sides. The molecular kinetic theory has been heavily criticized throughout
420 the XIX century, but the explanation of the Brownian motion [3] has secured its dominance from there
421 on lying a foundation for what is to become the statistical physics. Of particular importance was the
422 discovery of the first subatomic particle in 1897, which was called the electron [4].

423 Further studies of radioactive materials have allowed to compose a seemingly consistent understanding
424 of what matter is composed of. By the time of neutron discovery in 1932 [5] the list of what was called
425 elementary particles was reasonably short: an electron, a proton, and a neutron. It was still left to figure
426 out how these elements interact forming the known atoms, molecules and all the matter around. That
427 required additional efforts on the theoretical side, including resolving the inconsistencies between the
428 two new branches of physics supposed to describe the microworld and the fields, namely the quantum
429 theory and the field theory.

430 To move forward the physicist have made use of another source of elementary particles - the cosmic
431 rays. Cosmic rays contained particles of much higher energies comparing to the radioactive materials.
432 Cosmic ray experiments have led to the discovery of the first known antiparticle - the positron [6],
433 confirming the theoretical predictions by Dirac [7]. Further discoveries of the muon [8], pion [9], kaon
434 [10] and Λ_0 [11] have shown that the list of elementary particles was still far from being completed.
435 The second half of the XX century has pronounced a new era in particle physics with the extensive use
436 of particle accelerators. Accelerators have become the main experimental tool in the discovery of new
437 particles and investigation of their properties. Comparing to the cosmic rays, accelerators could offer
438 higher energies and better control over the experimental conditions. Thanks to these new tools by the
439 end of 1960s the number of newly discovered particles has exceeded one hundred and kept growing,

440 apparently taking away the reductionistic dream of having a reasonably small number of elementary
441 particles.
442 On the other hand, the properties of the newly discovered particles (sometimes called "the particle
443 zoo") had provided enough experimental data for theorists to make further assumptions. The particles,
444 if grouped by their properties, have formed patterns - a situation resembling the old story with the
445 atoms of the periodic table. This observation has allowed to assume the existence of even smaller
446 fundamental particles with a fractional charge that would make up all the visible hadrons. These
447 particles were eventually called quarks [12], [13]. By the late 1960s hypothesizing the existence of only
448 three quarks was enough to explain all the visible particles and successfully predict new ones [14].
449 Since then three more quarks were discovered and as of now all the experimental evidence suggests
450 that the quarks are truly fundamental particles being indivisible in the Ancient Greek sense.
451 At the same time serious theoretical efforts were taken in order to describe the interactions between
452 fundamental particles, taking into account the known fundamental forces. In the mid-1970s a theory
453 called The Standard Model was finalized. It included three out of four known fundamental forces
454 (excluding the gravity) and predicted a number of particles which were not discovered by that time.
455 All the key predictions of the theory were successfully confirmed by further experiments, making it a
456 dominant theory in particle physics. The theory was able to describe all the surrounding matter with
457 only 12 fundamental fermions (and their antiparticles) and 5 bosons. The SM is described in more
458 detail in the Chapter 1.
459 Theoretical efforts aimed to further simplify the list of fundamental particles are ongoing, but up to
460 the time of this thesis writing none of them were confirmed experimentally.

461 **0.1.2 Actual challenges**

462 The establishment of the Standard Model was a colossal step forward in understanding of the mi-
463 croworld physics. Nevertheless despite its great success and very good agreement with vast majority of
464 the experimental data there is a number inconsistencies and lacunae in the theory, which do not allow
465 to think of the SM as of the final theory. Here are most notable of these problematic questions:

- 466 1. A number of neutrino experiments have established that the neutrinos have a tiny though non-
467 zero mass. The minimal Standard Model assumes neutrinos to be massless and does not allow to
468 provide mass to the neutrinos.
- 469 2. Astrophysical and cosmological evidences confirm the existence of the dark matter which does
470 not correspond to any of the SM particles.
- 471 3. Cosmological observations show a substantial disproportion between observed matter and anti-
472 matter in favour of the former. The SM does not provide an explanation how such an imbalance
473 could have been formed.

474 4. The discovery of the gravitational waves in 2016 had confirmed the existence of the graviton - the
475 mediator of the gravitational force. The gravitational force is not represented in any way in the
476 SM.

477 5. No explanation is provided to the vastly different magnitude of the fundamental forces, i.e. why
478 the gravity is 10^{24} times weaker than the weak force.

479 In order to attack these and other problems numerous efforts have been taken to either modify
480 the SM or to replace it with a more fundamental theory, but so far none of these Beyond Standard
481 Model (BSM) theories were ever confirmed experimentally. The SM is still a source of most accurate
482 predictions for any physical process that involves elementary particle interactions. Description of the
483 BSM theories goes beyond the scope of current thesis.

484 The SM depends on the list of 18 free parameters (to be described in more detail in Chapter 1).
485 These parameters can not be calculated intrinsically and must be measured experimentally. The more
486 precisely we know the values of these parameters - the better is the accuracy of the SM prediction.
487 Precise knowledge of the SM input parameters can also give hints on where to look for a more
488 fundamental theory.

489 The LHC experiments have already contributed greatly by discovering the last missing piece of the SM,
490 the Higgs boson. This has ended the era of SM particle discoveries but at the same time started the era
491 of LHC precision measurements. The LHC experiments were capable to measure some parameters
492 of the SM for the first time (like the mass of the Higgs boson), but also could improve the existing
493 measurements, boosting the predictive power of the SM.

494 This thesis is a part of an ongoing effort at the ATLAS experiment to improve the precision of the W
495 boson mass, which is also among the SM free parameters. The mass of the W boson was first measured
496 at Large Electron-Positron (LEP) after its discovery in 1983. The precision of the measurement was
497 further improved by the experiments at Tevatron collider. The only LHC result performed so far was
498 published by ATLAS collaboration in 2018.

499 Hadron colliders are a challenging environment for the W boson-related measurements, the precision
500 is highly impacted by a number of factors one of them being the pile-up. Current analysis is based on
501 the data collected during two special LHC runs with low pile-up, taken in 2017 and 2018.

502 0.1.3 Thesis composition

503 The first chapter contains the description of the Standard Model, its constituents and input parameters.
504 Chapter 2 is dedicated to W boson and its properties. Chapter 3 tells about the Large Hadron Collider
505 (LHC) and its operations. ATLAS detector is described in Chapter 4. Chapter 5 is dedicated to the
506 description of the shower shapes reweighting. And so on and so forth...

507 Bibliography

- 508 [1] Dmitri Mendeleev. *The principles of chemistry*. Saint Petersburg, 1869.
- 509 [2] F. Soddy. "The Radio-Elements and the Periodic Law". In: *Nature* 91 (20 Mar. 1913), pp. 57–58.
510 doi: 10.1038/091057a0. URL: <https://doi.org/10.1038/091057a0>.
- 511 [3] A. Einstein. "Über die von der molekularkinetischen Theorie der Wärme geforderte Bewegung
512 von in ruhenden Flüssigkeiten suspendierten Teilchen". In: *Annalen der Physik* 322 (5 May
513 1905), pp. 549–560. doi: 10.1002/andp.19053220806. URL: <https://doi.org/10.1002/andp.19053220806>.
- 514
- 515 [4] J.J. Thompson. "Cathode Rays". In: *Philosophical Magazine* 44 (Oct. 1897). doi: 10.1002/andp.19053220806. URL: <https://doi.org/10.1002/andp.19053220806>.
- 516
- 517 [5] J. Chadwick. "The existence of a neutron". In: *Proceedings of the Royal Society A*. 151 (June 1932),
518 pp. 479–493. doi: 10.1098/rspa.1932.0112. URL: <https://doi.org/10.1098/rspa.1932.0112>.
- 519
- 520 [6] C. D. Anderson. "The Positive Electron". In: *Physical Review* 46 (Mar. 1933), pp. 491–494. doi:
521 10.1103/PhysRev.43.491. URL: <https://doi.org/10.1103/PhysRev.43.491>.
- 522
- 523 [7] P. A. M. Dirac. "The quantum theory of the electron". In: *Proceedings of the Royal Society A*. 117
524 (Feb. 1928), pp. 610–624. doi: 10.1098/rspa.1928.0023. URL: <https://doi.org/10.1098/rspa.1928.0023>.
- 525
- 526 [8] Seth H. Neddermeyer and Carl D. Anderson. "Note on the Nature of Cosmic-Ray Particles".
In: *Phys. Rev.* 51 (10 May 1937), pp. 884–886. doi: 10.1103/PhysRev.51.884. URL: <https://link.aps.org/doi/10.1103/PhysRev.51.884>.
- 527
- 528 [9] C. M. G. LATTES et al. "PROCESSES INVOLVING CHARGED MESONS". In: *Nature* 159.4047
529 (May 1947), pp. 694–697. ISSN: 1476-4687. doi: 10.1038/159694a0. URL: <https://doi.org/10.1038/159694a0>.
- 530
- 531 [10] G. D. ROCHESTER and C. C. BUTLER. "Evidence for the Existence of New Unstable Elementary
532 Particles". In: *Nature* 160.4077 (Dec. 1947), pp. 855–857. ISSN: 1476-4687. doi: 10.1038/160855a0. URL: <https://doi.org/10.1038/160855a0>.
- 533
- 534 [11] V. D. Hopper and S. Biswas. "Evidence Concerning the Existence of the New Unstable Elementary
535 Neutral Particle". In: *Phys. Rev.* 80 (6 Dec. 1950), pp. 1099–1100. doi: 10.1103/PhysRev.80.1099.
536 URL: <https://link.aps.org/doi/10.1103/PhysRev.80.1099>.
- 537
- 538 [12] Murray Gell-Mann. "A Schematic Model of Baryons and Mesons". In: *Phys. Lett.* 8 (1964), pp. 214–
215. doi: 10.1016/S0031-9163(64)92001-3.
- 539
- 540 [13] G Zweig. "An SU₃ model for strong interaction symmetry and its breaking; Version 2". In:
541 CERN-TH-412 (Feb. 1964). Version 1 is CERN preprint 8182/TH.401, Jan. 17, 1964, 80 p. URL:
<http://cds.cern.ch/record/570209>.
-

- 542 [14] V. E. Barnes et al. “Observation of a Hyperon with Strangeness Minus Three”. In: *Phys. Rev. Lett.*
543 12 (8 Feb. 1964), pp. 204–206. doi: 10.1103/PhysRevLett.12.204. URL: <https://link.aps.org/doi/10.1103/PhysRevLett.12.204>.
544

1

The Standard Model

545

546

547 "Potentielle citation sans aucun rapport avec le sujet"

548 — Personne inconnue, contexte à déterminer

549 The SM of particle physics is a quantum field theory that postulates the existence of three generations
550 of quarks and leptons interacting through three fundamental forces: electromagnetic, weak and strong.
551 From the mathematical point of view the SM is a gauge quantum field theory that has internal sym-
552 metries of the unitary product group $SU(3) \times SU(2)_L \times U(1)$. The fourth fundamental force, namely
553 the gravity, is not included in the SM. Nevertheless, since the magnitude of the gravity interaction is
554 negligible on the microscopic scale, it has little to no effect on the precision of the SM predictions. The
555 model has 18¹ free input parameters - the physical constants that can not be predicted from within
556 the theory and must be measured experimentally. Evidently, the SM predictions are based on these
557 parameters, so the better we know them - the better we can predict how nature behaves on the micro-
558 level. The free parameters of the SM are briefly described in section 1.1

559

560 A comprehensive description of the quantum field theory formalism goes beyond the scope of
561 current dissertation and can be found in the corresponding textbooks [1], [2], [3], [4], [5], [6]. In the
562 following sections a brief overview of key SM features and constituent parts is provided.

563

564 1.1 General composition and key parameters

565 In this section I will describe the fields that enter the SM. Their existence and interactions result in
566 the three fundamental forces that are taken into account by the theory. The quanta of these fields are
567 also called fundamental particles and possess a number of properties like mass, charge (or charges),
568 spin etc (see figure 11). The fundamental particles are divided into two groups based on their spin:
569 particles with integer spin are called fermions and those with half-integer spin are bosons.
570 Let's start from the fermion sector. According to the Pauli exclusion principle[7] two fermions can not
571 occupy the same quantum numbers. This in turn, has a consequence that the fermions must occupy a

¹There are SM extensions that take into account the non-zero neutrino mass. Then the model gets 7 additional parameters, so their total number reaches 25. Although current thesis only considers the SM where neutrinos are massless.

572 finite volume in space-time and as a result make up matter. Half of the fundamental fermions have
573 colour charge and therefore take part in strong interaction - they are called quarks. The other six
574 fermions do not have colour charge and are called leptons (from Greek " $\lambda\epsilonπτοσ$ " meaning "little", as
575 they are lighter than the quarks of the same generation). Different types of quarks and leptons are also
576 called flavours, so there are 6 flavours of quarks and 6 flavours of leptons.

577 For some reason which is yet unknown the twelve elementary fermions make three generations.
578 Particles in the second and third generations have exactly the same charge and spin as the particles of
579 the first generation, but are heavier and also unstable. Normally the particles of higher generations
580 quickly decay down to their lighter kin of the first generation and can only be observed in cosmic rays
581 and particle accelerators. That means all the matter that surrounds us consists of four fundamental
582 fermions of the first generation²(the first column in Fig. 11).

583 The two quarks of the first generation are called up-quark and down-quark (or u-quark and d-quark
584 for short). All the nuclei of the ordinary matter we see around are built out of these two types of
585 quarks. Quarks are capable of interacting through all three SM forces: electromagnetic, weak and
586 strong. Electrons, muons and tau-leptons are sensitive to electromagnetic and weak interaction, while
587 neutrinos can interact (and therefore be detected) only through weak force. For this reason in particle
588 physics the term "leptons" is sometimes used in a narrow sense referring to electron-like particles only.
589 For all quarks and electron-like particles the antiparticles were observed as well as the corresponding
590 annihilation phenomena. It is still not clear if neutrinos annihilate

591 From our experience we know that matter interacts with matter. But within the SM fermions do not
592 interact with each other immediately. The interaction is mediated by boson-type particles. The SM
593 includes five types of bosons: four vector bosons serving as force carriers for electromagnetic, weak
594 and strong interactions, and a spinless Higgs boson whose role would be described in more detail in
595 the corresponding subsection 1.4.1. The Higgs boson along with W and Z bosons are massive, while
596 photons and gluons are massless.

597 The masses of the fundamental particles make 12 out of 18 free parameters of the SM³.
598 As it was mentioned, bosons interact with fermions through fundamental interactions. The interaction
599 depends on the charge of the interacting particles and on the type of the interaction itself. Each type
600 interaction has a coupling constant that defines the scale of the interaction. Hence two more parameters
601 to the SM: the strong and electromagnetic coupling constants (the latter is also called the fine structure
602 constant). Weak coupling constant is redundant since it can be obtained from other parameters.
603 And the remaining four parameters are coming from the Cabibbo-Kobayashi-Maskawa (CKM), that
604 contains information on the strength of the flavour-changing weak interaction. [8].

605 An important feature of the Quantum Field Theory (QFT) is that particles also interact with physical
606 vacuum. For instance, a charged particle polarizes the physical vacuum, so the vacuum screens the

²Strictly speaking we already know that this is not completely true for the neutrinos, as they oscillate between the flavours due to their tiny mass. But in the SM neutrinos are assumed massless.

³The masses of W and Z bosons can be replaced by other parameters, e.g. weak mixing angle θ_W and Higgs potential vacuum expectation value (v. e. v.).

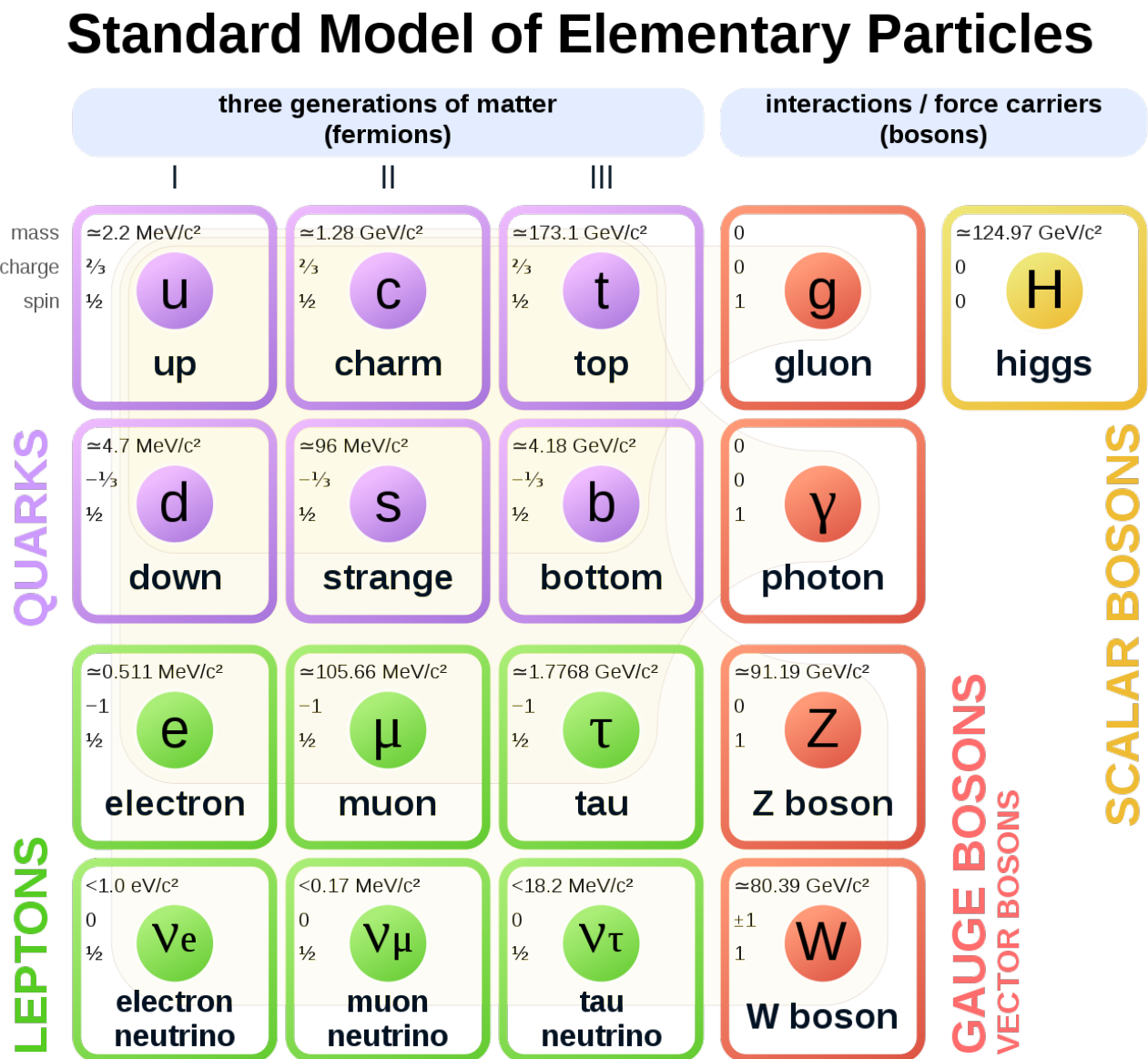


Figure 11: The list of particles that enters the SM[9].

607 charge of the particle[10].This interaction with virtual particles depends on the energy scale and so
 608 do the observed quantities like charge, mass etc. The SM is able to predict parameter evolution, so
 609 if the value of a certain input parameter q_0 is known at the energy Λ_0 then it is possible to predict
 610 its measurable value q at the energy Λ . This changing of physical parameters is an integral part of
 611 the QFT and is called *renormalisation* [2], [11]. In the picture 12 the dependence of the SM coupling
 612 constants on the energy is shown.

613

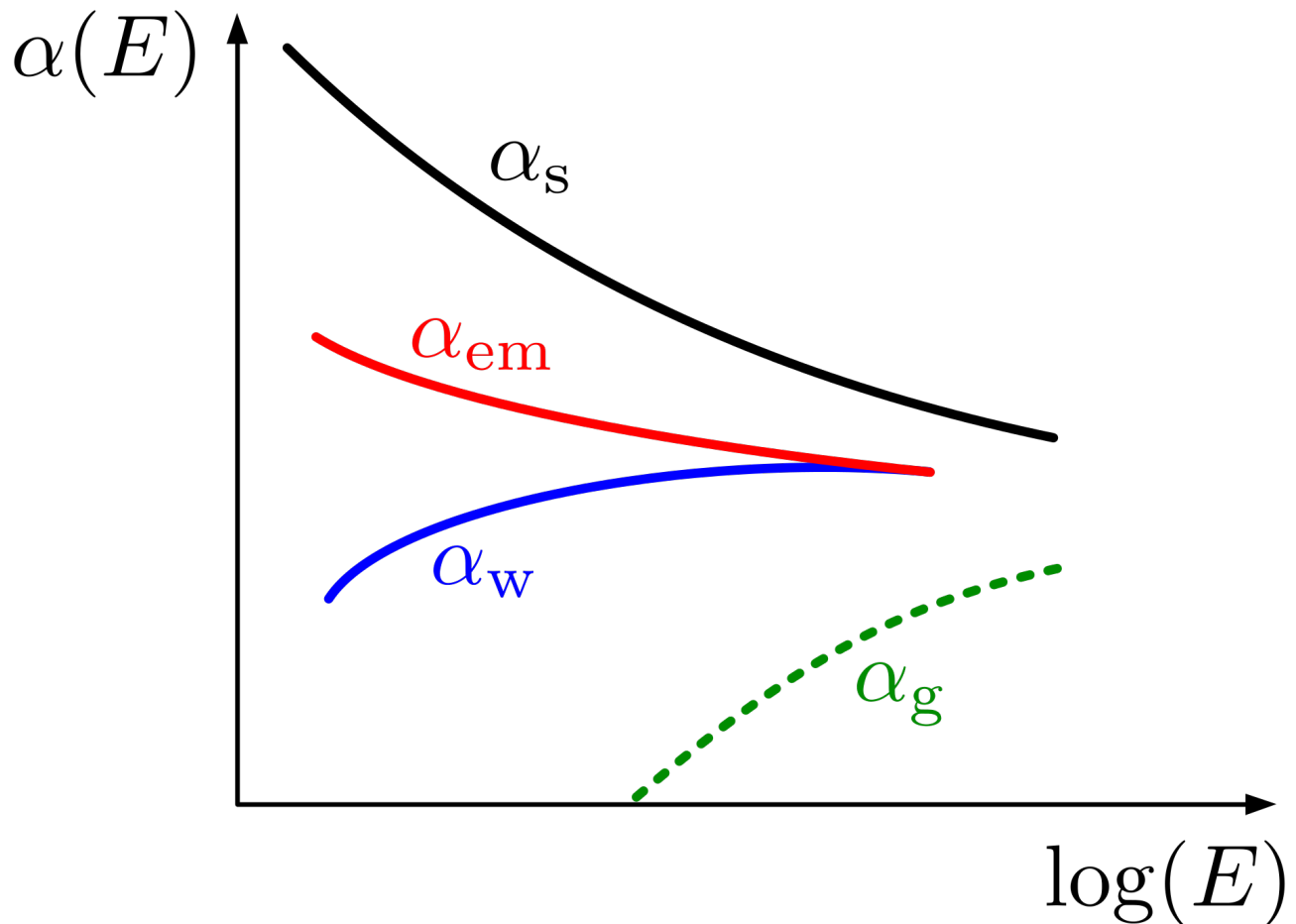


Figure 12: The evolution of the SM running coupling constants [12].

614 As we can see from picture 12 the strong coupling constant is getting smaller with the energy. This
 615 phenomena is called *the asymptotic freedom* [13], [14], [15].

616 1.2 Classical fields and gauge invariance principle

617 A consistent mathematical description of fields appears to be more challenging task compared to the
 618 description of physical objects that have definite size and shape. The derivation of Maxwell's equations

619 has been a great success and allowed to obtain the first equations of motion of relativistic fields. It has
 620 also subsequently led to understanding of special relativity [16], [17], [18]. Although for a more general
 621 case of fields other than electromagnetic it would be very useful to adopt a more systematic approach
 622 like that of Lagrangian or Hamiltonian in classical mechanics.

623 It has turned out that for the relativistic case Hamiltonian approach was not quite convenient, as
 624 the dedicated role of time over other degrees of freedom was in discord with relativistic space-time
 625 unification. However it was found possible to describe the fields within the Lagrangian approach. In
 626 the classic mechanics the action of a mechanical system of i mechanical objects is defined as:

$$S = \int L dt = \int \left(\sum_i T_i - U_i \right) dt,$$

627 where T_i and U_i are the kinetic and potential energies of the i^{th} object. Considering that by definition
 628 a field exists in every point of space-time, we need to define the Lagrangian density such that $L =$
 629 $\int \mathcal{L}(\phi, \partial_k \phi, \dot{\phi}) d^3x$, where ϕ is a field and $\partial_k \phi = \nabla \phi$ - the field gradient, $\partial_k = \frac{\partial}{\partial x^k}$, $k = 1, 2, 3$. Here and
 630 further Latin indices run through (1, 2, 3) and are used to denote spacial coordinates, while Greek
 631 indices denote space-time coordinates and run though (0, 1, 2, 3). So the action would look like:

$$S = \int L dt = \int \mathcal{L}(\phi, \partial_\mu \phi, \dot{\phi}) d^4x, \quad (1.1)$$

632 Now we may use the principle of least action to obtain the equations of motion using the Euler-
 633 Lagrange formalism. Let's check it with the example of electromagnetic fields. The Lagrangian density
 634 of electromagnetic fields in a vacuum can be written like:

$$S = -\frac{1}{4} \int F^{\mu\nu} F_{\mu\nu} d^4x. \quad (1.2)$$

635 Electromagnetic tensor can be defined in terms of electric and magnetic field intensities: $F_{i0} = -F_{0i} = E_i$,
 636 $F_{ij} = \epsilon_{ijk} H_k$, where ϵ_{ijk} - anti-symmetric Levi-Civita symbol. Alternatively $F_{\mu\nu}$ can be defined in terms
 637 of 4-potential A_μ :

$$F_{\mu\nu} = \partial_\mu A_\nu - \partial_\nu A_\mu. \quad (1.3)$$

638 Now we can safely apply the variational principle and putting $\delta S = 0$ obtain the Maxwell equations in
 639 a vacuum:

$$\partial_\mu F_{\mu\nu} = 0. \quad (1.4)$$

640 Noticing the symmetries of the system and using the Noether's theorem[19] we can find the invariants
 641 of electromagnetic field. For example, translational symmetry in time and space ensures conservation
 642 of energy and momentum. Let's now consider a symmetry of a different kind. The field potential can
 643 be shifted by a gradient of an arbitrary function $\alpha = \alpha(x^\mu)$:

$$\begin{aligned} A_\mu(x) &\rightarrow A'_\mu(x) = A_\mu(x) + \partial_\mu \alpha(x) \\ F_{\mu\nu} &\rightarrow F'_{\mu\nu} = \partial_\mu(A_\nu(x) + \partial_\nu \alpha(x)) = \partial_\mu A_\nu - \partial_\nu A_\mu = F_{\mu\nu}. \end{aligned} \quad (1.5)$$

644 Let's now consider the electromagnetic theory in the presence of charges and currents:

$$\mathcal{L} = -\frac{1}{4}F^{\mu\nu}F_{\mu\nu} + j^\mu A_\mu. \quad (1.6)$$

645 Now we have an interaction of a field potential A_μ with 4-current $j^\mu = (-\rho, j^i)$. It turns out to be a
646 general property of the field theories: the only form of interaction allowed is between a gauge field and
647 a current. After applying the gradient field transformation and the least action principle we can obtain
648 the corresponding conservation law:

$$\partial_\mu j^\mu = 0. \quad (1.7)$$

649 So this gradient symmetry[2] or as it is called more often gauge symmetry leads to the conservation of
650 electric current. If a theory is invariant under gauge transformations then it is called a gauge invariant
651 theory. As we have just seen electrodynamics is the simplest example of such a theory. Taking gauge
652 symmetries into consideration [20] has played a huge role in the development of the SM.

653 Gauge degree of freedom can be constrained in arbitrary way by applying additional conditions on the
654 gauge function. This is called fixing the gauge and becomes necessary after quantization. Any physical
655 result must be gauge-invariant, i.e. must not depend on the gauge.

656 1.3 Quantum electrodynamics

657 Quantum Electrodynamics (QED) is a theory of interaction between light and electrically charged
658 particles. Historically it was the first quantum field theory to reach good agreement between quantum
659 mechanics and special relativity. QED vacuum has zero expectation value. Nowadays it is considered
660 to be one of the most precise physical theories ever: theory predictions and experiment results agree up
661 to $O(10^{-8})$. It has also served as a model for composition of the subsequent parts of the SM, describing
662 other fundamental interactions.

663 Let's consider free Dirac field based Lagrangian:

$$\mathcal{L} = \bar{\psi}(x)(i\cancel{\partial} + m)\psi(x), \quad (1.8)$$

664 where ψ and $\bar{\psi}$ are Dirac wave function and its complex conjugate respectively, $\cancel{\partial} \equiv \gamma_\mu \partial^\mu$, γ_μ is one of
665 the four gamma-matrices and m is the mass of the Dirac field. Such a theory, though, would not be
666 physically consistent. This reflects the fact the quantum nature of spin and spinor fields have to be
667 treated as quantum fields. For instance, an attempt to calculate the energy of a Dirac field would lead
668 to a contradiction: the energy would not be positively defined, as some spinors would have negative
669 energies.

670 This Lagrangian has an internal symmetry to the U(1) transformation: $\psi \rightarrow e^{-i\alpha(x)}\psi$, $\bar{\psi} \rightarrow e^{i\alpha(x)}\bar{\psi}$.
671 According to Noether's theorem this symmetry implies current conservation: $j^\mu = \bar{\psi}\gamma^\mu\psi$. Now let's get
672 the combined Lagrangian of electromagnetic and Dirac fields, adding the interaction term:

$$\mathcal{L} = \mathcal{L}_{Dirac^{free}} + \mathcal{L}_{EM^{free}} + \mathcal{L}_{Interaction} = -\frac{1}{4}F^{\mu\nu}F_{\mu\nu} + \bar{\psi}(x)(i\cancel{\partial} + m)\psi(x) - q\bar{\psi}\gamma^\mu A_\mu\psi, \quad (1.9)$$

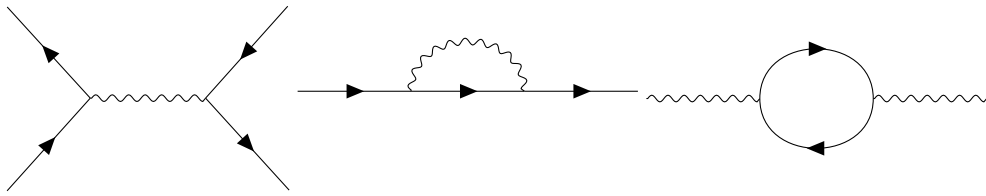


Figure 13: The QEQ diagrams: Compton scattering, electron self-energy, photon self-energy.

673 where q represents the elementary electric charge. This Lagrangian above is gauge invariant and can be
674 rewritten in a more convenient form:

$$\mathcal{L} = -\frac{1}{4}F^{\mu\nu}F_{\mu\nu} + \bar{\psi}(x)(iD + m)\psi(x), \quad (1.10)$$

675 where $D_\mu = \partial_\mu + iqA_\mu$ is a covariant derivative. If one considers space-time in the presence of a field as
676 curved, then A_μ would play a role of connectivity. It must be noted that values like m and q meaning
677 electron mass and charge⁴ are the SM input parameters mentioned in 1.1.

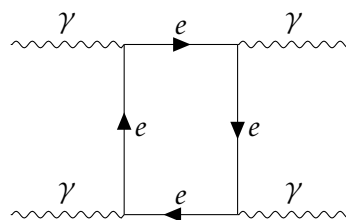
678 Further calculations are to be performed by the means of the quantum field theory formalism that
679 treats interaction terms like a perturbation to the free fields, making power series expansion in the
680 coupling constant. In the case of electrodynamics the coupling constant is quite small so good precision
681 is reached soon. Since the photons do not directly interact with other photons, QED allows only one
682 type of vertex - with two electron lines and one photon line.

683

684 Although the tree-level processes and diagrams were well understood by 1930th, the loop diagrams
685 were properly explained only by the end of the 1940th making it possible obtain numerical results
686 of the higher orders of power series expansion and achieve higher precision predictions for QED
687 processes[21], [10], [22], [23], [24], [25], [26], [27].

688 It must be noted that although direct photon-photon interaction is impossible, light-by-light scattering
689 is still possible through loops:

690



691

692 This process was theoretically described in 1936 [28] and experimentally observed 83 years after in
693 heavy ion collisions at the LHC [29].

⁴Charge of the electron is related to the electromagnetic coupling constant.

694 1.4 Electroweak theory and the Higgs mechanism

695 All the fermions of the standard model are subject to weak interaction, so its importance for physical
 696 processes can not be underestimated. At low energy weak interaction manifests itself mainly through
 697 flavour-changing decays like beta-decay and muon decay. The electroweak theory was created in the
 698 end of 1950s[11] [5] [30] thanks to numerous experimental results that allowed to shape its properties.
 699 The theory assumed that the electromagnetic and weak fundamental forces are actually manifestation
 700 of the same field that has a gauge symmetry $SU(2)_L \times U(1)$ with massive charged and neutral bosons.
 701 A few years later the structure of electroweak vacuum was explained along with the mechanism that
 702 has allowed the bosons to gain mass [31], [32]. Assuming this the Lagrangian of the electroweak theory
 703 must consist of three parts[33]:

- 704 • Gauge fields that would mediate the interaction.
- 705 • Fermions that interact with gauge fields
- 706 • A scalar Higgs field with non-zero vacuum energy that breaks the $SU(2)$ symmetry and couples
 707 to the fermions.

$$\mathcal{L}_{EW} = \mathcal{L}_{Gauge} + \mathcal{L}_{Higgs} + \mathcal{L}_{Fermions} \quad (1.11)$$

708 1.4.1 Electroweak gauge fields

709 As it was already pointed out before, knowing the symmetries of a physical system allows one to
 710 compose the gauge fields Lagrangian. The part with $U(1)$ symmetry would look like the electromagnetic
 711 field from 1.2 having the hypercharge Y , a vector potential B_μ and a gauge coupling g_1 . The $SU(2)$ field
 712 would have 3 vector components $W_\mu^{1,2,3}$, three isospin operators I_1, I_2, I_3 and a gauge coupling g_2 . We
 713 can pick the Pauli matrices σ^i as the representation of generators of the $SU(2)$ group, then the structure
 714 constants are ϵ_{abc} - Levi-Civita symbol.

$$\begin{aligned} \mathcal{L}_G &= -\frac{1}{4}B_{\mu\nu}B^{\mu\nu} - \frac{1}{4}W_{\mu\nu}^a W^{\mu\nu,a}B_{\mu\nu} = \partial_\mu B_\nu - \partial_\nu B_\mu \\ W_{\mu\nu}^a &= \partial_\mu W_\nu - \partial_\nu W_\mu + g_2 \epsilon_{abc} W_\mu^b W_\nu^c, \end{aligned} \quad (1.12)$$

715 where the term $g_2 \epsilon_{abc} W_\mu^b W_\nu^c$ appears due to the non-Abelian nature of the $SU(2)$ group (the generators
 716 don't commute).

717 1.4.2 Fermion sector

718 Each fundamental fermion generation expressed as left-handed doublets and right-handed singlets is a
 719 fundamental representation of the group $SU(2) \times U(1)$:

$$\begin{pmatrix} \nu_e \\ e \end{pmatrix}_L, \begin{pmatrix} \nu_\mu \\ \mu \end{pmatrix}_L, \begin{pmatrix} \nu_\tau \\ \tau \end{pmatrix}_L, (e_R), (\mu_R), (\tau_R), \quad (1.13)$$

$$\begin{pmatrix} u \\ d \end{pmatrix}_L, \begin{pmatrix} c \\ s \end{pmatrix}_L, \begin{pmatrix} b \\ t \end{pmatrix}_L, (u_R), (d_R), (c_R), (s_R), (t_R), (b_R). \quad (1.14)$$

720 Their quantum states are classified using the following quantum numbers: weak isospin I_3, I , weak
 721 hypercharge Y . Their electric charge can be obtained using the Gell-Mann-Nishijima relation:

$$Q = I_3 + \frac{Y}{2}. \quad (1.15)$$

722 The fermions are divided by their chirality: only the left-handed particles take part in weak
 723 interaction. The left-handed fermion fields of each lepton and quark generation j

$$\psi_j^L = \begin{pmatrix} \psi_{j+}^L \\ \psi_{j-}^L \end{pmatrix} \quad (1.16)$$

724 make SU(2) doublets, with indices $\sigma = \pm$, while the right-handed fermions can be written as singlets:

$$\psi_j^R = \psi_{j\sigma}^L. \quad (1.17)$$

725 Like in the electromagnetic case we can define the covariant derivative that would ensure the gauge
 726 invariance of the Lagrangian:

$$D_\mu = \partial_\mu - ig_2 I_a W_\mu^a + ig_1 \frac{Y}{2} B_\mu, \quad (1.18)$$

727 with $I_a \equiv \frac{\sigma_a}{2}$, then fermion Lagrangian takes the following form:

$$\mathcal{L}_{Fermions} = \sum_f \bar{\psi}_j^L i \gamma^\mu D_\mu \psi_j^L + \sum_{f,\sigma} \bar{\psi}_{f,\sigma}^R i \gamma^\mu D_\mu \psi_{f,\sigma}^R. \quad (1.19)$$

728 1.4.3 Higgs fields breaking the symmetry

729 The Higgs field is represented by single complex scalar doublet field $\Phi(x)$, that has 4 independent
 730 components. It spontaneously breaks the $SU(2) \times U(1)$ gauge symmetry, leaving the $U(1)_{EM}$ symmetry
 731 intact. The Higgs field doublet has the hypercharge $Y = 1$:

$$\Phi(x) = \begin{pmatrix} \phi^+(x) \\ \phi^0(x) \end{pmatrix}. \quad (1.20)$$

732 The Higgs field Lagrangian with non-zero vacuum expectation value:

$$\mathcal{L}_{Higgs} = (D_\mu \Phi)^+ (D_\mu \Phi) - V(\Phi) + \mathcal{L}_{Yukawa}. \quad (1.21)$$

733 The gauge invariance of the Higgs Lagrangian is ensured in the traditional way by using the covariant
734 derivative:

$$D_\mu = \partial_\mu - ig_2 I_a W_\mu^a + i\frac{g_1}{2} B_\mu. \quad (1.22)$$

735 Higgs potential contains the mass term and quartic self-interaction:

$$V(\Phi) = -\mu^2 \Phi^+ \Phi + \frac{\lambda}{4} \partial_\mu (\Phi^+ \Phi)^2. \quad (1.23)$$

736 Valuum expectation value $\langle \Phi \rangle$ does not vanish:

$$\langle \Phi(x) \rangle = \frac{1}{\sqrt(2)} \begin{pmatrix} 0 \\ v \end{pmatrix}, \quad v = \frac{2\mu}{\sqrt(\lambda)}. \quad (1.24)$$

737 Applying the unitarity gauge [34] we can constraint three out of four degrees of freedom of the Higgs
738 field and rewrite the Higgs doublet in the following way:

$$\Phi(x) = \frac{1}{2} \begin{pmatrix} 0 \\ v + H(x) \end{pmatrix}, \quad (1.25)$$

739 which leaves us with a physical real neutral scalar field $H(x)$ with

$$M_H = \sqrt(2)\mu. \quad (1.26)$$

740 This real field would couple to itself forming triple and quartic self-coupling vertices, to the gauge
741 fields through the covariant derivatives and to the charged fermions, giving them mass. Yukawa term
742 in Lagrangian the unitary gauge:

$$\mathcal{L}_{Yukawa} = - \sum_f m_f \bar{\psi}_f \psi_f - \sum_f \frac{m_f}{v} \bar{\psi}_f \psi_f H, \quad (1.27)$$

743 where

$$m_f = g_f \frac{v}{\sqrt(2)} = \sqrt(2) \frac{g_f}{g_2} M_W. \quad (1.28)$$

744 Higgs coupling constants to the corresponding fermion flavour are denoted as g_f . This relation
745 between the Higgs coupling and the mass of the W boson illustrates how much the SM parameters are
746 intertwined and particularly underlines the importance of the M_W measurement.

747 1.4.4 Physical interpretation of gauge fields and parameters

748 Higgs coupling to the gauge fields results in the following terms in the Lagrangian:

$$\frac{1}{2} \frac{g_2}{2} v (W_1^2 + W_2^2) + \frac{v^2}{4} (W_\mu^3, B_\mu) \begin{pmatrix} g_2^2 & g_1 g_2 \\ g_1 g_2 & g_1^2 \end{pmatrix} \begin{pmatrix} W_\mu^3 \\ B_\mu \end{pmatrix}. \quad (1.29)$$

749 In order to get the physical meaning of this expression let us make a transition to the basis of physical
 750 fields:

$$\begin{aligned} W_\mu^\pm &= \frac{1}{\sqrt{2}}(W_\mu^+ \mp iW_\mu^-) \\ \begin{pmatrix} Z_\mu \\ A_\mu \end{pmatrix} &= \begin{pmatrix} \cos\theta_W & \sin\theta_W \\ -\sin\theta_W & \cos\theta_W \end{pmatrix} \begin{pmatrix} W_\mu^3 \\ B_\mu \end{pmatrix}, \end{aligned} \quad (1.30)$$

751 where θ_W is called the weak mixing angle or the Weinberg angle. In the new basis expression 1.29 has
 752 transparent physical sense:

$$M_W^2 W_\mu^+ W^{-\mu} + \frac{1}{2}(A_\mu, Z_\mu) \begin{pmatrix} 0 & 0 \\ 0 & M_Z^2 \end{pmatrix} \begin{pmatrix} A_\mu \\ Z_\mu \end{pmatrix}, \quad (1.31)$$

753 with

$$\begin{aligned} M_W &= \frac{1}{2}g_2 v \\ M_Z &= \frac{1}{2}\sqrt{g_1^2 + g_2^2}v. \end{aligned} \quad (1.32)$$

754 The mixing angle θ_W also has a very clear physical meaning:

$$\cos\theta_W = \frac{g_2}{g_1^2 + g_2^2} = \frac{M_W}{M_Z}. \quad (1.33)$$

755 With A_μ having a sense of electromagnetic potential its coupling to the electron must have a physical
 756 meaning of the electric charge $e = \sqrt{4\pi\alpha}$ we can express e in terms of gauge couplings:

$$e = \frac{g_1 g_2}{g_1^2 + g_2^2}, \quad g_2 = \frac{e}{\sin\theta_W}, \quad g_1 = \frac{e}{\cos\theta_W}. \quad (1.34)$$

757 Thus the demonstrated Weinberg rotation fully replaces the original parameters $g_1, g_2, \lambda, \mu^2, g_f$ by
 758 another set of measurable values e, M_W, M_Z, M_H, m_f which are the input parameters of the SM.

759 1.5 Chromodynamics

760 The Quantum Chromodynamics (QCD) is a non-Abelian gauge theory that describes strong interaction.
 761 The QCD is symmetric under unbroken SU(3) colour symmetry, so the interaction scheme is built in
 762 the same way as electromagnetic and electroweak theories. To preserve the gauge invariance the gauge
 763 field of gluons is introduced with 8 components, since SU(N) group has $\frac{N^2-1}{2}$ independent elements.
 764 The gluons are massless vector bosons like the photons, although because of the non-Abelian nature of
 765 the gauge group they couple not only to the fermions but also to the other gluons. The gauge invariant
 766 QCD Lagrangian with kinetic term containing covariant derivative would look like:

$$\begin{aligned} \mathcal{L}_{QCD} &= -\frac{1}{4}F_{\mu\nu}^a F_a^{\mu\nu} + \bar{\psi}_a(i(\gamma^\mu D_\mu)^{ab} - m\delta^{ab})\psi_b, \\ F_{\mu\nu}^a &= \partial_\mu A_\nu^a - \partial_\nu A_\mu^a + g_s f^{abc} A_\mu^b A_\nu^c, \\ D_\mu &= \partial_\mu + ig_s A_\mu^a t_a. \end{aligned} \quad (1.35)$$

767 with ψ being the quark field, m is the mass of the quark, $a, b = 1, 2, \dots, 8$ are the colour indices, g_s is the
 768 strong coupling constant, f^{abc} are the structure constants of the SU(3) group and t_a are the generators

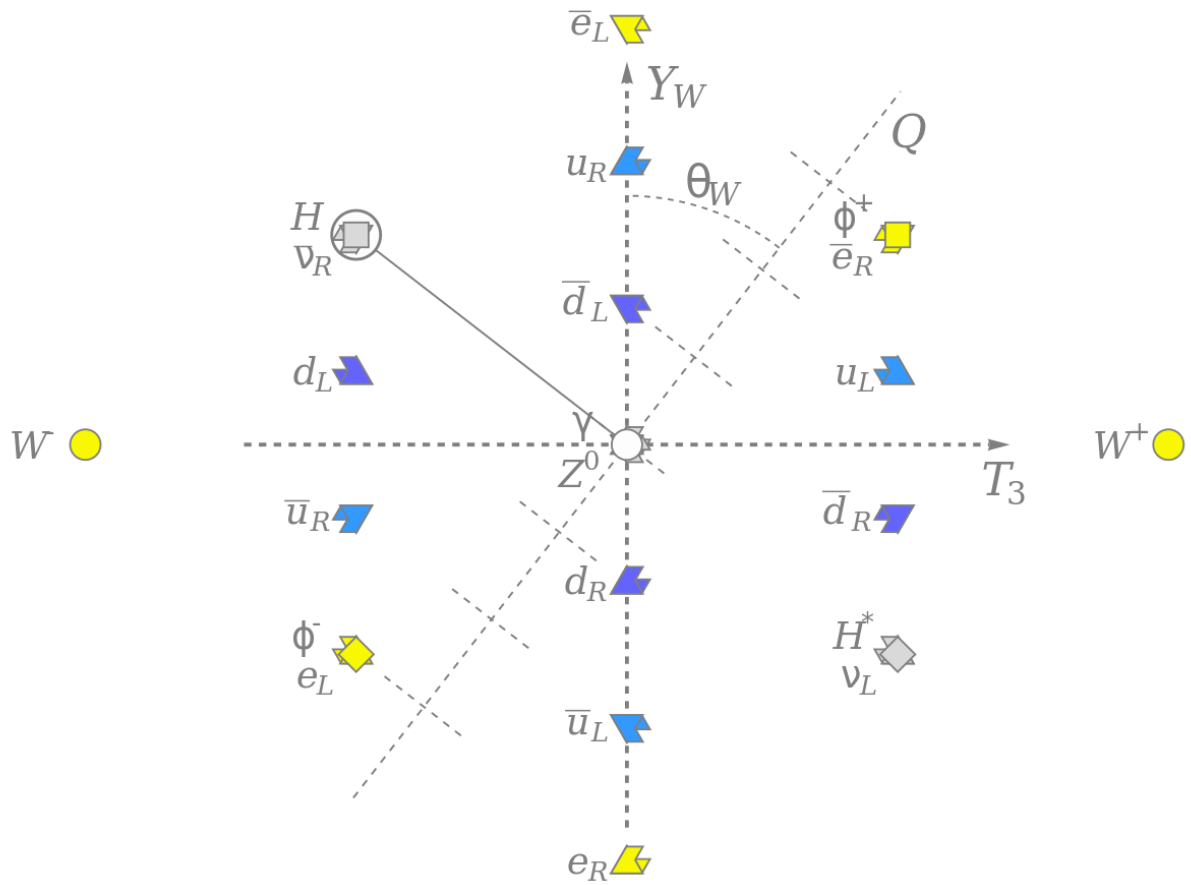


Figure 14: Electroweak sector and the Weinberg rotation [12].

769 of the SU(3) group.

770 As it was already mentioned in 1.3 quantitative calculations in QFT treat particle interaction as a
 771 perturbation to the free field theory. Coupling constant is considered to be a small parameter so every
 772 next power of the coupling constant is much smaller than the previous. Thanks to the asymptotic
 773 freedom α_s becomes small at higher energies and allows perturbative calculations. But at certain
 774 energy scale called $\Lambda_{QCD} \approx 200$ MeV, QCD becomes non-perturbative. It means we may no longer
 775 assume that interaction is a small perturbation of the free fields. This phenomena is known as the
 776 *colour confinement*.

777 Because of the colour confinement we can only observe colourless objects like baryons and mesons,
 778 but not quarks and gluons. If a high-energetic parton gets torn out of a hadron then it creates an
 779 avalanche-like process creating quark-antiquark pairs until fully hadronizes (see pic. 15) confining its
 780 colour. Such an avalanche is called a hadronic jet.

781

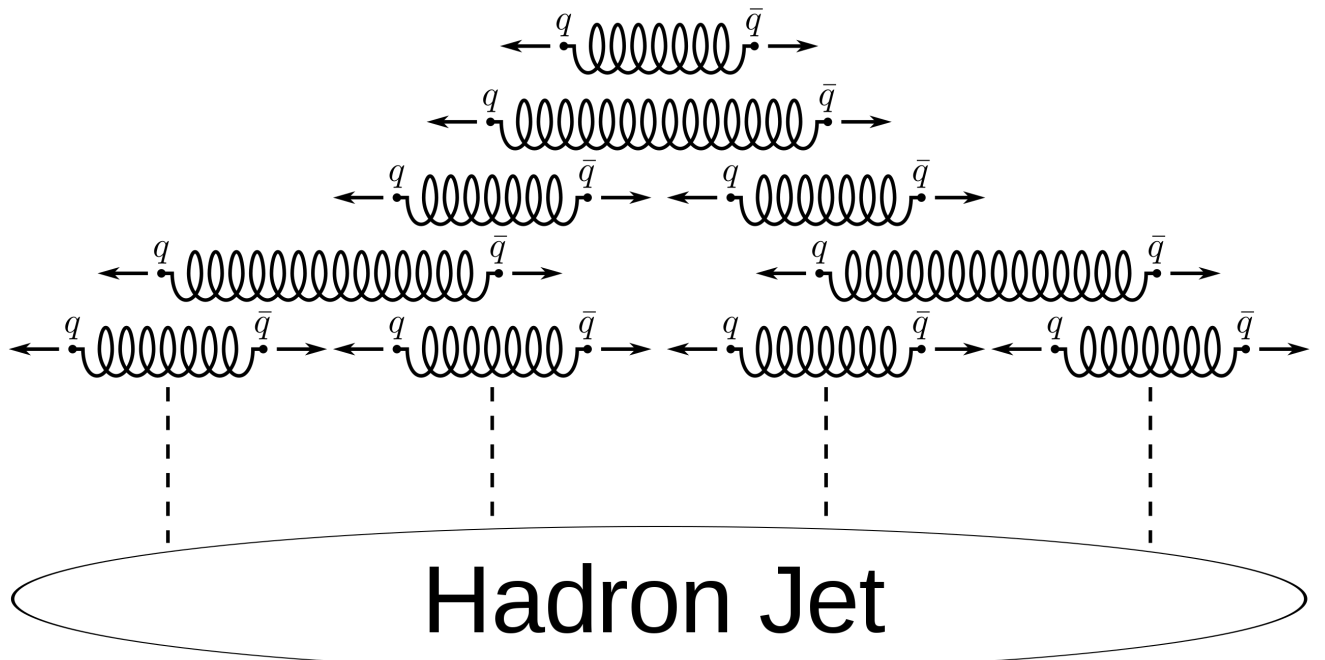


Figure 15: The formation of a jet [35].

782 Currently there is no viable physical theory that would describe QCD vacuum and low-energy
 783 behaviour of quarks and gluons. This also means that although nuclear forces are evidently residuals
 784 of the QCD interaction of partons within the baryons, there is no continuity between the QCD and
 785 nuclear physics. Confinement and low-energy QCD remain to be an unsolved problem of modern
 786 physics.

787 **Bibliography**

- 788 [1] Michael E Peskin and Daniel V Schroeder. *An introduction to quantum field theory*. Includes
789 exercises. Boulder, CO: Westview, 1995. URL: <https://cds.cern.ch/record/257493>.
- 790 [2] D.V. Shirkov N.N. Bogolyubov. *Quantum fields*. Addison-Wesley, 1982.
- 791 [3] Mark Srednicki. *Quantum Field Theory*. Cambridge: Cambridge Univ. Press, 2007. URL: <https://cds.cern.ch/record/1019751>.
- 792 [4] V.B. Berestetskii. A.I. Akhiezer. *Quantum Electrodynamics*. Interscience Publishers, 1965.
- 793 [5] Steven Weinberg. *The Quantum Theory of Fields, Volume 1: Foundations*. Cambridge University
794 Press, 2005. ISBN: 0521670535. URL: <http://www.amazon.com/Quantum-Theory-Fields-Foundations/dp/0521670535>SubscriptionId%3D13CT5CVB80YFWJEPWS02%26tag%3Dws%
795 26linkCode%3Dxm%26camp%3D2025%26creative%3D165953%26creativeASIN%3D0521670535.
- 796 [6] David J Griffiths. *Introduction to elementary particles; 2nd rev. version*. Physics textbook. New York,
797 NY: Wiley, 2008. URL: <https://cds.cern.ch/record/111880>.
- 798 [7] W Pauli. "Über den EinfluSS der Geschwindigkeitsabhängigkeit der Elektronenmasse auf den
799 Zeeman-Effekt". In: *Z. Phys.* 31 (1925), pp. 373–385.
- 800 [8] J. Beringer et al. "Review of Particle Physics". In: *Phys. Rev. D* 86 (1 July 2012), p. 010001. doi:
801 [10.1103/PhysRevD.86.010001](https://doi.org/10.1103/PhysRevD.86.010001). URL: <https://link.aps.org/doi/10.1103/PhysRevD.86.010001>.
- 802 [9] *Standard Model particles*. URL: https://en.wikipedia.org/wiki/Standard_Model.
- 803 [10] Julian Schwinger. "Quantum Electrodynamics. II. Vacuum Polarization and Self-Energy". In:
804 *Phys. Rev.* 75 (4 Feb. 1949), pp. 651–679. doi: [10.1103/PhysRev.75.651](https://doi.org/10.1103/PhysRev.75.651). URL: <https://link.aps.org/doi/10.1103/PhysRev.75.651>.
- 805 [11] Sheldon L. Glashow. "The renormalizability of vector meson interactions". In: *Nucl. Phys.* 10
806 (1959), pp. 107–117. doi: [10.1016/0029-5582\(59\)90196-8](https://doi.org/10.1016/0029-5582(59)90196-8).
- 807 [12] *Standard Model particles*. URL: https://en.wikipedia.org/wiki/Coupling_constant.
- 808 [13] David J. Gross and Frank Wilczek. "Ultraviolet Behavior of Non-Abelian Gauge Theories". In:
809 *Phys. Rev. Lett.* 30 (26 June 1973), pp. 1343–1346. doi: [10.1103/PhysRevLett.30.1343](https://doi.org/10.1103/PhysRevLett.30.1343). URL:
810 <https://link.aps.org/doi/10.1103/PhysRevLett.30.1343>.
- 811 [14] H. David Politzer. "Reliable Perturbative Results for Strong Interactions?" In: *Phys. Rev. Lett.* 30
812 (26 June 1973), pp. 1346–1349. doi: [10.1103/PhysRevLett.30.1346](https://doi.org/10.1103/PhysRevLett.30.1346). URL: <https://link.aps.org/doi/10.1103/PhysRevLett.30.1346>.
- 813 [15] V. S. Vanyashin and M. V. Terent'ev. "The Vacuum Polarization of a Charged Vector Field". In:
814 *Soviet Journal of Experimental and Theoretical Physics* 21 (Aug. 1965), p. 375.

- 820 [16] Albert Einstein. "Zur Elektrodynamik bewegter Körper. (German) [On the electrodynamics of
821 moving bodies]". In: *Annalen der Physik* 322.10 (1905), pp. 891–921. doi: <http://dx.doi.org/10.1002/andp.19053221004>.
- 823 [17] M. H. Poincare. "Sur la dynamique de l'électron". In: *Rendiconti del Circolo Matematico di Palermo*
824 (1884-1940) 21.1 (Dec. 1906), pp. 129–175. issn: 0009-725X. doi: 10.1007/BF03013466. url:
825 <https://doi.org/10.1007/BF03013466>.
- 826 [18] H. A. Lorentz. "Simplified Theory of Electrical and Optical Phenomena in Moving Systems". In:
827 *Koninklijke Nederlandse Akademie van Wetenschappen Proceedings Series B Physical Sciences* 1 (Jan.
828 1898), pp. 427–442.
- 829 [19] E. Noether. "Invariante Variationsprobleme". ger. In: *Nachrichten von der Gesellschaft der Wis-*
830 *senschaften zu Göttingen, Mathematisch-Physikalische Klasse* 1918 (1918), pp. 235–257. url: <http://eudml.org/doc/59024>.
- 832 [20] C. N. Yang and R. L. Mills. "Conservation of Isotopic Spin and Isotopic Gauge Invariance".
833 In: *Phys. Rev.* 96 (1 Oct. 1954), pp. 191–195. doi: 10.1103/PhysRev.96.191. url: <https://link.aps.org/doi/10.1103/PhysRev.96.191>.
- 835 [21] J. Schwinger. "Quantum Electrodynamics. I. A Covariant Formulation". In: *Physical Review (U.S.)*
836 *Superseded in part by Phys. Rev. A, Phys. Rev. B: Solid State, Phys. Rev. C, and Phys. Rev. D* 74 (Nov.
837 1948). doi: 10.1103/PhysRev.74.1439.
- 838 [22] R. P. Feynman. "Mathematical Formulation of the Quantum Theory of Electromagnetic Inter-
839 action". In: *Phys. Rev.* 80 (3 Nov. 1950), pp. 440–457. doi: 10.1103/PhysRev.80.440. url:
840 <https://link.aps.org/doi/10.1103/PhysRev.80.440>.
- 841 [23] R. P. Feynman. "The Theory of Positrons". In: *Phys. Rev.* 76 (6 Sept. 1949), pp. 749–759. doi:
842 10.1103/PhysRev.76.749. url: <https://link.aps.org/doi/10.1103/PhysRev.76.749>.
- 843 [24] R. P. Feynman. "Space-Time Approach to Quantum Electrodynamics". In: *Phys. Rev.* 76 (6 Sept.
844 1949), pp. 769–789. doi: 10.1103/PhysRev.76.769. url: <https://link.aps.org/doi/10.1103/PhysRev.76.769>.
- 846 [25] S. Tomonaga. "On a Relativistically Invariant Formulation of the Quantum Theory of Wave
847 Fields*". In: *Progress of Theoretical Physics* 1.2 (Aug. 1946), pp. 27–42. issn: 0033-068X. doi:
848 10.1143/PTP.1.27. eprint: <https://academic.oup.com/ptp/article-pdf/1/2/27/24027031/1-2-27.pdf>. url: <https://doi.org/10.1143/PTP.1.27>.
- 850 [26] F. J. Dyson. "The Radiation Theories of Tomonaga, Schwinger, and Feynman". In: *Phys. Rev.* 75 (3
851 Feb. 1949), pp. 486–502. doi: 10.1103/PhysRev.75.486. url: <https://link.aps.org/doi/10.1103/PhysRev.75.486>.
- 853 [27] F. J. Dyson. "The S Matrix in Quantum Electrodynamics". In: *Phys. Rev.* 75 (11 June 1949),
854 pp. 1736–1755. doi: 10.1103/PhysRev.75.1736. url: <https://link.aps.org/doi/10.1103/PhysRev.75.1736>.

- 856 [28] A. AKHIESER, L. LANDAU, and I. POMERANCHOOK. "Scattering of Light by Light". In: *Nature*
857 138.3483 (Aug. 1936), pp. 206–206. issn: 1476-4687. doi: 10.1038/138206a0. url: <https://doi.org/10.1038/138206a0>.
- 859 [29] G. et al. Aad. "Observation of Light-by-Light Scattering in Ultraperipheral Pb+Pb Collisions with
860 the ATLAS Detector". In: *Phys. Rev. Lett.* 123 (5 July 2019), p. 052001. doi: 10.1103/PhysRevLett.
861 123.052001. url: <https://link.aps.org/doi/10.1103/PhysRevLett.123.052001>.
- 862 [30] Abdus Salam and J. C. Ward. "Weak and electromagnetic interactions". In: *Il Nuovo Cimento*
863 (1955-1965) 11.4 (Feb. 1959), pp. 568–577. issn: 1827-6121. doi: 10.1007/BF02726525. url:
864 <https://doi.org/10.1007/BF02726525>.
- 865 [31] F. Englert and R. Brout. "Broken Symmetry and the Mass of Gauge Vector Mesons". In: *Phys.*
866 *Rev. Lett.* 13 (9 Aug. 1964), pp. 321–323. doi: 10.1103/PhysRevLett.13.321. url: <https://link.aps.org/doi/10.1103/PhysRevLett.13.321>.
- 868 [32] Peter W. Higgs. "Broken Symmetries and the Masses of Gauge Bosons". In: *Phys. Rev. Lett.* 13
869 (16 Oct. 1964), pp. 508–509. doi: 10.1103/PhysRevLett.13.508. url: <https://link.aps.org/doi/10.1103/PhysRevLett.13.508>.
- 871 [33] Wolfgang Hollik. "Electroweak Theory". In: *Journal of Physics: Conference Series* 53 (Nov. 2006),
872 pp. 7–43. doi: 10.1088/1742-6596/53/1/002. url: <https://doi.org/10.1088%2F1742-6596%2F53%2F1%2F002>.
- 874 [34] Steven Weinberg. "Physical Processes in a Convergent Theory of the Weak and Electromagnetic
875 Interactions". In: *Phys. Rev. Lett.* 27 (24 Dec. 1971), pp. 1688–1691. doi: 10.1103/PhysRevLett.
876 27.1688. url: <https://link.aps.org/doi/10.1103/PhysRevLett.27.1688>.
- 877 [35] *Standard Model particles*. url: https://en.wikipedia.org/wiki/Color_confinement.

The W boson

880 “Potentielle citation sans aucun rapport avec le sujet”

— Personne inconnue, contexte à déterminer

882 2.1 The motivation for the W mass measurement

883 Being one of the cornerstones of the SM, the W boson is tightly connected to the other parameters of
884 the theory. In the leading order of the perturbation theory the W mass depends only on the electroweak
885 parameters [1]:

$$M_W = \sqrt{\frac{\pi\alpha}{\sqrt{2}G_F}} \frac{1}{\sin\theta_W}, \quad (2.1)$$

886 where G_F stands for the Fermi constant. The factor $\sqrt{\frac{\pi\alpha}{\sqrt{2}G_F}} \approx 40$ GeV sets the lower bound for the
 887 possible W mass. Higher order corrections enter the equation in the following way:

$$M_W = \sqrt{\frac{\pi\alpha}{\sqrt{2}G_F}} \frac{1}{\sin\theta_W} \frac{1}{1+\Delta r}, \quad (2.2)$$

where Δr contains the sum of all possible radiative corrections and depends also on other parameters of the SM, first of all on top quark and Higgs boson masses. The correction term is also sensitive to possible BSM effects. As it was mentioned in Chapter 1 the mass of the W boson is one of the input parameters of the SM, so the predictions of the theory directly depend on how precisely we know the value of the boson mass. On the other hand, we can theoretically constrain the value of the W boson mass assuming the already known values of the other SM parameters. Fig. 22 demonstrates that the uncertainty of the theoretical estimate for the W boson mass is about two times lower than that of the best available experimental measurement. This motivates the effort for a more precise experimental

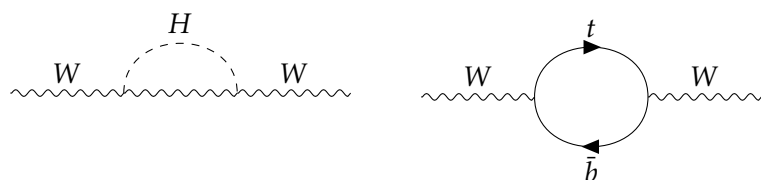
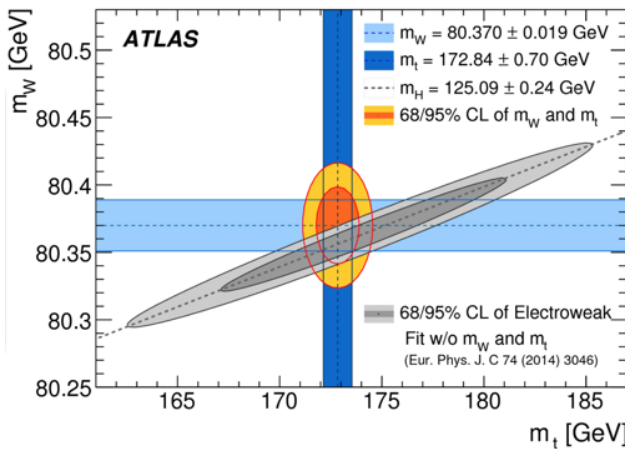
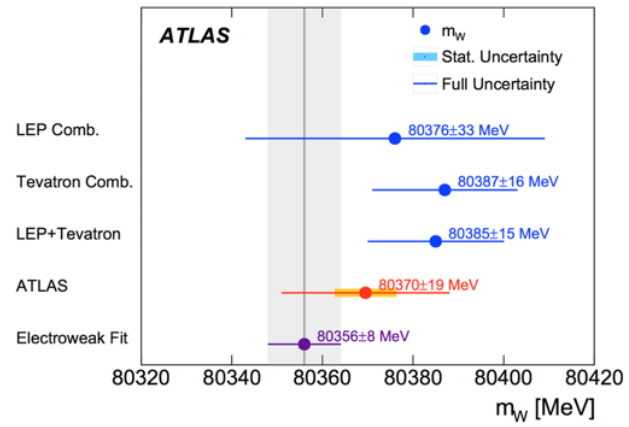


Figure 21: Next-to-leading order diagrams for W boson propagator containing contributions from heavy quarks and the Higgs boson.

896 measurement in order to test the consistency of the SM. Should the improved measurement reveal the inconsistency of the Standard Model - it would also allow to reveal viable BSM theories.



(a) W mass constraint [2]



(b) W mass measurements

Figure 22: W mass measurements and predictions

897

898 2.2 Massive boson production at hadron colliders

899 Hadron colliders provide a fruitful environment for the production and study of massive electroweak
900 bosons - all of them were discovered at hadron colliders. Hadron colliders allow to achieve much
901 higher centre-of-mass collision energy and luminosity comparing to their lepton counterparts. At the
902 same time precision measurements at hadron colliers demand much deeper theoretical understanding
903 of different aspects of the SM.
904 The main theoretical complication of the proton-proton colliders lies in the fact that in contrary to
905 leptons, protons are complex objects. This raises the following problems:

- 906 • A proton-proton collision is in general case a many-body problem. The absence of a consistent
907 theory for the QCD vacuum does not allow to describe the initial state of the proton constituents
908 in a consistent way.
- 909 • The initial energy of the whole proton is well known, but we don't know how this energy is
910 distributed between the proton constituents.
- 911 • We know that the proton consists of three valence quarks that have non-zero expectation value
912 and interact through gluons. In the course of these interactions all flavours of quarks (called sea
913 quarks) are appearing off-shell. The contribution of these sea quarks to the scattering cross-section
914 must also be taken in account.

915 In order to attack these problems and get accurate predictions for the proton-proton collisions it is
 916 necessary to take into account the asymptotic freedom that QCD demonstrates at short distances or
 917 high energies. At a certain energy scale of the momentum Q , transferred during the collision, we can
 918 assume that the interacting parts of the proton are asymptotically free and neglect the interaction
 919 with the rest of the proton. This is called *the factorization theorem*. The factorization occurs only if
 920 the transferred momentum $Q \gg \Lambda_{QCD}$ is large, and that is why these processes are called "hard". The
 921 physical conditions of the hard processes allow to use the perturbative QCD formalism, since at large
 922 energy scale the strong coupling constant α_s becomes small. Processes with lower energy scale of the
 923 transferred momentum are called "soft" and do not allow to use the perturbative QCD formalism. As it
 924 was mentioned in Section 1, a lot of things in the low-energy non-perturbative sector of the QCD are
 925 still unclear.
 926 The on-shell production of massive vector bosons occurs during the hard processes, however, precise
 927 measurements at hadron colliders require understanding of both hard and soft QCD regimes. It is
 928 common that the hard scattering of the proton constituents is accompanied by a soft scattering of the
 929 remaining proton parts. This forms what is called *underlying event* and also must be taken into account.

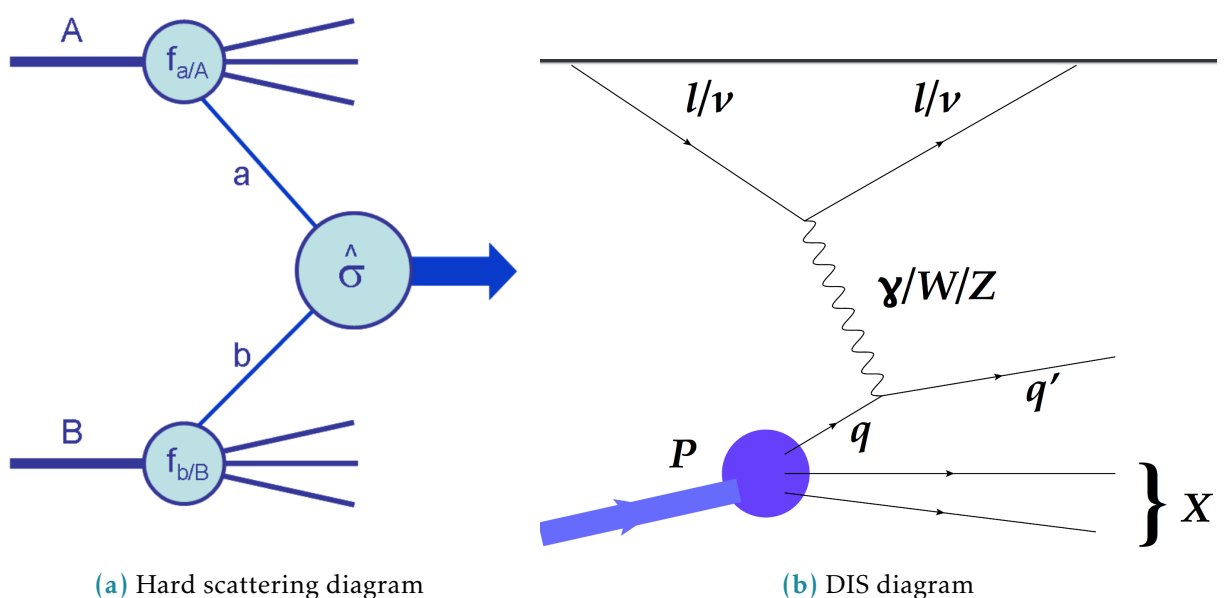


Figure 23: Examples of hard QCD scatterings.

930

931 2.2.1 Deep Inelastic scattering

932 In order to better illustrate the factorization approach let us first consider the lepton-hadron process
 933 called the Deep Inelastic Scattering (DIS). Historically it was the first experimental evidence for the
 934 complex structure of the proton and still serves an indispensable tool for the proton structure study.

935 Let's try to write a matrix element for a DIS process $e + A \rightarrow e + X$, exchanging a virtual photon with
 936 momentum q^μ :

$$|M|_{DIS}^2 = 4\pi M_N \frac{\alpha}{q^4} L_{\mu\nu} W_{hadron}^{\mu\nu}, \quad (2.3)$$

937 where $L_{\mu\nu}$ is the transverse lepton tensor, $q^\mu L_{\mu\nu} = q^\nu L_{\mu\nu} = 0$. The hadronic tensor $W_{\mu\nu}$ along with
 938 its normalization factor $4\pi M_N$ is unknown, but we can write it down in general form introducing
 939 longitudinal and transverse parts¹ [4]:

$$W_{\mu\nu} = F_1(x, Q^2) \left(-g_{\mu\nu} + \frac{q_\mu q_\nu}{q^2} \right) + F_2(x, Q^2) \frac{(p_\mu - q_\mu p \cdot q/q^2)(p_\nu - q_\nu p \cdot q/q^2)}{p \cdot q}, \quad (2.4)$$

940 with p_μ being the momentum of the hadron A, Q^2 is the exchange momentum, $x = \frac{Q^2}{2p \cdot q}$ and the form-
 941 factor functions $F_1(x, Q^2), F_2(x, Q^2)$ are unknown.

942 The cross-section of the DIS process can be measured experimentally, leaving the possibility to study
 943 the form-factor functions. It turned out that these functions do not depend (at least in the first
 944 approximation) on Q^2 [dis]. Further experiments have revealed that they form-factors depend only on
 945 the ratio x , as it was predicted before [5]. This type of behaviour was called the Bjorken scaling.
 946 These results have led to the idea of partons - point-like constituents of the proton [6]. Keeping in
 947 mind the idea of factorization we can assume the lepton only interacts with one of the partons. Then
 948 we can express the hadronic tensor $W_{\mu\nu}$ as a sum of all available partons:

$$W_{\mu\nu}(q_\mu, p_\nu) = \sum_a \int_x^1 \frac{d\xi}{\xi} f_{a/A}(\xi, \mu) H_{\mu\nu}^a(q_\mu, p_\nu, \mu, \alpha_s(\mu)) + NLO. \quad (2.5)$$

949 The functions $H_{\mu\nu}^a(q_\mu, p_\nu, \mu, \alpha_s(\mu))$ are called the hard scattering structure functions and only depend
 950 on parton type a , but not on hadron type A . These functions describe the high-energy behaviour and
 951 can be calculated in the framework of perturbative QCD. At the same time $f_{a/A}(\xi, \mu)$ is called Parton
 952 Density Function (PDF) and has a physical meaning of finding a parton of type a (gluon, u-quark,
 953 d-quark etc) in a hadron of type A (proton, neutron, meson) carrying the fraction of ξ of the hadron's
 954 momentum. These PDFs contain information on the momentum distribution of quarks and gluons
 955 within the hadron. This corresponds to the non-perturbative sector of the QCD which is beyond the
 956 reach of theoretical methods available so far. Note that they do not directly depend on the momentum
 957 Q^2 , but only on the energy scale μ .

958 The DGLAP equations show that once the PDFs are known at a certain energy scale μ they can be
 959 perturbatively extrapolated to a different energy scale [7], [8], [9], [10]. This means that the PDFs
 960 are universal - they can be measured experimentally at certain conditions in the course of the DIS
 961 (or any other) process and then used for numerical calculations of any other process (e.g. Drell-Yan
 962 (DY) process) at different conditions. Such a measurement allows a workaround - we may not be able
 963 to solve the many-body problem and perform non-perturbative calculations starting from the first
 964 principles, yet we still get a theoretical prediction with a good precision. Currently there exist a number

¹Given example assumes only electromagnetic interaction. For the more general electroweak case the tensor structure is more complicated and there are more than two scalar structure functions [3].

965 of different groups working on the PDF parametrizations and fits, constantly improving the fits using
 966 the data coming from hadron colliders. Using different PDF sets may give different results and also
 967 helps to estimate the systematic uncertainties implied by the PDFs.
 968 Historically the DIS experiments at HERA electron-proton collider have allowed to perform proton
 969 PDFs measurements with a good level of precision in the x region up to $x \sim 10^{-4}$ at high Q^2 . The HERA
 970 experiments operated until 2008, paving the path for precision predictions for the Drell-Yan process.
 971 Currently there are prospects for new experiments like Large Hadron Electron Collider (LHeC) that
 would involve DIS and further improve the PDF precision [11].

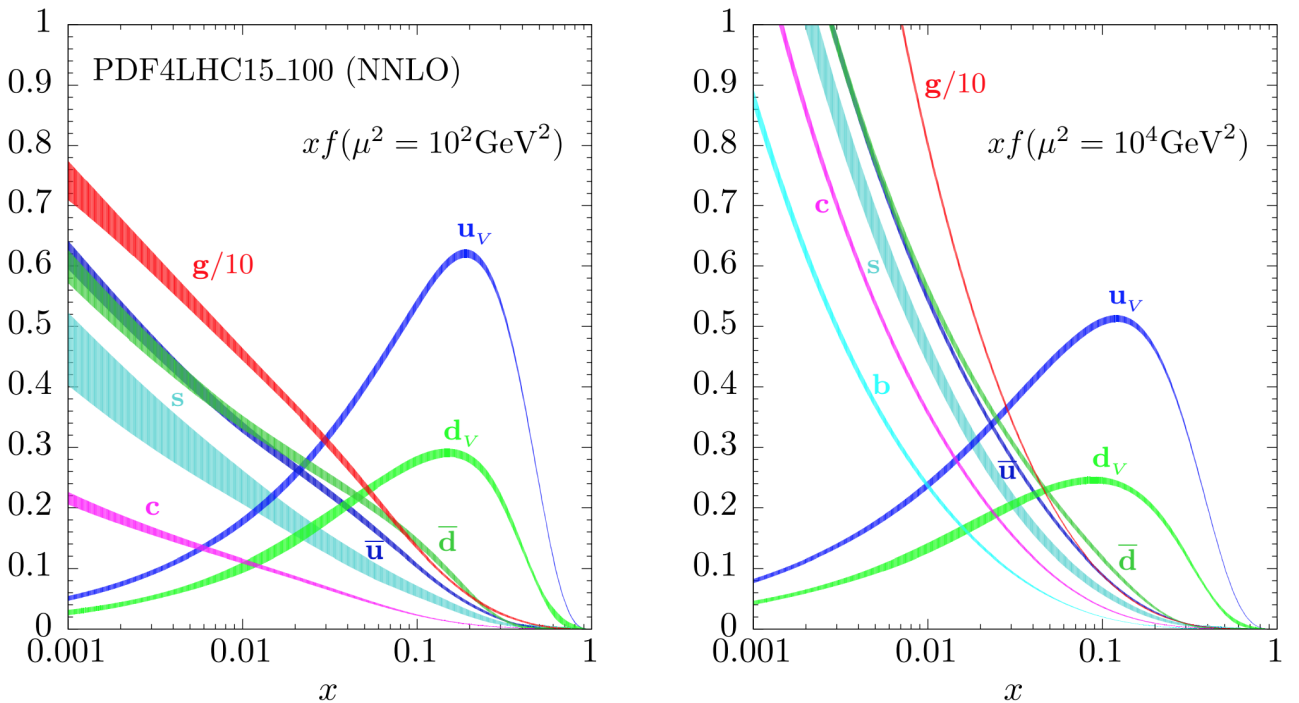


Figure 24: The evolution of a PDF4LHC15 NNLO Hessian set from $Q^2 = 10^2$ GeV to $Q^2 = 10^4$ GeV using the DGLAP. Notice the increase in the sea quark density. The PDFs include one standard deviation uncertainty band.

972

973 2.2.2 The Drell-Yan process

974 The DY process happens during the high-energy hadron-hadron scattering when quark and antiquark
 975 annihilate to form an electroweak boson [12]. It is postulated that DY cross-section in a proton-
 976 proton scattering $\sigma^{DY}(pp \rightarrow l^+l^- + X)$ can be expressed through the cross-sections of the corresponding
 977 parton-parton scattering cross-section convoluted with the PDFs of these partons:

$$\frac{d^2\sigma^{DY}}{dydM^2} = \sum_{a,b=q,\bar{q},g} \int_{\tau_1}^1 dx_1 f_a(x_1, \mu_F^2) \int_{\tau_2}^1 dx_2 f_b(x_2, \mu_F^2) \frac{d^2\hat{\sigma}_{ab}^{DY}}{dydM^2}(x_1, x_2, y, M^2, \mu_R^2, \mu_F^2). \quad (2.6)$$

In this equation $y = \frac{1}{2} \log \frac{E+p_z}{E-p_z}$ represents rapidity, M^2 is the invariant mass of the lepton pair, μ_F and μ_R are factorization and renormalisation scales correspondingly. Integration limits $\tau_{1,2} = \sqrt{\frac{Q^2}{s}} e^{\pm y}$ with s being the centre-of-mass energy of the two incoming protons. The partonic cross-sections can be in turn computed perturbatively as a series expansion in α_s [3]:

$$\frac{d^2\hat{\sigma}_{ab}^{DY}}{dydM^2}(x_1, x_2, y, M^2, \mu_R^2, \mu_F^2) = \sum_{n=0}^{\infty} \left(\frac{\alpha_s \mu_R^2}{2\pi} \right)^n \frac{d^2\hat{\sigma}_{ab}^{(n)DY}}{dydM^2}. \quad (2.7)$$

The exact sum of the expansion does not depend on the μ_F and μ_R parameters. However, finite-order calculations demand a specific choice for the two parameters. One of the common choices for the DY process is putting $\mu_F = \mu_R = M$, with M being the mass of the dilepton pair.
 From equation 2.6 we can see that the rapidity distribution of the vector boson explicitly depends on the PDFs both in terms of flavour decomposition and in the sense of a particular PDF set. Figure 25 demonstrates different rapidity distributions for two centre-of-mass energies and two different PDF sets.

Let us consider partonic cross-sections, which can be constructed using an analogy from QED

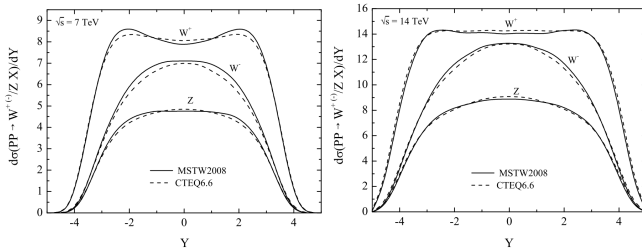


Figure 25: Rapidity distribution for the vector bosons using MSTW2008 and CTEQ6.6 PDF sets for the centre-of-mass energies of 7 and 14 TeV [13].

$e^+e^- \rightarrow \mu^+\mu^-$ - a flavour-changing process:

$$\hat{\sigma}(q\bar{q} \rightarrow e^+e^-) = \frac{4\pi\alpha_s^2}{3s} \frac{1}{N} Q_q^2. \quad (2.8)$$

Here Q_q^2 is the quark charge, $1/N$ stands for the colour factor and underlines the fact that quark and antiquark must have the matching colour in order to annihilate. In a similar way we can obtain the cross-section of the sub-processes of W and Z bosons production:

$$\begin{aligned} \hat{\sigma}^{q\bar{q}' \rightarrow W} &= \frac{\pi}{3} \sqrt{2} G_F M_W^2 |V_{qq'}|^2 \delta(s - M_W^2), \\ \hat{\sigma}^{q\bar{q}' \rightarrow Z} &= \frac{\pi}{3} \sqrt{2} G_F M_W^2 (v_q^2 + a_q^2) \delta(s - M_Z^2), \end{aligned} \quad (2.9)$$

where $V_{qq'}$ is the element of the CKM matrix, v_q (a_q) is a vector (axial vector) that couples the Z boson to the quarks. Figure 27 shows the contributions of different parton flavours into W^+ and W^- cross-sections. An assumption of narrow W resonance was used. The fact that the bosons with opposite charges are formed from different quarks makes a notable difference at the LHC experiments. Figure 26 contains the comparison of the results obtained at the LHC experiments with the NNLO theoretical predictions that use different PDF sets.

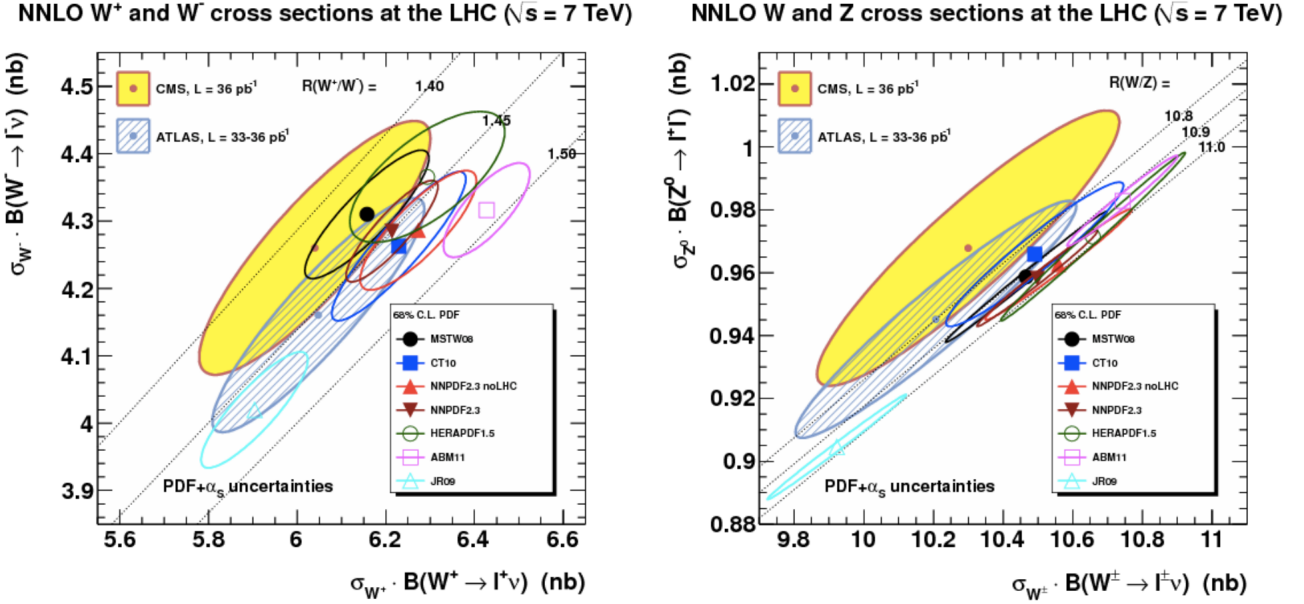


Figure 26: W and Z boson cross sections LHC at 7 TeV. ATLAS and CMS results, compared to NNLO predictions for various PDF sets [14].

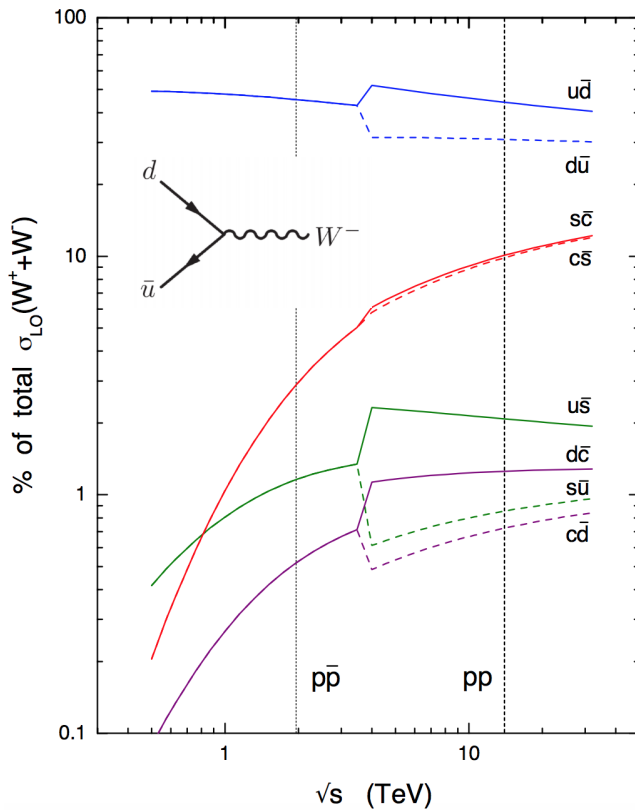


Figure 27: Parton contributions to the cross-sections of W^+ and W^- bosons for LHC and Tevatron cases [15].

1000 2.3 Transverse momentum of massive vector bosons

1001 The leading-order model of the DY process assumes the colliding partons to have their momentum
 1002 perfectly collinear with the proton as a whole, which would mean that the vector boson p_T should
 1003 peak at zero. However, most of the massive vector bosons produced in the DY process have a small
 1004 yet non-zero transverse momentum $p_T \ll M_V$. This occurs due to a non-perturbative effect of partons
 1005 moving within the colliding protons, having an intrinsic momentum of their own. This intrinsic
 1006 momentum $\langle k_T \rangle \sim \Lambda_{QCD}$ is well parametrized using a Gaussian distribution with average value of
 1007 500 [16] or 700 GeV [17], although there are ongoing efforts for a more sophisticated parametrization
 1008 that would allow a better modelling of the lower part of vector boson p_T spectrum [18].
 1009 The spectrum at higher values of p_T is determined by hard perturbative parton emission(s) like
 1010 $q\bar{q} \rightarrow Vg$, $qg \rightarrow Vq$. The corresponding amplitudes can be conveniently expressed using Mandelstam
 1011 variables:

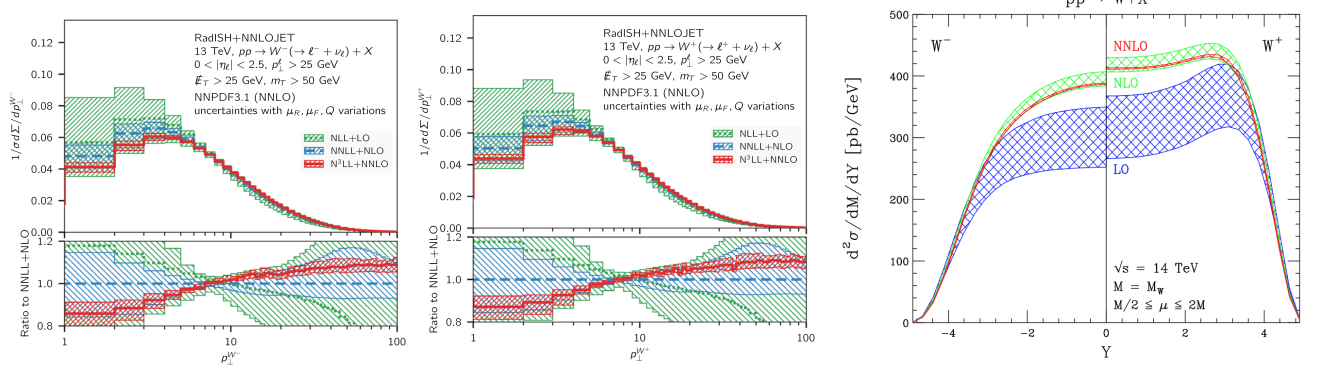
$$\begin{aligned}\sum |\mathcal{M}^{q\bar{q}' \rightarrow Wg}|^2 &= \alpha_s \sqrt{2\pi} G_F M_W^2 |V_{q\bar{q}'}|^2 \frac{8}{9} \frac{t^2 + u^2 + 2M_W^2 s}{tu}, \\ \sum |\mathcal{M}^{qg \rightarrow Wq'}|^2 &= \alpha_s \sqrt{2\pi} G_F M_W^2 |V_{q\bar{q}}|^2 \frac{1}{3} \frac{s^2 + u^2 + 2M_W^2 t}{-su},\end{aligned}\quad (2.10)$$

1012 where the summation is performed over colours and spins in the final and initial states. Integrating
 1013 these partonic matrix elements with the PDFs one can obtain the transverse momentum distribution
 1014 $d\sigma/dp_T$. Further precision can be obtained by considering corrections from next-to-leading order
 1015 processes $\sim O(\alpha_s^2)$ like $q\bar{q} \rightarrow Vgg$ - that would mainly affect the high p_T tail of the distribution.
 1016 The matrix elements in 2.10 become singular when the emitted partons become soft or collinear to the
 1017 initial-state partons - it is related to the poles at $u = 0$ and $t = 0$ in the denominator. Also for the NLO
 1018 processes like $q\bar{q} \rightarrow Vgg$ a singularity arises if the two final-state gluons are collinear. This creates a
 1019 problem for the calculation of the low- p_T part of the spectrum. Mathematically it is reflected in the
 1020 appearance of different powers of logarithms like $\log M_W^2/p_T^2$ in all orders of cross-section expansion in
 1021 α_s , which leads to divergences when p_T is small. This forces us to look for alternative approach that
 1022 would take into account all the orders of the expansion.
 1023 All-order resummation may be performed in a variety of approaches, one of the most popular is
 1024 provided by parton showers. Its numerical implementation is available in a number of Monte-Carlo
 1025 generators, PYTHIA, HERWIG and SHERPA are among the most used. It appears that for the case
 1026 of soft and collinear gluon emission it is possible to factorize and exponentiate the logarithms in a
 1027 *Sudakov form factor*, such that:

$$\begin{aligned}\frac{d\sigma}{dp_T^2} &= \sigma \frac{d}{dp_T^2} \exp\left\{-\frac{\alpha_s C_F}{2\pi} \log^2 \frac{M_W^2}{p_T^2}\right\}, \\ \exp\left\{-\frac{\alpha_s C_F}{2\pi} \log^2 \frac{M_W^2}{p_T^2}\right\} &= 1 - \frac{\alpha_s}{2\pi} C_F \ln^2 \frac{M_W^2}{p_T^2} + \frac{1}{2!} \left(\frac{\alpha_s}{2\pi}\right)^2 C_F^2 \ln^4 \frac{M_W^2}{p_T^2} - \frac{1}{3!} \left(\frac{\alpha_s}{2\pi}\right)^3 C_F^3 \ln^6 \frac{M_W^2}{p_T^2} + \dots\end{aligned}\quad (2.11)$$

1028 The exponential $\exp\{G(\alpha_s, L)\}$, where $L = \log M_W^2/p_T^2$ is called the Sudakov form-factor. Its expansion
 1029 by the powers of α_s defines the resummation accuracy: the term $\sim O(\alpha_s)$ is called the leading logarithm
 1030 (LL), term with $\sim O(\alpha_s^2)$ is the next-to-leading logarithm (NLL) and so on.
 1031 The cross-sections obtained with the resummation methods provide a good prediction for soft and

1032 collinear emissions at low $p_T \ll M_W$. In order to get a combined cross-section for higher p_T region the
 1033 resummed cross-section has to be *matched* with the fixed-order cross-sections of the corresponding power in α_s .



(a) W^- transverse momentum spectrum [19]. (b) W^+ transverse momentum spectrum [19].

(c) W^\pm rapidity distribution [20].

Figure 28: Kinematic distributions for W^\pm with corrections.

1034

1035 **Bibliography**

- 1036 [1] M. Awramik et al. "Precise prediction for the W boson mass in the standard model". In: *Phys.*
1037 *Rev. D* 69 (2004), p. 053006. doi: 10.1103/PhysRevD.69.053006. arXiv: hep-ph/0311148.
- 1038 [2] J. Haller et al. "Update of the global electroweak fit and constraints on two-Higgs-doublet
1039 models". In: *The European Physical Journal C* 78.8 (Aug. 2018), p. 675. issn: 1434-6052. doi:
1040 10.1140/epjc/s10052-018-6131-3. URL: [https://doi.org/10.1140/epjc/s10052-018-
1041 6131-3](https://doi.org/10.1140/epjc/s10052-018-6131-3).
- 1042 [3] Jun Gao, Lucian Harland-Lang, and Juan Rojo. "The Structure of the Proton in the LHC Precision
1043 Era". In: *Phys. Rept.* 742 (2018), pp. 1–121. doi: 10.1016/j.physrep.2018.03.002. arXiv:
1044 1709.04922 [hep-ph].
- 1045 [4] John C. Collins, Davison E. Soper, and George F. Sterman. "Factorization of Hard Processes in
1046 QCD". In: vol. 5. 1989, pp. 1–91. doi: 10.1142/9789814503266_0001. arXiv: hep-ph/0409313.
- 1047 [5] J. D. Bjorken. "Asymptotic Sum Rules at Infinite Momentum". In: *Phys. Rev.* 179 (5 Mar. 1969),
1048 pp. 1547–1553. doi: 10.1103/PhysRev.179.1547. URL: <https://link.aps.org/doi/10.1103/PhysRev.179.1547>.
- 1049 [6] Richard P. Feynman. "Very High-Energy Collisions of Hadrons". In: *Phys. Rev. Lett.* 23 (24 Dec.
1050 1969), pp. 1415–1417. doi: 10.1103/PhysRevLett.23.1415. URL: <https://link.aps.org/doi/10.1103/PhysRevLett.23.1415>.
- 1051 [7] L.N. Lipatov. "The parton model and perturbation theory". In: *Sov. J. Nucl. Phys.* 20 (1975),
1052 pp. 94–102.
- 1053 [8] G. Altarelli and G. Parisi. "Asymptotic freedom in parton language". In: *Nuclear Physics B* 126.2
1054 (1977), pp. 298–318. issn: 0550-3213. doi: [https://doi.org/10.1016/0550-3213\(77\)90384-4](https://doi.org/10.1016/0550-3213(77)90384-4).
1055 URL: <http://www.sciencedirect.com/science/article/pii/0550321377903844>.
- 1056 [9] V.N. Gribov and L.N. Lipatov. "Deep inelastic e p scattering in perturbation theory". In: *Sov. J.*
1057 *Nucl. Phys.* 15 (1972), pp. 438–450.
- 1058 [10] Yuri L. Dokshitzer. "Calculation of the Structure Functions for Deep Inelastic Scattering and e+
1059 e- Annihilation by Perturbation Theory in Quantum Chromodynamics." In: *Sov. Phys. JETP* 46
1060 (1977), pp. 641–653.
- 1061 [11] Max Klein. "Future Deep Inelastic Scattering with the LHeC". In: *From My Vast Repertoire ...:*
1062 *Guido Altarelli's Legacy*. Ed. by Aharon Levy, Stefano Forte, and Giovanni Ridolfi. 2019, pp. 303–
1063 347. doi: 10.1142/9789813238053_0015. arXiv: 1802.04317 [hep-ph].
- 1064 [12] Sidney D. Drell and Tung-Mow Yan. "Massive Lepton-Pair Production in Hadron-Hadron Col-
1065 lisions at High Energies". In: *Phys. Rev. Lett.* 25 (5 Aug. 1970), pp. 316–320. doi: 10.1103/
1066 PhysRevLett.25.316. URL: <https://link.aps.org/doi/10.1103/PhysRevLett.25.316>.

- 1069 [13] Francis Halzen, Yu Seon Jeong, and C.S. Kim. “Charge Asymmetry of Weak Boson Production
1070 at the LHC and the Charm Content of the Proton”. In: *Phys. Rev. D* 88 (2013), p. 073013. doi:
1071 10.1103/PhysRevD.88.073013. arXiv: 1304.0322 [hep-ph].
- 1072 [14] Michelangelo L. Mangano. “Production of electroweak bosons at hadron colliders: theoretical
1073 aspects”. In: vol. 26. 2016, pp. 231–253. doi: 10.1142/9789814733519_0013. arXiv: 1512.00220
1074 [hep-ph].
- 1075 [15] A D Martin et al. “Parton Distributions and the LHC: W and Z Production; rev. version”. In: *Eur.*
1076 *Phys. J. C* 14.hep-ph/9907231. DTP-99-64. OUTP-99-31-P. RAL-TR-99-047 (July 1999), 133–145.
1077 30 p. doi: 10.1007/s100520000324. URL: <https://cds.cern.ch/record/392675>.
- 1078 [16] A. Bermudez Martinez et al. “Production of Z bosons in the parton branching method”. In: *Phys. Rev. D* 100 (7 Oct. 2019), p. 074027. doi: 10.1103/PhysRevD.100.074027. URL: <https://link.aps.org/doi/10.1103/PhysRevD.100.074027>.
- 1081 [17] R.Keith Ellis, W.James Stirling, and B.R. Webber. *QCD and collider physics*. Vol. 8. Cambridge
1082 University Press, Feb. 2011. ISBN: 978-0-511-82328-2, 978-0-521-54589-1.
- 1083 [18] Francesco Hautmann, Ignazio Scimemi, and Alexey Vladimirov. “Non-perturbative contributions
1084 to vector-boson transverse momentum spectra in hadronic collisions”. In: *Physics Letters B* 806
1085 (2020), p. 135478. issn: 0370-2693. doi: <https://doi.org/10.1016/j.physletb.2020.135478>.
1086 URL: <http://www.sciencedirect.com/science/article/pii/S0370269320302823>.
- 1087 [19] Wojciech Bizon et al. “The transverse momentum spectrum of weak gauge bosons at N³ LL +
1088 NNLO”. In: *Eur. Phys. J. C* 79.10 (2019), p. 868. doi: 10.1140/epjc/s10052-019-7324-0. arXiv:
1089 1905.05171 [hep-ph].
- 1090 [20] Charalampos Anastasiou et al. “High precision QCD at hadron colliders: Electroweak gauge
1091 boson rapidity distributions at NNLO”. In: *Phys. Rev. D* 69 (2004), p. 094008. doi: 10.1103/
1092 PhysRevD.69.094008. arXiv: hep-ph/0312266.

3

The Large Hadron Collider

1093

1094

1095 "Potentielle citation sans aucun rapport avec le sujet"

1096 — Personne inconnue, contexte à déterminer

1097 3.1 Introduction

1098 The study of elementary particles naturally demands a stable source of particles. At the dawn of
1099 particle physics the two main sources were radioactive materials and the cosmic rays. However soon
1100 researchers became in need of a more reliable source of particles in terms of particle energy, luminosity
1101 and experimental repeatability. This has commenced the era of particle accelerators.

1102 The first examples of particle accelerators were designed in late 1920s and early 1930s. Two different
1103 designs emerged: linear and circular. The former accelerates particles via electric field during the
1104 single pass through the machine, while the latter uses magnetic field to make accelerated particles go
1105 in circles allowing to re-accelerate the same beam many times. On the other hand the circular design
1106 comprises energy losses due to Bremsstrahlung radiation.

1107 In the second half of the XX century the accelerators gradually got bigger and bigger in both size and
1108 centre-of-mass energy of the accelerated particles. This has allowed to create an experimental basis for
1109 the development of modern particle physics, notably the Standard Model.

1110 Up to this day the biggest particle accelerator with the highest centre-of-mass energy is the Large
1111 Hadron Collider (LHC). LHC is a circular collider that lies in a tunnel of 27 km under the French-Swiss
1112 border next to Geneva [1]. In 2012 two biggest experiments of LHC have claimed the discovery of
1113 the Higgs boson, the last elementary particle predicted by the Standard Model which was not yet
1114 discovered by that time. [2], [3].

1115 3.2 The LHC running sequence

1116 It takes quite a journey for a proton to travel from a hydrogen tank (Fig. 31) into one of the LHC's
1117 collision points. A resourceful system of pre-accelerators is necessary to make the proton beam ready
1118 to get injected into one of the two LHC beam pipes. The LHC accelerator complex was not built from
1119 scratch - it uses vast CERN infrastructure, that was built for the previous particle physics experiments.
1120 After stripping the electrons off the atoms of hydrogen using the magnetic field the yielded protons get



Figure 31: ATLAS A hydrogen tank supplies LHC with protons [4].

1121 accelerated to the energy of 50 MeV by Linac 2¹ [5]. After that the beam gets into Proton Synchrotron
 1122 Booster (PSB) to be accelerated to 1.4 GeV. The next link of the pre-acceleration chain is the Proton
 1123 Synchrotron (PS) - a true veteran among CERN accelerators that first accelerated protons in 1959
 1124 holding the world record in acceleration energy. Currently thanks to PSB and other modifications it
 1125 can sustain proton beam intensity 1000 times larger than back in 1959. The PS accelerates the beam
 1126 up to 25 GeV and conveys it further to the Super Proton Synchrotron (SPS) - the second-largest particle
 1127 accelerator at CERN. Back in 1983 the massive electroweak bosons were discovered at the SPS but even
 1128 now it serves as a main accelerator for a NA61/SHINE, NA62 and COMPASS experiments. The SPS
 1129 raises the beam energy to 450 GeV and finally injects it into the LHC beam pipes (see Fig 32).

1130

1131 The LHC has inherited its 27 km tunnel from the predecessor, an electron-positron collider called
 1132 Large Electron-Positron (LEP). However, all the LEP hardware has been replaced to sustain the
 1133 conditions of the LHC beam. About 2/3 of the LHC circumference length is occupied by the dipole
 1134 magnets that bend the trajectory of the proton beam to keep it within the pipe. These magnets use
 1135 superconducting coils that conduct a current of 11080 amperes to produce a magnetic field of 8.3 tesla
 1136 Proton acceleration is maintained by the radio-frequency (RF) cavities (Fig. 33a). Besides acceleration
 1137 particles the RF cavities are also responsible for beam bunching i.e. separating the beam into a train of
 1138 separated particle packs, each containing about 10^{11} protons. During LHC Run 2 the bunches were
 1139 separated by 7 meters (25 ns) with a maximum of 2556 circulating bunches. The LHC has four crossing
 1140 points, where the two beams are crossed in order to collide protons. Naturally, the particle detectors
 1141 are installed at these four points. Before getting directed at the crossing point the beams get squeezed
 1142 to make their cross-section as small as $16 \mu m^2$ (Fig 34a).

¹After Run 2 Linac 2 has been decommissioned to be succeeded by Linac 4.

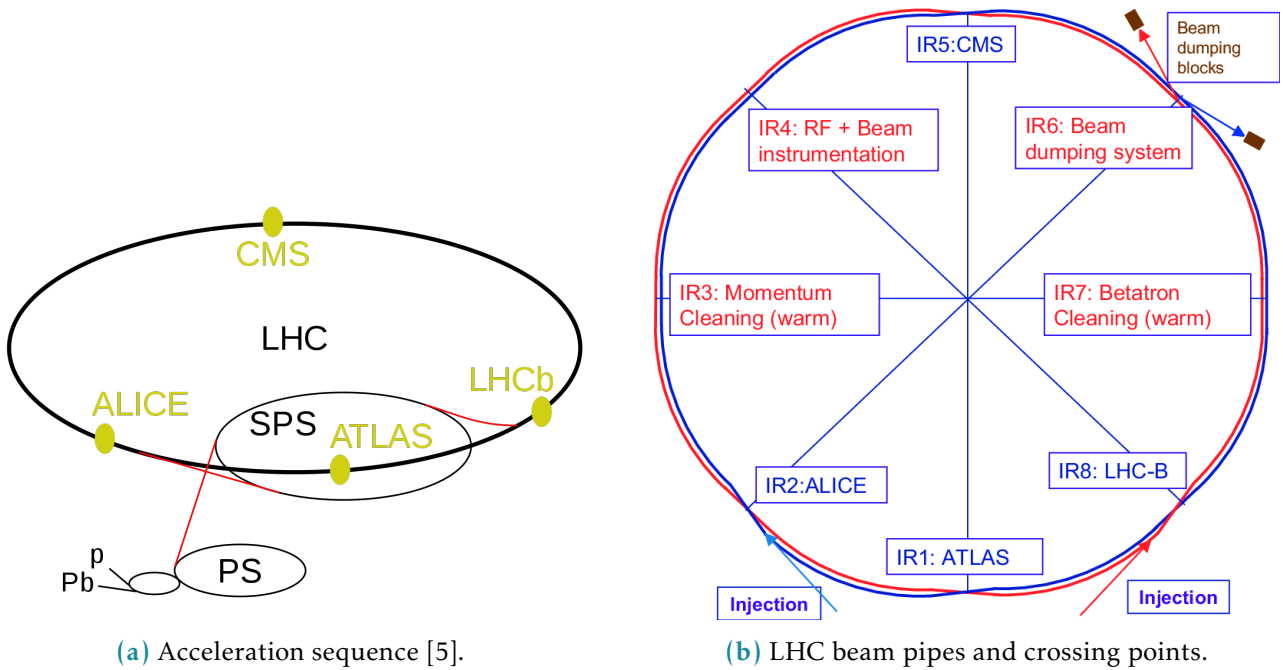


Figure 32: Schematic depiction of the LHC ring.

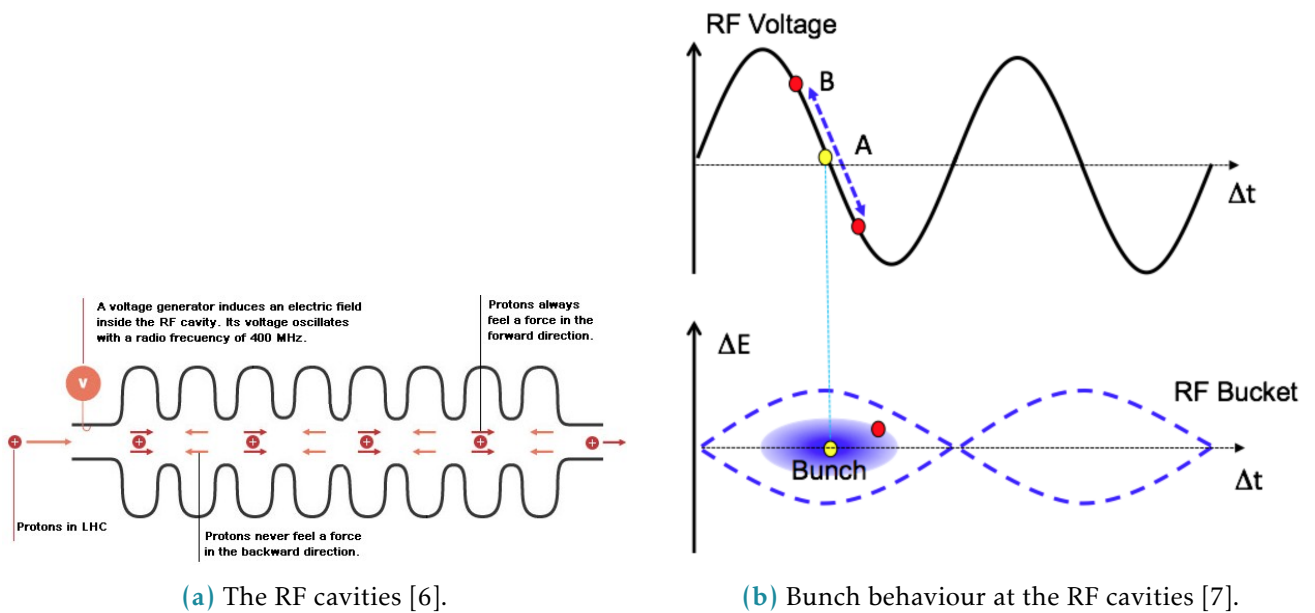
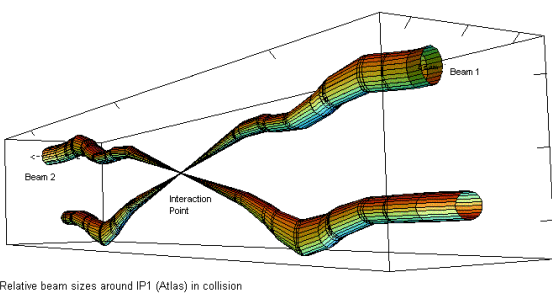
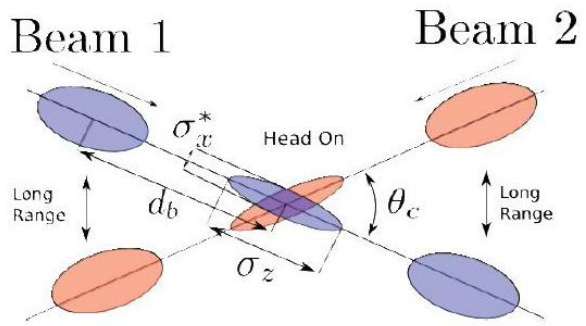


Figure 33: Bunching at RF cavities



(a) The two beams getting squeezed at the IP [8].



(b) Bunches at the collision point [9].

Figure 34: The crossing

1143 In order to estimate the number of single proton-proton interactions in the crossing beams a value
 1144 called instantaneous luminosity (simply called luminosity) is introduced. It is the proportionality
 1145 factor between the number of events per second dR/dt and the cross-section σ_p :

$$\frac{dR}{dt} = \mathcal{L} \cdot \sigma_p.$$

1146 For the case of head-on collisions the luminosity would equal to [10]:

$$\mathcal{L} = \frac{N_1 N_2 f N_b}{4\pi \sigma_x \sigma_y}, \quad (3.1)$$

1147 with N_1 and N_2 being the intensities of the two colliding beams, f is the revolution frequency, N_b -
 1148 number of bunches per beam, σ_x, σ_y - r.m.s. beam widths in the corresponding dimensions, assuming
 1149 that the bunches in both beams have the same size and Gaussian profiles.

1150

1151 Head-on crossing of the beams would ensure maximal luminosity given the same beams, but on the
 1152 other hand the measurement would suffer from unwanted beam-to-beam effects. To avoid it the beams
 1153 at the LHC are crossed at an angle, which is called the crossing angle 34b. For the case of head-on
 1154 collisions the luminosity gets a factor \mathcal{F} [10]:

$$\mathcal{L} = \frac{N_1 N_2 f N_b}{4\pi \sigma_x \sigma_y} \cdot \mathcal{F}, \quad (3.2)$$

1155 with geometric factor

$$\mathcal{F} = \frac{1}{\sqrt{1 + \left(\frac{\sigma_s}{\sigma_x} \frac{\theta_c}{2}\right)}},$$

1156 where σ_s is the r.m.s. of the bunch length and θ_c is the crossing angle. Varying the parameters like
 1157 beam intensity, bunch spacing, beam profile, crossing angle and others becomes a flexible tool for
 1158 luminosity control. This comes in handy for different physics analysis, as some processes are rare
 1159 and demand as much luminosity as possible (this is true, for example, for most of the Higgs studies),

Collision energy	Year	Integrated luminosity, pb^{-1}	Total uncertainty, %
5 TeV	2017	258	1.6
13 TeV	2017	148	2.1
13 TeV	2018	193	1.5

Table 31: Energy and luminosity of the special low- μ runs.

1160 whereas the others suffer from high pile-up conditions. Instantaneous luminosity integrated over a
 1161 period of time is called the integrated luminosity:

$$\mathcal{L}_{int} = \int_0^T \mathcal{L}(t) dt, \quad (3.3)$$

1162 and is directly related to the number of observed events $\mathcal{L}_{\text{int}} \cdot \sigma_p = N_{events}$. Precise measurement of the
 1163 integrated luminosity is crucial for the LHC results and serves as one of the nuisance parameters for
 1164 most of the analyses. A comprehensive overview on the luminosity determination at proton colliders
 1165 can be found here [11]. Absolute luminosity measurements at the LHC are performed predominantly
 1166 using the van-der-Meer (vdM) scan method [12], [13].

1167 3.3 Special low pile-up run during LHC Run 2

1168 During the Run 2 that lasted from 2015 to 2018 the ATLAS experiment has collected $146.9 fb^{-1}$ of data
 1169 under different bunch crossing conditions. However the precise measurement of the W boson-related
 1170 processes demands special conditions. High number of proton-proton collisions per bunch crossing
 1171 leads to contamination of the final state signal with soft collisions products. This effect, known as
 1172 pile-up, complicates object reconstruction and results in systematic uncertainties growth. For this
 1173 reason two special runs with low number of interactions per bunch crossing have been performed by
 1174 the LHC in 2017 and 2018 at the energies of 5 and 13 TeV.

1175 The table ?? contains information on the data collected at ATLAS experiment during the special low
 1176 pile-up run with $\langle \mu \rangle \approx 2$.

1177

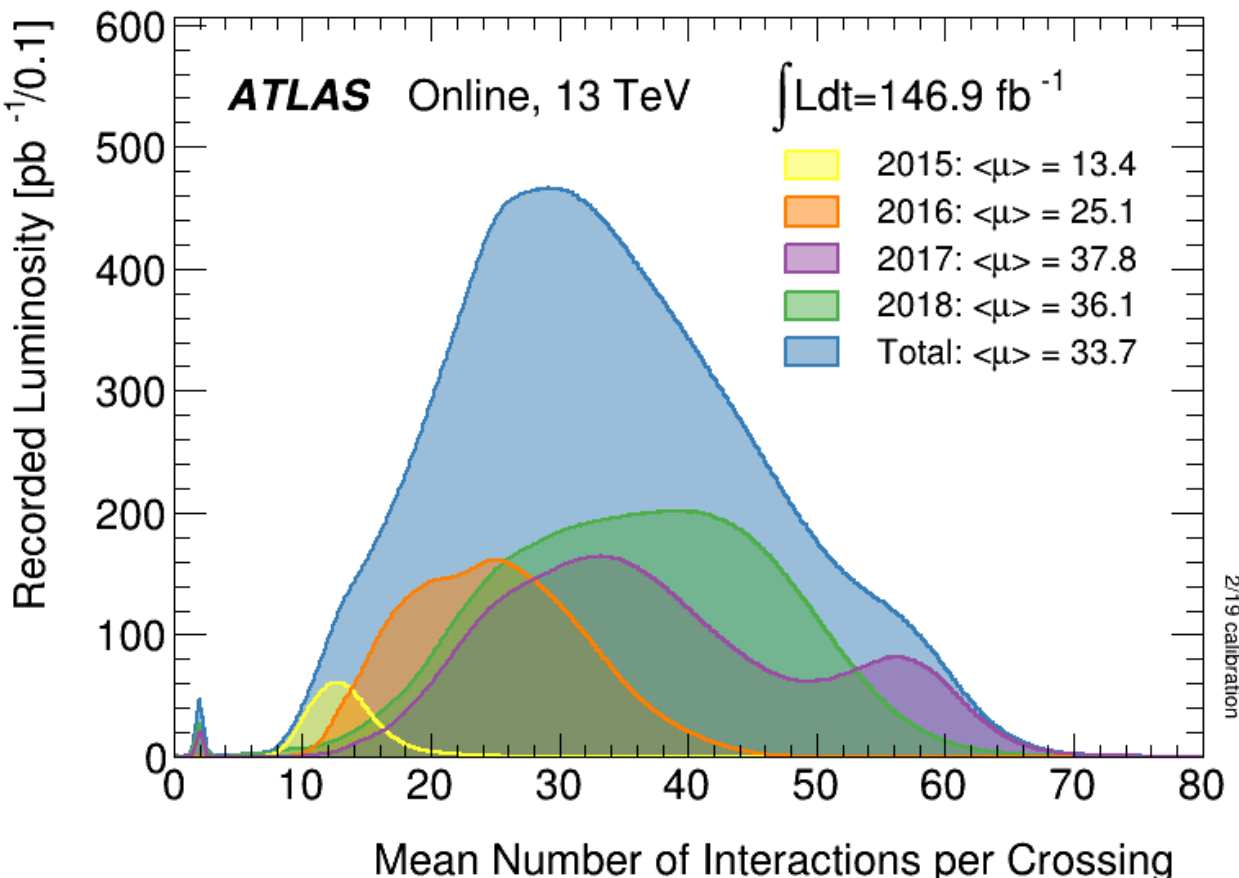


Figure 35: Number of Interactions per bunch crossing in ATLAS Run 2 [14]. A little bump around $\mu \approx 2$ corresponds to special low pile-up runs.

1178 Bibliography

- 1179 [1] Oliver Bruning and Lucio Rossi. "The High-Luminosity Large Hadron Collider". In: *Nature Rev. Phys.* 1.CERN-ACC-2019-0039 (Mar. 2019), 1. 3 p. doi: 10.1038/s42254-019-0050-6. URL: <https://cds.cern.ch/record/2668521>.
- 1180 [2] Georges Aad et al. "Observation of a new particle in the search for the Standard Model Higgs
- 1181 boson with the ATLAS detector at the LHC". In: *Phys. Lett.* B716 (2012), pp. 1–29. doi: 10.1016/j.physletb.2012.08.020. arXiv: 1207.7214 [hep-ex].
- 1182 [3] Serguei Chatrchyan et al. "Observation of a New Boson at a Mass of 125 GeV with the CMS
- 1183 Experiment at the LHC". In: *Phys. Lett.* B716 (2012), pp. 30–61. doi: 10.1016/j.physletb.2012.
- 1184 08.021. arXiv: 1207.7235 [hep-ex].
- 1185 [4] *The source of protons*. URL: https://www.lhc-closer.es/taking_a_closer_look_at_lhc/0_proton_source.

- 1190 [5] CERN. *CERN's accelerator complex*. URL: <https://home.cern/science/accelerators/accelerator-complex>.
- 1191
- 1192 [6] *RF cavities*. URL: https://www.lhc-closer.es/taking_a_closer_look_at_lhc/0_rf_cavities.
- 1193
- 1194 [7] Edmund J N Wilson. *An introduction to particle accelerators*. Oxford: Oxford Univ. Press, 2001. doi: 10.1093/acprof:oso/9780198508298.001.0001. URL: <http://cds.cern.ch/record/513326>.
- 1195
- 1196 [8] Riccardo De Maria, Oliver Brüning, and Rivkin Leonid. "LHC Interaction region upgrade". In: (Jan. 2008).
- 1197
- 1198 [9] LHC outreach. *CERN's accelerator complex*. URL: <https://lhc-machine-outreach.web.cern.ch/collisions.htm>.
- 1199
- 1200 [10] Werner Herr and B Muratori. "Concept of luminosity". In: (2006). doi: 10.5170/CERN-2006-002.361. URL: <https://cds.cern.ch/record/941318>.
- 1201
- 1202 [11] P Grafström and W Kozanecki. "Luminosity determination at proton colliders". In: *Prog. Part. Nucl. Phys.* 81 (2015), 97–148. 52 p. doi: 10.1016/j.ppnp.2014.11.002. URL: <http://cds.cern.ch/record/2153734>.
- 1203
- 1204
- 1205 [12] S van der Meer. *Calibration of the effective beam height in the ISR*. Tech. rep. CERN-ISR-PO-68-31. ISR-PO-68-31. Geneva: CERN, 1968. URL: <https://cds.cern.ch/record/296752>.
- 1206
- 1207 [13] Carlo Rubbia. *Measurement of the luminosity of p-overlinep collider with a (generalized) Van der Meer Method*. Tech. rep. CERN-p \bar{p} -Note-38. Geneva: CERN, Nov. 1977. URL: <https://cds.cern.ch/record/1025746>.
- 1208
- 1209
- 1210 [14] The ATLAS collaboration. *Number of Interactions per Crossing*. Jan. 2018. URL: <https://twiki.cern.ch/twiki/bin/view/AtlasPublic/LuminosityPublicResultsRun2>.
- 1211

The ATLAS detector

1214 "Potentielle citation sans aucun rapport avec le sujet"

1215 — Personne inconnue, contexte à déterminer

1216 4.1 General description and layout

1217 ATLAS experiment is a multipurpose detector at the LHC built, along with its peer Compact Muon
1218 Solenoid (CMS), in order to probe the p-p, A-A and p-A collisions using the full LHC luminosity [1].
1219 Being the largest (but not the heaviest) detector ever built for a collider experiment the ATLAS detector
1220 comprises 44m in length, 25m in height and weights 7000 tonnes.

1221 The detector has a cylindrical shape and is an onion-like arrangement of several detector systems
1222 centered at the Interaction Point (IP) as shown in fig. 41. The sub-detectors operate in the magnetic
1223 field created by the solenoid and toroid magnets (ATLAS owes its name to the latter). Data acquisition
1224 and recording is controlled by the Trigger and Data Acquisition (TDAQ) systems, allowing eventually
1225 to lower the event rate to a value, acceptable for the data storage [2]. The named systems are described
1226 in more detail in this chapter.

1227 4.2 Coordinate system

1228 The ATLAS results often reference ATLAS coordinates briefly described in this subsection. The origin
 1229 of the right-handed coordinate system is placed at the IP with z -axis directed along the beam direction.
 1230 This, in turn, defines the transverse x - y plane with x axis pointing towards the center of the LHC ring
 1231 and y axis directed upwards. All transverse observables like p_T and E_T are defined in this 2D plane.
 1232 Besides the mentioned Cartesian coordinates the azimuthal angle ϕ is defined in the transverse plane
 1233 around the beam axis. Polar angle θ is the elevation angle measured from the beam axis. The following
 1234 metric quantities are also to be mentioned:

- Pseudorapidity $\eta = -\ln \tan(\theta/2)$,
 - Rapidity $y = 1/2 \ln [(E+p_z)/(E-p_z)]$
 - The distance between particles $\Delta R = \sqrt{\Delta\eta^2 + \Delta\phi^2}$

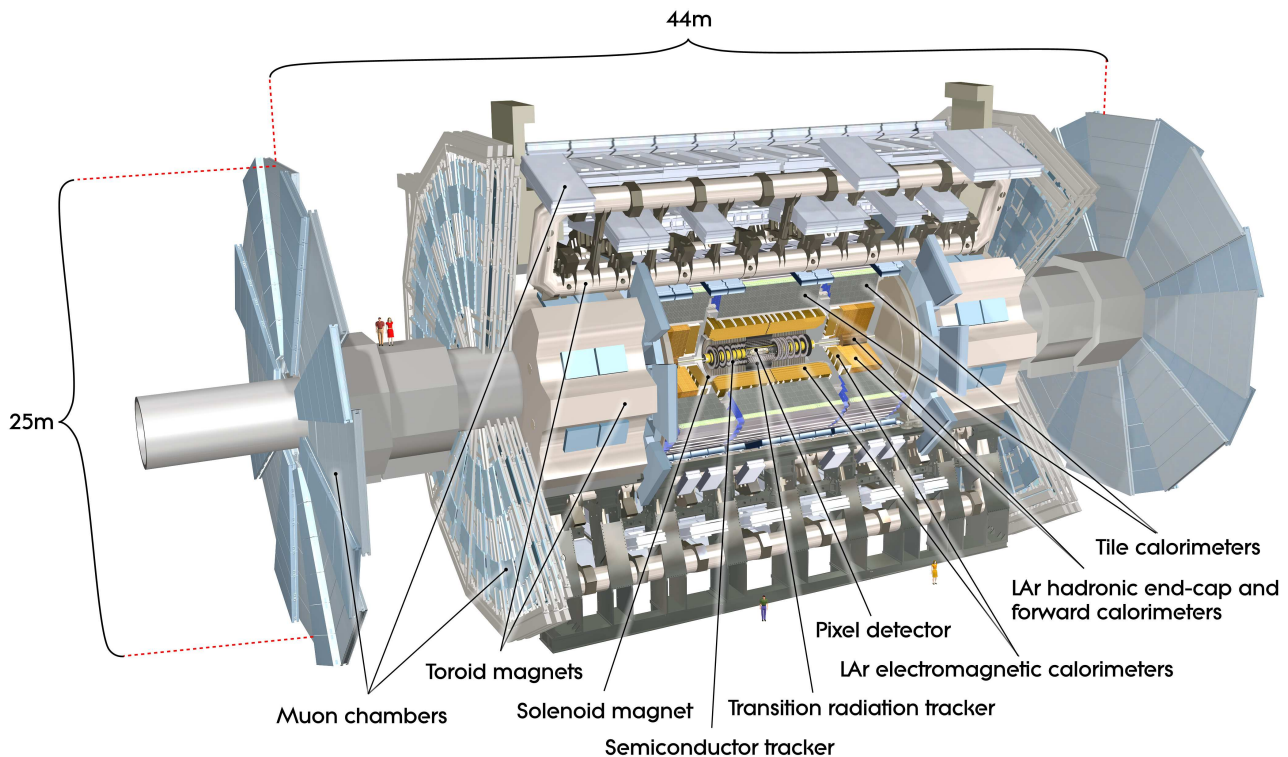


Figure 41: ATLAS detector general layout

1238 4.3 Magnet system and magnetic field

1239 ATLAS has a hybrid system of four superconducting magnets which has 22 m in diameter, 26 m in
 1240 length and stores an energy of 1.6 GJ [3]. The windings of the magnets are schematically shown in fig.
 1241 42. The four magnets that comprise the magnet system are the following:

- 1242 • The central solenoid is aligned with the beam axis providing 2T axial magnetic field for the inner
 1243 detector.
- 1244 • A barrel toroid produces toroidal magnetic field of about 0.5T for the muon detectors in the
 1245 barrel region.
- 1246 • Two end-cap toroids produce toroidal magnetic field of approximately 1T for the muon detectors
 1247 in the end-cap regions.

1248 4.4 Inner detector

1249 The ATLAS Inner Detector (ID) is designed to deliver pattern recognition, high-resolution momentum
 1250 measurement [4],[5] along with primary and secondary vertex determination for charged particle tracks

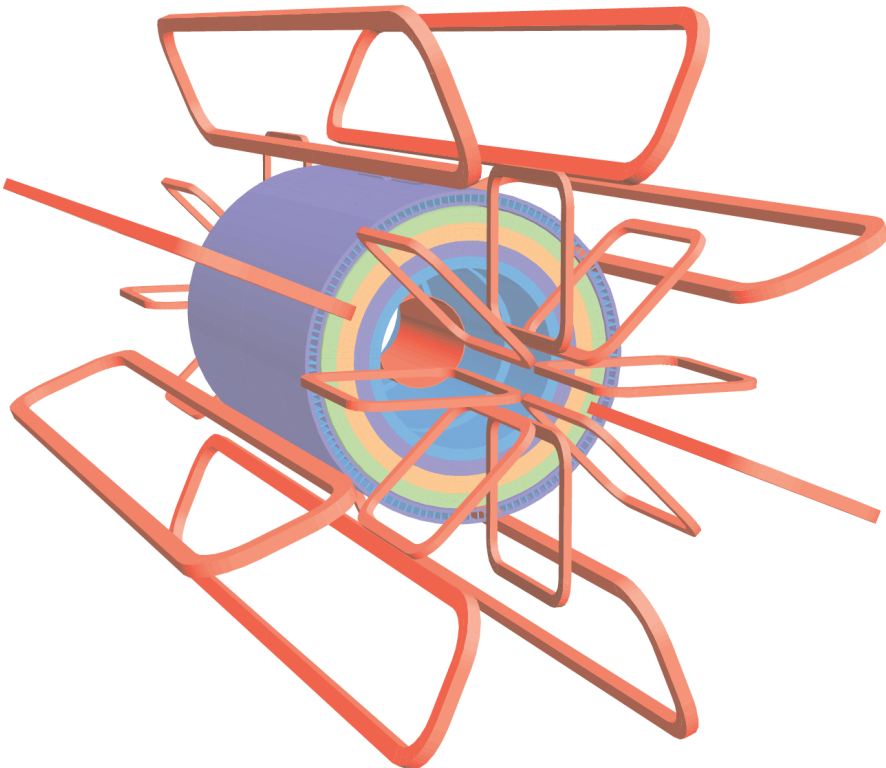


Figure 42: Geometry of ATLAS magnet windings

1251 above a designated p_T threshold of 0.5 GeV (in some cases being capable of going as low as 0.1 GeV)
1252 within the pseudorapidity range $|\eta| < 2.5$. The inner detector provides reliable electron identification
1253 in rapidity range of $|\eta| < 2.0$ for energies from 0.5 GeV to 150 GeV.

1254 The ID layout is a result of the technical requirements: it is assembled in a cylindrical envelope of 3512
1255 mm in length and 1150 mm in radius. It is surrounded by the magnetic field of 2T imposed by the
1256 superconducting solenoid (see section 4.3).

1257 Three independent sub-detectors complement each other in the inner detector (see fig. 511a (a)):

- 1258 • Silicon pixel with 3 cylindrical layers for the barrel and 3 discs on each side for the end-cap. It
1259 provides the highest granularity around the vertex region. Normally each track hits three pixel
1260 layers. The pixel detector has about 80.4 million readout channels. Each of 1744 identical pixel
1261 sensors has 47232 pixels and 46080 readout channels. About 90% of the pixels have the size of
1262 $50 \times 400 \mu\text{m}^2$, the remaining pixels are a bit longer: $50 \times 600 \mu\text{m}^2$.
- 1263 • Silicon microstrip layers (SCT) with 4 cylindrical layers and 9 discs on each side for the end-cap.
1264 A track typically crosses the strip layers in four space points. SCT has approximately 6.3 millions
1265 readout channels from its 15912 sensors. There are 768 active strips of 12 cm lenght and $80 \mu\text{m}$
1266 width per sensor plus two bias potential strips on the sensor edges.
- 1267 • Transition radiation tracker (TRT) with 73 straw planes in the barrel and 160 straw planes in

the end-cap. The TRT has around 351,000 readout channels and detects in average 36 hits per track. The straw tubes that make up the TRT module are 4 mm thick and 1.44 m long (0.37 m in the endcap) and made out of polyamide films reinforced with carbon fibers. The straws are filled with gas mixture of 70% Xe, 27% CO₂ and 3%O₂ and supplied with gilded tungsten anodes which are directly connected to the readout channels. The pixel and SCT sensors are highly radiation-proof and operate in the temperature range from -5°C to -10°C to minimize the radiation damage, while the TRT module operates at room temperature.

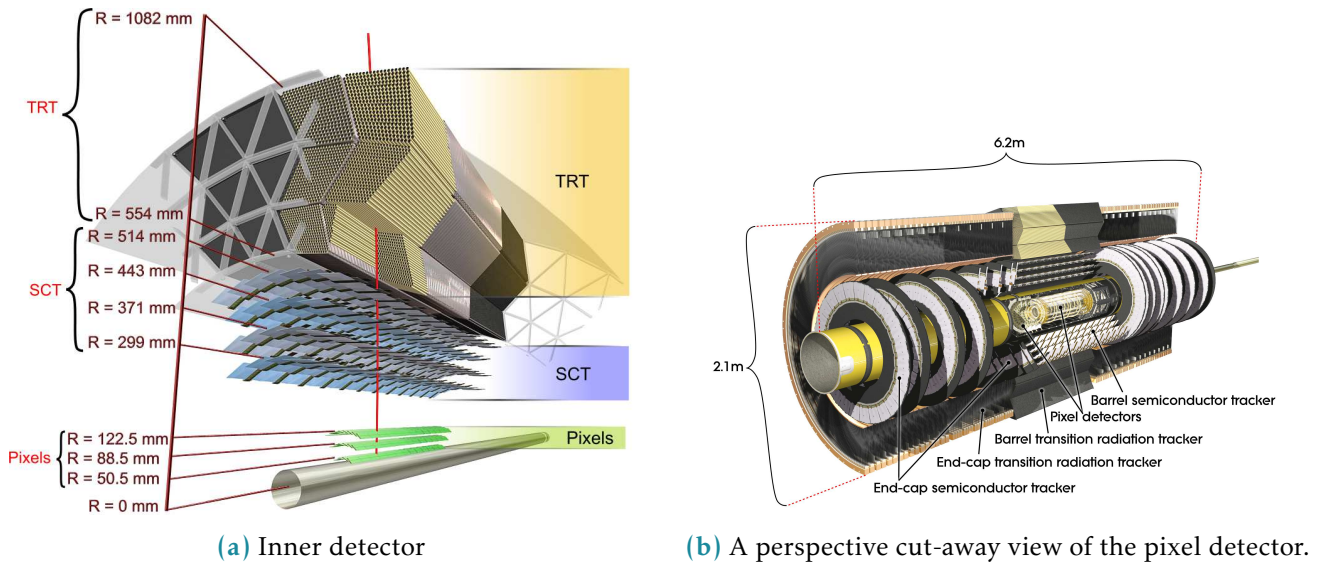


Figure 43: Fichier Gerber des modèles d CFR-34 et CFR-35.

4.5 Calorimeter system

The ATLAS calorimeter system covers the rapidity range within $|\eta| < 4.9$ and consists of several different detector systems. A rapidity region matched to the inner detector possesses fine granularity perfectly suited for high-precision measurements of photons and electrons. The remaining part's granularity is coarser but enough to perform jet reconstruction and measure E_T^{miss} . The view of ATLAS calorimeter is presented on fig. 44. Besides measuring the energy of travelling particles calorimeters must also contain electromagnetic and hadronic showers, limiting their ability to go penetrate the calorimeter completely and get to the muon chambers. This provides a typical scale for size of the calorimeter modules: the EM calorimeter[6] is >22 radiation lengths (X_0) in the barrel and $>24X_0$ in the end-caps. The hadronic calorimeter has the thickness of 9.7 interaction lengths (λ) in the barrel and 10λ of in the endcap, which is enough to keep the leakage level below the typical muon background. This size also provides good resolution for the E_T^{miss} measuremet. The detailed description of the calorimeter system can be found in the table 41.

1288 The tile calorimeter[7] uses scintillating tiles as active material alternated with steel absorbers. All the other calorimeter systems use liquid argon as an active medium with lead sampling.

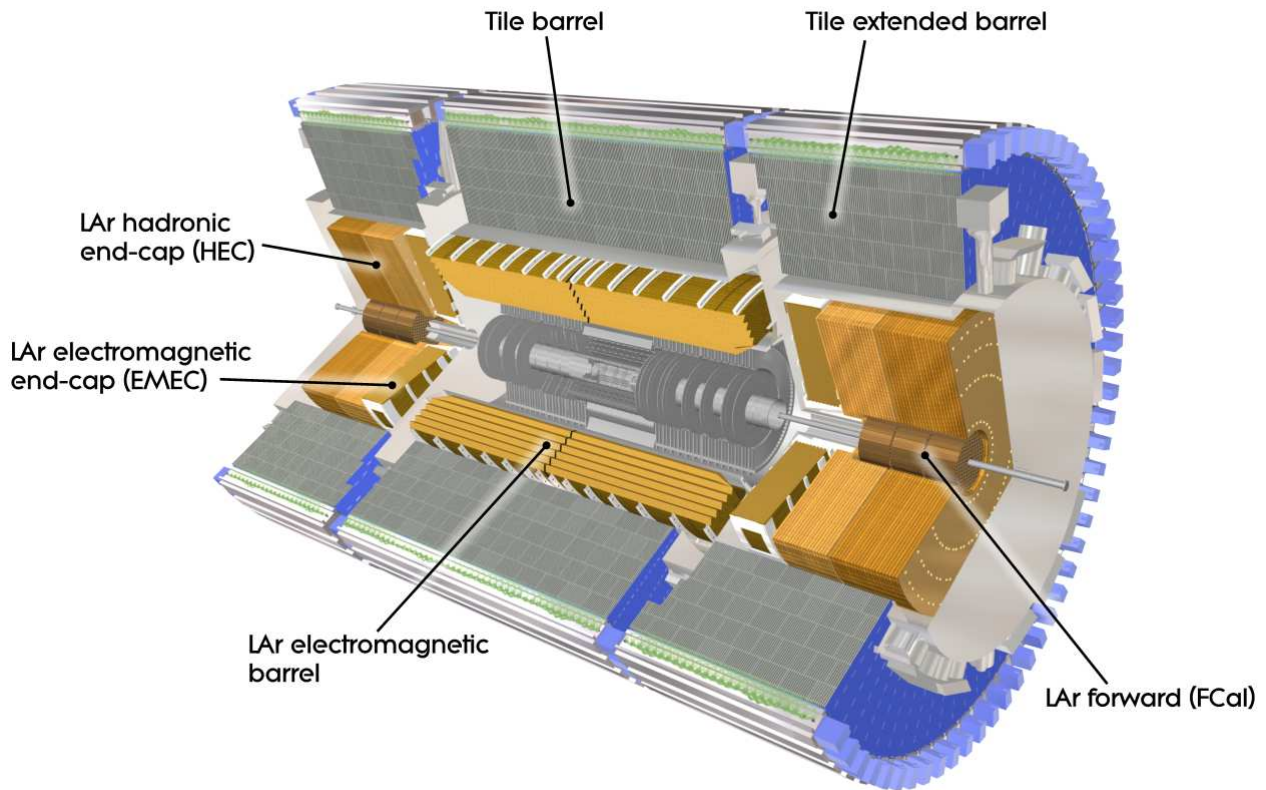


Figure 44: ATLAS calorimeter general layout

1289

1290 4.5.1 Electromagnetic calorimeter

1291 The EMC has two submodules:

- 1292 • EMC barrel detector.
1293 • Electromagnetic end-cap calorimeter (EMEC) end-cap detector.

1294 The EMC barrel module consists of two identical half-barrels 3.2 meters long with inner and outer radii
1295 2.8 m and 4 m respectively. There is a 4mm gap at $z = 0$ between the half-barrels. The second crack is
1296 situated between the barrel and the end-cap at $1.37 < |\eta| < 1.52$. The EMEC comprises of two pairs of
1297 coaxial wheels of 63 cm thick having inner and outer radii of 330 mm and 2098 mm respectively. The
1298 crack between the two wheels makes a third crack at $|\eta| = 2.5$. Both barrel and end-cap electromagnetic
1299 calorimeters are designed to have an accordion-shaped absorbers made out of lead plates, coated in
1300 stainless steel sheets. The readout electrodes are placed in the gaps between the absorbers. This type

	Barrel	End-cap			
EM Calorimeter					
Number of layers and $ \eta $ coverage					
Presampler	1	$ \eta < 1.52$	$1.5 < \eta < 1.8$		
Calorimeter	3	$ \eta < 1.35$	$1.375 < \eta < 1.5$		
Granularity $\Delta\eta \times \Delta\phi$ versus $ \eta $					
Presampler	0.025×0.1	$ \eta < 1.52$	$1.5 < \eta < 1.8$		
Calorimeter 1st layer	$0.025/8 \times 0.1$	$ \eta < 1.40$	$1.375 < \eta < 1.425$		
	0.025×0.025	$1.425 < \eta < 1.5$	$1.425 < \eta < 1.5$		
			$0.025/8 \times 0.1$		
			$1.5 < \eta < 1.8$		
			$0.025/6 \times 0.1$		
			$1.8 < \eta < 2.0$		
			$0.025/4 \times 0.1$		
Calorimeter 2nd layer	0.025×0.025	$ \eta < 1.40$	$1.375 < \eta < 1.425$		
	0.075×0.025	$1.4 < \eta < 1.475$	$1.425 < \eta < 2.5$		
			0.1×0.1		
Calorimeter 3rd layer	0.050×0.025	$ \eta < 1.35$	$1.5 < \eta < 2.5$		
Number of readout channels					
Presampler	7808	1536 (both sides)			
Calorimeter	101760	62208 (both sides)			
LAr hadronic end-cap					
$ \eta $ coverage		$1.5 < \eta < 3.2$			
Number of layers		4			
Granularity $\Delta\eta \times \Delta\phi$		0.1×0.1	$1.5 < \eta < 2.5$		
		0.2×0.2	$2.5 < \eta < 3.2$		
Readout channels		5632 (both sides)			
LAr forward calorimeter					
$ \eta $ coverage		$3.1 < \eta < 4.9$			
Number of layers		3			
Granularity $\Delta x \times \Delta y$		$F\text{Cal } 3.0 \times 2.6$	$3.15 < \eta < 4.30$		
		$F\text{Cal: } \sim\text{four times finer}$	$3.10 < \eta < 3.15$		
			$4.30 < \eta < 4.83$		
		$F\text{Cal2 } 3.3 \times 4.2$	$3.24 < \eta < 4.50$		
		$F\text{Cal2: } \sim\text{four times finer}$	$3.20 < \eta < 3.24$		
			$4.50 < \eta < 4.81$		
		$F\text{Cal3 } 5.4 \times 4.7$	$3.32 < \eta < 4.60$		
		$F\text{Cal3: } \sim\text{four times finer}$	$3.29 < \eta < 3.32$		
Readout channels		$4.60 < \eta < 4.75$			
		3524 (both sides)			
Scintillator tile calorimeter					
	Barrel	Extended barrel			
$ \eta $ coverage	$ \eta < 1.0$	$0.8 < \eta < 1.7$			
Number of layers	3	3			
Granularity $\Delta\eta \times \Delta\phi$		0.1×0.1	0.1×0.1		
		0.2×0.2	0.2×0.1		
Readout channels	5760	4092 (both sides)			

Table 41: ATLAS calorimeter in numbers

1301 of geometry allows full coverage in ϕ without cracks together with fast extraction of the signal from
 1302 both sides of the electrodes. The orientation of the accordion waves is axial in the barrel and radial in
 1303 the end-caps (see fig. 44). These features of the calorimeter lead to virtually uniform performance in ϕ
 1304 dimension.
 1305 Segmentation in η is very different in the layers of the calorimeter, but the second layer always has
 1306 the finest granularity because the egamma particles are supposed to leave most of their energy in the
 1307 second calorimeter layer. In order to correct for the energy losses upstream the barrel calorimeter is
 1308 preceded by a thin LAr active layer of 11mm thick called a presampler. For more details on η coverage
 1309 and granularity see table 41.

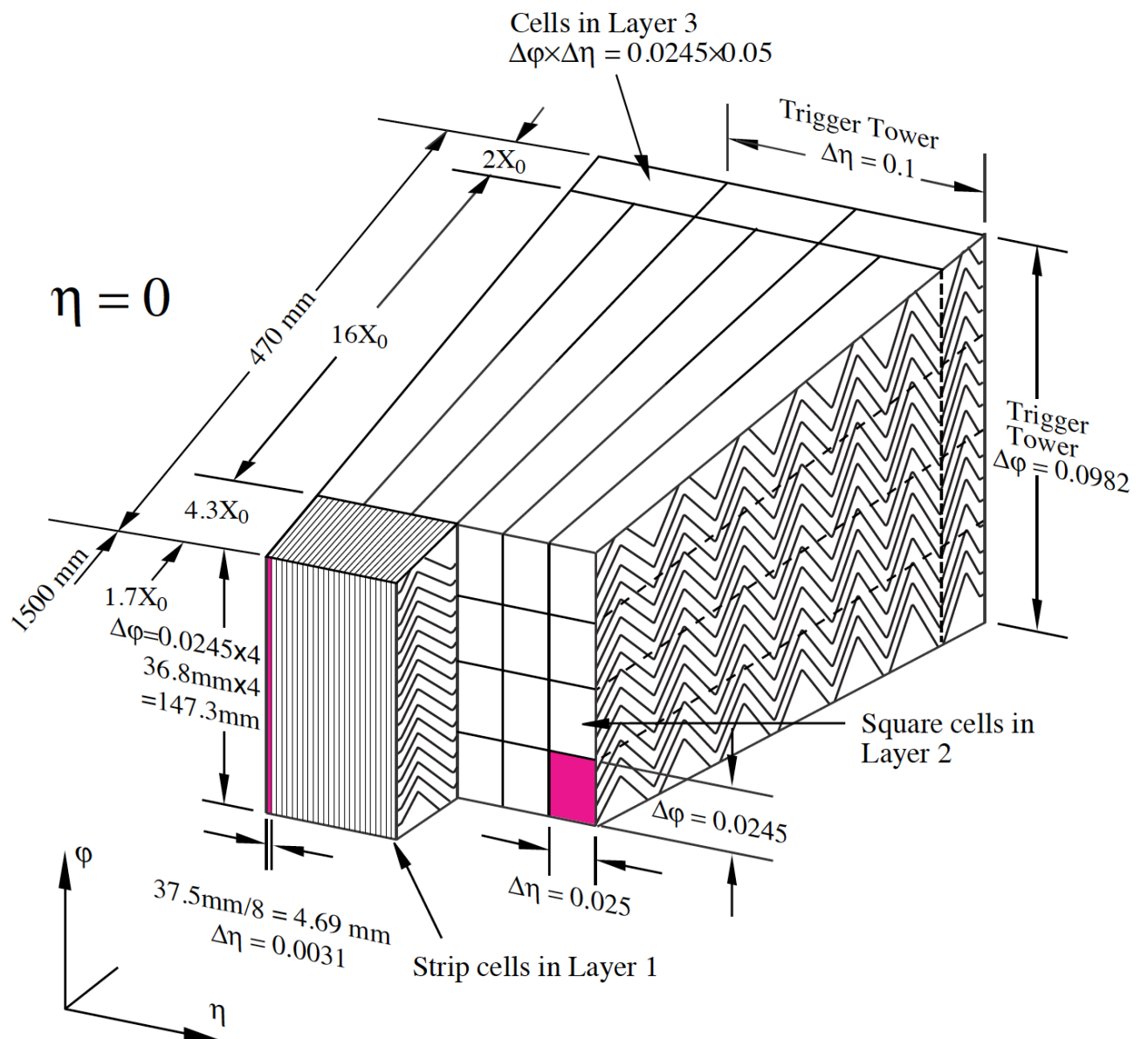
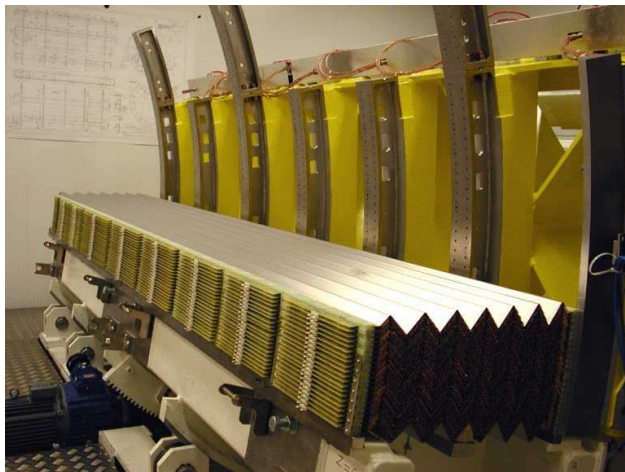


Figure 45: ATLAS EM calorimeter layers



(a) Barrel



(b) End-cap

Figure 46: Accordion absorbers of the EMC

1310 4.5.2 Hadronic calorimeter

1311 The hadronic calorimeter (HC) is combined of three submodules:

- 1312 • HC scintilating tile detector, a steel sampled detector divided in turn into central barrel having
1313 5.8 m in length and two extended barrels 2.6 m in length each. The extended barrels have inner
1314 radii of 2.28 m and outer radii of 4.25 m. The tile calorimeter consists of three layers having
1315 about 1.5, 4.1 and 1.8 interaction lengths λ in the barrel and 1.5, 2.6 and 3.3 λ s in the extended
1316 barrel.
- 1317 • Hadronic end-cap calorimeter (HEC) detector is a liquid argon calorimeter sampled with copper.
1318 It has two pairs of independent wheels symmetrically located behind the EMEC called the frona
1319 and the rear wheel. The wheels are cylindrical, their outer radius is 2030mm.
- 1320 • Forward calorimeter (FCal) detector modules are located about 4.7 m from the IP and are
1321 subjected to very high particle flux and radiation. It consists of three wheels 45 cm deep each.
1322 The first one, FCal1 is sampled with copper intended for the measurement of electromagnetic
1323 processes. The two other wheels FCal2 and FCal3 are sampled with tungsten and designed for
1324 the hadronic showers measurement.

1325 The number of the readout channels as well as the η coverage of every module and submodule is
1326 described in the Table 41.

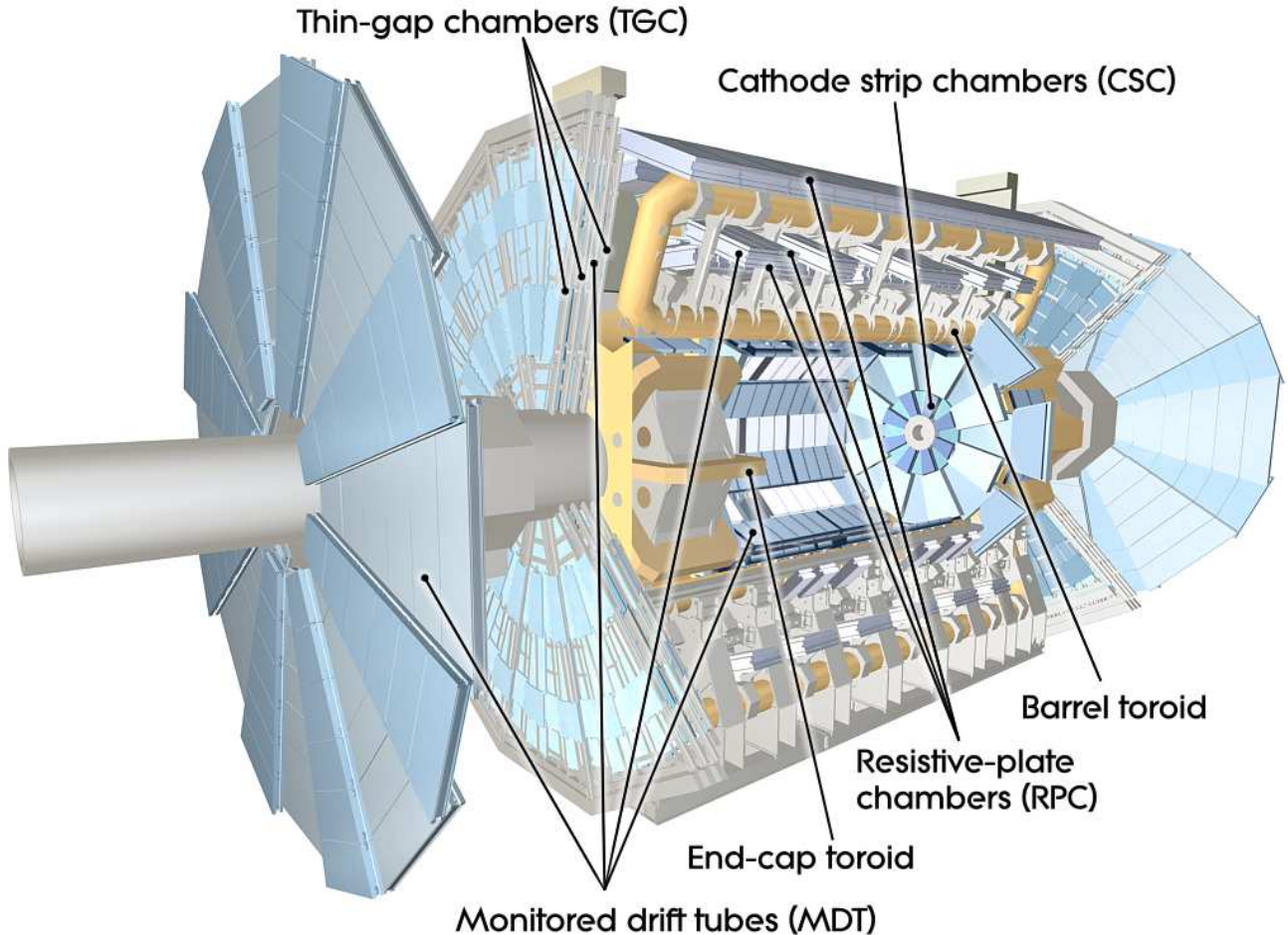


Figure 47: ATLAS muon system

1327 4.6 Muon detectors

1328 Most of the muons produced as a result of the p-p collisions are able to penetrate through calorimeters
 1329 and make it to the muon detectors where their tracks are getting measured. The spectrometer provides
 1330 high-precision measurement of the muon momenta in the rapidity range of $|\eta| < 2.7$ and approximate
 1331 transverse momentum range of $3 \text{ GeV} < p_T < 3 \text{ TeV}$. The lower bound on the momentum is mainly due
 1332 to energy losses in the calorimeter, while the upper bound is caused by the saggita bias coming from
 1333 the tracking chambers alignment. The goal p_T resolution is about 10% for a 1 TeV muon track.
 1334 The muon tracks[8],[9] are bent by the torroidal magnets allowing to determine muon kinematic prop-
 1335 erties. The large barrel toroid covers the rapidity range of $|\eta| < 1.4$, while at $1.6 < |\eta| < 2.7$ the tracks
 1336 are bent by the smaller end-cap magnets. The deflection in the transition region of $1.4 < |\eta| < 1.6$ is
 1337 provided by the barrel and end-cap fields combined.
 1338 The general layout of the muon spectrometer is depicted on fig. 47, the parameters of the muon systems
 1339 can be found in table ??.

1340 the barrel and the end-cap parts.
1341 The muon spectrometer possesses a fast triggering system able to trigger for muons in the rapidity
1342 range of $|\eta| < 2.4$. It delivers the track information within a few tens of nanoseconds after the particle
1343 passage which also allows to use it for the bunch-crossing identification. The trigger chambers measure
1344 both η and ϕ coordinates of a track of which the former is in the bending plane and the latter is in the
1345 non-bending plane.

1346 There are two types of fast triggering detectors used in the muon spectrometer:

- 1347 • The Resistive Plate Chambers (RPCs) is a gaseous electrode-plate detector filled with a $C_2H_2F_4/Iso-$
1348 C_4H_{10}/SF_6 gas mixture (94.7/5/0.3). Two resistive plates of phenolic-melaminic plasctic lami-
1349 nate are separated by insulating spacers of 2 mm thickness. The plates contain an electric field of
1350 about 4.9 kV/mm such that the ionizing tracks cause avalanches towards the anode. The signal is
1351 read out through the capacitive coupling of metalic strips, mounted to the resistive plates. The
1352 RPCs have nominal operating voltage of 9.8 kV and provides an excellent time resolution of a
1353 few ns with a supported local rate capability of 1000 Hz/cm^2
- 1354 • Thin Gap Chambers (TGCs) are multi-wire proportional chambers with the wire-to-cathode
1355 ditance of 1.4 mm and wire-to-wire distance of 1.8 mm and wire potential of 2900 V. The 2.8-mm
1356 gas gap is filled with highly quenching gas mixture of CO_2 and $n-C_5H_{12}$ (55/45). Small distance
1357 between the wires allows a very good time resolution of <25 ns in 99% of cases .

1358 The precision-tracking chambers measure the coordinate of a track in the bending plane which is then
1359 matched with the second coordinate, measured by the trigger chamber.

1360 There are two types of precision tracking systems used:

- 1361 • The Monitored Drift Tubes (MDTs) are pressurised drift tubes with a diameter of 29.970 mm
1362 filled with Ar/CO_2 at 3 bar. Once the muon penetrates the tube it ionises the gas and the
1363 ionised electrons are collected at the central tungsten-renium wire of $50 \mu\text{m}$ in diameter and at a
1364 potential of 3080 V. This type of design carries several advantages: mechanical stiffness hence
1365 the alignment precision, reliability coming from the fact that a failure of a single tube would
1366 not cause malfunction of the others. MDTs counting rate is limited to 150 Hz/cm^2 which is not
1367 sufficient for the innermost layer in the forward region of $2.0 < |\eta| < 2.7$.
- 1368 • Cathode Strip Chambers (CSCs) are gas detectors filled with Ar/CO_2 in 80/20 proportion. The
1369 ionised electrons are collected at the wires which are oriented in the radial direction and operate
1370 at a potential of 1900 V. They are installed in the so-called Small Wheels and there are 16 CSCs
1371 on either side of the ATLAS detector. . The CSCs are able to provide a countng rate of 1000
1372 Hz/cm^2 which makes it a reasonable replacement for the MDTs in the region close to the beam.

1373 The precision-tracking chambers in the barrel are positioned between and on the coils of the supercon-
1374 ducting barrel thoroid magnet. They form three concentric cylindrical shells around the beam axis

at the approximate radii of 5 m, 7.5 m and 10 m. In the barrel region the RPCs were chosen for the fast triggering whereas the MDTs provide the precision tracking. The end-cap muon spectrometer is assembled in the form of large wheels perpendicular to the beam axis and located at distances about 7.4 m, 10.8 m, 14m and 21.5 m from the interaction point. The triggering in the end-cap is provided by the TGCs. Most of the precision tracking chambers are the MDTs similarly to the barrel, except for the forward region of $2.0 < |\eta| < 2.7$ where the CSCs are installed in the innermost tracking layer. The reason for that is their higher resistance to radiation and increased particle flow which becomes an issue if you get closer to the beam.

Barrel and end-cap alignment is illustrated on fig. 48 which contains the side and transverse views of the muon spectrometer.

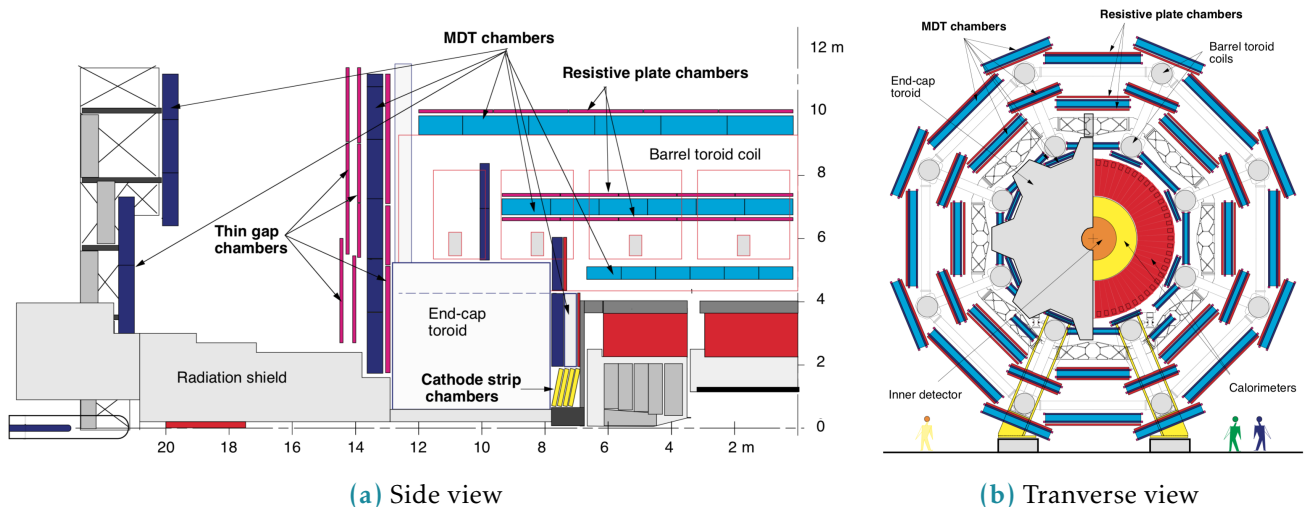


Figure 48: Cut views of the muon systems

1384

4.7 Forward detectors

There are three detector systems that cover the ATLAS forward region (see fig. 49): LUminosity measurement using Cherenkov Integrating Detector (LUCID), Zero-Degree Calorimeter (ALFA) and Absolute Luminosity for ATLAS (ZDC). The measurement of luminosity is the main goal of the first two detectors and has fundamental importance: it provides the normalization scale for all the observed processes.

LUCID[10], [11] is the main ATLAS relative luminosity monitor. The main purpose of the LUCID detector is to detect inelastic p-p scattering in the forward region measuring the integrated luminosity and performing online monitoring of the instantaneous luminosity and beam conditions with uncertainty of about few percent. It is symmetrically installed at ± 17 m from the interaction point and at a radial distance of about 10 cm from the beam line (resulting in $|\eta| \approx 5.8$). On each side four bundles of quartz fibers are used as a medium producing Cherenkov radiation directing the Cherenkov light into the 16

Monitored drift tubes	MDT
Coverage	$ \eta < 2.7$ (innermost layer: $ \eta < 2.0$)
Number of chambers	1088 (1050)
Number of channels	339 000 (354 000)
Function	Precision tracking
Cathode strip chambers	CSC
Coverage	$2.0 < \eta < 2.7$
Number of chambers	32
Number of channels	31 000
Function	Precision tracking
Resistive plate chambers	RPC
Coverage	$ \eta < 1.05$
Number of chambers	544 (606)
Number of channels	359 000 (373 000)
Function	Triggering, second coordinate
Thin gap chambers	TGC
Coverage	$1.05 < \eta < 2.7$
Number of chambers	3588
Number of channels	318 000
Function	Triggering, second coordinate

Table 42: ATLAS muon spectrometer subsystems coverage and parameters

1397 Photomultipliator Tubes (PMTs) placed outside the radiation shielding.

1398 The ALFA[12] detector is used to measure the absolute luminosity through elastic scattering at small
1399 angles. In order to perform such measurement we need to meet the following conditions:

1400

1401 • The beam has to be more parallel than normally. Special collider beam optics allowing high values
1402 of the amplitude function at the interaction point β^* together with reduced beam emittance.

1403 • To be sensitive to small angles the detectors have to be placed as far as possible from the
1404 interaction point and close to the beam. This is why the detectors are located inside the Roman
1405 pots at ± 240 from the interaction point. On each side there are two Roman pots separated by
1406 four meters.

1407 The Roman pot windows allow the elastically scattered protons reach the square scintillating fibres of
1408 0.5 mm width which are in turn connected to multi-anode PMTs through the light-guides. The detector
1409 provides a spacial resolution of $30 \mu\text{m}$ and allows to measure absolute luminosity with uncertainty of
1410 1.7% for the Run 2[13].

1411 ZDC are used to detect forward neutrons at $|\eta| > 8.3$ in heavy-ion collisions, which in turn allows to
1412 determine the centrality of such collisions. The detector is installed at ± 140 m from the interaction

point. Every ZDC arm consists of 4 modules: one electromagnetic and three hadronic. These modules are quartz rods shielded by the tungsten plates and connected to the PMTs via the light-guides allowing to measure incending particle energy and position. The EM module has a better position resolution mapping each of 96 quartz rods into a single pixel, while the hadronic modules map a bundle of four rods into a pixel. Only one of the three hadronic modules per arm provide position-sensing rods and only the arm at -140 m has the position-sensing EM module.

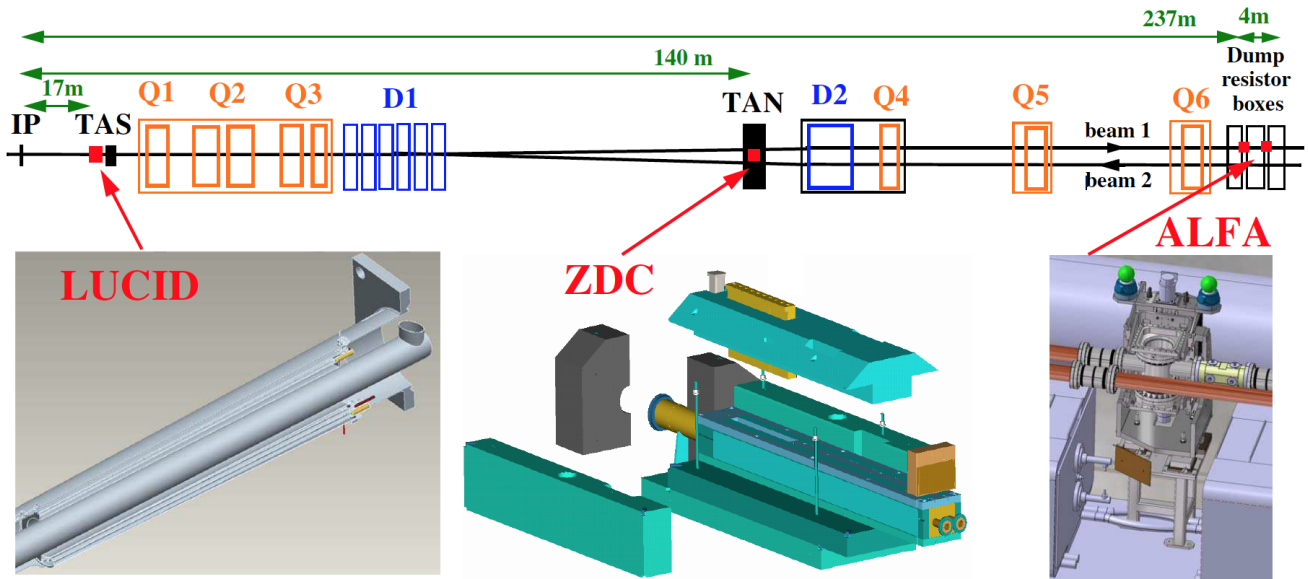


Figure 49: ATLAS forward detectors

1418

1419 4.8 Trigger system

Considering that the bunch crossing rate at LHC is about 40 MHz and that ATLAS detector has over one million read-out channels it would never be possible to store all the raw data without significant preselection that would decrease the data rate. The selection criteria are picked to retain and store only the events which might be interesting for the LHC physics. The preselection and storage is conducted with the help of TDAQ systems.

The trigger system has three distinct levels: L1, L2 and the event filter, the two latter levels are also called High-level Trigger (HLT). Each next level refines the decisions made before and, if necessary, applies additional selection, further lowering the event rate. The data acquisition system receives and buffers the event data from the readout electronics at the L1 trigger accept rate which for Run 2 is about 100 kHz [14]. The HLT then lowers the rate down to 1.5 kHz which is then stored for the offline analysis.

The L1 trigger looks for muons, electrons, photons, jets at hadrons from τ -lepton decays with high transverse momentum, large missing and total transverse energy. The muons of interest are identified

1433 using the muon spectrometer trigger system described in section 4.6. The rest of the particles are
 1434 selected using the information from all the calorimeters with reduced granularity. During the Run 2 an
 1435 intermediate L1Topo trigger was also added allowing to combine the information from the spectrometer
 1436 and calorimeter and extend possible trigger selections. Results from these triggers gets processed by
 1437 the central trigger processor which implements the trigger menu made up of different combinations of
 1438 trigger selections. The decision latency for the L1 trigger must not exceed $2.5 \mu\text{s}$ after the corresponding
 1439 bunch crossing.

1440 For every selected event the L1 defines one or more regions called Region of Interest (RoI) which
 1441 include the η and ϕ coordinates of these regions for their subsequent use by the HLT. The L2 selection
 1442 is seeded RoI and uses full granularity and precision along with other detector data available. The
 trigger block diagram is presented in fig. 410.

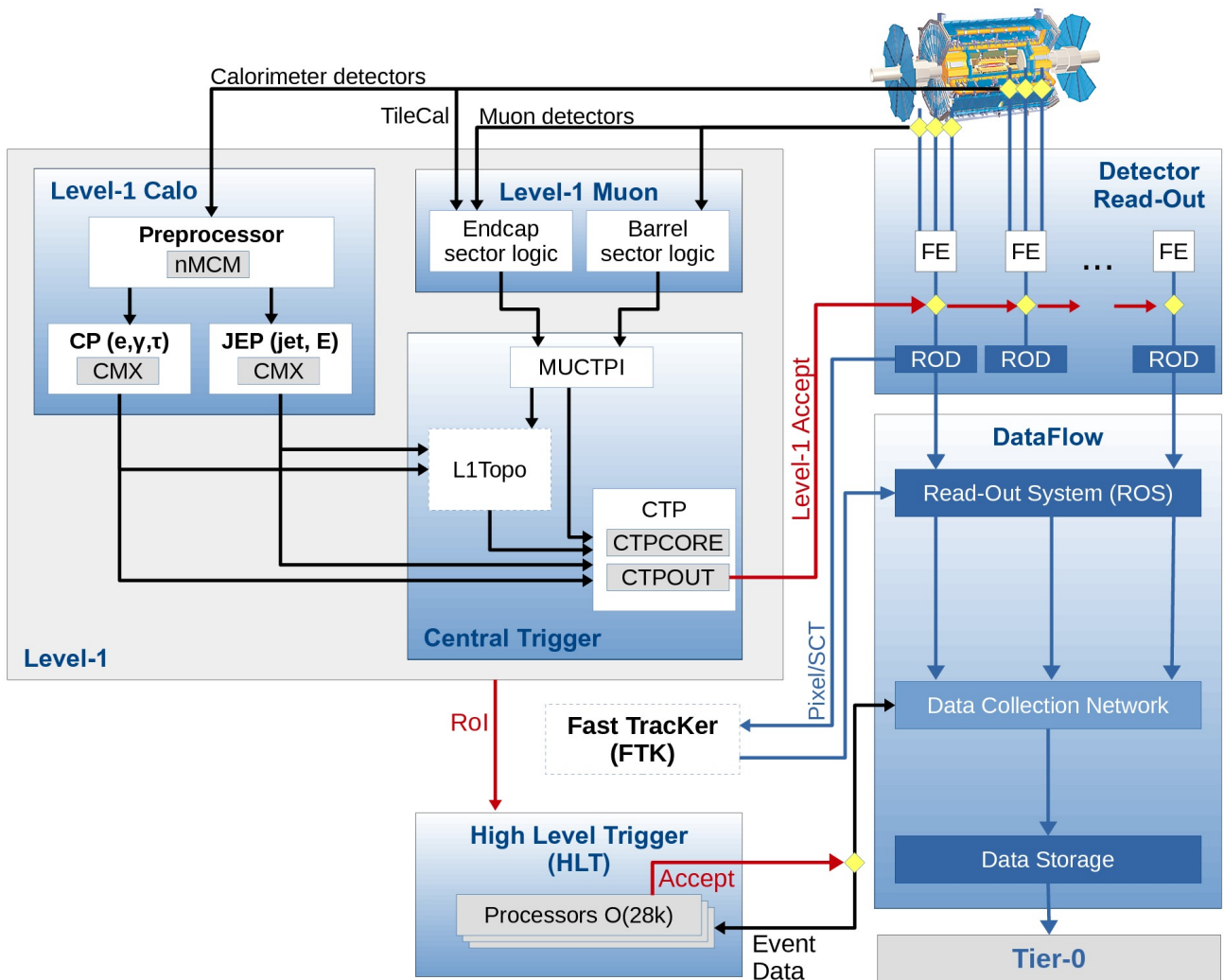


Figure 410: The scheme of ATLAS trigger systems

1444 Bibliography

- 1445 [1] G. Aad et al. “The ATLAS Experiment at the CERN Large Hadron Collider”. In: *JINST* 3 (2008),
1446 S08003. doi: 10.1088/1748-0221/3/08/S08003.
- 1447 [2] Aranzazu Ruiz-Martinez and ATLAS Collaboration. *The Run-2 ATLAS Trigger System*. Tech. rep.
1448 ATL-DAQ-PROC-2016-003. Geneva: CERN, Feb. 2016. doi: 10.1088/1742-6596/762/1/012003.
1449 URL: <https://cds.cern.ch/record/2133909>.
- 1450 [3] *ATLAS magnet system: Technical Design Report*, 1. Technical Design Report ATLAS. Geneva: CERN,
1451 1997. URL: <https://cds.cern.ch/record/338080>.
- 1452 [4] *ATLAS inner detector: Technical Design Report*, 1. Technical Design Report ATLAS. Geneva: CERN,
1453 1997. URL: <https://cds.cern.ch/record/331063>.
- 1454 [5] S Haywood et al. *ATLAS inner detector: Technical Design Report*, 2. Technical Design Report ATLAS.
1455 Geneva: CERN, 1997. URL: <https://cds.cern.ch/record/331064>.
- 1456 [6] *ATLAS liquid-argon calorimeter: Technical Design Report*. Technical Design Report ATLAS. Geneva:
1457 CERN, 1996. URL: <https://cds.cern.ch/record/331061>.
- 1458 [7] *ATLAS tile calorimeter: Technical Design Report*. Technical Design Report ATLAS. Geneva: CERN,
1459 1996. URL: <https://cds.cern.ch/record/331062>.
- 1460 [8] *ATLAS muon spectrometer: Technical Design Report*. Technical Design Report ATLAS. Geneva:
1461 CERN, 1997. URL: <https://cds.cern.ch/record/331068>.
- 1462 [9] ATLAS Collaboration. *Technical Design Report for the Phase-II Upgrade of the ATLAS Muon Spec-
1463 trometer*. Tech. rep. CERN-LHCC-2017-017. ATLAS-TDR-026. Geneva: CERN, Sept. 2017. URL:
1464 <https://cds.cern.ch/record/2285580>.
- 1465 [10] g chiodini g, n orlando n, and s spagnolo s. *ATLAS RPC time-of-flight performance*. Tech. rep.
1466 ATL-MUON-PROC-2012-002. Geneva: CERN, Apr. 2012. URL: <https://cds.cern.ch/record/1437020>.
- 1468 [11] Marco Bruschi. *The new ATLAS/LUCID detector*. Tech. rep. ATL-FWD-PROC-2015-002. Geneva:
1469 CERN, June 2015. URL: <https://cds.cern.ch/record/2025000>.
- 1470 [12] S. Abdel Khalek et al. “The ALFA Roman Pot Detectors of ATLAS”. In: *JINST* 11.11 (2016),
1471 P11013. doi: 10.1088/1748-0221/11/11/P11013. arXiv: 1609.00249 [physics.ins-det].
- 1472 [13] *Luminosity determination in pp collisions at $\sqrt{s} = 13$ TeV using the ATLAS detector at the LHC*.
1473 Tech. rep. ATLAS-CONF-2019-021. Geneva: CERN, June 2019. URL: <https://cds.cern.ch/record/2677054>.
- 1475 [14] William Panduro Vazquez and ATLAS Collaboration. *The ATLAS Data Acquisition system in LHC
1476 Run 2*. Tech. rep. ATL-DAQ-PROC-2017-007. 3. Geneva: CERN, Feb. 2017. doi: 10.1088/1742-
1477 6596/898/3/032017. URL: <https://cds.cern.ch/record/2244345>.

5

Electromagnetic shower shapes correction in the electromagnetic calorimeter

“Potentielle citation sans aucun rapport avec le sujet”

— Personne inconnue, contexte à déterminer

5.1 Introduction

The design and functionality of the ATLAS electromagnetic calorimeter was described in 4.5.1. Let's consider a bit more in detail the physical processes happening in the EMC. It order to measure particle's energy within the calorimeter we must make the particle to loose its entire energy within the calorimeter. For the electrons and photons with energies over few MeV (which is the case for the ATLAS experiment) the primary energy loss mechanism lies in bremsstrahlung radiation and pair creation). The two processes complete each other, so when a high-energy electron or photon gets into the calorimeter, it creates an avalanche-like processus called the electromagnetic shower when a bremsstrahlung-radiated photons create more electron-positron pairs which in turn radiate more bremsstrahlung photons and so on and so forth (see fig. 51.)

The longitudinal and transverse development of the shower depends on the type of the initial particle

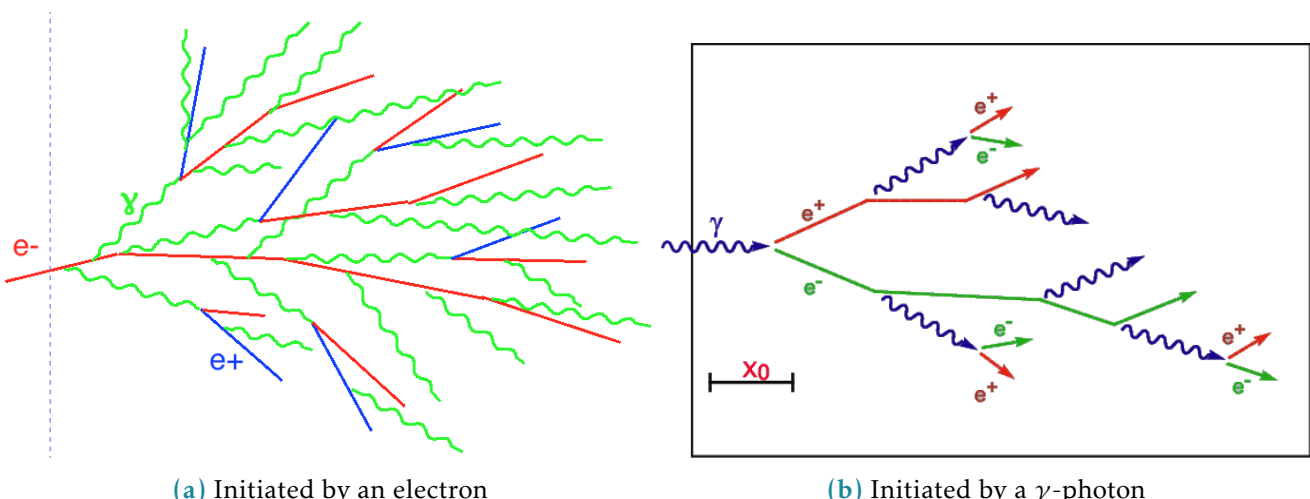
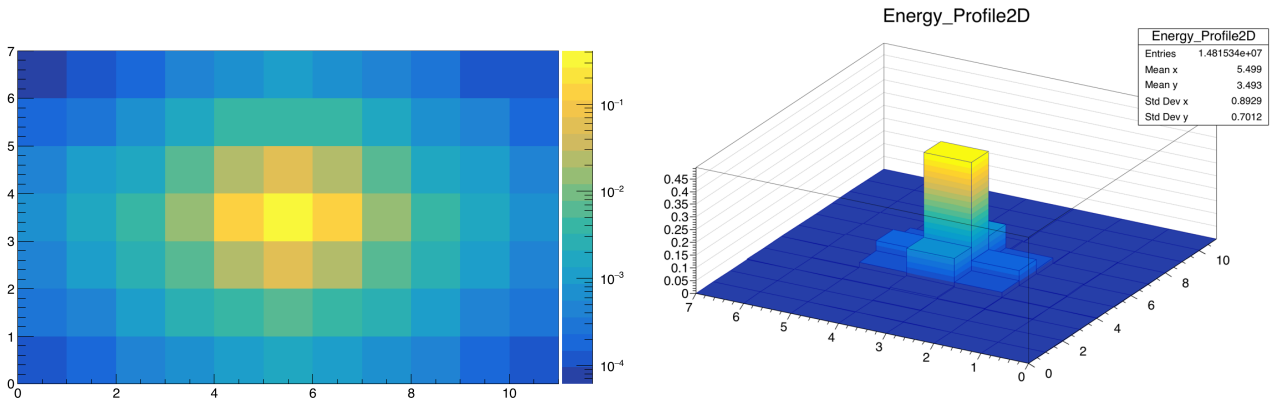


Figure 51: The schematic portrayal of EM shower development

and on its energy. The energy is well measured by the calorimeter, but identifying the particle still remains a challenging task. The transverse granularity of the ATLAS calorimeter allows to resolve the

1495 energy distribution within the electromagnetic shower in the transverse plane. This information can
 1496 later be used for particle identification.
 1497 When an e/ γ particle hits the calorimeter its footprint in the second layer of the calorimeter is visible as
 1498 a cluster of calorimeter cells centered at the central cell having the most energy deposited (sometimes
 1499 referred to as "the hottest cell"). Roughly 90% of shower energy is contained in the core 3x3 cells. We
 1500 have considered a cluster of 7x11 ($\eta \times \phi$) cells, which is schematically depicted on fig. 52a.

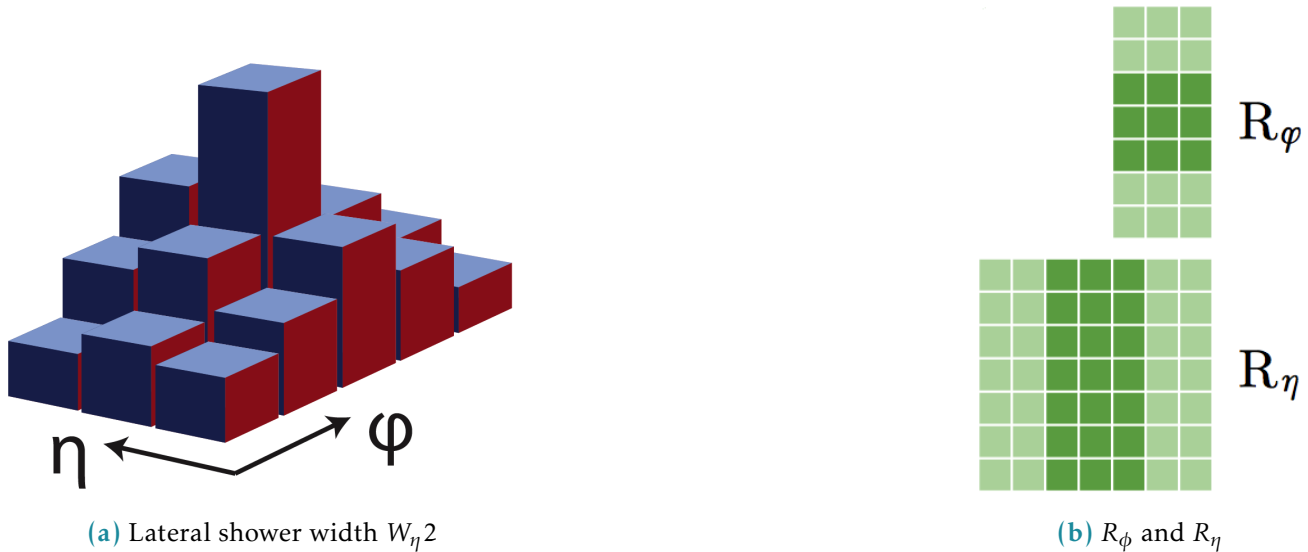


(a) Energy profile of a window of 7x11 cells in the 2nd calorimeter layer (logarithmic scale)

(b) 2D profile of the cluster

Figure 52: Visualisations of the 7x11 calorimeter cluster

1501 In order to characterise the energy distribution within the shower profile a number of observables
 1502 called shower shapes are used. They are then used as an input for particle identification MVA algorithm.
 1503 Current study focuses on the second layer of the calorimeter for which there are three shower shape
 1504 observables described below [1]:



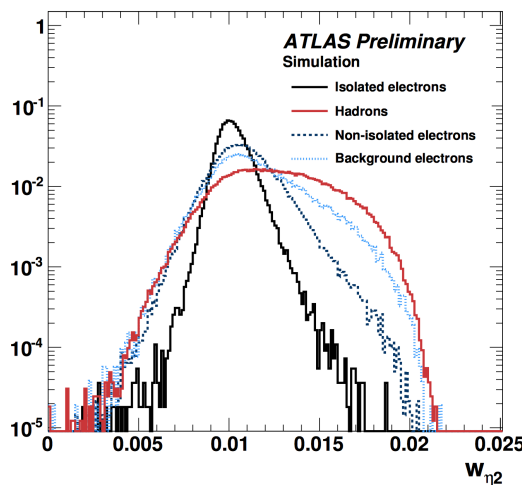
(a) Lateral shower width $W_{\eta}/2$

(b) R_ϕ and R_η

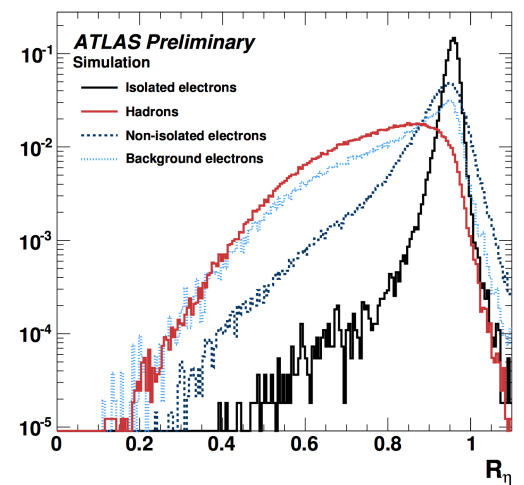
Figure 53: Shower shapes in the second layer of the electromagnetic calorimeter

- Lateral shower width $W_{\eta 2} = \sqrt{\sum(E_i \eta_i^2) - (\sum(E_i \eta_i)/\sum(E_i))^2}$ calculated within a window of 3x5 cells.
- R_ϕ - ratio of the energy in 3x3 cells over the energy in 3x7 cells centered around the hottest cell.
- R_η - ratio of the energy in 3x7 cells over the energy in 7x7 cells centered around the hottest cell.

The shower shapes distributions for different types of particles is shown in fig. ?? - although the distributions overlap, combining the shower shapes information with the inputs from other detectors allow to identify the particle.



(a) $W_{\eta 2}$ distribution simulation



(b) R_η distribution simulation

Figure 54: Distribution of R_η in simulation (GEANT4) for electrons and jets [2].

Figure ?? shows how R_η distribution is different in jets, signal electrons and background electrons. Background electrons denote non-prompt electrons which are not originated from primary vertex.

The shower shapes appear to be extremely sensitive to the detector material modelling. A simplification in the geometry of the EMCAL absorber geometry in GEANT4 9.2 (a layered structure of the accordion was represented as a homogenous material) has lead to visible discrepancies in the shower shapes between the data and MC. This was corrected in GEANT4 9.4 significantly improving the agreement, although not eliminating it completely (see fig. 55). The origin for the remaining discrepancy is not clear.

Disagreement in shower shapes between the data and MC leads to discrepancies in particle ID which are later fixed using η - and p_T -dependent scale factors. Correction of the shower shapes aims to get the scale factors closer to unity, reducing the corresponding systematic uncertainties and improving the precision of the measurements with electrons in the final states.

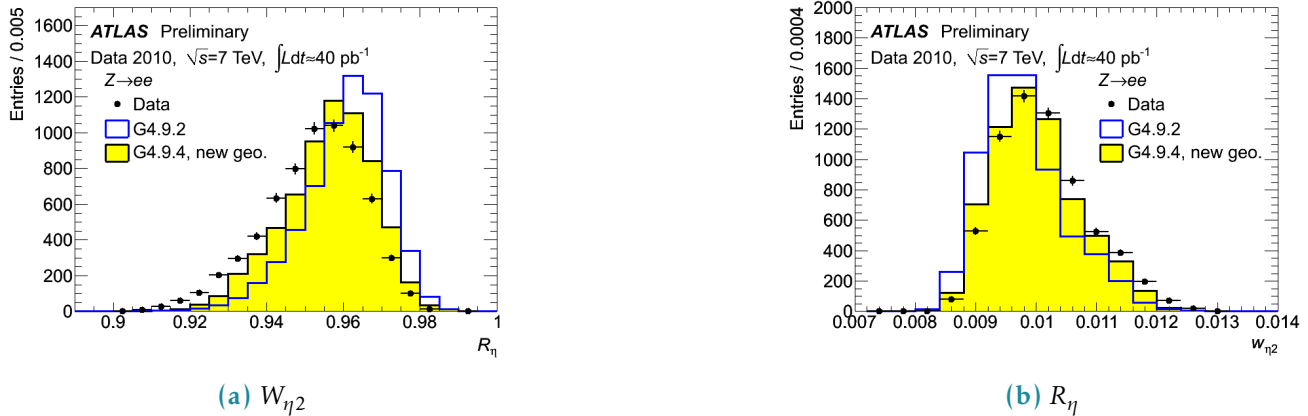


Figure 55: Data/MC Comparison for Calorimeter Shower Shapes of High Et Electrons [3].

1526 5.2 Shower shapes measurement and correction

1527 5.2.1 Event selection

1528 For this study we have considered electrons from the $Z \rightarrow ee$ decay. A set of recommended single
 1529 electron triggers was used (HLT_e26_lhtight_nod0_ivarloose, HLT_e60_lhmedium_nod0,
 1530 HLT_e140_lhloose_nod0, HLT_e300_etcut). Each event was required to have 2 electrons at least one
 1531 of which has $p_T > 25$ GeV. In order to suppress the background both electrons had to pass gradient
 1532 isolation. Z invariant mass cut was applied with a window of 80 – 120GeV. To avoid identification bias
 1533 from triggering the tag and probe approach was used with only probe electrons taken into consideration
 1534 [4]. The electron cluster in the second calorimeter layer was required to contain information from 77
 1535 calorimeter cells. No pile-up reweighting has been applied. Datasets of 264786295 events in data (2017
 1536 proton-proton collisions) and 79340000 events in MC (Powheg+Pythia8) were used.

1537 5.2.2 Data/MC discrepancies

1538 Our consideration begins with the energy deposit of an electron in the second layer of the calorimeter.
 1539 A window of 7 cells in η and 11 cells in ϕ is centered around the cell with the highest energy.

1540 Shower shapes were considered in 14 η bins in the range between $|\eta| = (0, 2.4)$ in order to investigate
 1541 how the discrepancy depends on η .

1542 The η -dependent shower shapes in data are wider than the MC and show a larger discrepancy in the
 1543 endcap ($|\eta| = (1.52, 2.4)$). For ϕ dimension the situation is the opposite: MC is wider than the data and
 1544 the barrel ($|\eta| = (0, 1.52)$) shows larger discrepancy. Figures ??, ??, ?? contain examples of shower shapes
 1545 in different eta bins.

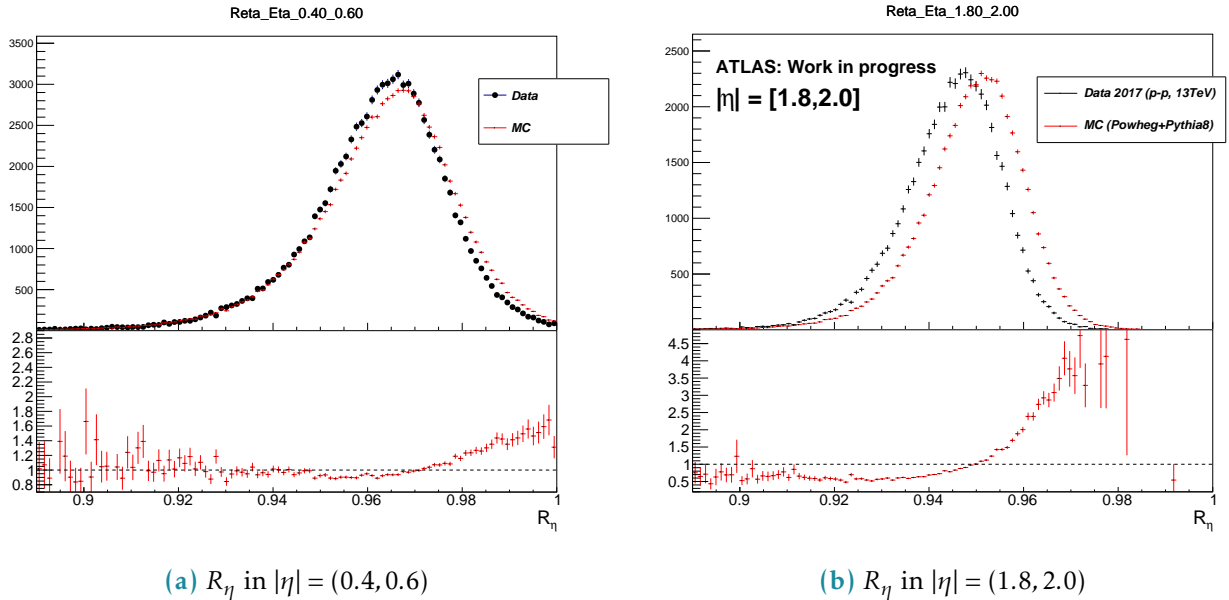


Figure 56: R_η in the barrel and in the end-cap, Data vs MC

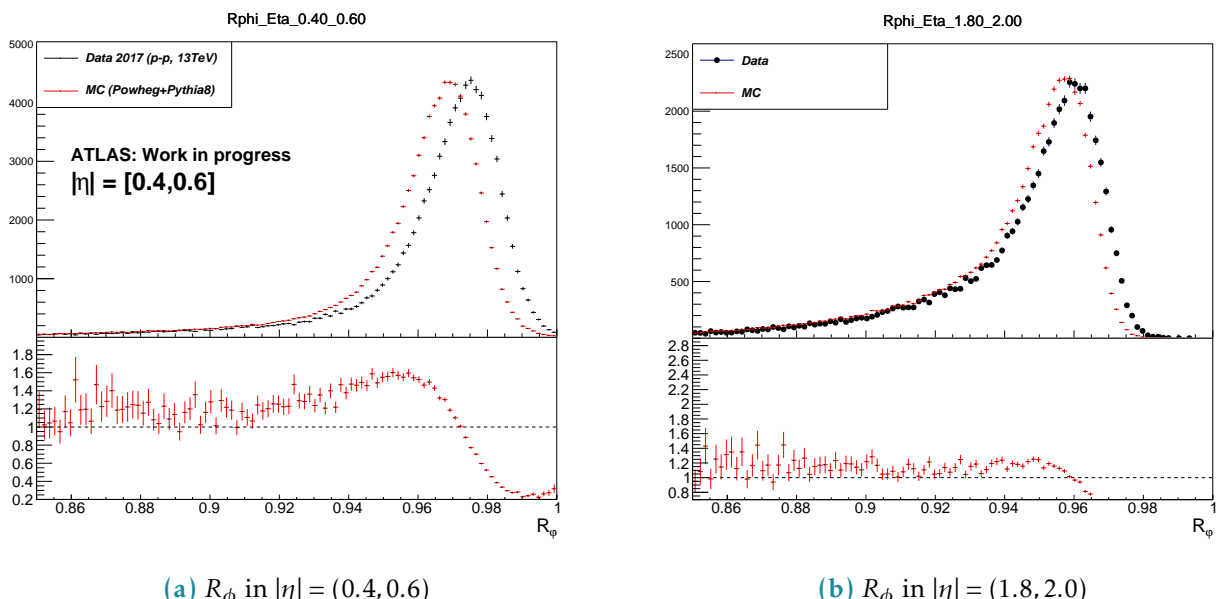


Figure 57: R_ϕ in the barrel and in the end-cap, Data vs MC

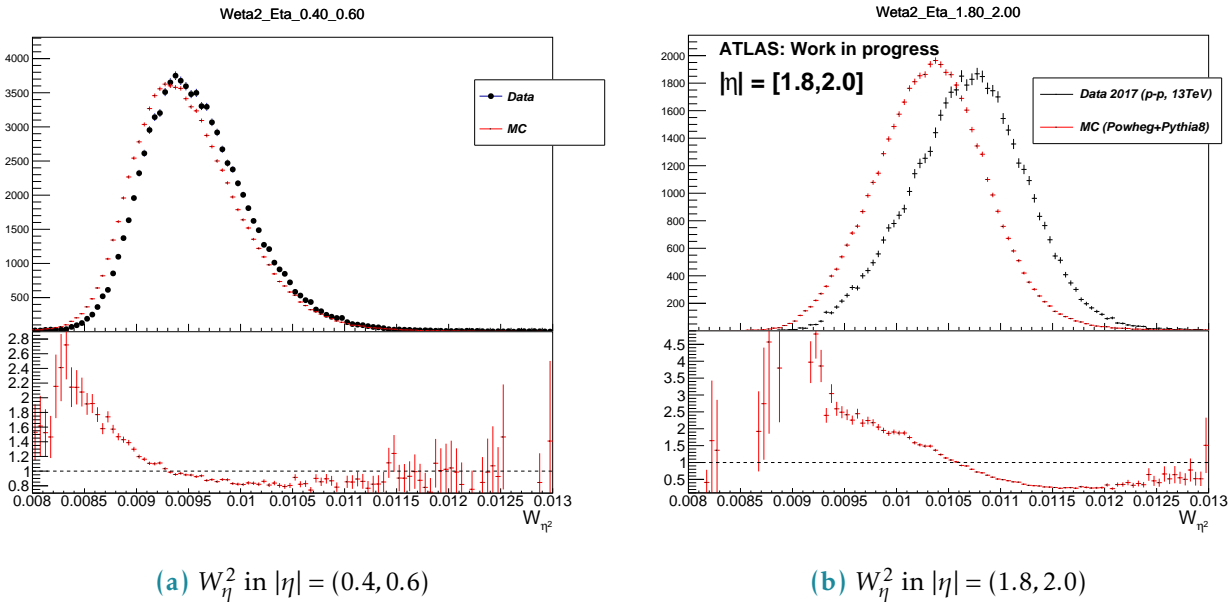


Figure 58: W_η^2 in the barrel and in the end-cap, Data vs MC

1546 5.2.3 The correction procedure

1547 The correction matrix

1548 The correction procedure is based on the redistribution of energy between the cluster cells in MC so
 1549 that the distribution becomes consistent with the data. For every η bin a correction matrix is derived in
 1550 the following way:

$$M_i^{Correction} = \frac{E_i^{Data}}{\sum E^{Data}} - \frac{E_i^{MC}}{\sum E^{MC}}$$

1551 $\sum_i M_i^{Correction} = 0$, $i = 1..77$.

1552 E_i^{Data} , E_i^{MC} - matrix elements of the averaged energy profiles. The correction is then applied to the
 1553 electron cluster cells on event-by-event basis:

$$E_i^{Reweighted} = E_i^{Non-reweighted} (1 + M_i^{Correction}).$$

1554 This redistributes the energy among the cells keeping the total energy exactly the same.

1555 Bremsstrahlung tails

1556 The magnetic field directed along the ϕ dimension leads to a significant asymmetry in energy deposits
 1557 for electrons and positrons (figure ??).

1558 Considering the fact that the reweighting is intended to correct for the data/MC discrepancies
 1559 themselves and not for the bremsstrahlung effect it makes sense to develop the bremsstrahlung-free
 1560 correction function based on e^+ and e^- correction matrices. The principle is schematically explained on

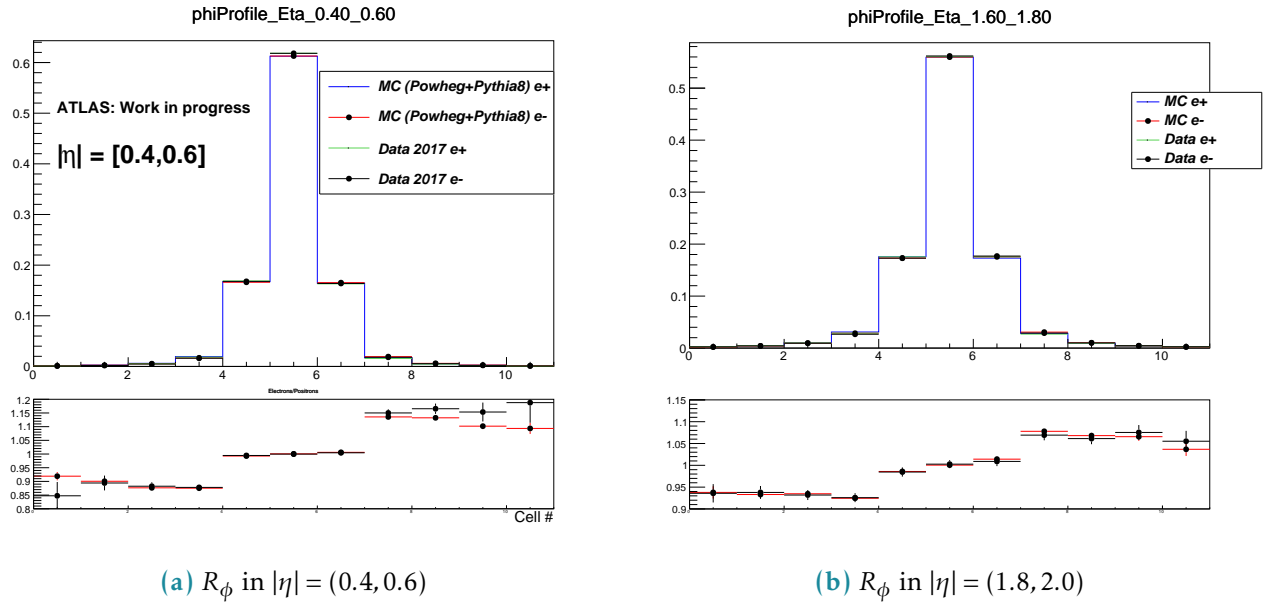


Figure 59: R_ϕ in the barrel and in the end-cap, Data vs MC

1561 figure 510.

Good agreement of data and MC description of e^+ and e^- asymmetry gives a hint that the material

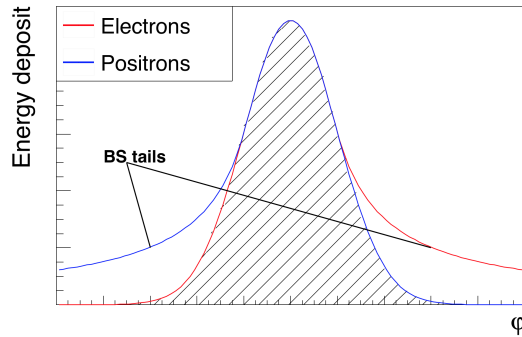


Figure 510: Schematic energy profile in ϕ dimension. Bremsstrahlung tails subtraction based on e^+ and e^- energy profiles.

1562

1563 mismodelling cannot be the main source of the data/MC disagreement.

1564

1565 5.3 Results

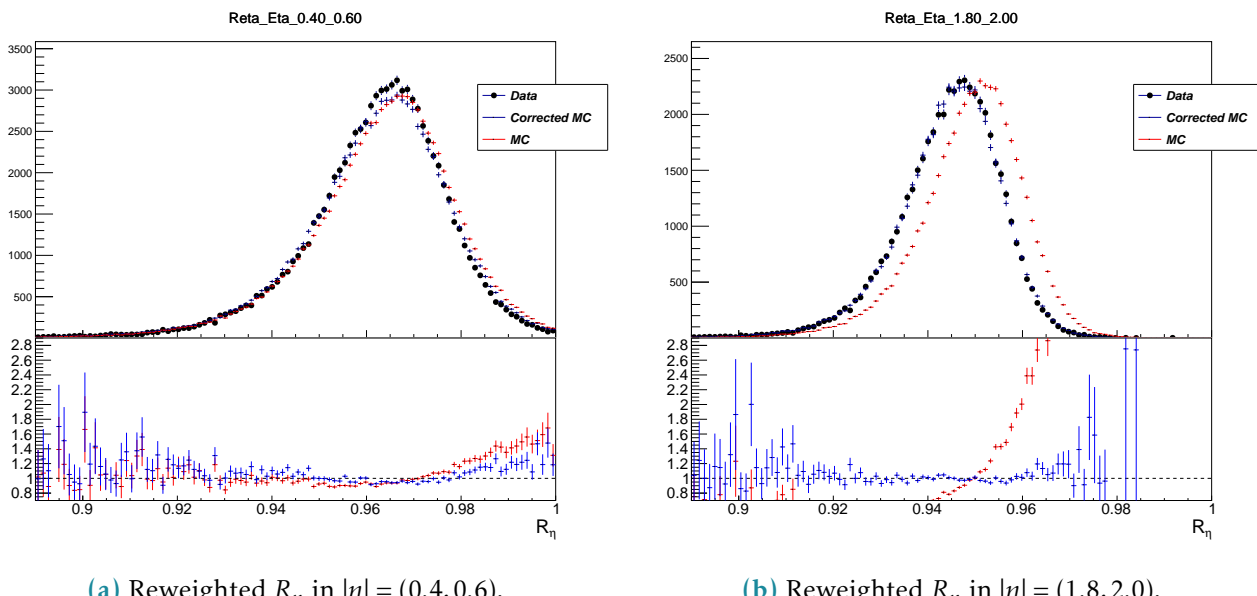
1566 Figures 511, 512, 513 show the effect of the correction. The shower shapes in MC become very close to
1567 the data, correcting a significant discrepancy.

1568 Figures 514 contain shower shapes vs p_T integrated over η . They demonstrate that the correction does

not depend on the p_T which allows to expect the decreased systematic uncertainties for p_T regions distant from 40 – 50 GeV.

Finally, figure 515 shows the effect of the correction on electron ID efficiency. We can see a visible improvement, notably in the endcap region. Nevertheless the barrel region shows little improvement. It can be explained by the fact that electron ID MVA relies on many variables while only a number of them were corrected during current study.

The proposed method is getting integrated into ATLAS Athena framework as an option and is planned to be used as a baseline for Run 3.



(a) Reweighted R_η in $|\eta| = (0.4, 0.6)$.

(b) Reweighted R_η in $|\eta| = (1.8, 2.0)$.

Figure 511: R_η in the barrel and in the end-cap

5.4 Appendix: control plots

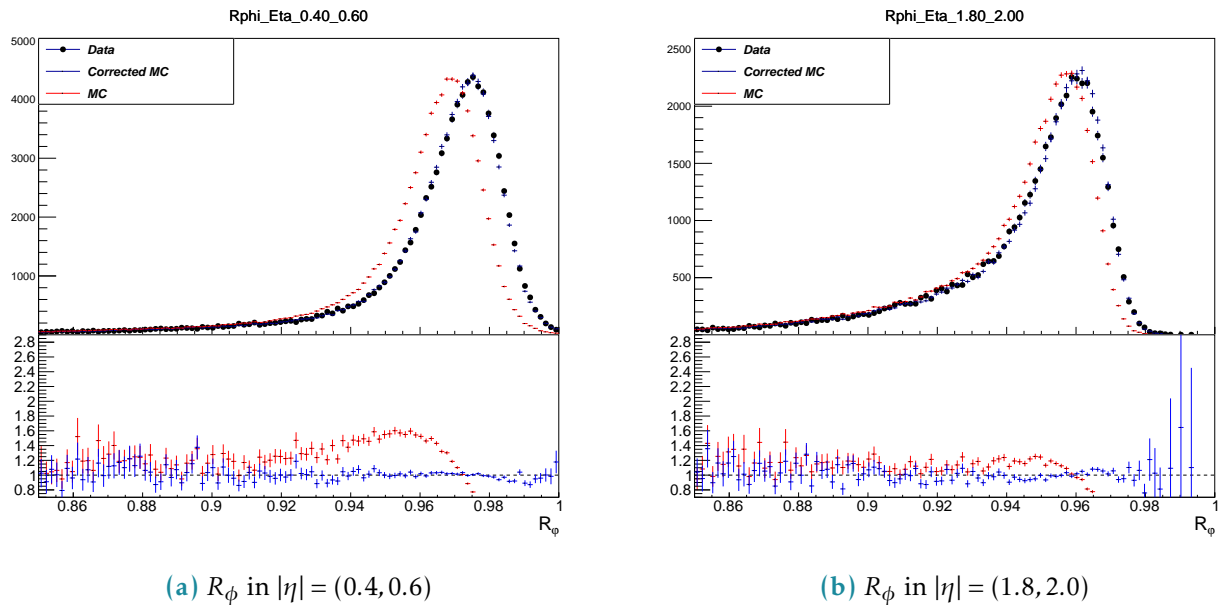


Figure 512: R_ϕ in the barrel and in the end-cap, Data, MC, reweighted MC

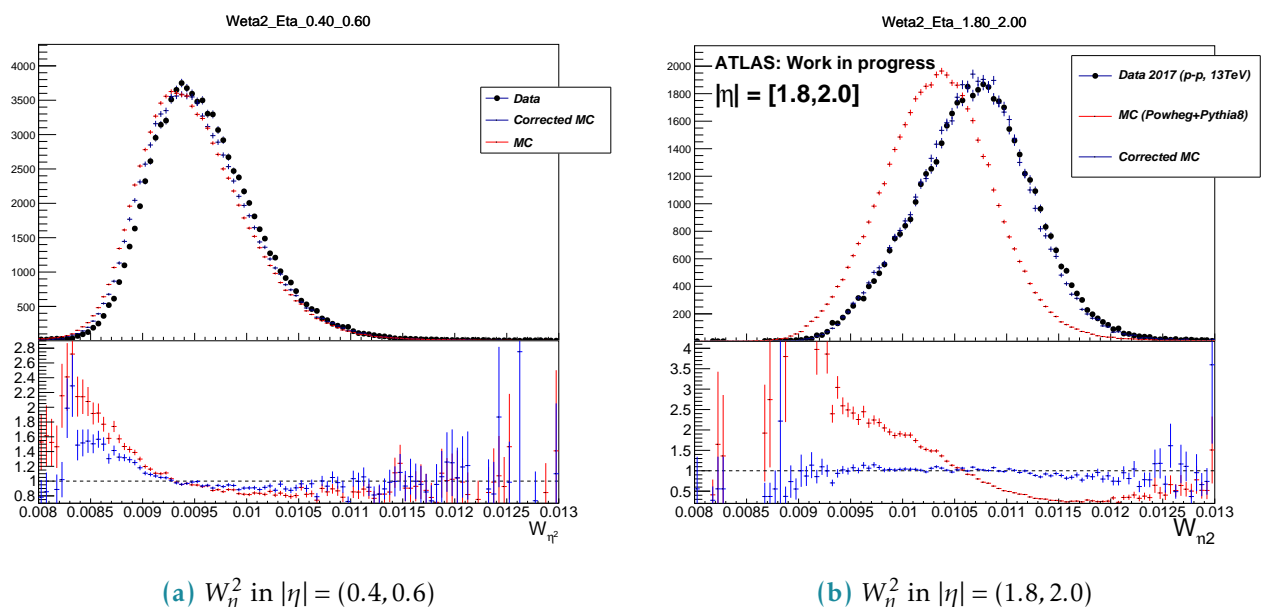


Figure 513: W_η^2 in the barrel and in the end-cap, Data, MC, reweighted MC

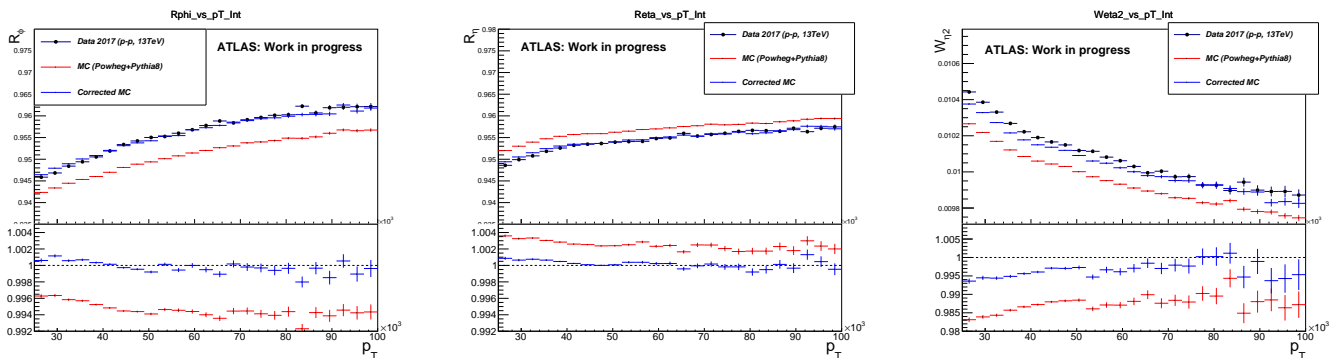


Figure 514: Distributions integrated over p_T (a) R_ϕ ; (b) R_η ; (c) $W_{\eta 2}$.

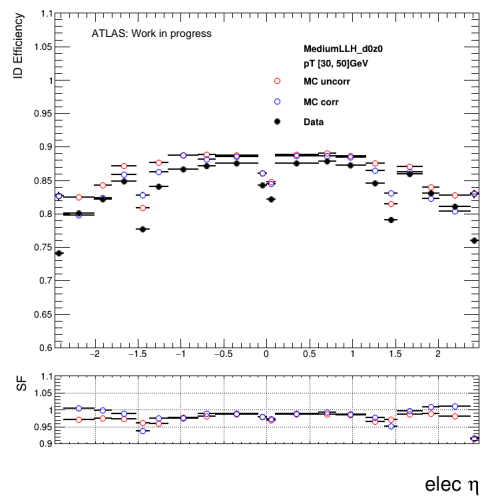


Figure 515: Electron identification efficiency as a function of the electron pseudo-rapidity

1578 Bibliography

- 1579 [1] “Electron and photon performance measurements with the ATLAS detector using the 2015-2017
1580 LHC proton-proton collision data”. In: *JINST* 14.arXiv:1908.00005. 12 (Aug. 2019). 31 figures,
1581 3 tables. All figures including auxiliary figures are available at <https://atlas.web.cern.ch/Atlas/GROUPS/PHYSICS/PAPERS/EGAM-2018-01>, P12006. 70 p. doi: 10.1088/1748-0221/14/12/P12006. URL: <https://cds.cern.ch/record/2684552>.
- 1584 [2] *Expected electron performance in the ATLAS experiment*. Tech. rep. ATL-PHYS-PUB-2011-006.
1585 Geneva: CERN, Apr. 2011. URL: <http://cds.cern.ch/record/1345327>.
- 1586 [3] *Data/MC Comparison for Calorimeter Shower Shapes of High Et Electrons*. Tech. rep. ATL-COM-
1587 PHYS-2011-1299. Geneva: CERN. URL: <https://atlas.web.cern.ch/Atlas/GROUPS/PHYSICS/EGAMMA/PublicPlots/2011005/ATL-COM-PHYS-2011-1299/index.html>.

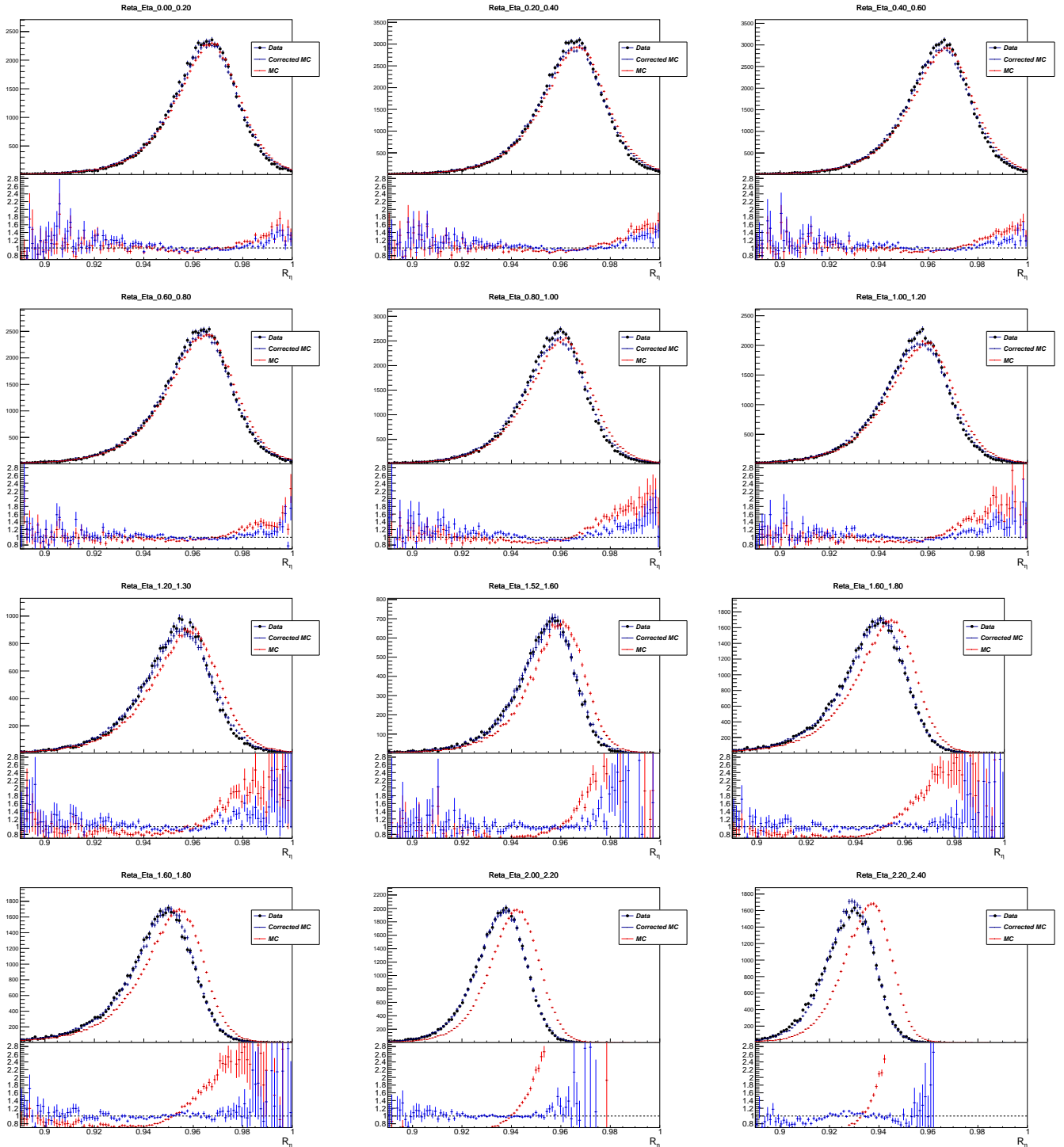


Figure 516: Reta 2

- 1589 [4] “Electron reconstruction and identification efficiency measurements with the ATLAS detector
 1590 using the 2011 LHC proton-proton collision data. Electron reconstruction and identification effi-
 1591 ciency measurements with the ATLAS detector using the 2011 LHC proton-proton collision data”.

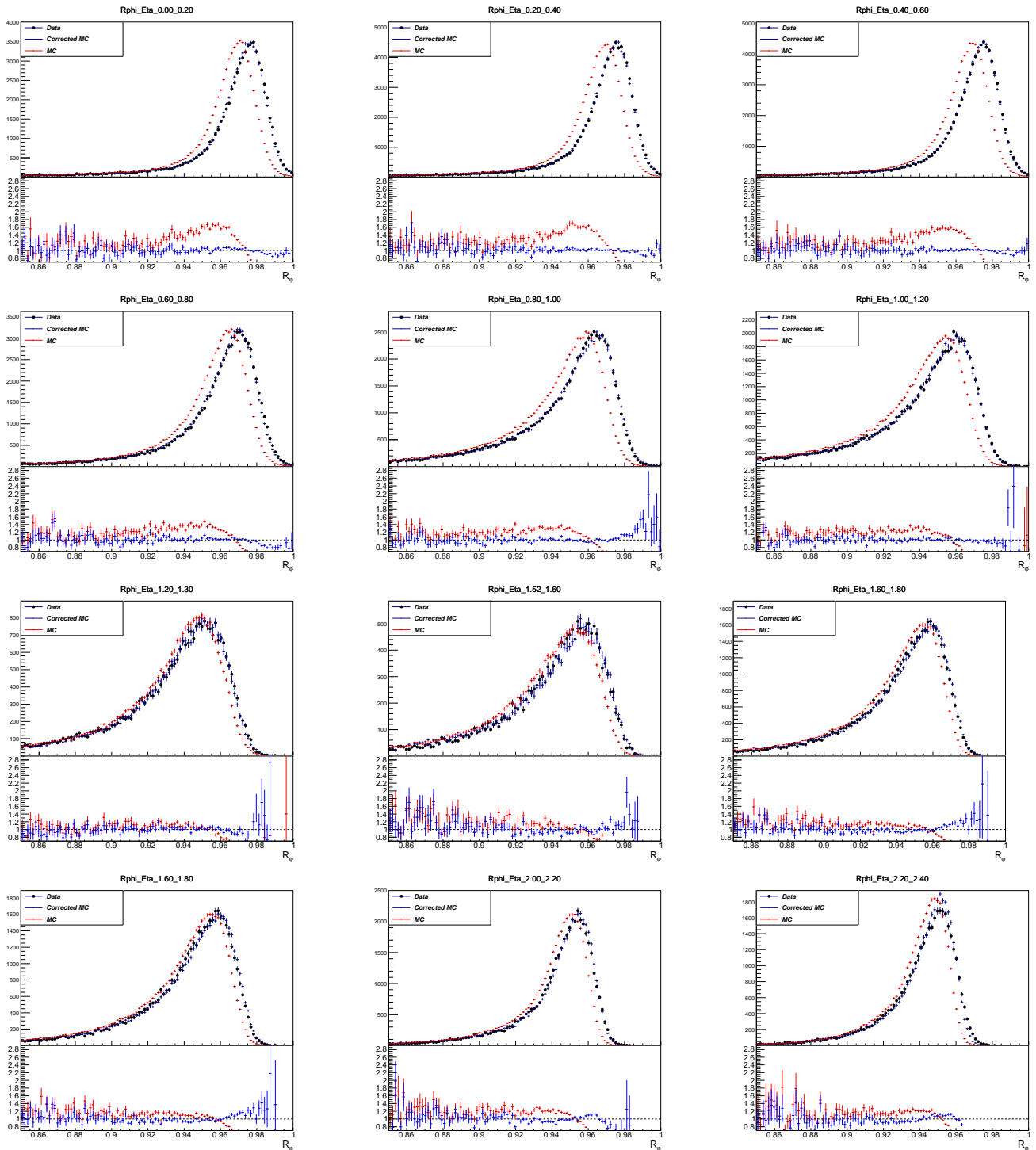


Figure 517: Rphi in all eta slices

1592
1593
1594

In: *Eur. Phys. J. C* CERN-PH-EP-2014-040. CERN-PH-EP-2014-040 (Apr. 2014). Comments: 38 pages plus author list (62 pages total), 20 figures, 4 tables, submitted to JHEP, All figures including auxiliary figures are available at <https://atlas.web.cern.ch/Atlas/GROUPS/PHYSICS/PA>

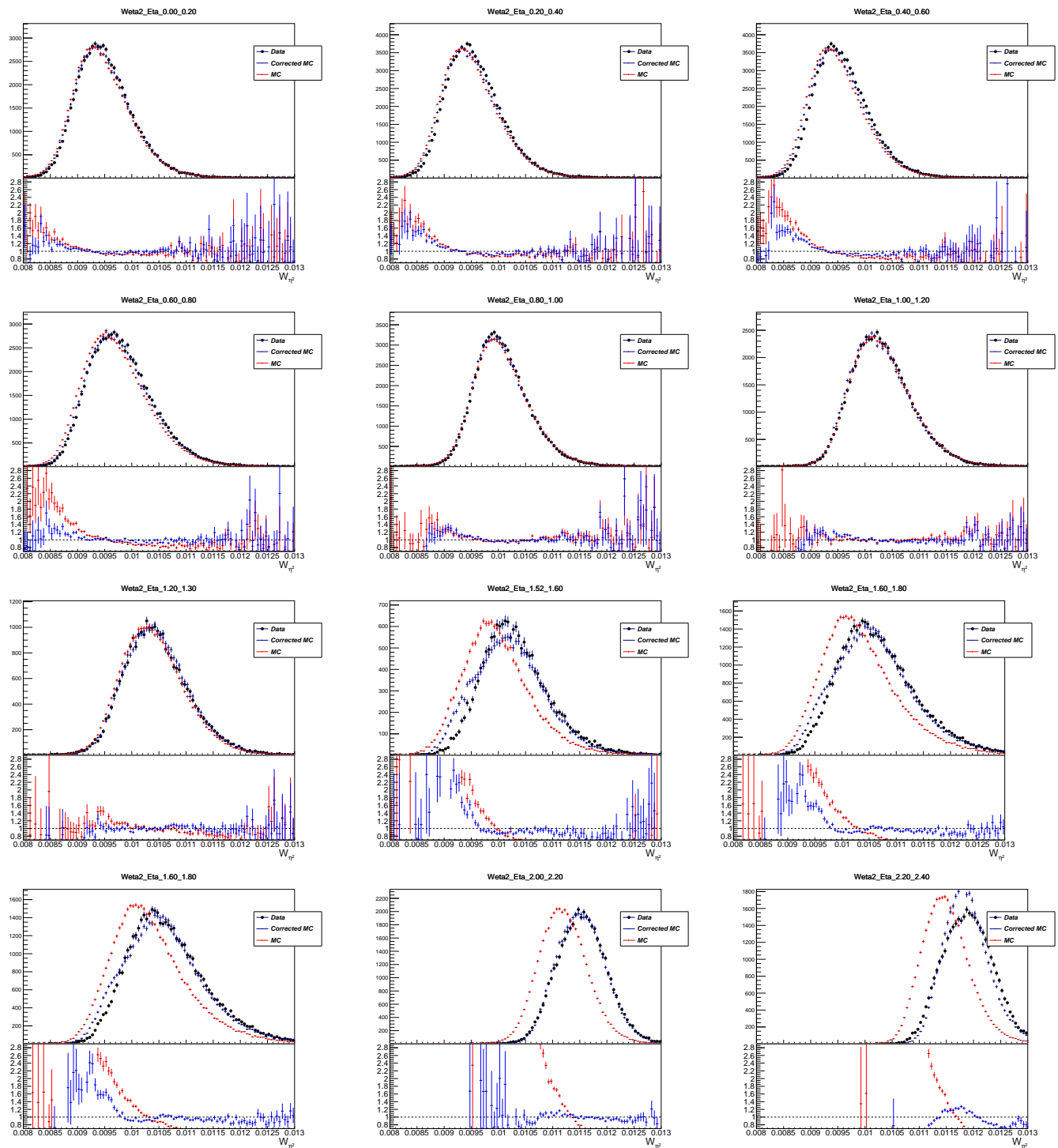


Figure 518: Reta 2

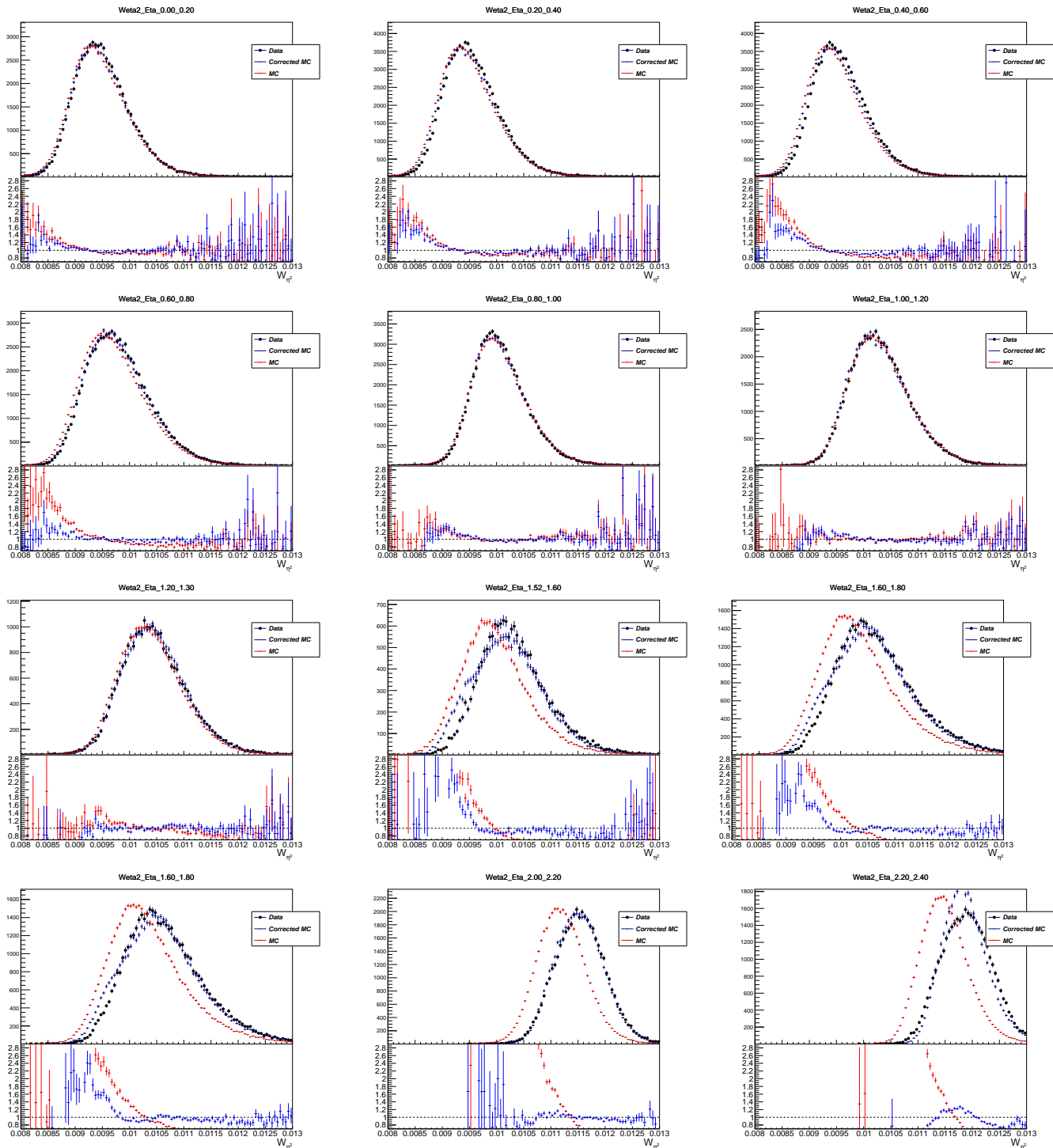


Figure 519: Reta 2

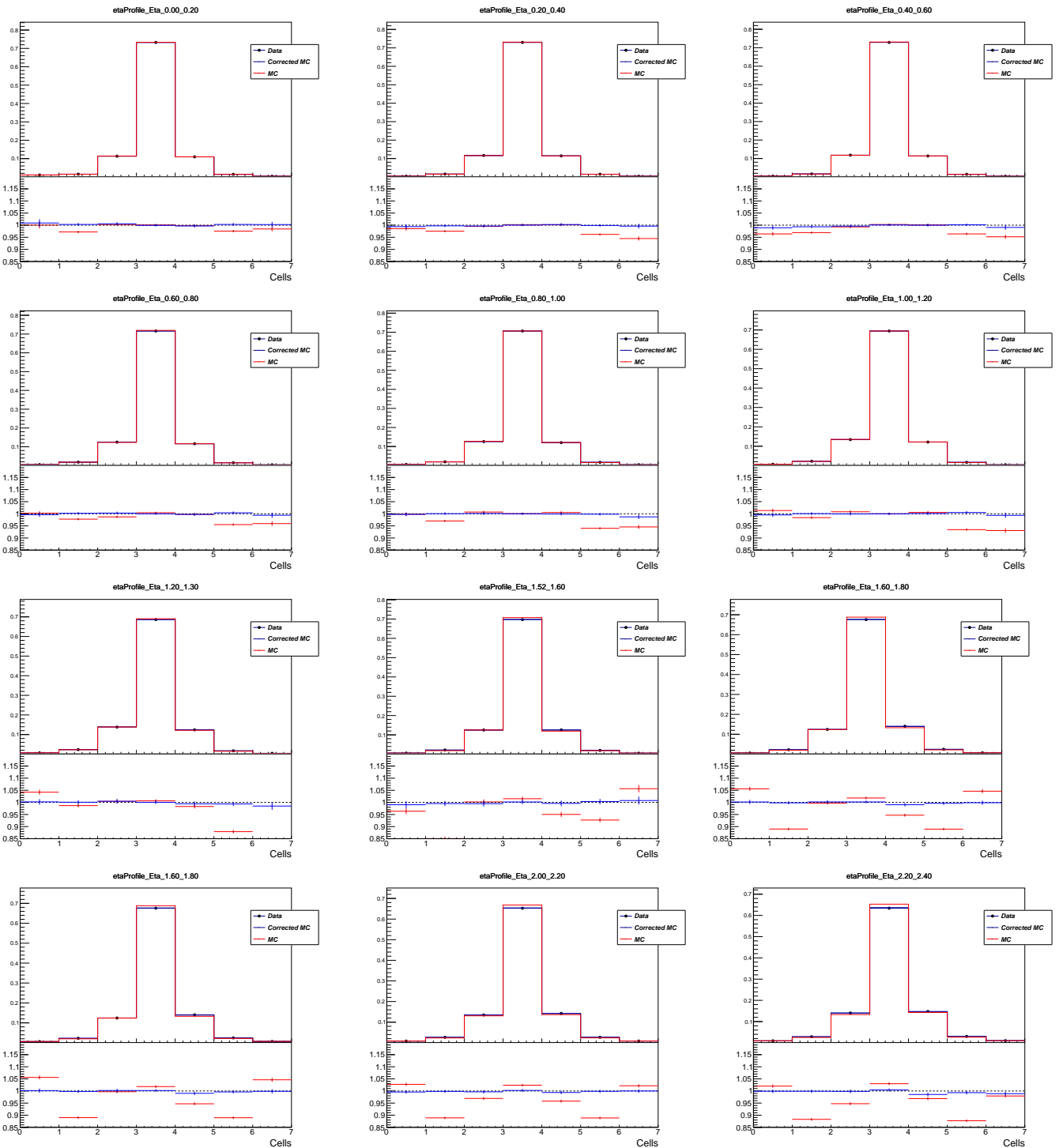


Figure 520: Reta 2

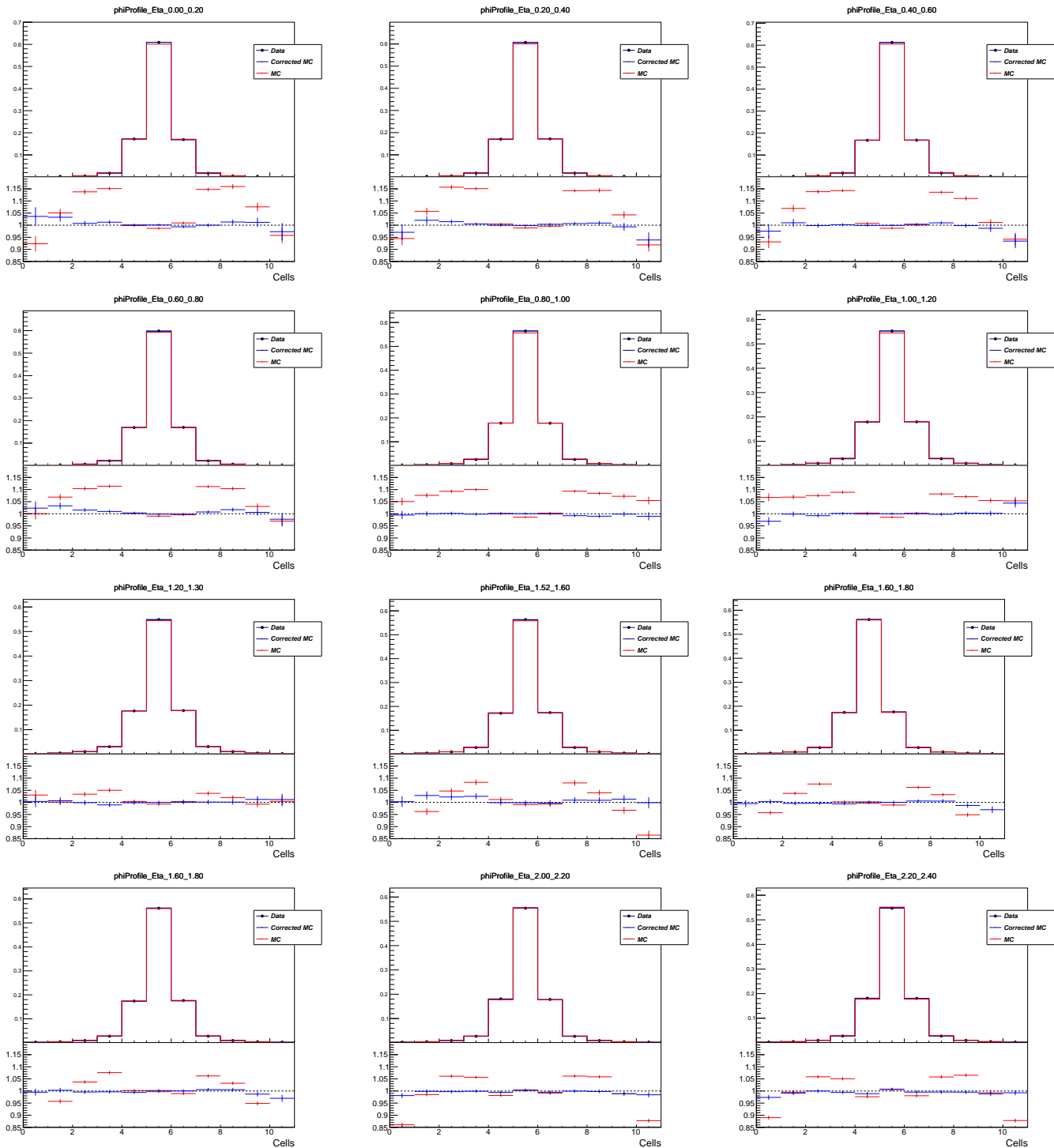


Figure 521: Reta 2

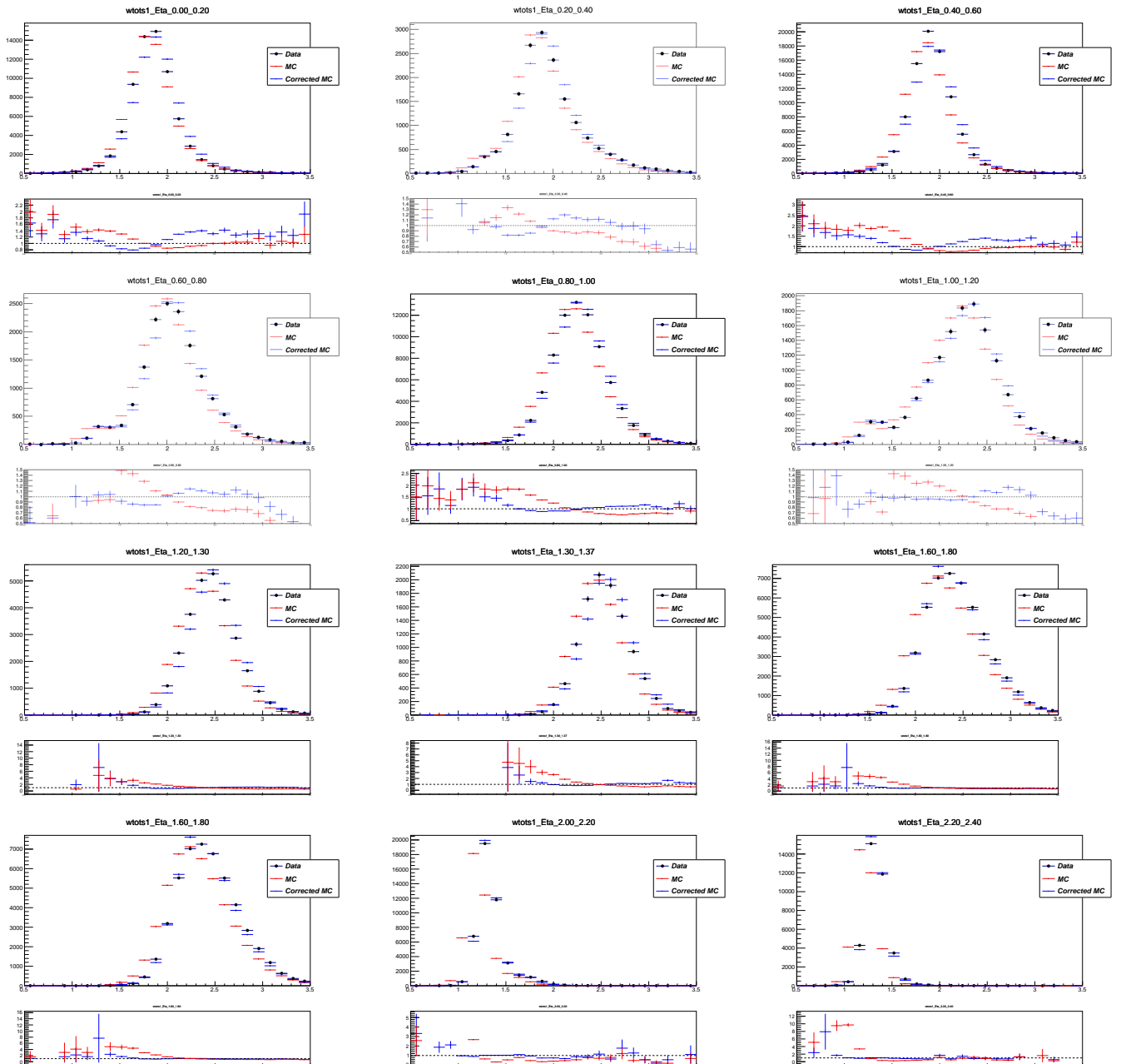


Figure 522: Reta 2

6

Event reconstruction

1597

1598

1599

“Potentielle citation sans aucun rapport avec le sujet”

1600

— Personne inconnue, contexte à déterminer

1601 6.1 Charged particles track reconstruction

1602 The track q is formed based on the information from the ID and contains five parameters: $q =$
1603 $(d_0, z_0, \phi, \theta, q/p)$, where d_0 is the distance from the track to the Z axis (transverse impact parameter), z_0
1604 is the Z coordinate of the perpendicular dropped from the track onto the Z axis (longitudinal impact
1605 parameter) (see fig. 61), ϕ and θ are the azimuthal and polar angles correspondingly and q/p is the
1606 charge to momentum ratio of the particle. The process of the track reconstruction is the same for lepton
1607 and charged hadron candidates.

To form tracks using the detector response information the following steps are performed [2]:

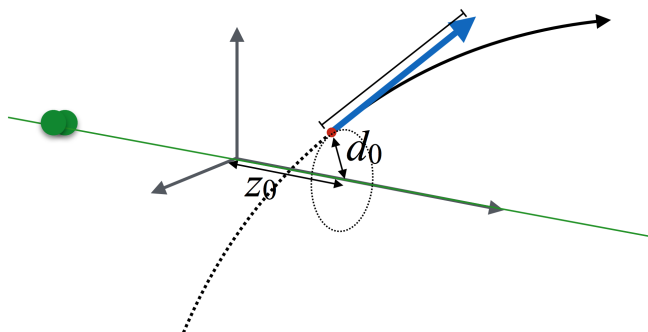


Figure 61: Impact parameters z_0 and d_0 [1].

1608

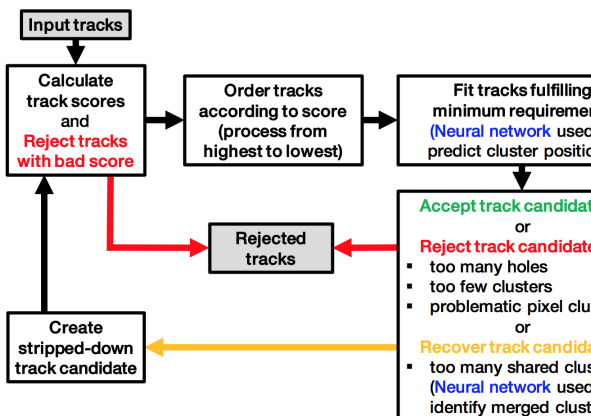
1609

- **Clustering** single hits in the pixel and SCT detectors. Neighbouring hits are combined to form a single cluster, clusters are then transformed into *space points* that have having 3D coordinates. A cluster may be identified as a single-particle cluster or as merged cluster, created by two or more particles. Identification of a cluster as a merged one and separation of energy deposits between the particles (possible only for two particles) is performed by means of a Neural Network (NN) algorithm.

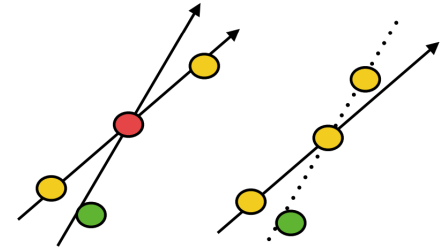
- **Forming seeds** out of the space points. To form a seed three space-points originating from unique layers of the silicon detectors (pixel or SCT) are used. All possible combinations of seeds are formed at this stage. For every seed a crude estimate of the track parameters is performed.
- **Track candidates** are formed out of the seeds by extending them within the silicon sub-detectors following the most likely path. Combinatorial Kalman filter [3] is used to build the track candidates. The purity of the seeds depends significantly on the sub-detector that recorded the corresponding space-points. SCT-only seeds are considered the most reliable, followed the seeds that origin only from the pixel detector space-points, and the least reliable are the seeds originating from both of these sub-detectors - that determines the order of seed consideration when composing track candidates.
Some fraction of the seeds that meet the necessary requirements become track candidates, the rest are discarded. A seed may be used for more than one track candidate if more than one space-point extension exists on the same layer.
- **Ambiguity solving** is the next step necessary to eliminate incorrectly assigned space-points or resolve conflicting track candidates that have and overlapping space-point. At this stage the track candidates are assigned a *track score*. The track score depends on the number of clusters associated to the track and which sub-detector these clusters originate from, the existence of holes (the absence of a cluster associated to a detector layer crossed by the track), the quality of the χ^2 fit of the track and track momentum.
The tracks are ordered by their track score and consequently fed to the ambiguity resolving sequence. A truck must pass a number of kinematic cuts, impact parameters cuts, number of holes, number of clusters and shared clusters cuts, otherwise the track candidate is rejected. If a track candidate has no shared clusters with other candidates it is accepted after that. If there are merged clusters then it is up to the NN to either accept the track, reject it or eliminate a space-point and recycle the updated track candidate (see Fig. 62a).
- **TRT extension** means matching of the track, composed using the information from silicon sub-detectors to the trace in the TRT tracker. This allows to improve momentum measurement benefiting from extended track length.
- Final high-resolution **track fit** is performed using all available information. Position and uncertainty of each cluster are determined by an additional NN allowing for more precise track parameters. The curvature of the particle track also serves for charge sign identification.

6.2 Determining the primary vertex of the event

Primary vertex determination is crucial for physics analyses for many reasons. One of them is the necessity to separate particles originating from hard events from pile-up. Another reason is to keep



(a) Track ambiguity resolver algorithm.



(b) Tracks sharing space-points.

Figure 62: Ambiguity solving.

1649 track of the decay chain and make difference between prompt and non-prompt particles. Flavour
 1650 tagging, background suppression and decay reconstruction also rely heavily on the primary vertex
 1651 determination.
 1652 After reconstructing the tracks of individual particles the obtained information is used to reconstruct
 1653 the Primary Vertex (PV) of the event [4]. The procedure relies on the reconstructed tracks and goes as
 1654 follows:

- 1655 • A seed from the first vertex is selected. The transverse position of the seed is taken as a centre of
 1656 the beam spot. The z-coordinate is the mode of z_0 coordinate of the tracks.
- 1657 • Using the seed and the available tracks an iterative fit is performed in order to find the best
 1658 position for the PV. In each iteration the tracks that are less compatible with the vertex are
 1659 down-weighted and the vertex position gets recomputed. With every iteration the spread in the
 1660 weight increases, separating track set into compatible tracks that mostly determine the vertex
 1661 position and incompatible tracks that have little weight and therefore very little influence on the
 1662 track position.
- 1663 • After the fit is done compatible tracks remain assigned to the vertex, while incompatible tracks
 1664 are removed from it. These incompatible tracks can be used in the determination of a different
 1665 vertex.
- 1666 • The procedure is repeated with the remaining tracks of the event.

1667 For the upcoming Run 3 of the LHC certain improvements and modifications are foreseen [5].

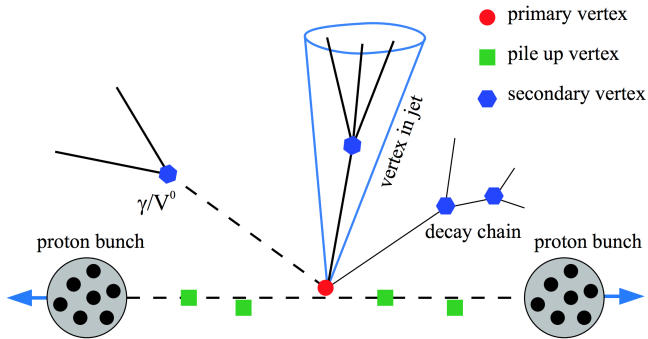


Figure 63: Primary, secondary and pile-up vertices [6].

1668 6.3 Muon reconstruction and identification

1669 Muon reconstruction relies primarily on the information from the ID (the muon track) and the Muon
 1670 Spectrometer (MS), sometimes also using additional information from the calorimeter. At the first
 1671 stage muon is independently reconstructed in the tracker and in the spectrometer, and then they are
 1672 combined to compose a muon track used in the physics analyses [7]. Track reconstruction is described
 1673 in subsection 6.1.

1674 6.3.1 Muon reconstruction

1675 Muon reconstruction on the muon spectrometer begins with a search for hit patterns in each muon
 1676 chamber and forming of the segments. Using the Hough transform [8] the hits in each MDT chamber
 1677 and nearby trigger chamber are aligned on trajectories in the bending plane. The orthogonal coordinate
 1678 is measured with RPC and TGC detectors. A separate combinatorial search is conducted in the CSC
 1679 detectors in ϕ and η detector planes.

1680 Then the track candidates are built by fitting hits from different layers. This algorithm starts a
 1681 combinatorial search first using the segments from the middle layers as seeds, as there are more trigger
 1682 hits in the middle layer. The search is later extended to include the segments from other layers as seeds.
 1683 Segment selection criteria are based on hit multiplicity and fit quality. The segments are matched using
 1684 their relative positions and angles. In all the regions, except barrel-endcap transition region, at least
 1685 two matching segments are needed to build a track (one segment is enough in the transition region).
 1686 A single segment can be used by two or more track candidates. An overlap removal algorithm decides
 1687 to which track should a segment belong or shares a segment between two tracks. A global χ^2 fit is used
 1688 to fit all the hits associated to every track. If the χ^2 fit meets the designated criteria then the track is
 1689 accepted. If a hit impair the χ^2 fit significantly, then this hit may be removed and the fit is repeated.
 1690 On the other hand, new hits may be recovered if they fit the track candidate trajectory.
 1691 Accurate fitting of the track trajectory is extremely important for the measurement of muon momentum.
 1692 A quantity called *sagitta* is measured by the MS (see Fig. 64). Knowing the length L and the sagitta S

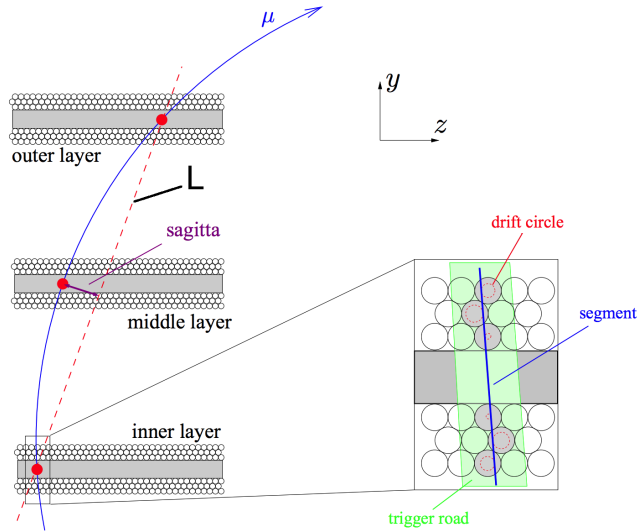


Figure 64: Sagitta used for the determination of the muon momentum [9].

1693 we can determine the momentum:

$$p = \frac{BL^2}{8S}, \quad (6.1)$$

1694 where B is the magnetic field strength.

1695 After the muon gets reconstructed in every detector system separately, the obtained information is
1696 combined to form a reconstructed muon object. Depending on the detectors used for the combined
1697 reconstruction there are *four types of muons* defined (see Fig. 65):

- 1698 • **Combined (CB) muon** is formed from a global refit of the tracks reconstructed independently
1699 in the ID and in the MS. During this global refit the hits from both detectors are used and also
1700 new hits may be added. Normally the outside-in pattern is used, when MS track is extrapolated
1701 inwards to match ID track. Inverse inside-out procedure is used as a complementary approach.
- 1702 • **Segment-tagged (ST) muon** is a particle with an ID track that was extrapolated to the MS and
1703 associated with at least one local track segment in the MDT or CSC chambers. Normally these
1704 are muons with low p_T or their trajectory crosses regions with reduced MS acceptance.
- 1705 • **Calorimeter-tagged (CT) muon** has a valid ID track that can be associated to an energy deposit
1706 in the calorimeter compatible with minimum-ionizing particle. The CT muons have the lowest
1707 purity among the muon types although they provide acceptance where the MS coverage may be
1708 absent, like the very central region with $|\eta| \leq 0.1$ for $15 < p_T < 100$ GeV.
- 1709 • **Extrapolated (ME) muon** (standalone muon) trajectory is reconstructed base only on the MS
1710 track and a loose requirement to match the IP. ME muons allow to extend the muon acceptance
1711 to the region which is not covered by the ID, namely $2.5 < |\eta| < 2.7$.

1712 In case of overlap between different muon types the preference is given to CB muons, then to ST and then to CT muons. ME muons overlaps are resolved based on the MS track quality.

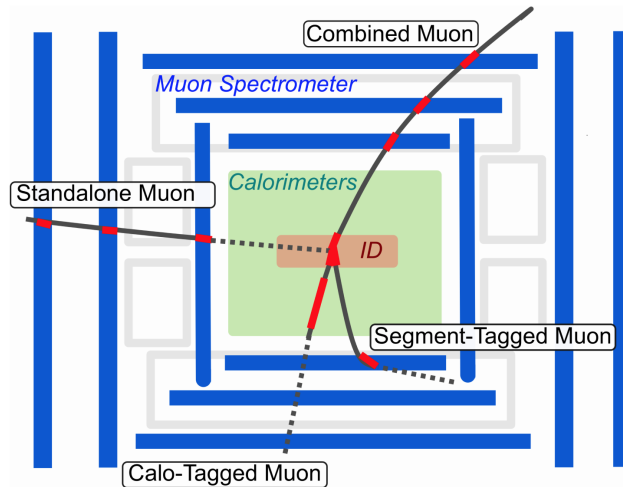


Figure 65: Four types of reconstructed muons.

1713

1714 6.3.2 Muon identification

1715 Muon identification is a set of measures to ensure that the registered particle has indeed the character-
 1716 istics of a muon and to identify the mechanism of its production. Muons created in the course of decay
 1717 of a short-lived particle (e.g. a massive boson) are called *prompt muons*, while those originating from
 1718 hadron or tau decays are called *non-prompt*. Muon identification plays an important role in background
 1719 suppression and guaranteeing a robust momentum measurement.

1720 Muons that are created during the in-flight decay of the charged hadrons in the ID usually have a
 1721 distinctive "kink" topology in their reconstructed track. This results in a decreased quality of the
 1722 resulting track fit and the incompatibility between the results of momentum measurement in the ID
 1723 and MS. Muons originating from W boson decays are called *signal*, while those coming from the hadron
 1724 decays are called *background*. For CB muons the three main identification variables are the following:

1725 • *q/p significance* is defined as $\frac{|(q/p)_{ID} - (q/p)_{MS}|}{\sqrt{\sigma^2(q/p)_{ID} + \sigma^2(q/p)_{MS}}}$ - an absolute difference between *q/p* measured in
 1726 the two detectors over the combined uncertainty.

1727 • Relative transverse momentum difference $\rho = \frac{|p_T^{ID} - p_T^{MS}|}{p_T^{combined}}$.

1728 • Normalized χ^2 fit of the combined track.

1729 Robust momentum measurement is ensured by specific requirements to the number of hits in the ID
 1730 and MS. A number of muon identification selections (working points) is developed to address specific
 1731 analyses.

1732 6.3.3 Muon isolation

1733 Isolated muons are a defining signature of massive boson decays. In the decays of W, Z and Higgs
1734 bosons muons are created separated from the rest of the particles. Quantitative measurement of
1735 detector activity around a muon candidate is called *muon isolation* and serves as an invaluable tool
1736 for background suppression. Muon isolation is assessed through two observables: one is track-based,
1737 another is calorimeter-based.

1738 The track-based observable $p_T^{varcone30}$ is defined as a scalar sum of all the particles with $p_T > 1$ GeV in a
1739 cone $\Delta R = \min(10\text{GeV}/p_T^\mu, 0.3)$ around the muon with transverse momentum p_T^μ excluding the proper
1740 track of the muon. The p_T dependence helps this definition to perform better for the muons created in
1741 the decay of the particles with high transverse momentum.

1742 The calorimeter-based isolation observable $E_T^{topocone20}$ is defined as the sum of the transverse energy of
1743 all the topological clusters in a cone of a size $\Delta R = 0.2$ around the muon after subtracting the proper
1744 muon energy deposit and correcting for the pile-up effects.

1745 Isolation criteria are normally defined using the relative isolation variables, using the ratio of $p_T^{varcone30}$
1746 and $E_T^{topocone20}$ to the transverse momentum. A number of working points exist, each having a certain
1747 requirements for one or both of the isolation variables.

1748 6.4 Electron reconstruction and identification**1749 6.4.1 Electron reconstruction**

1750 Electron reconstruction starts with two separate parts: track reconstruction in the ID and cluster
1751 reconstruction in the calorimeter, which are then matched to each other in order to make an electron
1752 candidate [10]. During Run 2 two algorithms were used for the cluster reconstruction, both of them are
1753 described below.

1754

1755 Sliding window

1756 The EMC is divided into a grid of 200x256 towers in $\eta \times \phi$ plane, each tower having a size of $\Delta\eta \times \Delta\phi =$
1757 0.025×0.025 , reproducing the granularity of the second layer in the EMC. Energy deposits in all
1758 available calorimeter layers (first, second and third layers of the EMC in the region $|\eta| < 2.47$ and the
1759 presampler in the region $|\eta| < 1.8$) are approximately calibrated at the EM scale and summed up for
1760 each tower. If the cumulative energy deposit in a certain tower exceeds 2.5 GeV then this tower is used
1761 as a seed. Then for every seed a sliding window algorithm of size 3×5 is used [11], forming a cluster
1762 around every seed.

1763 It happens that two seed-cluster candidates are found in close proximity. When their towers overlap

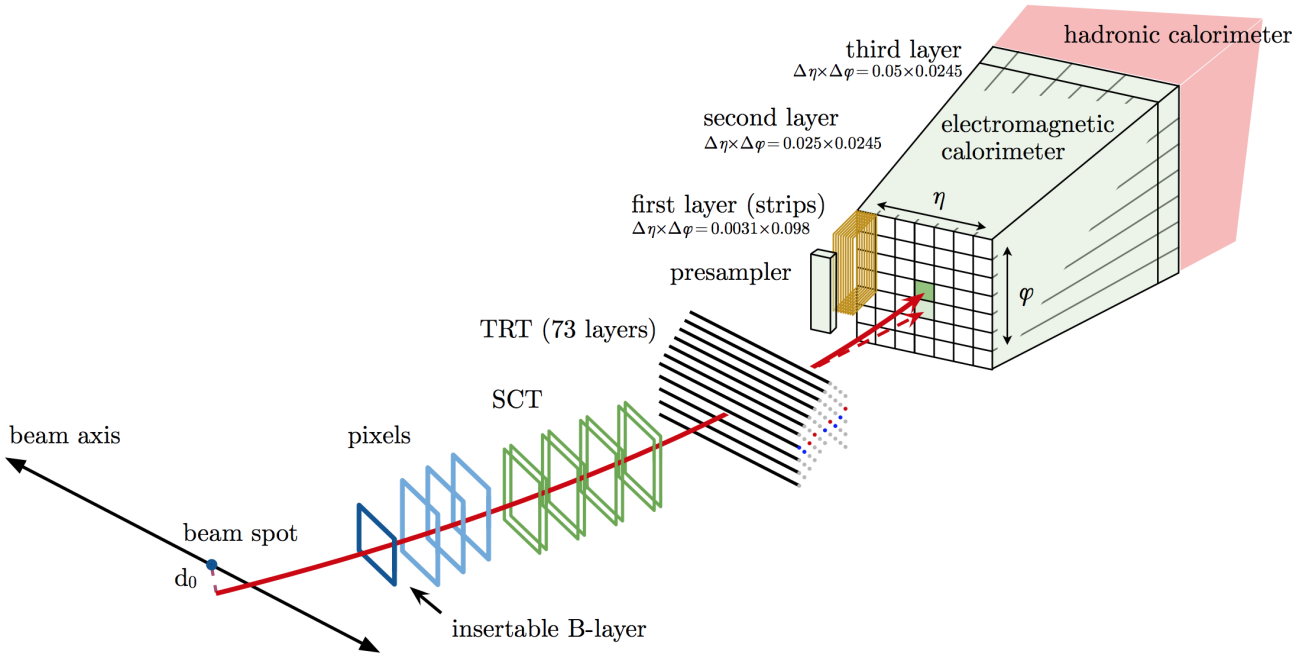


Figure 66: The path of an electron through the detector is shown by solid red line. The dashed red line denotes the trajectory of a photon, produced as a Bremsstrahlung radiation in the TRT.

1764 within an area of $\eta \times \phi = 5 \times 9$ in units of 0.025×0.025 the two clusters are considered overlapping. In
1765 this case two options are possible:

- 1766 • If the transverse energies of the two clusters are more than 10% different then the cluster with
1767 higher E_T is retained.
1768 • If the difference in the transverse energies is within 10% then the cluster with higher value of the
1769 E_T in the central tower is kept.

1770 After the overlap is resolved the duplicate cluster gets removed.
1771

1772 Topocluster reconstruction

1773 The algorithm for topocluster reconstruction [12], [13] starts with composing proto-clusters in the
1774 calorimeter using the noise threshold:

$$\zeta_{cell}^{EM} = \frac{E_{cell}^{EM}}{\sigma_{noise,cell}^{EM}}, \quad (6.2)$$

1775 where E_{cell}^{EM} is the cell energy at the EM scale and $\sigma_{noise,cell}^{EM}$ is the expected cell noise. The latter
1776 comprises of the electronic noise and pile-up noise estimate base on the expected instantaneous

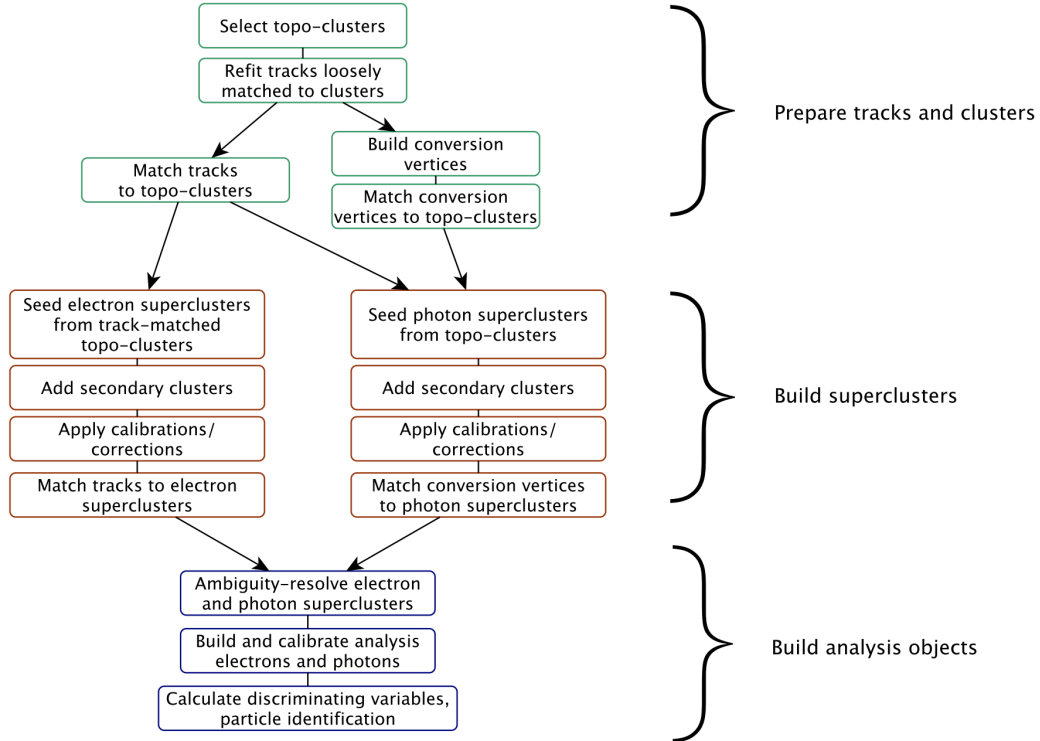


Figure 67: The algorithm scheme for topocluster reconstruction.

luminosity. The proto-cluster is formed around a cell with $|\zeta_{cell}^{EM}| \geq 4$. Then the neighbouring cell that pass the requirement of $|\zeta_{cell}^{EM}| \geq 2$ are added to the proto-cluster and serve as a seed for the next iteration, collecting all of its neighbours to the proto-cluster. If the two proto-clusters share a cell with $|\zeta_{cell}^{EM}| \geq 2$ then these proto-clusters are merged together. At every iteration neighbouring cells are added to the cluster even if they don't make the threshold. Proto-clusters with two local maxima are split into two clusters. For the proto-cluster to be considered as EM topocluster it must have at least 50% of its energy being contained in the EMC. At the stage of track reconstruction the tracks are first extended and fitted with the global χ^2 fitter using the pion hypothesis [14]. If it fails, then a more complicated pattern reconstruction algorithm based on Kalman filter is used [15]. This algorithm uses the electron hypothesis and allows up to 30% energy loss at each material surface. Then the tracks are loosely matched to the EM clusters if they meet one of the following criteria:

- The tracks extrapolated to the second layer of the EMC are consistent in ϕ and η (matching in η is not required for TRT-only tracks).
- The extrapolated tracks are consistent in ϕ (with a bit tighter requirements) and η after rescaling the track momentum to cluster momentum.

1792 **Track-cluster matching**

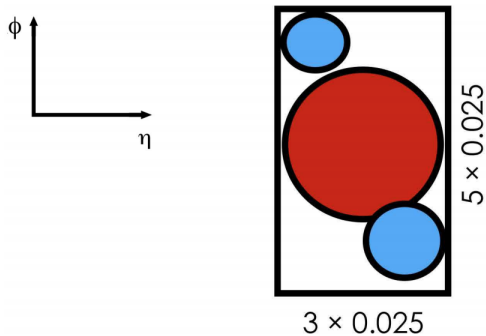
1793 Matching in ϕ coordinate assumes charge asymmetry to account for different direction of possible
 1794 Bremsstrahlung radiation for positive and negative particles. Then the loosely matched tracks that have
 1795 at least four silicon hits are refitted using the optimized Gaussian-sum filter (GSF) [16], that allows to
 1796 better take into account the energy losses in solid material.
 1797 After the track is fitted with the GSF algorithm the final matching with the cluster is performed using
 1798 tighter matching requirements between the track and the cluster barycentre. If matching criteria are
 1799 met with two or more tracks then an ambiguity resolving algorithm is used. This algorithm takes into
 1800 account a number of parameters like the distance between the cluster barycentre and the track in ϕ
 1801 and η , number of hits in the silicon detector and in the innermost silicon layer, association to photon
 1802 conversion vertex, E/p ration and p_T . This allows to rule out converted photons as electron candidates
 1803 and also helps to maintain high photon reconstruction efficiency. After track-cluster matching the
 1804 electron cluster is extended around the seed to 3×7 in the barrel region or 5×5 in the end-cap region
 1805 by adding one row of the cells on each side.

1806

1807 **Supercluster reconstruction**

All e^\pm, γ :

Add all clusters within 3×5 window
around seed cluster.



Electrons only:

Seed, secondary cluster
match the same track.

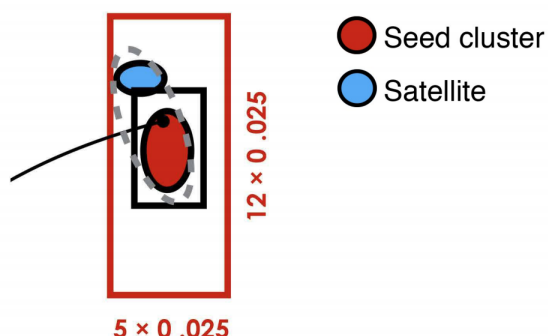


Figure 68: Supercluster reconstruction for electrons. Seed clusters are shown in red, satellite clusters in blue.

1808 The composition of electron supercluster is performed in two stages: first, the candidate EM topoclus-
 1809 ter is tested to be used as a seed for the supercluster. In the second stage the nearby EM topoclusters
 1810 can be identified as satellite clusters, emerging from Bremsstrahlung radiation or topocluster splitting.
 1811 First the EM topoclusters are sorted by their E_T in descending order. For the cluster to be considered
 1812 a seed it must have the $E_T > 1$ GeV, must be matched to a track with at least four hits in the silicon

detectors and should not be assigned as a satellite cluster to any other seed. If these requirements are met then the algorithm described in Fig. 68 is started. First, all topoclusters within a window of $\Delta\eta \times \Delta\phi = 0.075 \times 0.125$ around the seed cluster barycentre are added as satellite cluster, as they most probably represent secondary EM showers coming from the same initial electron. Also, if a cluster within $\Delta\eta \times \Delta\phi = 0.125 \times 0.3$ window around the seed cluster barycentre share the "best-matched" track with the seed cluster - it is also added as a satellite. Finally the energy of the reconstructed cluster must be calibrated. The calibration is performed using the multivariate technique based on data and MC samples using $Z \rightarrow ee$ events [17], [18]. The shower shapes and other discriminating variables are computed at this stage.

6.4.2 Electron identification

Prompt electrons in the central region of the ATLAS detector ($|\eta| < 2.47$) are selected using a likelihood-based (LH) identification. The LH uses a number of inputs from ID and calorimeter detectors, as well as combined information from both detectors (see Table 1 in [10]). The probability density functions (pdfs) for the likelihoods of Run 2 were obtained using the simulated events.

The electron LH is based on the products of n pdfs P for signal L_S and background L_B :

$$L_{S(B)}(\mathbf{x}) = \prod_{i=1}^n P_{S(B)}^i(x_i), \quad (6.3)$$

where \mathbf{x} is the vector of the LH input parameters, P_S^i and P_B^i are the pdf values for parameter i at value x_i for signal and background respectively. The LH operates at a number of working points, the higher the likelihood - the lower is the efficiency. For example, the efficiencies for identifying a prompt electron with $E_T = 40$ GeV for Loose, Medium and Tight working points are 93%, 88% and 80% respectively. Prompt electrons are assumed to be the signal, while background includes the jets that mimic the prompt electrons, electrons from photon conversions and non-prompt electrons from hadron decays.

For each electron candidate a discriminant d_L is composed:

$$d_L = \frac{L_S}{L_S + L_B}, \quad (6.4)$$

that defines the electron likelihood identification. This discriminant d_L has a sharp peak at unity for the signal and at zero for the background, which is not very convenient for picking working points. That is why the discriminant distribution is transformed using the inverse sigmoid function:

$$d'_L = -\tau^{-1} \ln(d_L^{-1} - 1), \quad (6.5)$$

where $\tau = 15$. Each operating point is assigned with a d'_L value - if a discriminant exceeds this value for a given electron then this electron is considered signal.

There are two advantages of using likelihood-based approach comparing to selection-criteria-based ("cut-based") identification:

- The drawback of a cut-based approach is that if an electron fails to pass one of the cuts - it is definitely removed from the selection, while in the LH approach it is still possible for this electron to pass the selection thanks to other parameters. This quality promotes the selection efficiency.
- In case of a significant overlap in signal and background distribution of a certain parameter using it in a cut-based identification would entail large losses in efficiency. In the likelihood-based identification this parameter may be added without penalty.

The likelihood input parameters were obtained from the simulated events, which means that real distributions in data may differ due to various mismodelling effects. These effects must be corrected in order to get the accurate and efficient identification. Mismodelling may depend on coordinates or energy. Chapter 5 of this dissertation is devoted to correction of electromagnetic shower shapes in the calorimeter, which are among the likelihood input parameters.

6.4.3 Electron isolation

Electron isolation plays a very important role in background suppression in physics analyses. Since electrons are reconstructed using the information from two different detectors - two different isolation definitions are possible, track-based and calorimeter-based. Let's first consider calorimeter-based isolation.

As depicted in Fig. 69 the raw isolation energy $E_{isol}^{T,raw}$ includes the energy of all the topoclusters,

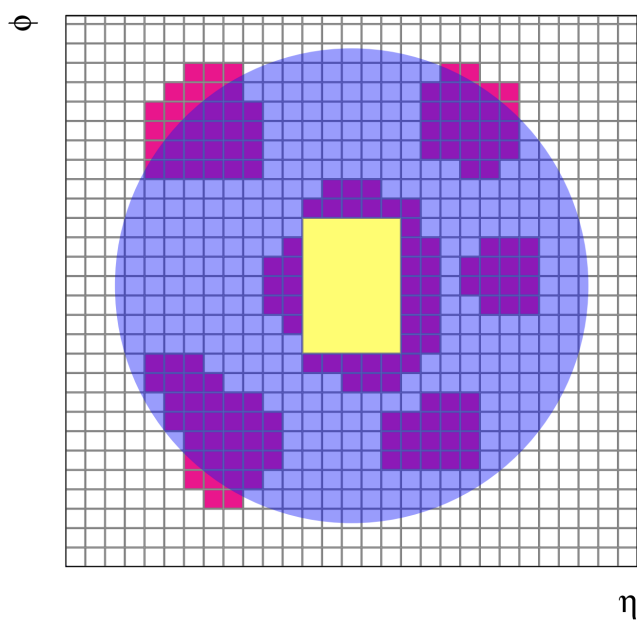


Figure 69: The isolation cone is centred at the candidate electron. All topological clusters, shown in red, are included in the raw isolation variable. The 5×7 cells included into core subtraction method are marked in yellow.

1858
 1859 barycentres of which fall within the isolation radius ΔR . It also includes core energy of the electron
 1860 candidate $E_{isol}^{T,core}$ which comprises the 5×7 cells within the area of $\Delta\eta \times \Delta\phi = 0.125 \times 0.175$. The fixed
 1861 size of the core ensures simplicity and stability, although it may happen that the topocluster is larger
 1862 than the size of the core resulting in attributing the proper energy of the electron to the outside activity.
 1863 This leakage effect is corrected for using no pile-up simulated events, parametrizing the leakage with a
 1864 Crystal Ball function as a function of the transverse energy $E_{T,leakage} = E_{T,leakage}(E_T)$.
 1865 Another effect that must be corrected for is the pile-up and underlying event contribution. This
 1866 contribution is estimated from the ambient energy density [19]. This implies the calculation of
 1867 the median energy density $\rho_{median}(\eta)$ - a rapidity-dependent estimate of jet densities for every event.
 1868 Then the pile-up correction can be evaluated in the following way:

$$E_{T,pile-up}(\eta) = \rho_{median}(\eta) \times (\pi \Delta R^2 - A_{core}), \quad (6.6)$$

1869 where ΔR is the radius of the isolation cone, and A_{core} is the area of the subtracted signal core. Finally
 1870 the calorimeter isolation variable may be defined as follows:

$$E_{T,cone}^{isol} = E_{T,raw}^{isol} - E_{T,core} - E_{T,leakage} - E_{T,pile-up}. \quad (6.7)$$

1871 The track-based isolation includes all tracks with $p_T > 1$ GeV within a fiducial region of the ID that
 1872 satisfy basic track quality requirements. Pile-up is mitigated by requiring that $|z_0 \sin \theta| < 3$ mm, to
 1873 ensure that the track points at the primary vertex. The track-based isolation is composed of all the
 1874 tracks that fall within the radius ΔR excluding the candidate electron track.
 1875 The own contribution of the candidate track into the isolation must also include possible Bremsstrahlung
 1876 radiation emitted by the candidate electron. For that reason the tracks are extrapolated to the second
 1877 layer of the EMC and if they fall within a window of $\Delta\eta \times \Delta\phi = 0.05 \times 0.1$ around the cluster position.
 1878 The resulting variable is called p_T^{isol} .
 1879 The track-based isolation allows to use variable-size cone, making the cone smaller for boosted particles.
 1880 The cone size for the $p_{T,var}^{isol}$ would be:

$$\Delta R = \min\left(\frac{10\text{GeV}}{p_T[\text{GeV}]}, R_{max}\right), \quad (6.8)$$

1881 where R_{max} is the maximum cone size and may vary depending on the analysis needs, typically between
 1882 0.2 and 0.4.

1883 6.5 Particle flow objects

1884 The measurement of hadronic objects and particle showers remains a complicated task due to large
 1885 variety of particle types and properties they posses and because of the large energy/momentum span of
 1886 the measured objects. For the low-energy charged particles the ID shows better momentum resolution
 1887 and angular resolution. On the other hand, the calorimeter shows better performance at high energy

and is also capable of detecting neutral particles. The idea behind the Particle Flow (PF) algorithm [20] is to combine the information from the two detectors to obtain the best result possible. To properly take into account every particle it has to be ensured that every particle detected in both detectors is counted only once. This means that for a charged particle its deposit in the calorimeter must be found and subtracted. The Particle Flow Object (PFO) reconstruction process is schematically presented in Fig. 610. The process starts with getting *tight* tracks from the ID, meaning these tracks must have at

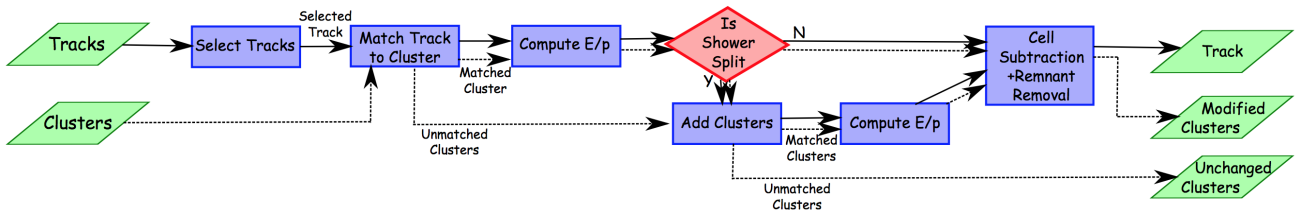


Figure 610: The algorithm scheme for particle flow object reconstruction.

least nine hits in the silicon detectors and no holes in the pixel detector. The tracks must have $|\eta| < 2.5$ and $0.5 < p_T < 40$ GeV, corresponding to the kinematic region where tracks offer better resolution than the calorimeter. The tracks associated to leptons are removed. The calorimeter topoclusters reconstructed like it was described in section 6.4.1 and calibrated using the EM scale are matched to the tracks based on their spacial position and measured momentum. First the ranked based on a distance metric:

$$\Delta R' = \sqrt{\left(\frac{\Delta\phi}{\sigma_\phi}\right)^2 + \left(\frac{\Delta\eta}{\sigma_\eta}\right)^2}, \quad (6.9)$$

where $\Delta\phi$ and $\Delta\eta$ are the angular distances between the topocluster barycentres and the track, σ_ϕ and σ_η are uncertainties in topocluster width. Preliminary matching is reached by requiring that $E^{clus}/p^{trk} > 0.1$, where E^{clus} is the cluster energy and p^{trk} is the track momentum. It often happens, that energy deposit of a particle is split between two (most often) or more clusters. Then a split shower recovery procedure is initiated, looking for matching clusters in the radius of $\Delta R = 0.2$ around the track extrapolated to the second layer of the EMC. Then it is estimated if the energy of the track and the energy of the associated topocluster is consistent. If it is the case then the topoclusters matched to the tracks are removed. Eventually two particle collections are obtained: a collection of charged particle flow objects (cPFOs) each with an associated track and neutral particle flow objects (nPFOs) with a calorimeter deposit. The former must also match the primary vertex, having $|z_0 \times \sin\theta| < 2$ mm.

1911 Bibliography

- 1912 [1] “Performance of the ATLAS Silicon Pattern Recognition Algorithm in Data and Simulation at
1913 $\sqrt{s} = 7$ TeV”. In: (July 2010).
- 1914 [2] M. Aaboud et al. “Performance of the ATLAS Track Reconstruction Algorithms in Dense Envi-
1915 ronments in LHC Run 2”. In: *Eur. Phys. J. C* 77.10 (2017), p. 673. doi: 10.1140/epjc/s10052-
1916 017-5225-7. arXiv: 1704.07983 [hep-ex].
- 1917 [3] R. Fruhwirth. “Application of Kalman filtering to track and vertex fitting”. In: *Nucl. Instrum.*
1918 *Meth. A* 262 (1987), pp. 444–450. doi: 10.1016/0168-9002(87)90887-4.
- 1919 [4] S. Boutle et al. “Primary vertex reconstruction at the ATLAS experiment”. In: *J. Phys. Conf. Ser.*
1920 898.4 (2017). Ed. by Richard Mount and Craig Tull, p. 042056. doi: 10.1088/1742-6596/898/4/
1921 042056.
- 1922 [5] *Development of ATLAS Primary Vertex Reconstruction for LHC Run 3*. Tech. rep. ATL-PHYS-PUB-
1923 2019-015. Geneva: CERN, Apr. 2019. URL: <https://cds.cern.ch/record/2670380>.
- 1924 [6] E. Bouhova-Thacker et al. “Vertex reconstruction in the ATLAS experiment at the LHC”. In: *2008*
1925 *IEEE Nuclear Science Symposium and Medical Imaging Conference and 16th International Workshop*
1926 *on Room-Temperature Semiconductor X-Ray and Gamma-Ray Detectors*. 2008, pp. 1720–1727. doi:
1927 10.1109/NSSMIC.2008.4774734.
- 1928 [7] Georges Aad et al. “Muon reconstruction performance of the ATLAS detector in proton–proton
1929 collision data at $\sqrt{s} = 13$ TeV”. In: *Eur. Phys. J. C* 76.5 (2016), p. 292. doi: 10.1140/epjc/s10052-
1930 016-4120-y. arXiv: 1603.05598 [hep-ex].
- 1931 [8] J. Illingworth and J. Kittler. “A survey of the hough transform”. In: *Computer Vision, Graphics,*
1932 *and Image Processing* 44.1 (1988), pp. 87–116. ISSN: 0734-189X. doi: [https://doi.org/10.1016/S0734-189X\(88\)80033-1](https://doi.org/10.1016/S0734-189X(88)80033-1). URL: <http://www.sciencedirect.com/science/article/pii/S0734189X88800331>.
- 1935 [9] Steffen Kaiser. “Search for the Higgs Boson in the Process $pp \rightarrow Hqq, H \rightarrow WW$ with the ATLAS
1936 Detector”. PhD thesis. Munich, Technische Universitaet Muenchen, 2010.
- 1937 [10] Morad Aaboud et al. “Electron reconstruction and identification in the ATLAS experiment using
1938 the 2015 and 2016 LHC proton-proton collision data at $\sqrt{s} = 13$ TeV”. In: *Eur. Phys. J. C* 79.8
1939 (2019), p. 639. doi: 10.1140/epjc/s10052-019-7140-6. arXiv: 1902.04655 [physics.ins-
1940 det].
- 1941 [11] W Lampl et al. *Calorimeter Clustering Algorithms: Description and Performance*. Tech. rep. ATL-
1942 LARG-PUB-2008-002. ATL-COM-LARG-2008-003. Geneva: CERN, Apr. 2008. URL: <https://cds.cern.ch/record/1099735>.

- 1944 [12] Georges et al. Aad. "Topological cell clustering in the ATLAS calorimeters and its performance in
1945 LHC Run 1. Topological cell clustering in the ATLAS calorimeters and its performance in LHC
1946 Run 1". In: *Eur. Phys. J. C* 77.CERN-PH-EP-2015-304 (Mar. 2016). Comments: 64 pages plus
1947 author list + cover page (87 pages in total), 41 figures, 3 tables, submitted to EPJC. All figures in-
1948 cluding auxiliary figures are available at <http://atlas.web.cern.ch/Atlas/GROUPS/PHYSICS/PAPERS/PERF-2014-07/>, 490. 87 p. doi: 10.1140/epjc/s10052-017-5004-5. url: <https://cds.cern.ch/record/2138166>.
- 1951 [13] Georges Aad et al. "Electron and photon performance measurements with the ATLAS detector
1952 using the 2015–2017 LHC proton-proton collision data". In: *JINST* 14.12 (2019), P12006. doi:
1953 10.1088/1748-0221/14/12/P12006. arXiv: 1908.00005 [hep-ex].
- 1954 [14] Thijs G. Cornelissen et al. "The global chi**2 track fitter in ATLAS". In: *J. Phys. Conf. Ser.* 119
1955 (2008). Ed. by Randall Sobie, Reda Tafirout, and Jana Thomson, p. 032013. doi: 10.1088/1742-
1956 6596/119/3/032013.
- 1957 [15] T Cornelissen et al. *Concepts, Design and Implementation of the ATLAS New Tracking (NEWT)*.
1958 Tech. rep. ATL-SOFT-PUB-2007-007. ATL-COM-SOFT-2007-002. Geneva: CERN, Mar. 2007.
1959 url: <https://cds.cern.ch/record/1020106>.
- 1960 [16] *Improved electron reconstruction in ATLAS using the Gaussian Sum Filter-based model for bremsstrahlung*.
1961 Tech. rep. ATLAS-CONF-2012-047. Geneva: CERN, May 2012. url: <https://cds.cern.ch/record/1449796>.
- 1963 [17] Morad Aaboud et al. "Electron and photon energy calibration with the ATLAS detector using
1964 2015–2016 LHC proton-proton collision data". In: *JINST* 14.03 (2019), P03017. doi: 10.1088/
1965 1748-0221/14/03/P03017. arXiv: 1812.03848 [hep-ex].
- 1966 [18] Morad Aaboud et al. "Measurement of the photon identification efficiencies with the ATLAS
1967 detector using LHC Run 2 data collected in 2015 and 2016". In: *Eur. Phys. J. C* 79.3 (2019), p. 205.
1968 doi: 10.1140/epjc/s10052-019-6650-6. arXiv: 1810.05087 [hep-ex].
- 1969 [19] Matteo Cacciari and Gavin P. Salam. "Pileup subtraction using jet areas". In: *Phys. Lett. B* 659
1970 (2008), pp. 119–126. doi: 10.1016/j.physletb.2007.09.077. arXiv: 0707.1378 [hep-ph].
- 1971 [20] Morad et al. Aaboud. "Jet reconstruction and performance using particle flow with the ATLAS
1972 Detector. Jet reconstruction and performance using particle flow with the ATLAS Detector". In:
1973 *Eur. Phys. J. C* 77.CERN-EP-2017-024. 7 (Mar. 2017). 67 pages in total, author list starting page 51,
1974 37 figures, 1 table, final version published in Eur. Phys. J C, all figures including auxiliary figures
1975 are available at <http://atlas.web.cern.ch/Atlas/GROUPS/PHYSICS/PAPERS/PERF-2015-09/>,
1976 466. 67 p. doi: 10.1140/epjc/s10052-017-5031-2. url: <https://cds.cern.ch/record/2257597>.

7

1978

1979

Calibrations and corrections

1980

“Potentielle citation sans aucun rapport avec le sujet”

1981

— Personne inconnue, contexte à déterminer

1982 7.1 Electron corrections

1983 This subsection describes the electron calibrations and corrections used in pTW analysis. They were
 1984 derived from the low- μ special run data collected in 2017 and 2018 at 5 and 13 TeV and the dedicated
 1985 Monte-Carlo (MC) samples [1], as well as from the standard ATLAS high pileup data collected during
 1986 the Run 2.

1987 7.1.1 Energy scale and resolution correction

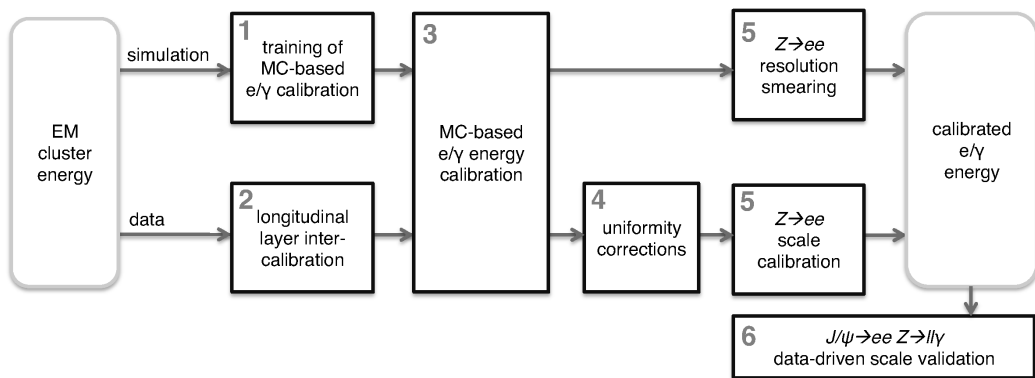


Figure 71: Schematic overview of energy response calibration procedure for electrons and photons.

1988 In order to obtain the energy scale and resolution corrections the electrons from $Z \rightarrow ee$ process
 1989 were used. The selection criteria were the same for data and MC simulation. For high- μ electron
 1990 candidates must pass the triggers HLT_2e12_lhloose_L12EM10VH (2015), HLT_2e17_lhvloose_nod0
 1991 (2016), HLT_2e24_lhvloose_nod0 (2017) and HLT_2e24_lhvloose_nod0 (2018) [2]. In low pile-up
 1992 case electron candidates must pass the triggers HLT_e15_lhloose_nod0_L1EM12. Both electrons are
 1993 required to have $p_T > 27$ GeV and $|\eta| < 2.47$, satisfying the medium LH ID criteria and loose isolation
 1994 criteria as described in Ref. [3]. Energy scale correction follows the method described in detail in

-2.47	-2.4	-2.1	-1.8	-1.55	-1.37	-1.2	-1	-0.8	-0.6	-0.4	-0.2	0	0.2	0.4	0.6	0.8	1	1.2	1.37	1.55	1.8	2.1	2.4	2.47
-------	------	------	------	-------	-------	------	----	------	------	------	------	---	-----	-----	-----	-----	---	-----	------	------	-----	-----	-----	------

Table 71: Values of η_{calo} bin frontiers for energy scale factors for low pile-up runs.

[4] and schematically described in Fig. 71. The scale in both data and MC is calibrated using the MVA-based algorithm, then the data is corrected for pile-up and uniformity. The energy response in data is calibrated using the $Z \rightarrow ee$ peak to match exactly the Z resonance in the simulation. Two correction factors are introduced: the energy scale factor α and the constant term c' . The correction factors are extracted using the template method described in Ref. [5]:

- The calorimeter is split into i slices in η and for each slice the energy response in data is corrected in the following way:

$$E^{\text{data,corr}} = E^{\text{MC}} = E^{\text{data,uncorr}} / (1 + \alpha_i),$$

where $E^{\text{data,uncorr}}$ and E^{MC} are the energy response in data and MC respectively, α_i is the energy correction factor for the i^{th} calorimeter slice in η .

- The relative energy measurement resolution can be represented as a quadratic sum of three uncorrelated terms:

$$\frac{\sigma(E)}{E} = \frac{a}{\sqrt{E}} \oplus \frac{b}{E} \oplus c,$$

where b term stands for electromagnetic and pile-up noise term, a is the stochastic term related to the development of the electromagnetic shower and c is constant. In order to widen the MC mass peak and match it to the data in each rapidity bin an additional constant term c' is added:

$$\left(\frac{\sigma(E)}{E} \right)_i^{\text{data}} = \left(\frac{\sigma(E)}{E} \right)_i^{\text{MC}} \oplus c'_i.$$

Normally in the standard high-pileup data, the energy scale factors corrections are obtained in 68 bins. For the low pile-up runs smaller bins were also considered due to smaller number of $Z \rightarrow ee$ events. Figure 72 demonstrates the need for wider bins, as 68 bins result in high uncertainty, especially in the endcap.

Two binnings were considered:

- 48 bins with smaller bins in the barrel and wider bins in the endcap
- 24 bins of equal size, as shown in Table 71.

As can be seen from Figure 72, the statistical instability for the endcap bins disappears if wider bins are used. Since the α factors are quite similar in 48 and 24 bin cases, the latter is chosen as the baseline.

The extracted constant c'_i correction term is presented in Figure 73. The constant term c' depends on the data taking conditions and pile-up, so its extrapolation from a dataset obtained under different conditions appears problematic. This issue is discussed in Ref. [6].

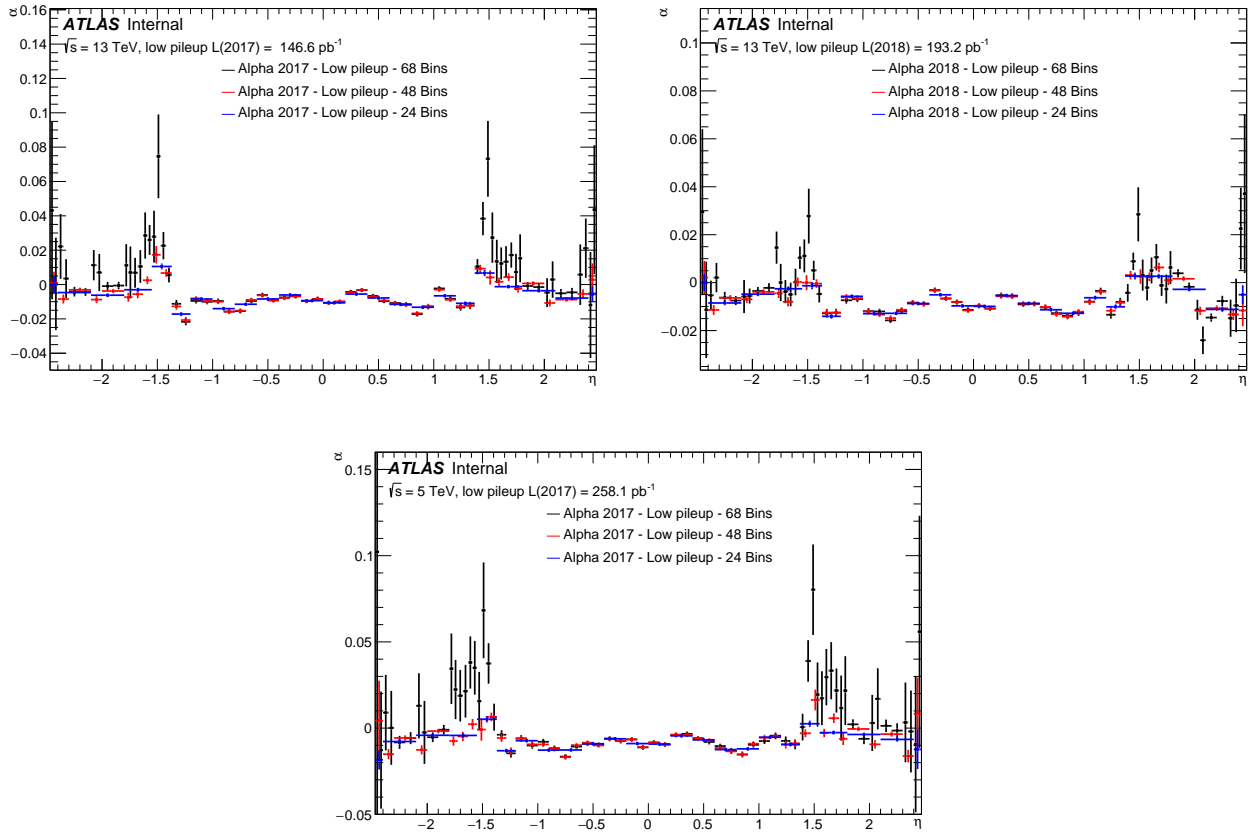


Figure 72: Energy scale factors α for low pile-up runs of 2017 (left), 2018 (right) and 2017 at 5TeV (bottom) using 68, 48 and 24 η bins. It can be seen, that the extraction is unstable in case of 68 bins, resulting in α factors with very large uncertainties.

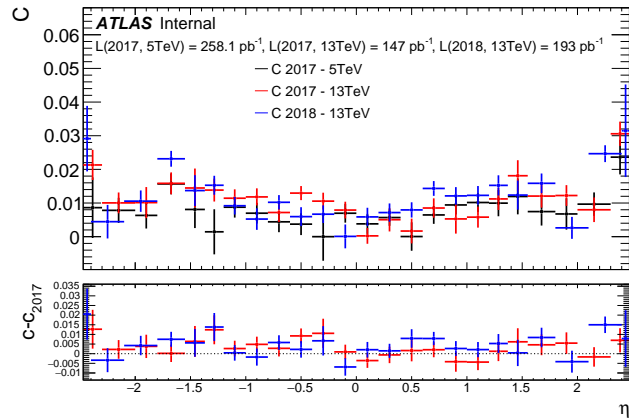


Figure 73: Additional constant term c'_i for low pile-up runs of 2017 (13 TeV), 2018 (13 TeV) and 2017 at 5 TeV using 24 bins. The lower panel shows the difference of c'_i to the 2017 5 TeV run.

2014 This correction entails experimental uncertainty, caused primarily by the statistical uncertainty of
 2015 α_i and c'_i factors measurement, other uncertainties are significantly smaller and therefore neglected.
 2016 The comparison between data and MC invariant mass distributions around the $Z \rightarrow ee$ peak are
 2017 presented in Figure 74 and Figure 75. The agreement is good around the $Z \rightarrow ee$ resonance and stays
 2018 within the uncertainty in other regions.

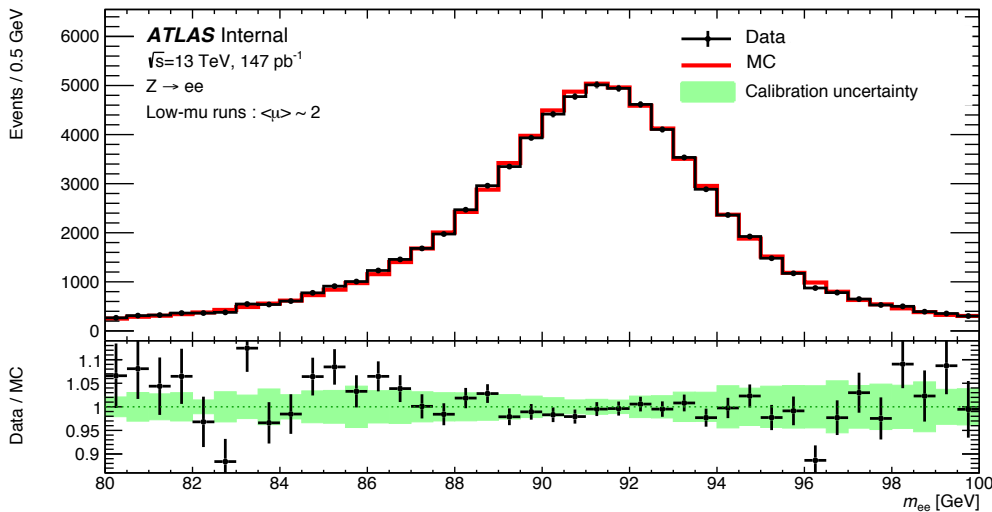


Figure 74: The invariant mass distribution around the Z-mass for low pile-up Data for 2017 (13 TeV)

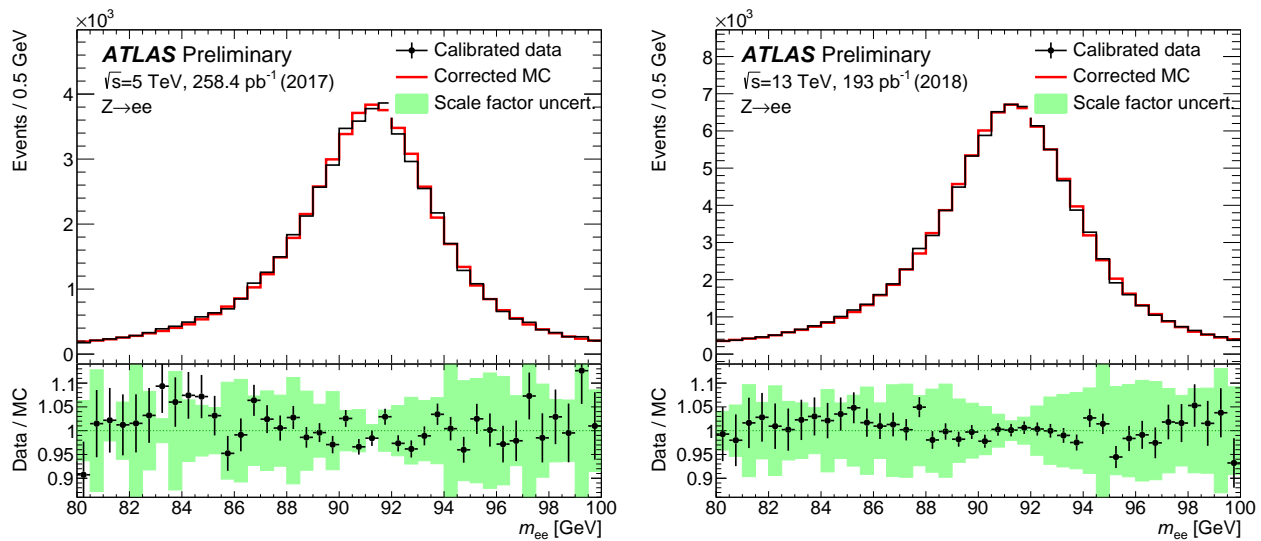


Figure 75: The invariant mass distribution around the Z-mass for low-pileup data for the $\sqrt{s} = 5\text{ TeV}$ data taken in 2017 (a) and the $\sqrt{s} = 13\text{ TeV}$ 2018 data (b).

2019 **7.1.2 Electron selection efficiency**

The electrons used in the analysis are selected based on certain requirements to the quality of their reconstruction, kinematic characteristics, passing certain identification, isolation and trigger matching criteria. A tag-and-probe method is used to measure these efficiencies in data and MC simulation, which may be different due to various aspects of physics and detector modelling. In order to match the MC simulation and the data in each of the aforementioned aspects the corresponding scale factor (SF)s are introduced. The SF is defined as the ratio of the data efficiency to MC efficiency:

$$SF_{(a)} = \frac{\epsilon_{(a)}^{data}}{\epsilon_{(a)}^{MC}},$$

where ϵ stand for efficiency and index a stands for reconstruction, ID, isolation or trigger. The SF extraction allows for better comparison between data and simulation, but also brings uncertainties. The total efficiency correction is used as an event weight during the analysis:

$$W_{event}^{W \rightarrow e\bar{e}} = SF_{reco} \dot{SF}_{trig} \dot{SF}_{ID} \dot{SF}_{iso}.$$

2020 The tag-and-probe method used for the measurement of electron efficiencies includes the following
2021 steps:

- 2022 • A kinematic selection is applied to $Z \rightarrow ee$ events (Cut1).
 - 2023 • A tight selection (Cut2) is applied to one of the two electrons along with matching it to the
2024 single-electron trigger. From now on this electron is called the *tag*.
 - 2025 • The other electron is called the *probe* and is used to probe the picked efficiency.
 - 2026 • Selections Cut1 and Cut2 are varied in order to evaluate the uncertainties.
- 2027 The details are presented in Refs. [2, 7, 8].

2028 **Reconstruction efficiency**

2029 The reconstruction efficiency is defined as a fraction of all electromagnetic clusters that are matched
2030 with the charged particle track from the ID that matches the designated quality criteria. An additional
2031 "PassTrackQuality" requirement of having at least 1 hit in the pixel detector and and least 7 hits in the
2032 silicon detectors is imposed on the track of successfully reconstructed electrons.
2033 So the electron reconstruction efficiency is calculated as:

$$\epsilon^{reco}(p_T, \eta) = \frac{N_{pass} - N_{pass}^{bkg}}{N_{pass} - N_{pass}^{bkg} + N_{fail} - N_{fail}^{bkg} + N_{photon} - N_{fit}}. \quad (7.1)$$

2034 $N_{pass(fail)}$ stands for the number of electrons passing (failing) the "PassTrackQuality" criterion. The
2035 background electron candidates $N_{pass(fail)}^{bkg}$ are obtained from the template fits of the background on
2036 subsets that pass (fail) the "PassTrackQuality" criterion. The number of electrons that are reconstructed
2037 as photons is denoted by N_{photon} . The non-electron background that is reconstructed as photons is
2038 estimated from analytical fit in the control region away from the $Z \rightarrow ee$ resonance and is called N_{fit} .
2039 An extrapolation of SF_{reco} from the high- μ data is used as a baseline for the reconstruction scale factors
2040 measurement. The benefits of higher statistics available in high- μ dataset outweigh the losses imposed
2041 by the extrapolation and provide lower uncertainty comparing to the SFs measured with low pileup
2042 dataset (see Fig. 76).

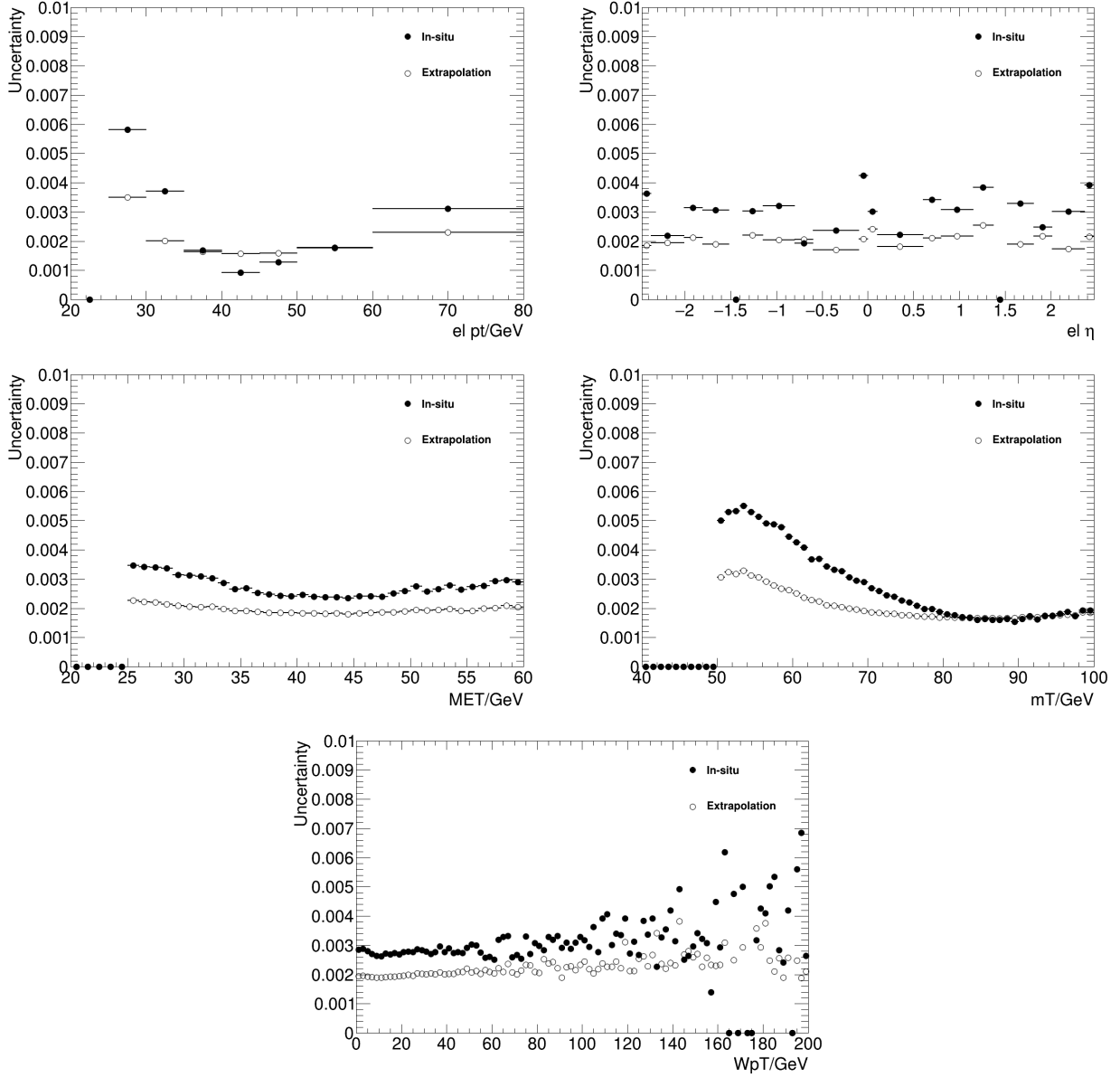


Figure 76: Comparison of the uncertainties due to electron reconstruction, contrasting the high- μ -extrapolated and in-situ-measured SF uncertainties in a $W^+ \rightarrow e^+ \nu$ selection at 13 TeV as function of typical kinematic variables.

2043 Identification efficiency

2044 The fraction of reconstructed electrons that pass a given working point define the electron identification
 2045 efficiency. The low pile-up $W \rightarrow ev$ measurement uses "Medium LH" working point. The methodology
 2046 is described in Ref. [7] and includes the combination of two background subtraction methods: $Zmass$
 2047 and $Ziso$.

2048 In the $Zmass$ method the background is estimated using a template method normalized in m_{ee} side
 2049 bands. The tag is required to be trigger-matched, pass ID and isolation cuts and have $p_T > 20$ GeV. The
 2050 probe has to pass the "PassTrackQuality" and the electron/photon ambiguity resolver, have $p_T > 15$
 2051 GeV and be separated from jets with $p_T^{jet} > 20$ GeV by $\Delta R > 0.4$.

2052 An alternative $Ziso$ method uses the calorimeter energy isolation E_T^{cone} of the probe electron to discrim-
 2053 inate between background and signal. Signal electrons are expected to have better isolation than the
 2054 background. On top of the requirements used for the $Zmass$ method the tag and probe pair is required
 2055 to have opposite sign and to fit into mass window of 15 GeV around the Z boson mass. Background tem-
 2056 plate shape is constructed from the probe electrons that have the same charge as the tag, pass the track
 2057 quality criteria but fail the shower shape cuts or fail the cut-based loose identification. The fraction of
 2058 real electrons that pass the described selection is modelled with MC and subtracted from the template.
 2059 The background template uses the tail region of probe isolation distribution $E_T^{cone0.3}/25\text{GeV} > 0.5$ is
 2060 scaled to data events. An example of the probe isolation estimate for the enumerator and denominator
 2061 in eq. 7.1 in the region $25 < E_T < 30$ and $0.8 < \eta < 1.15$ is presented in Fig. 77.

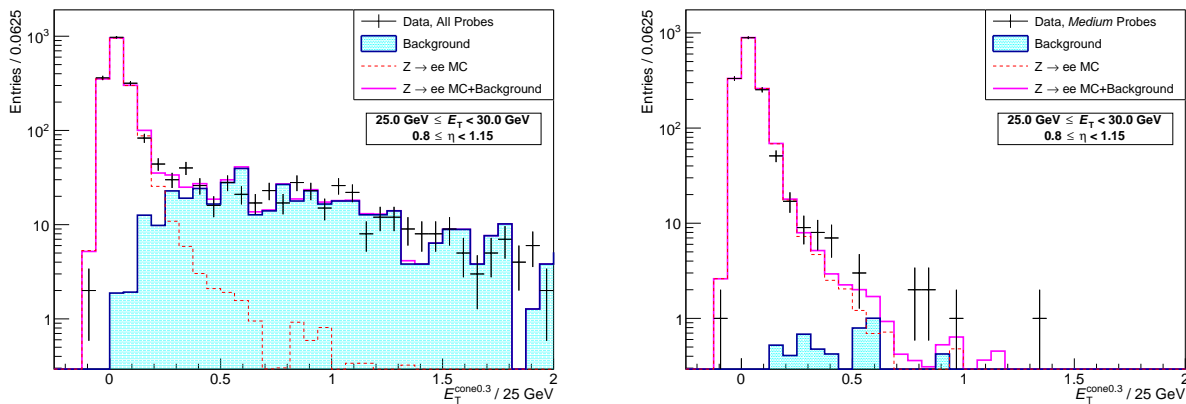


Figure 77: Isolation $E_T^{cone0.3}/25\text{GeV}$ distribution of probe electrons in the $Ziso$ -method using 13 TeV 339 pb^{-1} low-pileup data. Left the denominator and right the numerator distributions are shown, with the data as crosses, the signal $Z \rightarrow ee$ expectation as open line and the background estimate as cyan area (template normalised at high values).

2062 The SF to be used in the analysis is constructed out of both methods. The merger of the results takes
 2063 into account the high degree of correlation of the two methods and includes the following steps:

- 2064 • the final SF is defined as an arithmetic mean of the two methods over all systematic variations;

- 2065 • the statistical uncertainty is calculated as an average of the statistical uncertainties of the variations;
2066
- 2067 • a covariance matrix is composed from all variations of the two methods and then decomposed
2068 into correlated and uncorrelated parts, providing the systematic uncertainty.

2069 The combined results are presented in Fig. 78 and show similar results between both methods and the
2070 combination. The SFs obtained from 5 and 13 TeV data samples were not combined due to significant
2071 difference in measured efficiency.

2072 Isolation efficiency

2073 Electron isolation efficiency is a fraction of reconstructed and MediumLLH-identified electrons that
2074 pass a designated isolation requirement. For this analysis the isolation requirement is chosen to be
2075 $p_{T\text{varcone}}^{20}/p_T^e < 0.1$. The results are presented in Fig. 79 and show that the efficiency is very high.
2076 The SFs for 5 and 13 TeV are not combined and used separately.

2077 Trigger efficiency

2078 During the data-taking at low pile-up the unprescaled trigger `HLT_e15_1hloose_nod0_L1EM12` was
2079 used. Thanks to the ID and isolation requirements to both tag and probe, the background is negligible
2080 for trigger efficiency measurement. Measurement results are shown in Fig. 710 and demonstrate
2081 relatively high efficiency in most of the regions. The scale factors are also very close to unity. No
2082 combination was performed between 5 and 13 TeV results.

2083 7.1.3 SF uncertainties propagation

2084 The main source of uncertainty for the measurement of the SFs is coming from the background. The
2085 uncertainties are estimated by varying the parameters that contribute to background suppression.
2086 These parameters include:

- 2087 • The Zmass window technique is used by identification, isolation and trigger efficiencies measure-
2088 ment. The size of the Zmass window was varied in a range of 10, 15 and 20 GeV. This variation
2089 dominates at higher values of p_T .
- 2090 • Tag identification and isolation criteria were varied between Medium ID + calorimeter isolation,
2091 TightLLH and Tight ID + calorimeter isolation.
- 2092 • Background template has a major influence on the estimate of signal contamination, especially
2093 at $p_T < 30$ GeV. In addition to the nominal rage of template extraction in $120 < m_{ee} < 250$ the
2094 templates are also normalized using the region of $60 < m_{ee} < 70$ GeV.

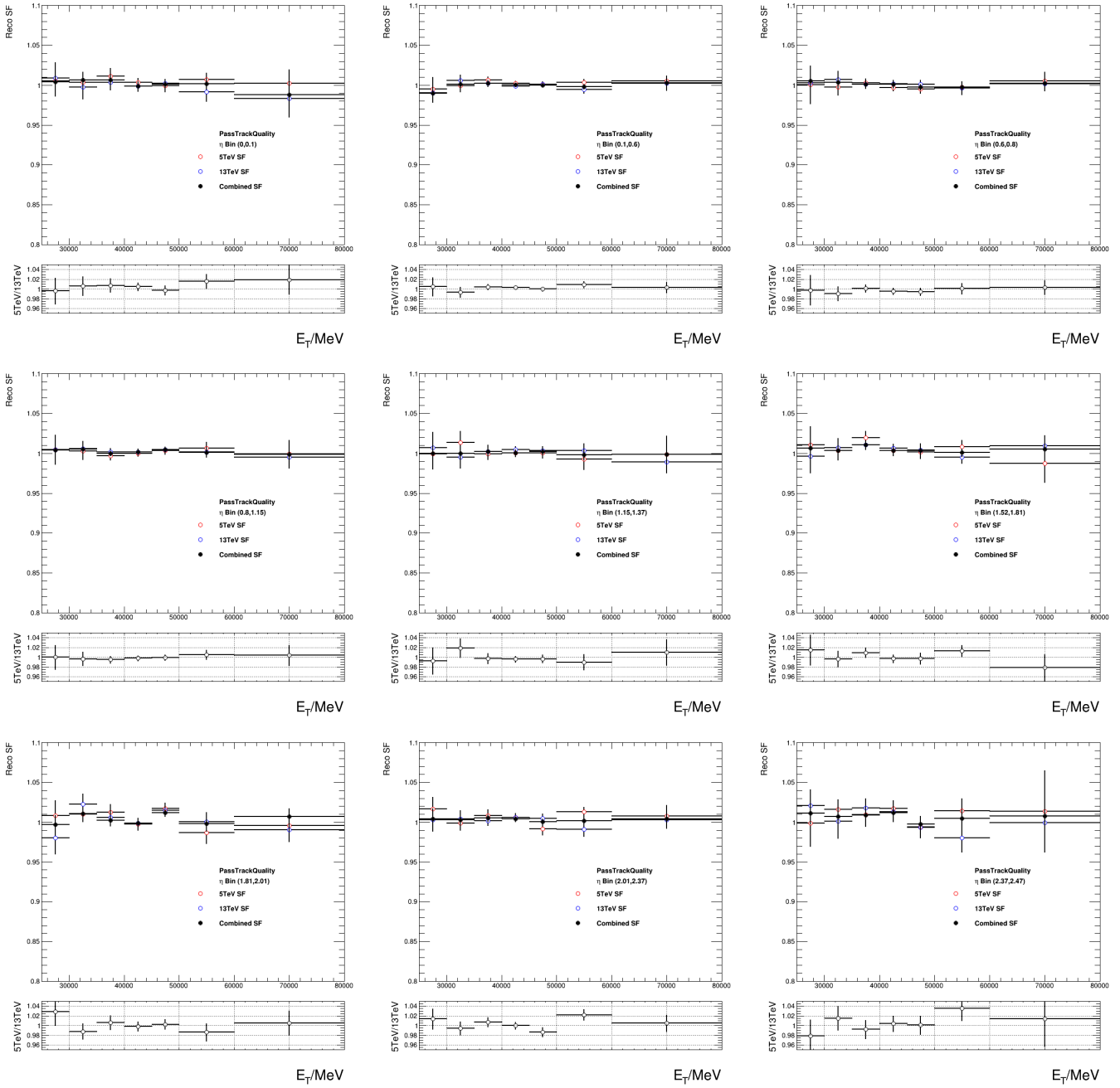
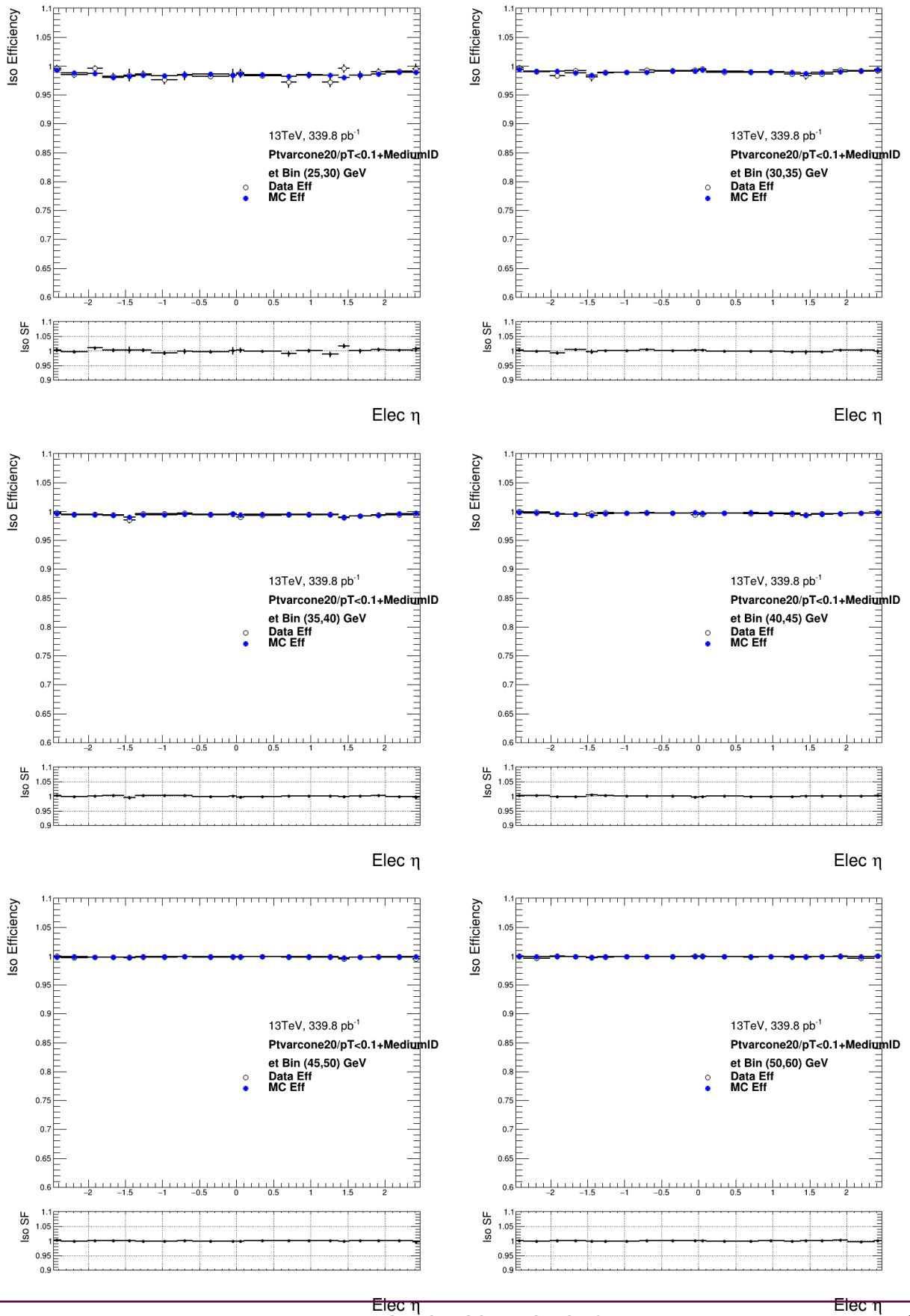


Figure 78: Comparison of electron reconstruction SFs with 5 TeV and 13 TeV data as well as the 5+13 TeV combination in nine η ranges as written in the plot legend, from most central $\eta = 0 - 0.1$ (top left) to most forward $\eta = 2.37 - 2.47$ (bottom right). The bottom panel shows the ratio of 5 TeV and 13 TeV SFs. The total uncertainties are shown.



7.1. ELECTRON CORRECTIONS

Figure 79: Electron isolation efficiencies (top panels) and scale factors (lower panels) for the $ptvarcone20/p_T^e < 0.1$ working point using 13 TeV 339 pb $^{-1}$ low-pileup data as function of η in bins of p_T .

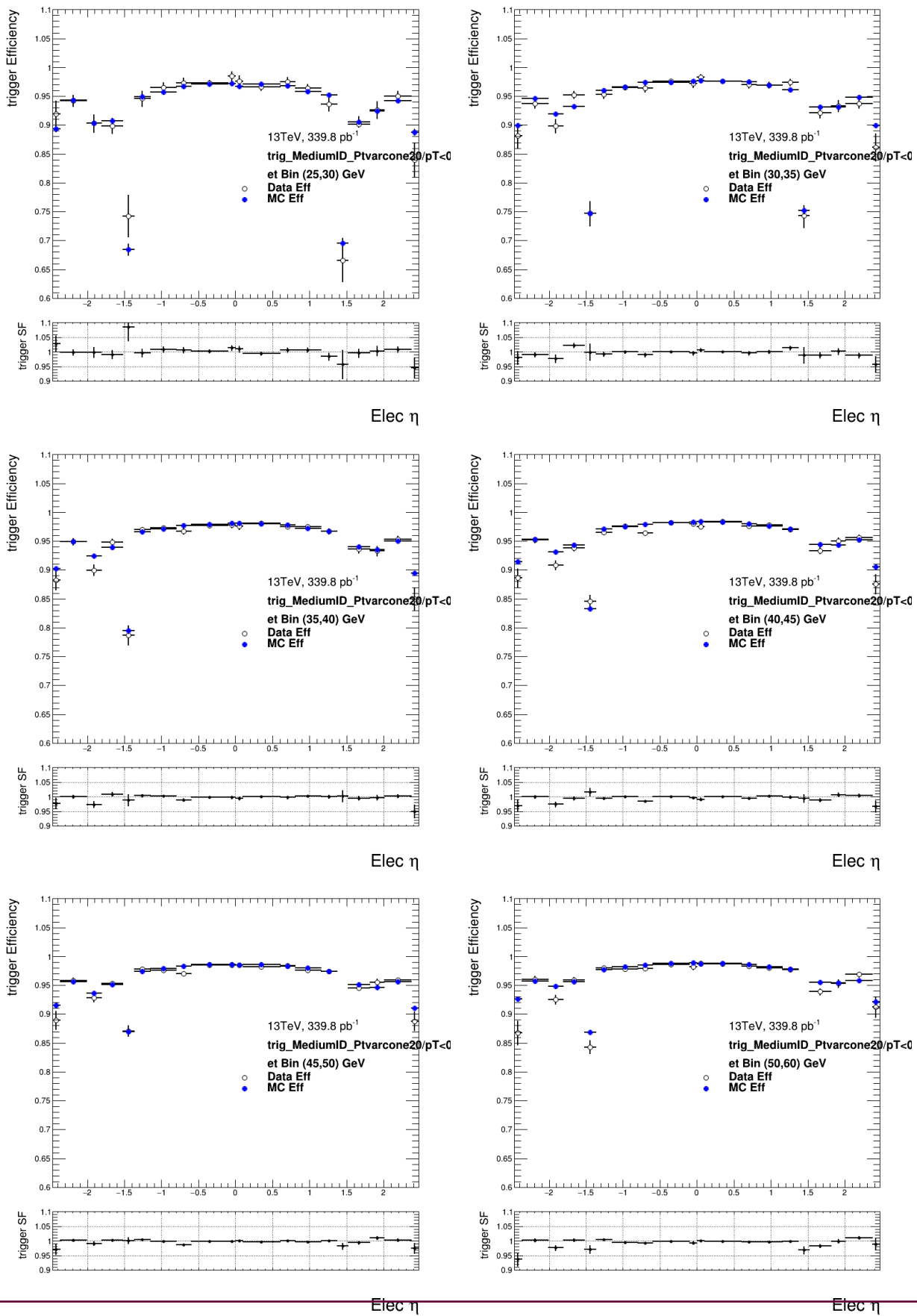


Figure 710: Electron trigger efficiencies (top panels) and scale factors (lower panels) for HLT_e15_1hloose_nod0_L1EM12 using 13 TeV 339 pb⁻¹ low-pileup data as function of η in bins of p_T .

- Side band range is varied for reconstruction efficiency measurement.
- Isolation criteria are varied in the measurement of ID efficiency: $E_T^{cone0.3}/25\text{GeV}$ is varied between 0.4, 0.5 and 0.6, also a larger cone isolation around the probe electron was used - $E_T^{cone0.4}/25\text{GeV}$.

Figure 711 shows the total relative uncertainties of the electron scale factors at 13 TeV in different η bins. Contributions from reconstruction and identification are the dominant ones. The uncertainties are propagated to the observables using the co-called Full correlation model (see Ref. [8]). The idea of the method is to split the sources of SF uncertainty into uncorrelated and correlated sources. Uncorrelated sources are of statistical nature and mostly related to the number of $Z \rightarrow ee$ pairs in different bins if p_T and η used for SF extraction. Correlated sources of systematic uncertainty arise from the flaws of background subtraction. In the Full correlation model includes about 10 sources of systematic uncertainty and around 200 $p_T \times \eta$ bins as sources of statistical uncertainty and allows to propagate these uncertainties to the observables. Figures 712 and 713 contain the results of error propagation for 13 and 5 TeV respectively. Again, identification and reconstruction uncertainties have the largest contribution to the total SF uncertainty.

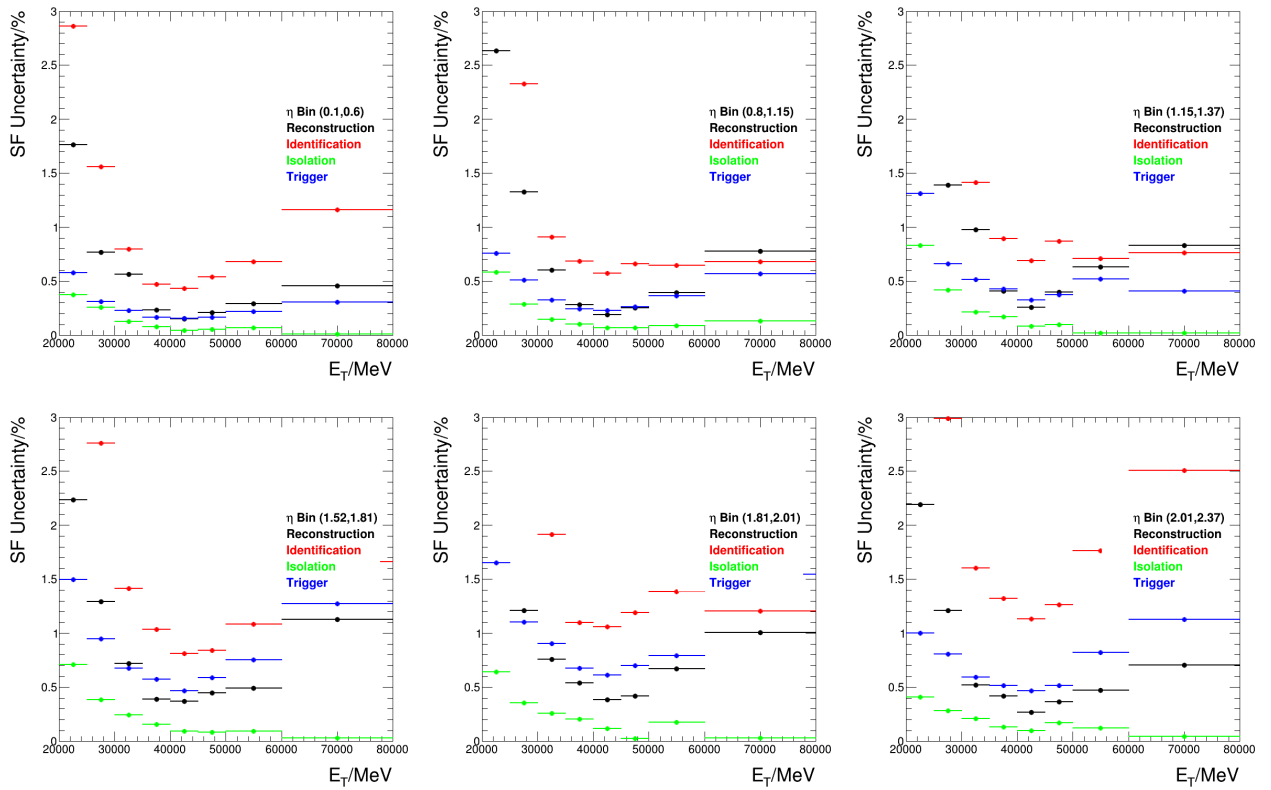


Figure 711: Total relative uncertainties of electron scale factors at 13 TeV measured with tag-and-probe method

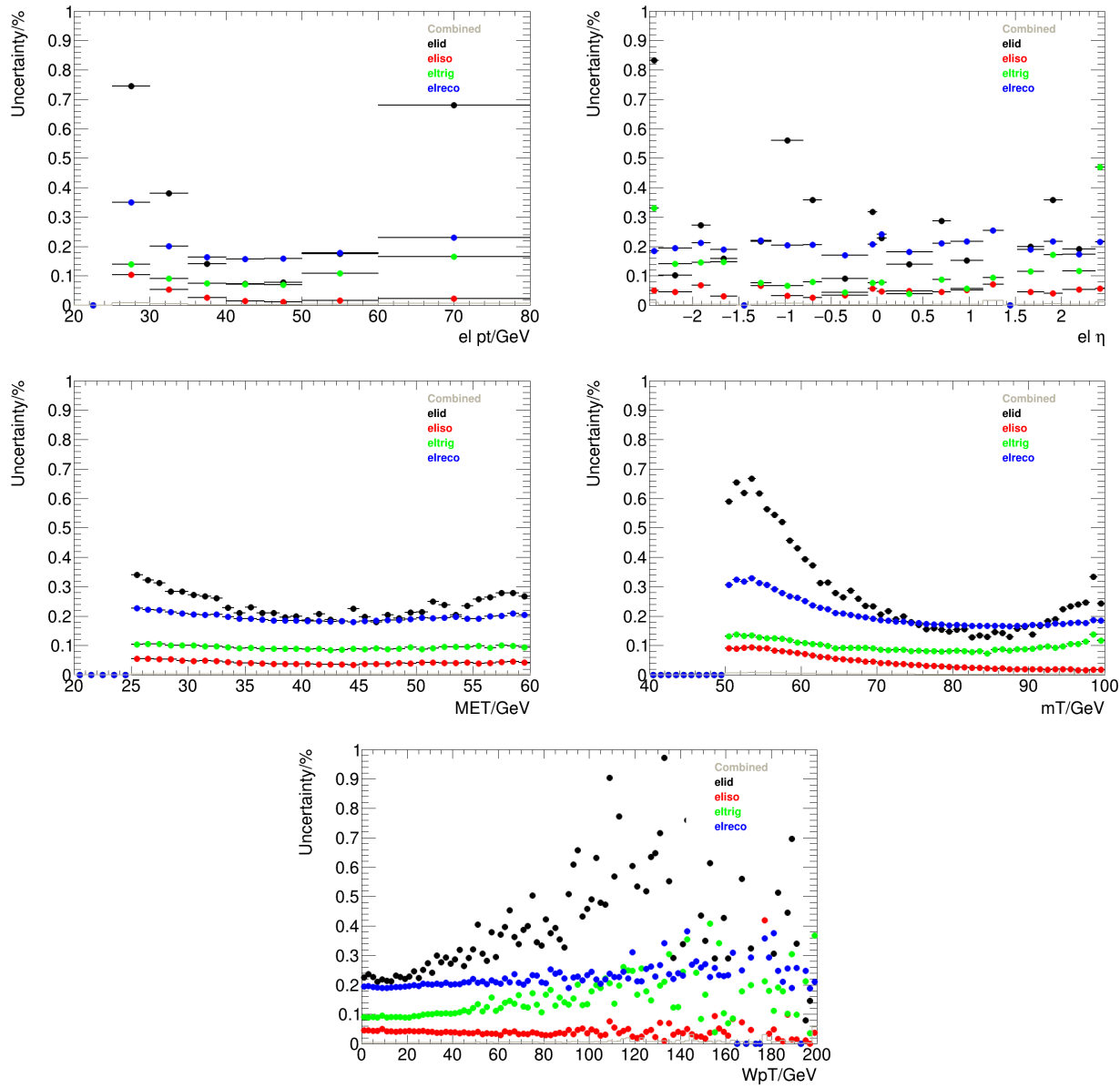


Figure 712: Contributions to the electron uncertainties related to efficiency SF (reconstruction, identification, isolation and trigger) in a $W^+ \rightarrow e^+\nu$ selection at 13 TeV as function of typical kinematic variables.

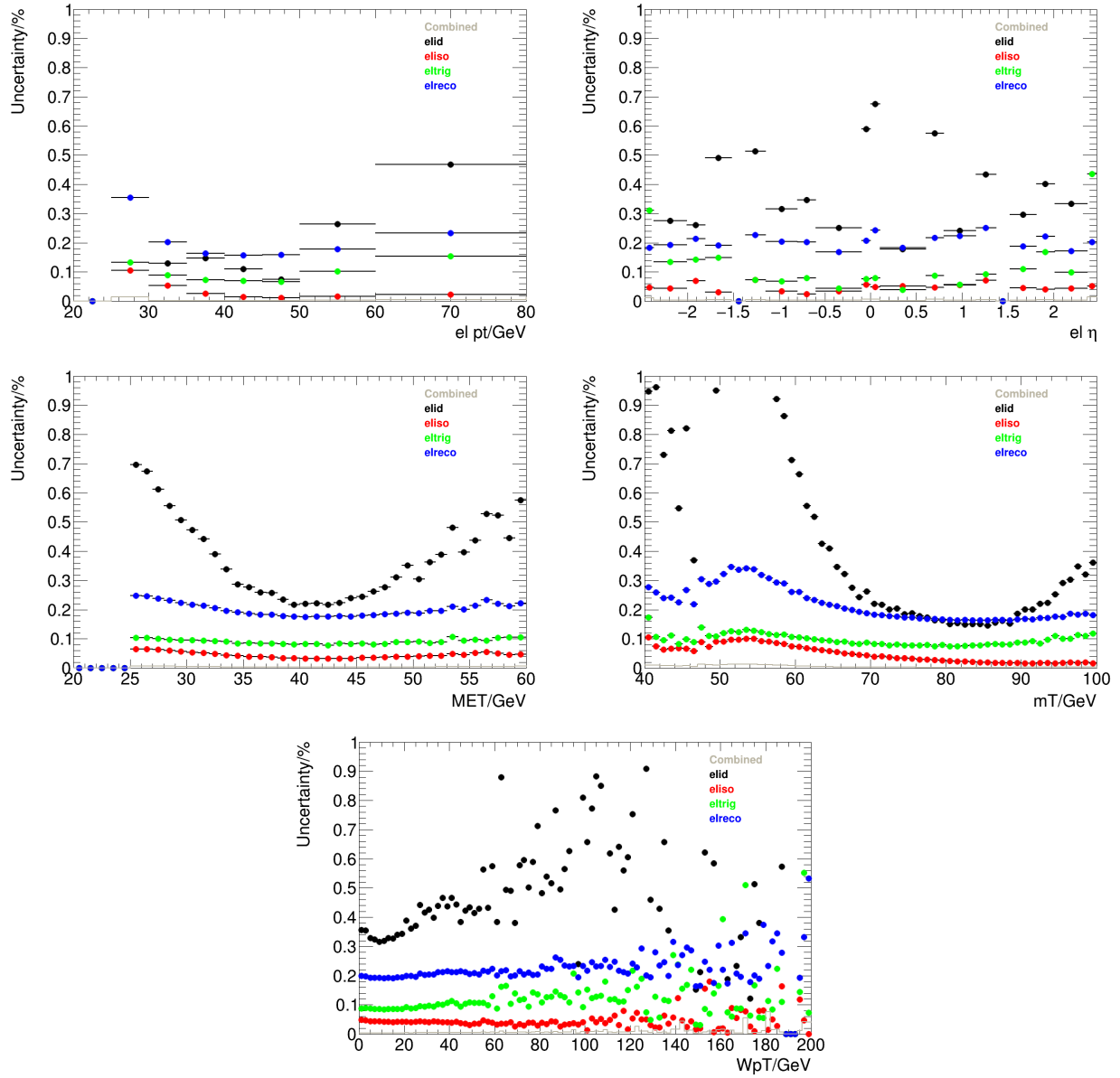


Figure 713: Contributions to the electron uncertainties related to efficiency SF (reconstruction, identification, isolation and trigger) in a $W^+ \rightarrow e^+ \nu$ selection at 5 TeV as function of typical kinematic variables.

2109 7.2 Muon corrections

2110 Muon corrections are in many aspects similar to the electron corrections described in the previous
 2111 section. Calibrations are used in order to match the data and MC simulation

2112 7.2.1 Muon momentum calibration

2113 The muon momentum calibration comprises corrections to the momentum scale and resolution. At
 2114 first the ID and MS tracks are reconstructed and corrected separately, and then the two corrections are
 2115 propagated to correct the CB muon tracks. Low energy muons with $5 < p_T < 30$ GeV are calibrated using
 2116 the $J/\psi \rightarrow \mu\mu$ resonance, while in higher energy region of $22 < p_T < 300$ GeV the $Z \rightarrow \mu\mu$ resonance is
 2117 used. The statistical uncertainties are directly linked to the number of Z and J/ψ candidates in the
 2118 data samples:

- 2119 • 5.02 TeV data (2017, period M): 660k J/ψ candidates, 75k Z candidates
- 2120 • 13 TeV data (2017, period N): 1.1M J/ψ candidates, 100k Z candidates
- 2121 • 13 TeV data (2018, periods G4 and J): 1.5M J/ψ candidates, 130k Z candidates

2122 The Z and J/ψ peaks are fitted with a function that is a sum of a Crystal Ball function (that fits the
 2123 mass peak), a Gaussian (that accounts for effects like multiple scattering) and an exponential that fits
 2124 the backgrounds. The examples of such fits are presented at Fig. 714.

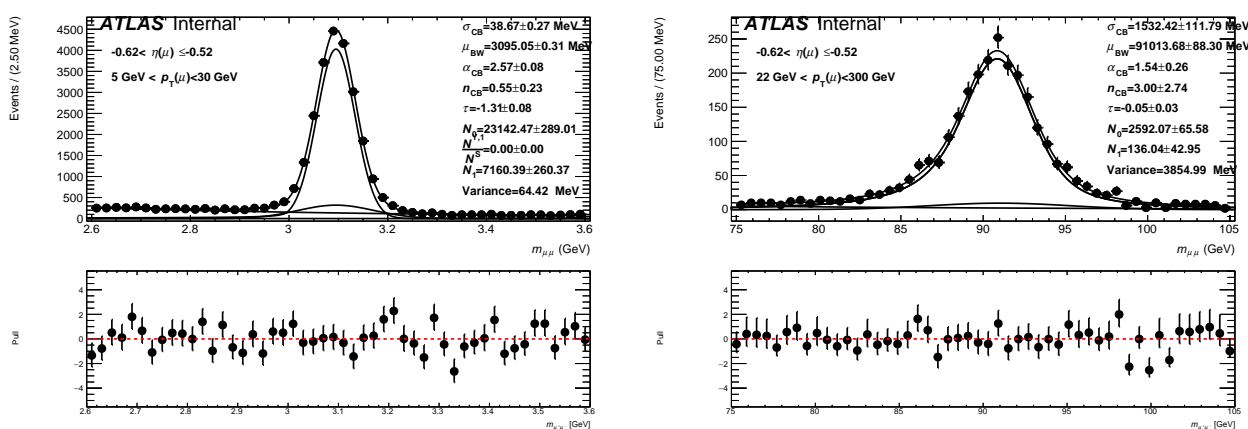


Figure 714: Example fits to $J/\psi \rightarrow \mu\mu$ (left) and $Z \rightarrow \mu\mu$ (right) mass peaks for pairs with leading muon pseudorapidity in the range $-0.62 < \eta < -0.52$ in low-pile-up 2017 13 TeV data.

2125 The measured correction parameters for Z and J/ψ peaks for 5 and 13 TeV are presented in Figures
 2126 715, 716, 717 and 718.

7.2.2 Correction for charge-dependent momentum bias

Misalignment in ID, MS or between the two systems can lead to a charge-dependent bias (also called *sagitta bias*) of muon reconstructed momentum. Its effect can be parametrized as follows:

$$p_T^{meas} = \frac{p_T^{reco}}{1 + q\dot{\delta}_{sagitta}\dot{p}_T^{reco}}, \quad (7.2)$$

where p_T^{meas} is the measured momentum that contains a bias, p_T^{reco} is the unbiased reconstructed momentum and the bias to be corrected is denoted as $\delta_{sagitta}$.

The sagitta correction is obtained as a function of η . There exist three methods of sagitta bias determination:

- The ID alignment and momentum measurement can be tested with electrons which have additional information from the charge-independent calorimeter. Using $Z \rightarrow ee$ and/or $W \rightarrow e\nu$ events it is possible to determine the charge bias of an electron track:

$$\delta_{sagitta} = \frac{\langle E/p_{track} \rangle^+ - \langle E/p_{track} \rangle^-}{2 \langle p_T^{calo} \rangle}, \quad (7.3)$$

where p_{track} is the momentum measured in the ID, E is the energy measured in the EMC, from which we can get the $p_T^{calo} = E \sin\theta$ transverse momentum. The $\langle \rangle$ brackets denote the averaging in η bins.

- The $p_T(\mu)$ method is used by muon combined performance (MCP) and alignment groups in high- μ data compares the muons and anti-muons spectra in $Z \rightarrow \mu\mu$ events.
- The Z-mass method uses the Z mass peak. This is the main method used by MCP and alignment groups, the results are denoted as $M_{\mu\mu_MCP}$ and $M_{\mu\mu_Align}$ on the plots (see [9]). The sagitta bias is calculated iteratively minimizing the difference between the reconstructed and expected position of the $Z \rightarrow \mu\mu$ mass peak position.

The results of these methods are presented in Fig. 719. The sagitta bias in low-pile-up data was found to be 10 times higher than in the MC simulation. Further results in the measurement rely on the following method: the differences between the data and MC are averaged over η using a fit, and also introduce a global offset. The results are shown in Fig. 720.

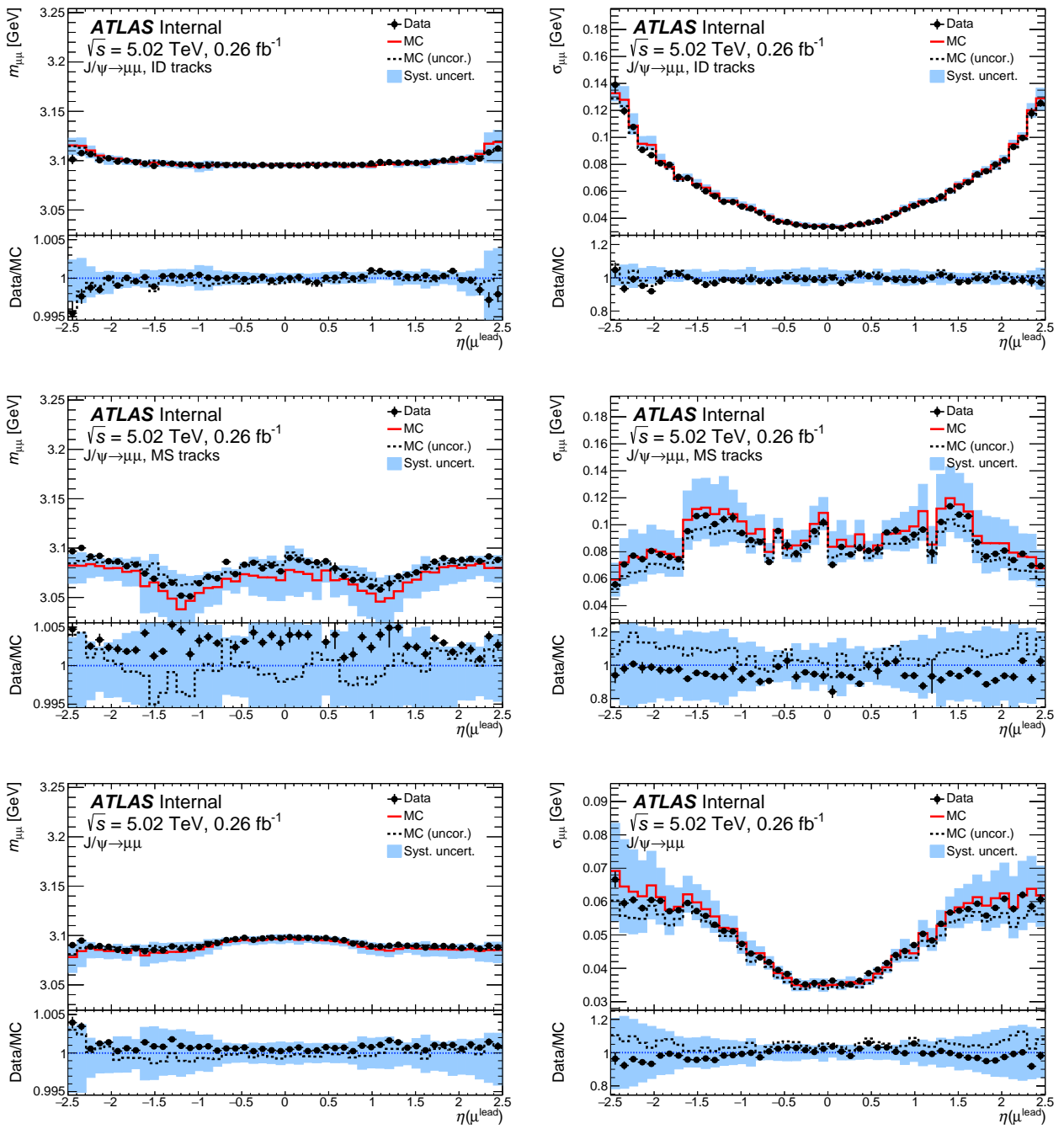


Figure 715: Mean (left) and width (right) of the $J/\psi \rightarrow \mu\mu$ mass peak as a function of the leading muon η in 5.02 TeV data and MC. The mean and width are extracted from Crystal Ball components of the fits. In case of the simulation, both the uncorrected (dashed histogram) and corrected parameters (solid histogram) are shown. The fit results are presented for mass peaks constructed using kinematics of the muon ID tracks (top), ME tracks (middle) or CB tracks (bottom). The bottom panels in each plot show the data/MC ratio for uncorrected (dashed histogram) and corrected simulation (points).

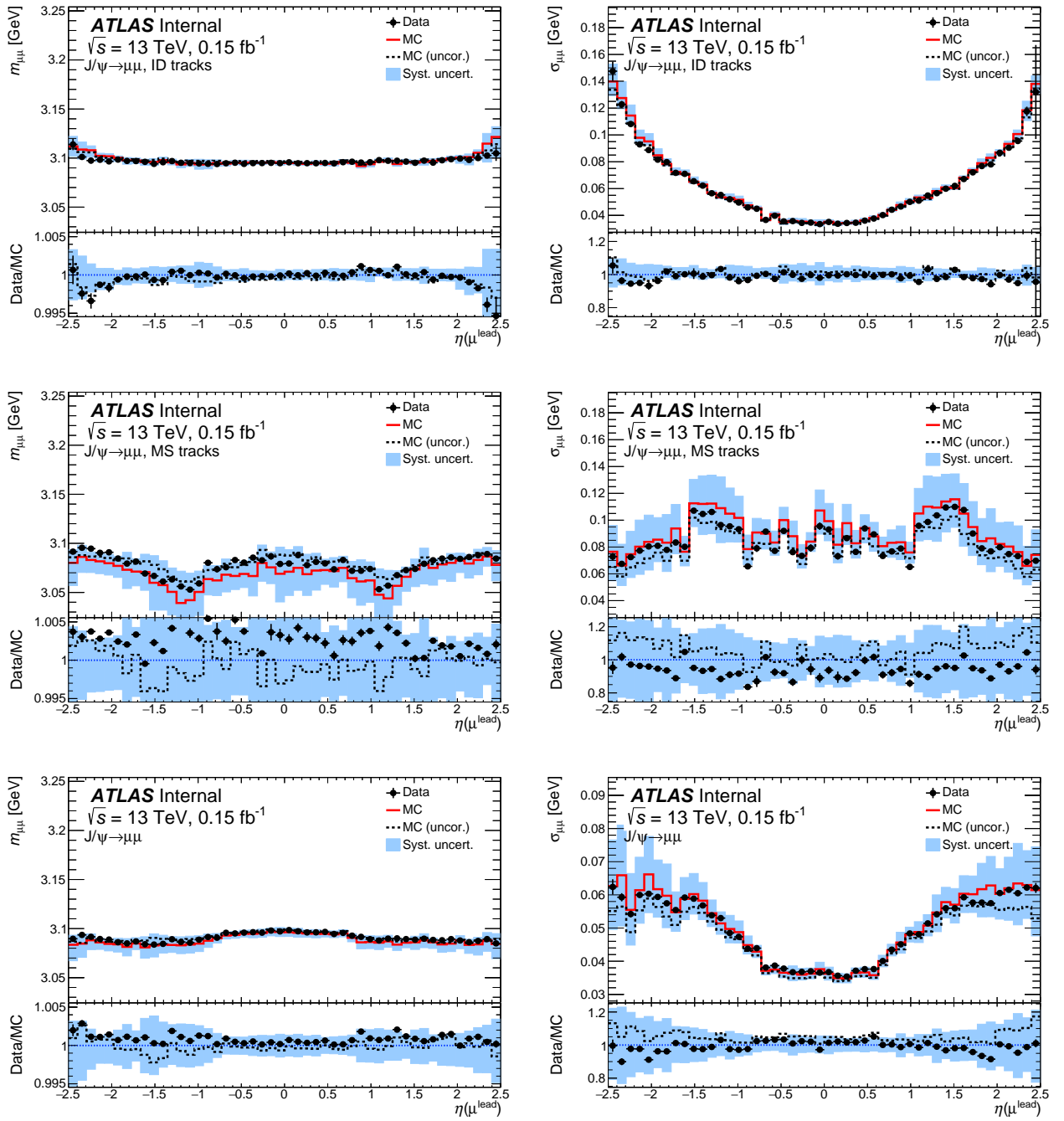


Figure 716: Mean (left) and width (right) of the $J/\psi \rightarrow \mu\mu$ mass peak as a function of the leading muon η in 2017 13 TeV data and MC at low pile-up. The mean and width are extracted from Crystal Ball components of the fits. In case of the simulation, both the uncorrected (dashed histogram) and corrected parameters (solid histogram) are shown. The fit results are presented for mass peaks constructed using kinematics of the muon ID tracks (top), ME tracks (middle) or CB tracks (bottom). The bottom panels in each plot show the data/MC ratio for uncorrected (dashed histogram) and corrected simulation (points).

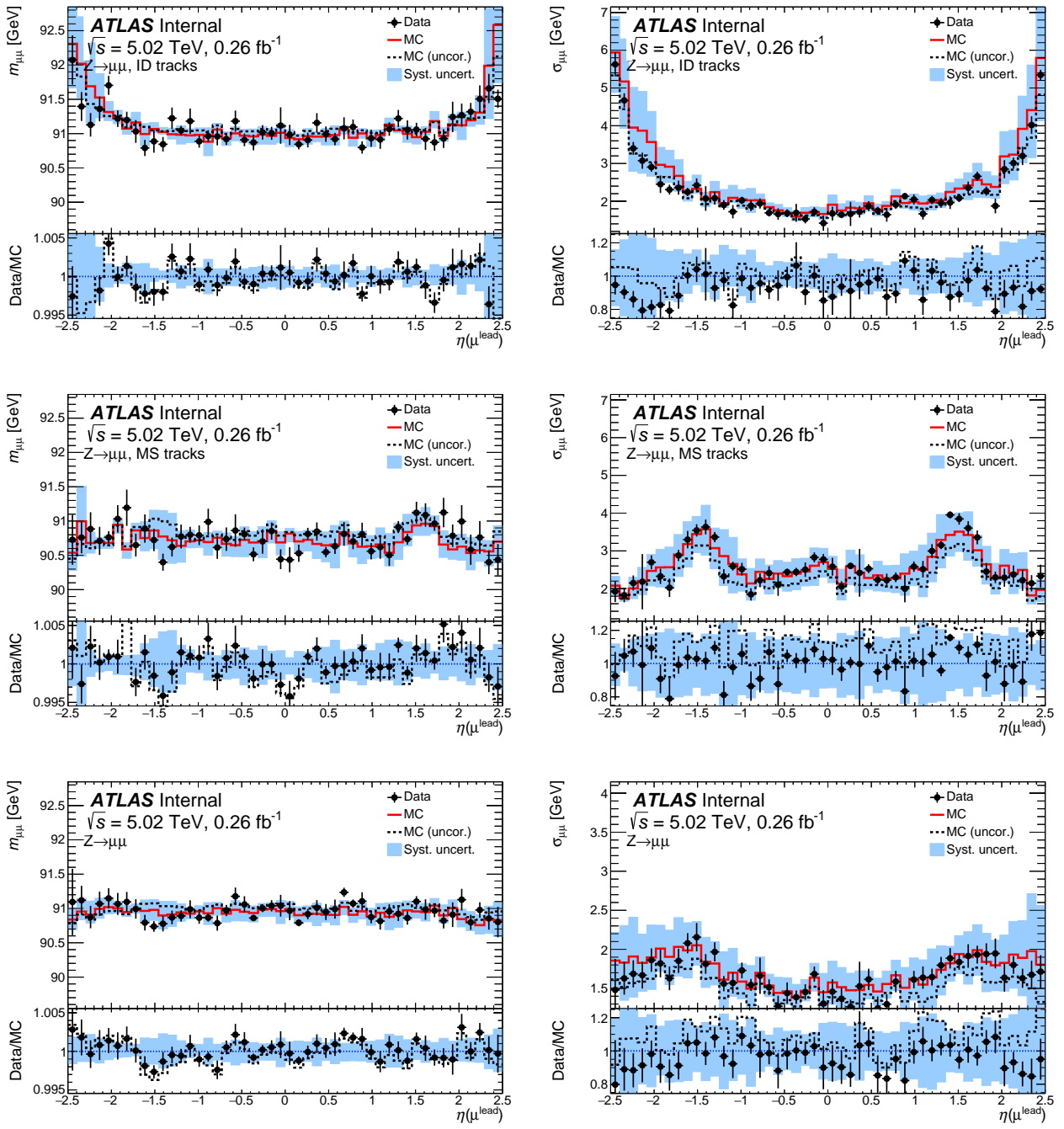


Figure 717: Mean (left) and width (right) of the $Z \rightarrow \mu\mu$ mass peak as a function of the leading muon η in 5.02 TeV data and MC. The mean and width are extracted from Crystal Ball components of the fits. In case of the simulation, both the uncorrected (dashed histogram) and corrected parameters (solid histogram) are shown. The fit results are presented for mass peaks constructed using kinematics of the muon ID tracks (top), ME tracks (middle) or CB tracks (bottom). The bottom panels in each plot show the data/MC ratio for uncorrected (dashed histogram) and corrected simulation (points).

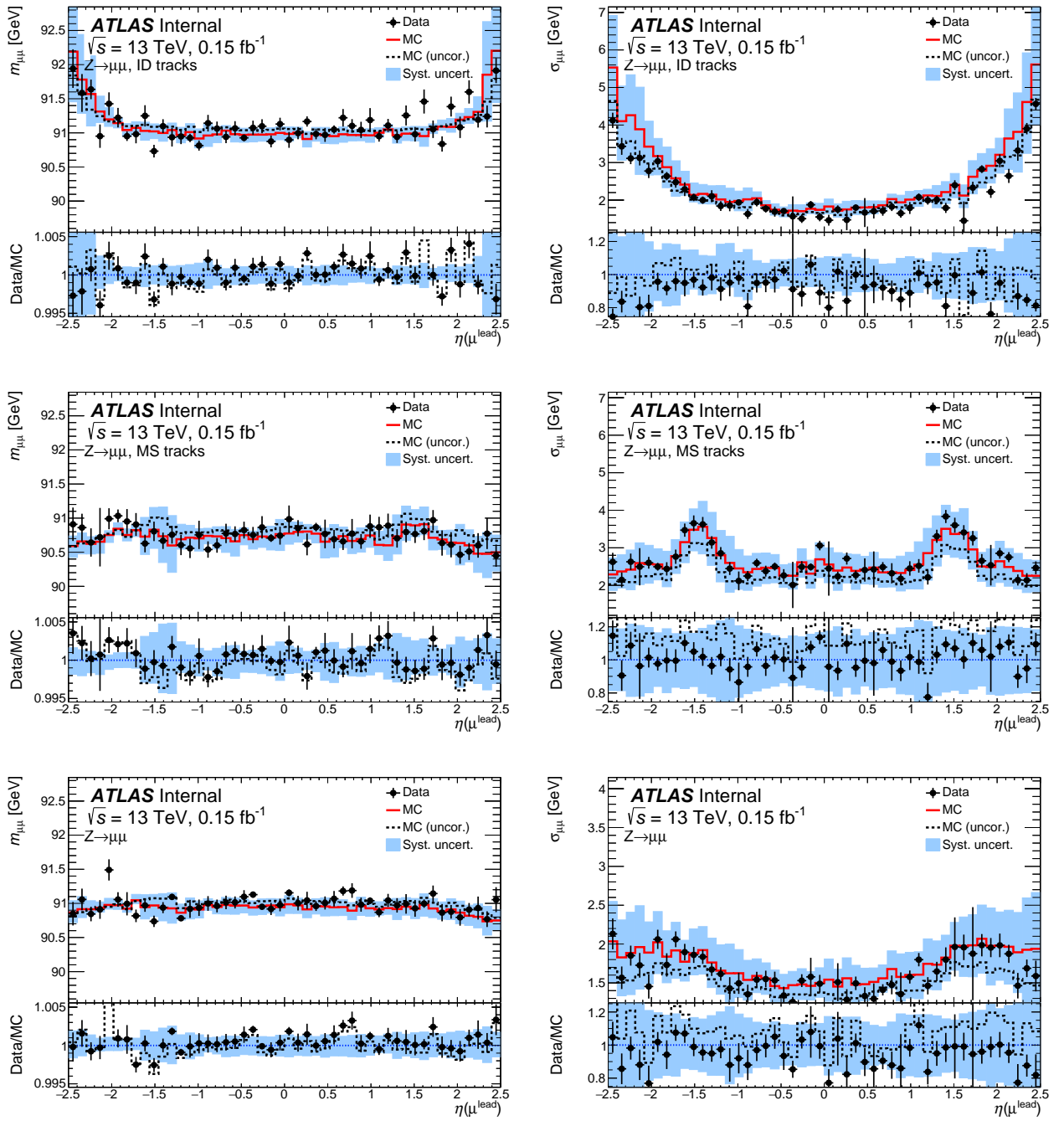


Figure 718: Mean (left) and width (right) of the $Z \rightarrow \mu\mu$ mass peak as a function of the leading muon η in 2017 13 TeV data and MC at low pile-up. The mean and width are extracted from Crystal Ball components of the fits. In case of the simulation, both the uncorrected (dashed histogram) and corrected parameters (solid histogram) are shown. The fit results are presented for mass peaks constructed using kinematics of the muon ID tracks (top), ME tracks (middle) or CB tracks (bottom). The bottom panels in each plot show the data/MC ratio for uncorrected (dashed histogram) and corrected simulation (points).

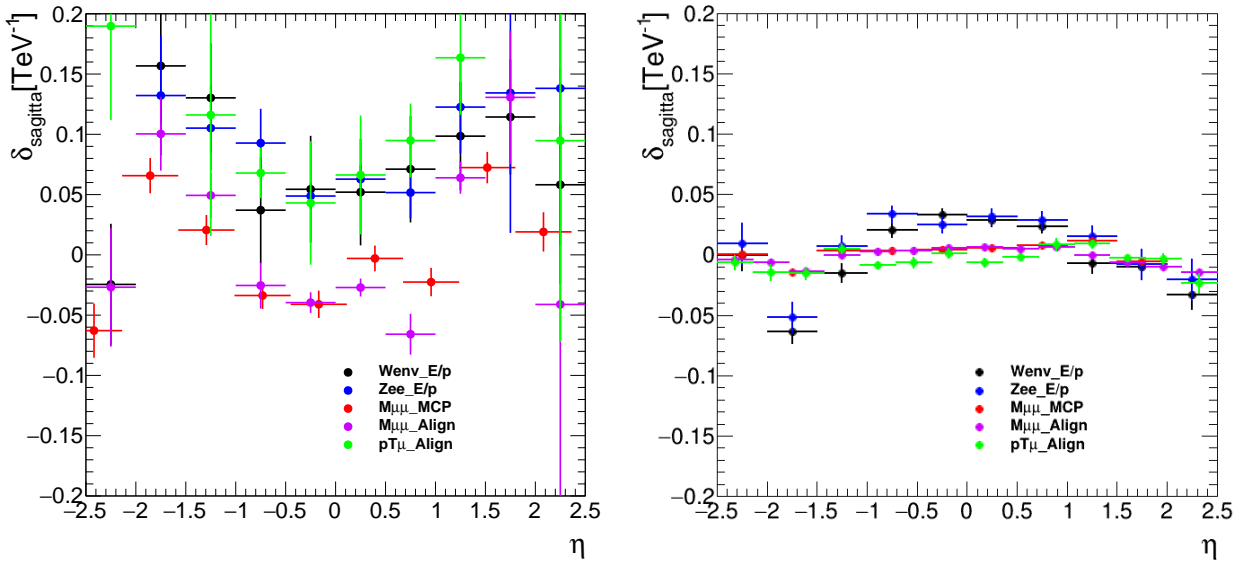


Figure 719: Sagitta bias corrections derived for 2017 low-pile-up data (left) and simulation (right) at $\sqrt{s} = 13$ TeV. The corrections are evaluated with two Z-mass methods (“ $M\mu\mu$ _MCP” and “ $M\mu\mu$ _Align”), the E/p method applied to $W \rightarrow e\nu$ (“Wenv_E/p”) and $Z \rightarrow ee$ (“Zee_E/p”) events, and the $p_T(\mu)$ method, all of which are discussed in the text. The top plot shows the data results, where clear η -dependent and overall biases are observed. The bottom plot shows MC, where a bias smaller by a factor of at least 10, with the exception of the electron E/p method.

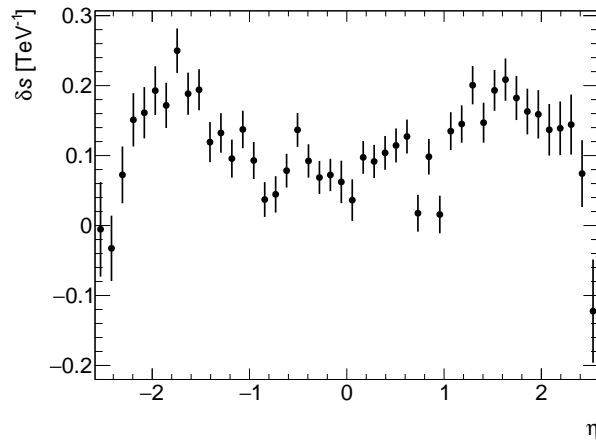


Figure 720: Sagitta bias correction based on 2017 low-pile-up data at $\sqrt{s} = 13$ TeV. The statistical uncertainty (combined from uncertainties of the η -dependent correction and the global offset correction) is represented by error bars.

2150 7.2.3 Muon efficiency measurements

2151 Just like in the case of electrons, muons have to pass a number of quality criteria in order to be used in
2152 the analysis:

- 2153 • Reconstruction and identification: the muon is successfully reconstructed and its ID and MS
2154 tracks as well as EMC deposit are matched. The *medium* identification criterion is adopted for the
2155 low- μ analysis. Only CB and ME muons with loose requirements between the tracks from ID and
2156 MS are used. The value of q/p significance is required to be < 7 .
- 2157 • Isolation: *LowMuWZPtvarcone20* selection was used, it has the track isolation requirement of
2158 $p_T^{varcone20}/p_T < 0.1$.
- 2159 • Trigger: the muons were required to pass the *HLT_mu14* trigger.
- 2160 • Track-to-vertex association (TTVA) includes requirement for the muon track to match the primary
2161 vertex. The muon objects are required to pass $|z_0| \sin \theta < 0.5$ mm and $d_0/\sigma(d_0) < 3$ requirements.

Just like in the case of electrons, possible discrepancies between the data and MC are corrected using the scale factors, which are in turn measured using the tag-and-probe method described in [10]. The product of the scale factors define the event weight:

$$W_{event}^{W \rightarrow ev} = SF_{reco/ID} \dot{SF}_{trig} \dot{SF}_{TTVA} \dot{SF}_{iso}.$$

2162 All muon efficiencies and scale factors used in current analysis are measured in-situ using the low- μ
2163 datasets at 5 and 13 TeV by the MCP group. The results for their measurements are presented in
2164 Figures

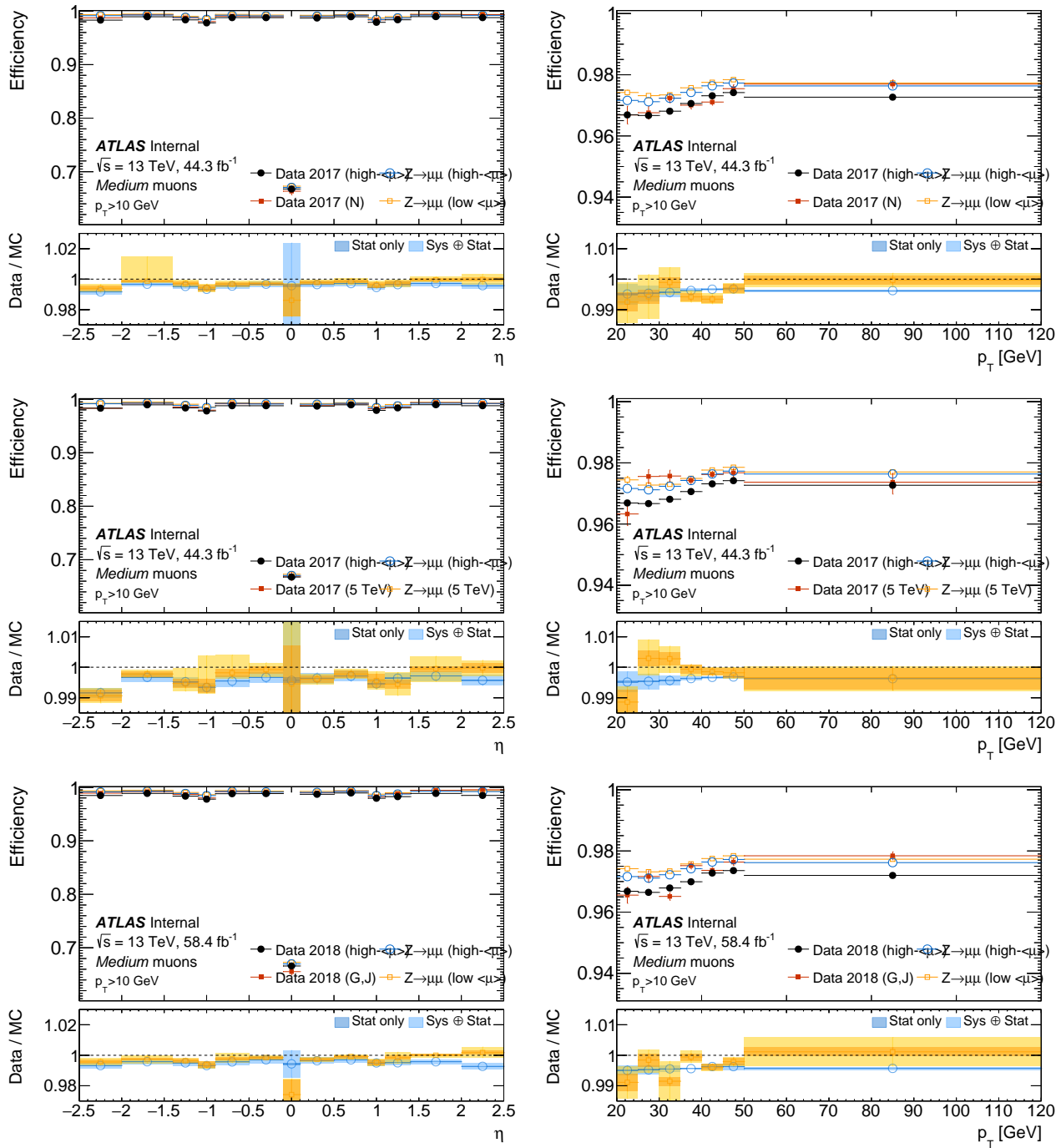


Figure 721: Comparison of reconstruction efficiencies for Medium muons using the low- μ runs of 2017 and 2018 at a centre-of-mass energy of $\sqrt{s} = 13 \text{ TeV}$ and $\sqrt{s} = 5 \text{ TeV}$. Efficiencies are shown as a function of muon η, p_T . Red (orange) points correspond to low- μ data (MC), while the black (blue) points are high- μ data (MC). The bottom panels show the data/MC ratio for the low- μ (orange) and high- μ (blue) sets with statistical and total uncertainties.

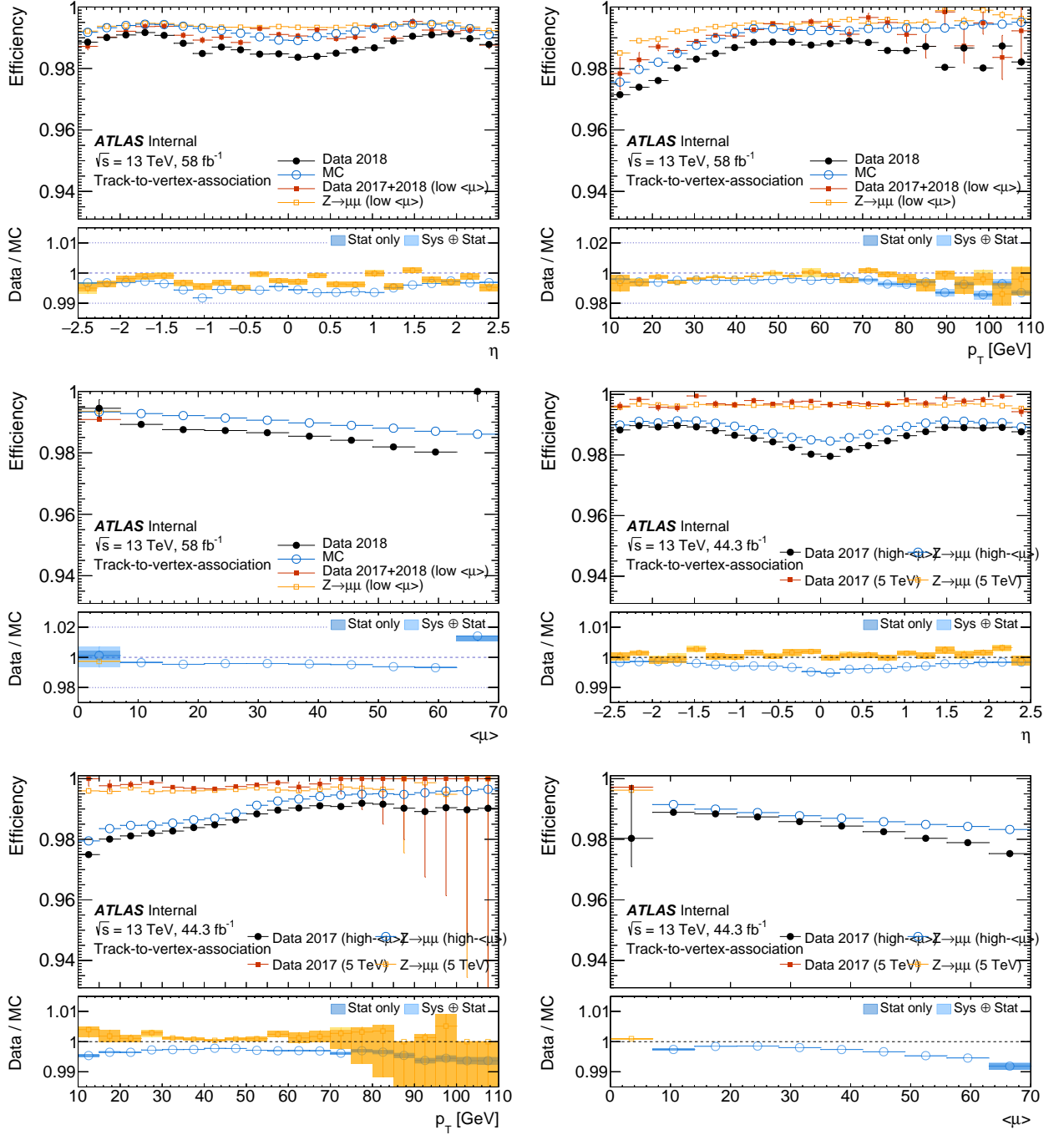


Figure 722: Comparison of TTVA efficiencies for Medium muons using the low- μ runs of 2017+18 at $\sqrt{s} = 13 \text{ TeV}$ (top row) and low- μ runs of 2017 at $\sqrt{s} = 5 \text{ TeV}$ (lower row). The low- μ results compared to a high- μ data set as specified in the plot legend. Efficiencies are shown as function of muon η (left) and p_T (middle) and the mean number of interactions $<\mu>$ (right). Red (orange) points correspond to low- μ data (MC), while the black (blue) points are high- μ data (MC). The bottom panels show the data/MC ratio for the low- μ (orange) and high- μ (blue) sets with statistical and total uncertainties.

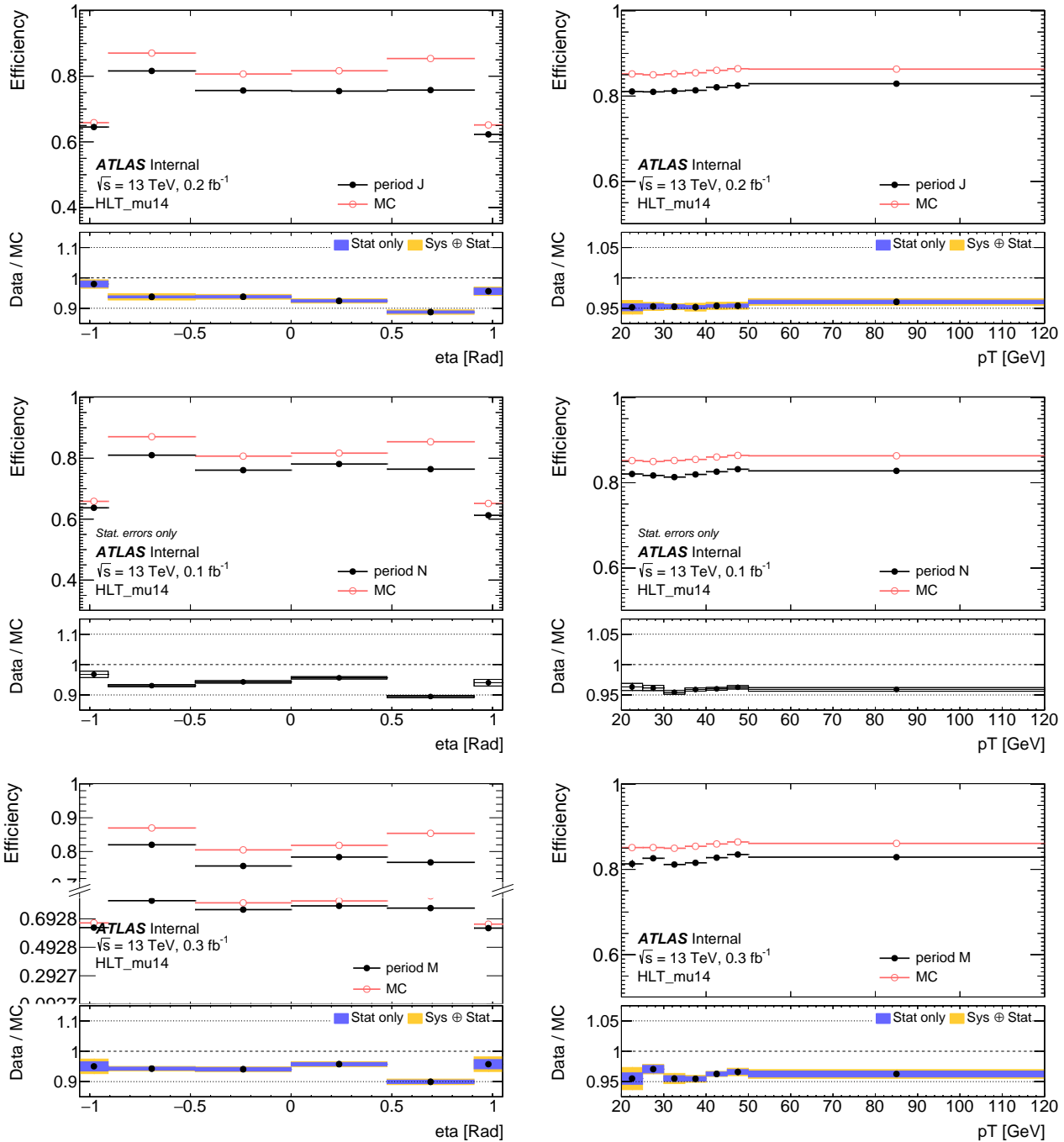


Figure 723: 1D trigger efficiency and systematic uncertainty in data and MC, 5 and 13 TeV from 2017 and 2018 for probes from the eta barrel region and inclusive ϕ, p_T distributions. Trigger sectors in the barrel and endcap regions are different, only the barrel trigger is shown here. The bin edges correspond to physical edges of the trigger sectors.

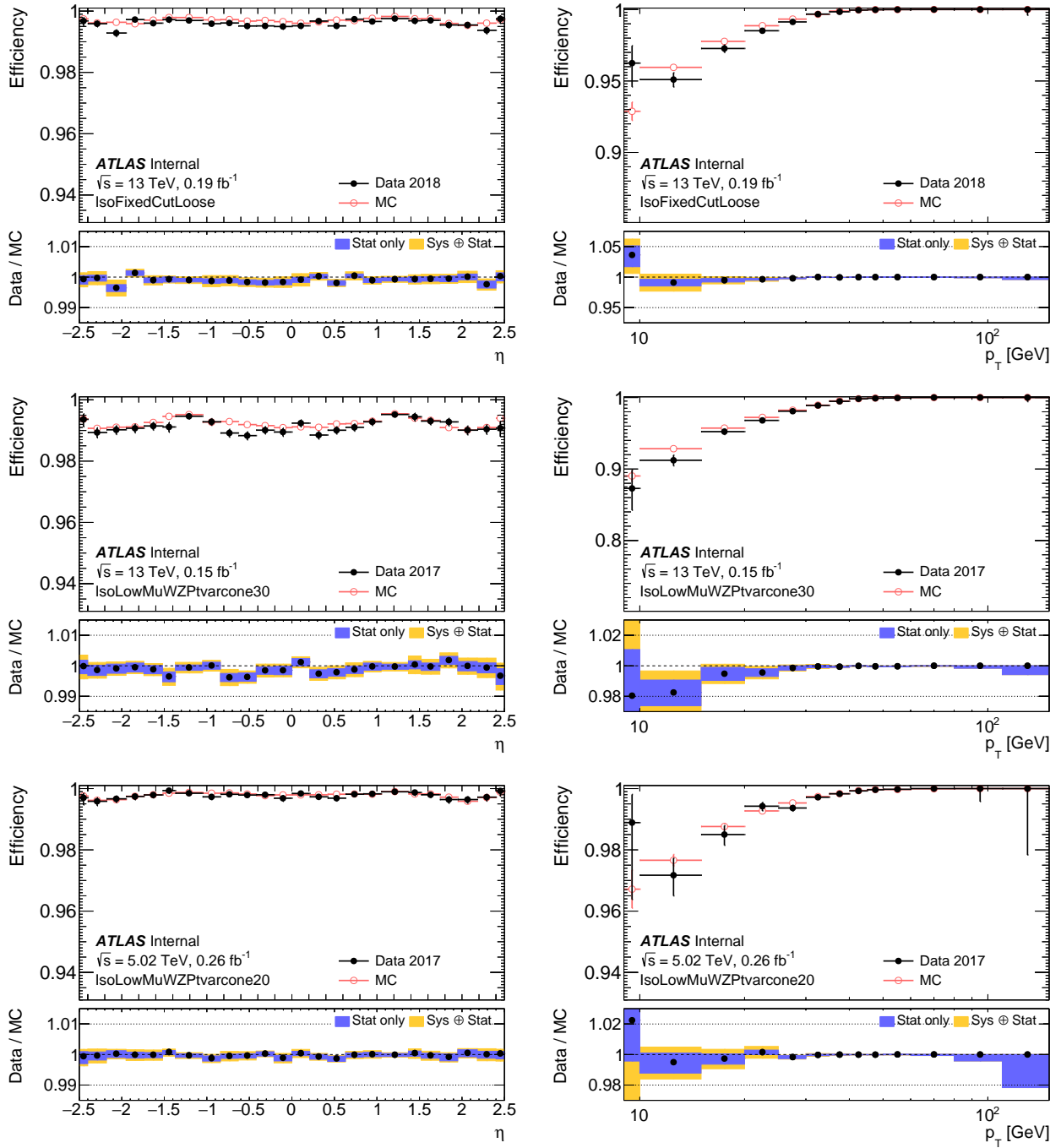


Figure 724: Efficiencies for Ptvarcone20 isolation selections measured in 2017 and 2018 data and MC 13 TeV and 5 TeV as a function of muon η (left) and p_T (right). The bottom panels show the data/MC scale factors with statistical uncertainties represented by blue boxes, while a sum in quadrature of statistical and systematic uncertainties is represented by orange boxes.

2165

7.3 Hadronic recoil calibration

2166 The study of the W boson kinematics by its leptonic decay products $W^\pm \rightarrow l^\pm \nu$ is complicated first
 2167 of all due to the escaping neutrino that carries away substantial information. However, the W boson
 2168 transverse momentum can still be measured. As it was shown in Chapter 5, the largest part of the W
 2169 boson p_T is coming from the initial state radiation. The energy of the created parton shower can be
 2170 measured:

$$p_T^V = p_T^\ell + p_T^\nu = - \sum_{i=\text{ISR } q,g} \vec{p}_{T,i} = -\vec{u}_T, \quad (7.4)$$

2171 where p_T^V , \vec{p}_T^ℓ and \vec{p}_T^ν are the transverse momenta of the vector boson, lepton and neutrino respectively.
 2172 The vector sum of all the partons from the ISR is called the *hadronic recoil*: $\sum_{i=\text{ISR } q,g} \vec{p}_{T,i} = \vec{u}_T$. Then the
 2173 missing transverse momentum E_T^{miss} of the escaping neutrino can be measured as:

$$E_T^{\text{miss}} = \vec{p}_T^\nu = -(\vec{u}_T + \vec{p}_T^\ell). \quad (7.5)$$

2174 The Hadronic Recoil (HR) reconstruction uses the Particle Flow Objects (PFO), which were defined
 2175 and described in Section 6.5. It is important to exclude lepton(s) from the HR of a W(Z) event to
 2176 avoid double counting. A cone of $\Delta R < 0.2$ is removed around the lepton(s) and is replaced by the
 2177 same-size cone in the same η and ϕ region, but $\Delta R > 0.4$ away from any lepton. Only the leptons above
 2178 $p_T > 10\text{GeV}$ and passing fiducial cuts in η and ID requirements are removed from the HR.

2179 Another important quantity for the HR is the $\sum E_T$ - a scalar sum of the transverse energies of all
 2180 the PFO. The $\sum E_T$ represents the total event activity, there is a relation between the $\sum E_T$ magnitude
 2181 and u_T resolution. The underlying event activity, pile-up and soft emissions can be characterized
 2182 by introducing another quantity: $\sum \tilde{E}_T = \sum E_T - u_T$, which has the meaning of $\sum E_T$ with hard activity
 2183 subtracted.

2184 For the calibration of the HR it is better to introduce quantities that are defined in a natural physical
 2185 way. The vector boson transverse momentum provides a natural axis which is convenient to use for the
 2186 2-component decomposition of the u_T vector. The u_T component parallel to the vector boson p_T :

$$u_{||} = \frac{\vec{p}_T^V \cdot \vec{u}_T}{p_T^V}, \quad (7.6)$$

2187 and a perpendicular component:

$$u_{\perp} = \frac{|\vec{p}_T^V \times \vec{u}_T|}{p_T^V}. \quad (7.7)$$

2188 Ideally we would like to have $u_{||} = 1$ and $u_{\perp} = 0$, but due to detector effects it is never the case. The
 2189 perpendicular component u_{\perp} can be thought of as the HR resolution, while $u_{||}$ has a physical meaning
 2190 of the recoil scale. Another important quantity is called the *bias*:

$$b = u_{||} + p_T^V, \quad (7.8)$$

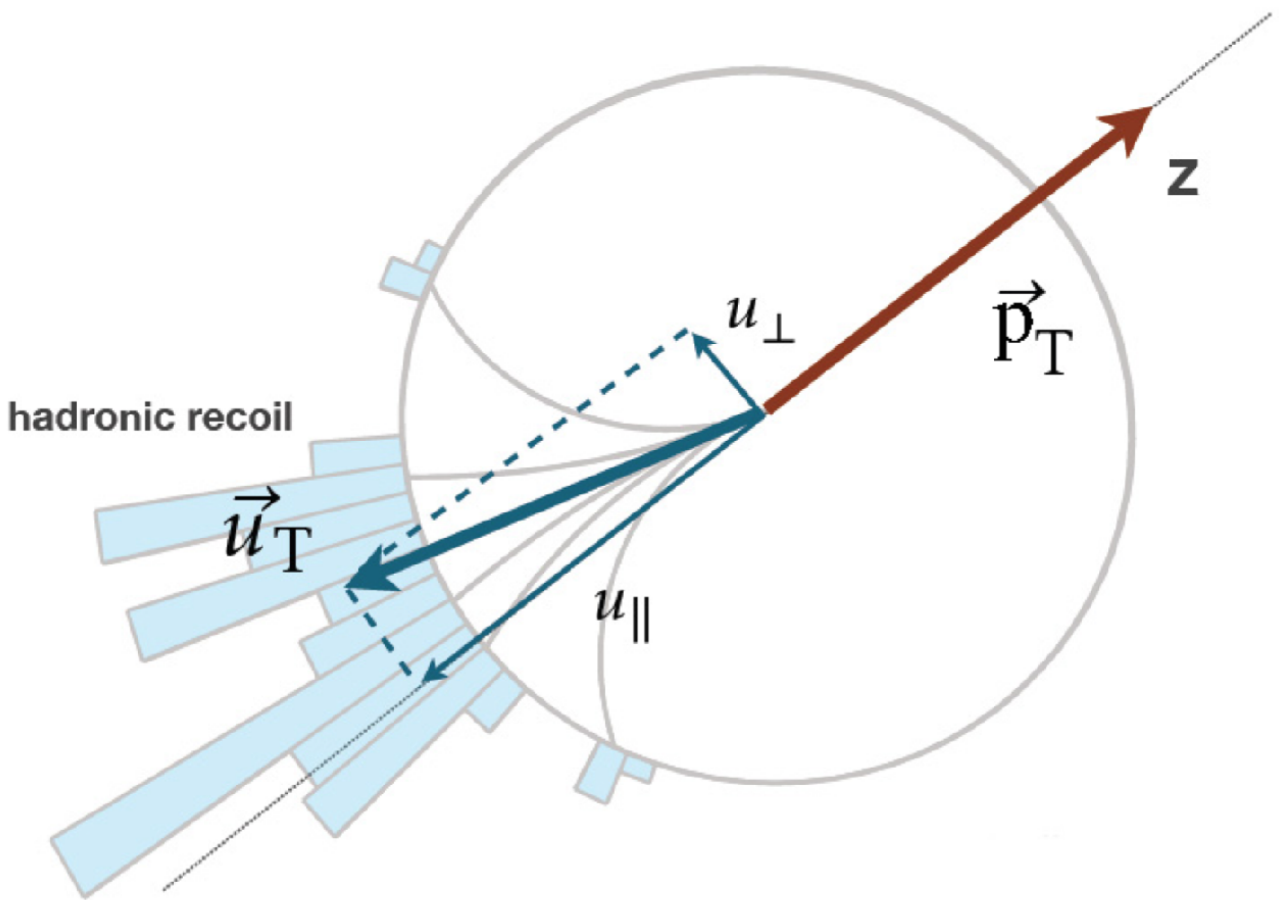


Figure 725: The hadronic recoil vector in the transverse plane and its components with respect to vector boson p_T .

which is expected to be centered around zero. In data, of course, we don't know the p_T^V of the truth boson. However, in Z decay events we can use the dilepton transverse momentum $p_T^{\ell\ell}$ as an axis for u_{\perp} and u_{\parallel} decomposition - considering the u_T resolution the difference between p_T^V and $p_T^{\ell\ell}$ is negligible. In W data events it is only possible to use p_T^l for u_T decomposition.

7.3.1 SET and u_T reweighting

Despite the fact that the two electroweak bosons, W and Z, share lot of similarities, there are also small but notable differences in valence quark content and PDFs, energy scale, etc. This leads to differences in underlying event and p_T^V spectra, which manifest themselves in the observables like ΣE_T , $\Sigma \bar{E}_T$, u_T . For the high-precision measurements it is important to ensure that these quantities as well as their correlations are modelled properly. It is also important to match these correlations in data and MC simulations. Figure 726 demonstrates that the baseline PowHEGMC simulations lead to a significant mismodelling of the $\Sigma \bar{E}_T$ - p_T^V correlation, while SHERPA shows much better agreement with the data

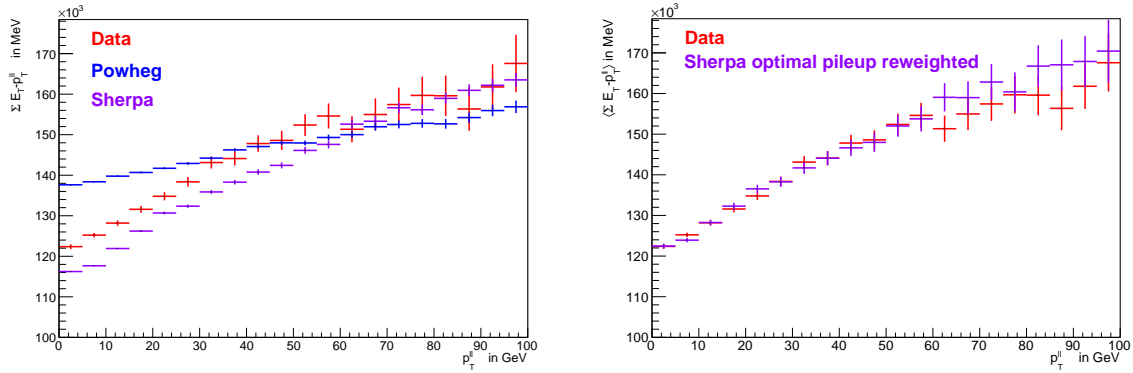


Figure 726: Comparison of the $\Sigma E_T - p_T^{\ell\ell}$ description in data of the two MC samples Powheg and SHERPA at 13 TeV, showing $\Sigma E_T - p_T^{\ell\ell}$ inclusively (left). Figure on the right shows the comparison of SHERPA to the data after a dedicated pileup reweighting.

from the very beginning. After applying a special pile-up reweighting of SHERPA samples a very good agreement with the data is achieved.

In order to obtain proper distributions in the MC samples, a three-step reweighting procedure is implemented.

First weight is obtained by from the 2D $\Sigma \bar{E}_T - p_T^V$ distributions ratio in Data and MC:

$$w_{2D}^Z(\Sigma \bar{E}_T, p_T^{\ell\ell}) = \frac{h^{\text{data}, Z}(\Sigma \bar{E}_T, p_T^{\ell\ell})}{h^{\text{MC}, Z}(\Sigma \bar{E}_T, p_T^{\ell\ell})}, \quad (7.9)$$

where the following binning is used:

$$\bullet p_T^{\ell\ell} (13 \text{ TeV}) = [0, 2, 3, 4, 5, 6, 7, 8, 9, 10, 12, 16, 20, 25, 30, 40, 50, 55, 65, 80, 100, 200, \infty] \text{ GeV}$$

$$\bullet p_T^{\ell\ell} (5 \text{ TeV}) = [0, 2, 3, 4, 5, 6, 7, 8, 9, 10, 12, 16, 20, 25, 27, 30, 40, 45, 50, 60, 70, 100, 200, \infty] \text{ GeV}$$

$$\bullet \Sigma \bar{E}_T (13 \text{ TeV}) = [0, 10, 20, 30, \dots, 380, \infty] \text{ GeV}$$

$$\bullet \Sigma \bar{E}_T (5 \text{ TeV}) = [0, 10, 20, 30, \dots, 280, \infty] \text{ GeV}$$

This reweighting is obtained from the $Z \rightarrow \mu\mu$ events for 5 and 13 TeV datasets and applied to both W and Z Monte-Carlo samples. In W events the p_T^V is used instead of $p_T^{\ell\ell}$ for obvious reasons. This reweighting assures very good agreement for the Z events, but perfect agreement is not guaranteed for the W events. For this reason a second reweighting is derived from the data: $\Sigma \bar{E}_T$ weight is extracted in bins of u_T of 4 GeV width and applied to W MC events on top of the first 2D reweighting:

$$w_{j, \text{sliced}}^{W^\pm}(\Sigma \bar{E}_T) = \frac{h_j^{\text{data}, W^\pm}(\Sigma \bar{E}_T)}{h_j^{\text{MC}, W^\pm, \text{Z2Dmod}}(\Sigma \bar{E}_T)}, \quad (7.10)$$

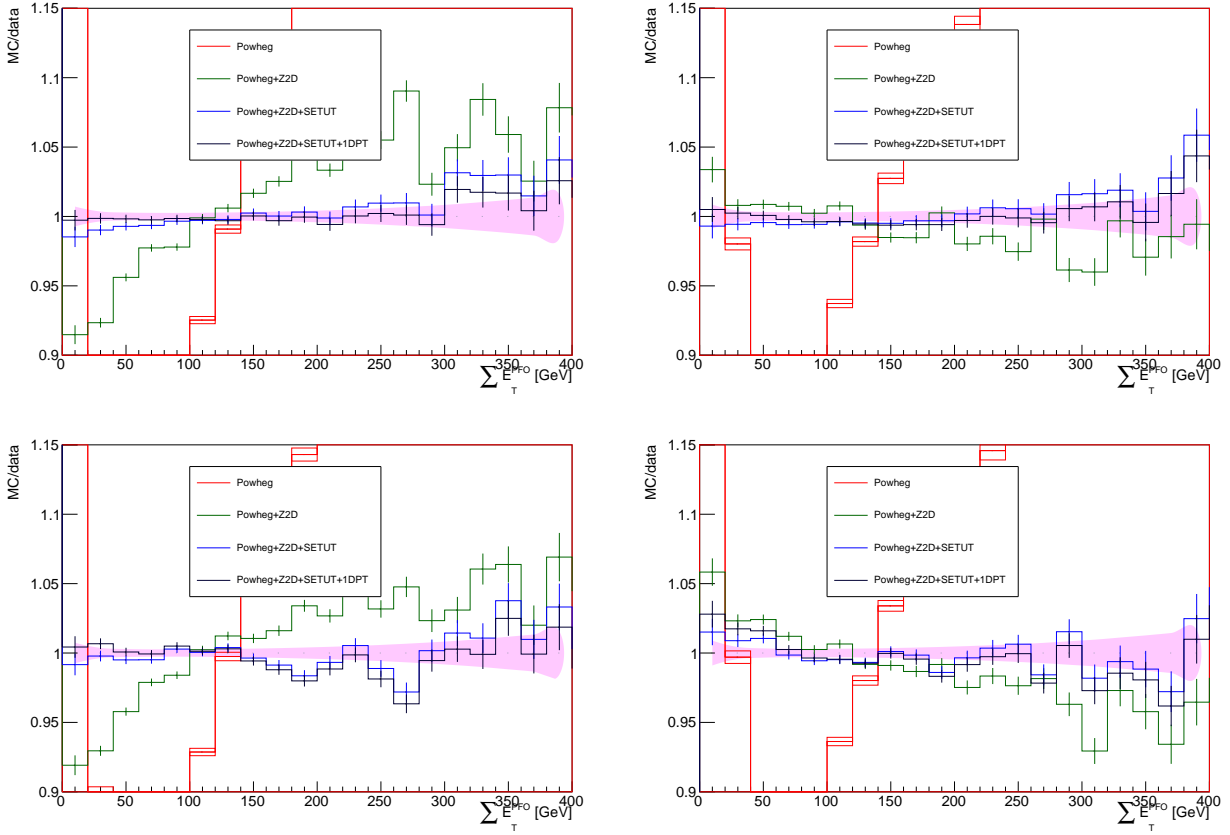


Figure 727: Ratio of data to predictions in $W \rightarrow \mu\nu$ events at 13 TeV for the $\Sigma\bar{E}_T$ distribution, before and after each $\Sigma\bar{E}_T$ modeling reweighting step. The color band is the data statistical uncertainty. The prediction uncertainty only includes the statistical uncertainty. 'Powheg' uses the baseline MC for the signal. 'Powheg+Z2D' has the 2D ($\Sigma\bar{E}_T, p_T^{true,V}$), Z-based reweighting applied. 'Powheg+Z2D+SETUT' adds the $\Sigma\bar{E}_T$ reweighting in bins of u_T . 'Powheg+Z2D+SETUT+1DPT' adds the 1D reweighting to recover the initial $p_T^{true,V}$ spectrum.

2218 where h_j stands for the normalized $\Sigma\bar{E}_T$ distribution in the u_T bin number j after the standard selection.
 2219 This reweighting improves the $\Sigma\bar{E}_T$ modelling, but distorts the p_T^V spectrum. This motivates the third
 2220 correction reweighting with the following weight:

$$w_{1D}^{W^\pm}(p_T^{true,V}) = \frac{h^{\text{MC}, W^\pm, \text{mod}}(p_T^{true,V})}{h^{\text{MC}, W^\pm, \text{orig}}(p_T^{true,V})}. \quad (7.11)$$

2221 The $h^{\text{MC}, W^\pm, \text{orig}}(p_T^{true,V})$ stands for the original $p_T^{true,V}$ spectrum before any reweightings were applied.
 2222 The total weight applied to an event is the product of the three weights described above: $w_{2D}^Z(\Sigma\bar{E}_T, p_T^{true,V}) \times$
 2223 $w_{j,\text{sliced}}^{W^\pm}(\Sigma\bar{E}_T) \times w_{1D}^{W^\pm}(p_T^{true,V})$. The results on the reweighting are shown in Figures 727 and 728 for 13
 2224 and 5 TeV respectively.

2225

2226 The closure of the procedure is checked with **SHERPA**MC simulation used as pseudo-data, as we

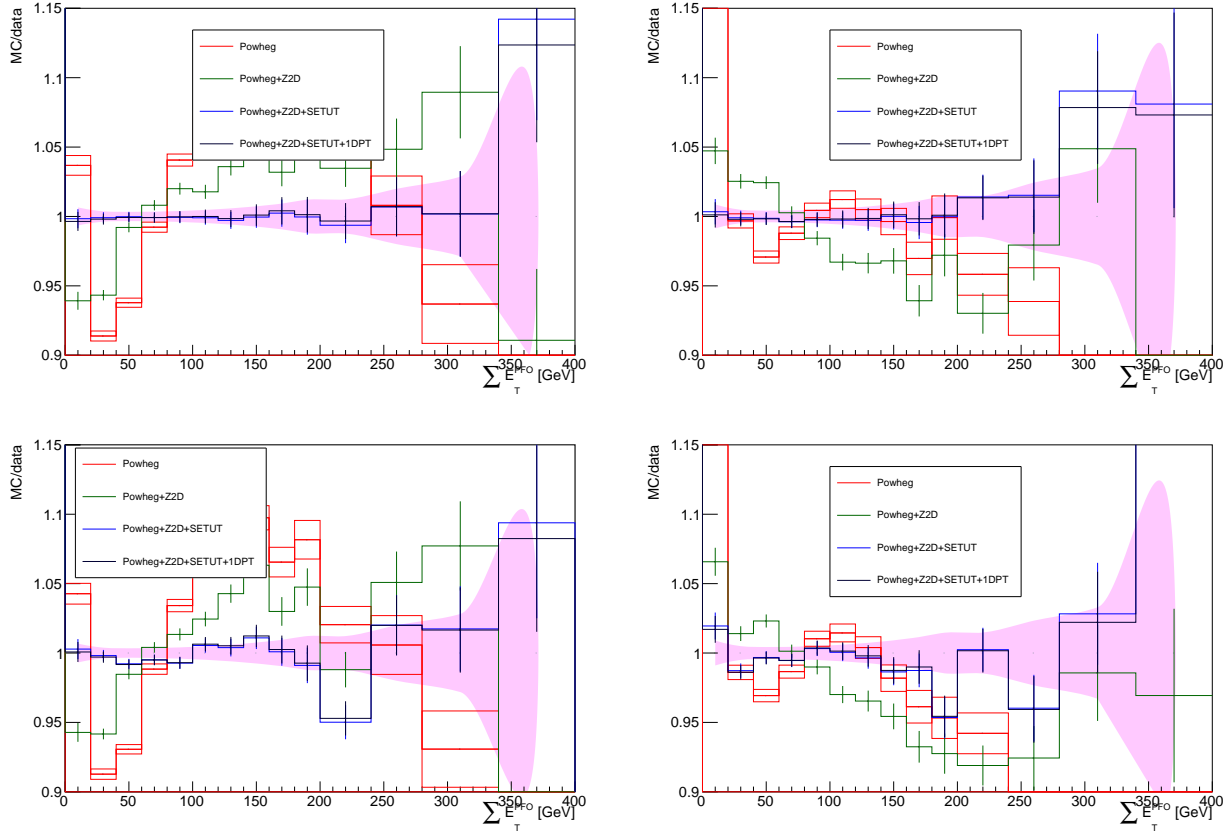


Figure 728: Ratio of data to predictions in $W \rightarrow \mu\nu$ events at 5 TeV for the $\Sigma\bar{E}_T$ distribution, before and after each $\Sigma\bar{E}_T$ modeling reweighting step. The color band is the data statistical uncertainty. The prediction uncertainty only includes the statistical uncertainty. 'Powheg' uses the baseline MC for the signal. 'Powheg+Z2D' has the 2D ($\Sigma\bar{E}_T$, $p_T^{true,V}$), Z-based reweighting applied. 'Powheg+Z2D+SETUT' adds the $\Sigma\bar{E}_T$ reweighting in bins of u_T . 'Powheg+Z2D+SETUT+1DPT' adds the 1D reweighting to recover the initial $p_T^{true,V}$ spectrum.

don't have the p_T^V distribution from the data. The residual non-closure of less than 1% is treated as a systematic uncertainty.

7.3.2 u_X and u_Y correction

Azimuthal angle distribution is another discrepancy between the MC simulation and the data. While the simulated events have a flat ϕ distribution, the data events show a non-uniform distribution which is probably caused by detector imperfections or ageing. The correction is performed by introducing additive corrections to the u_X and u_Y components of the HR. The corrections are derived as a mean difference between the data and MC as a function of $\Sigma\bar{E}_T$:

$$\begin{aligned} u_X^{\text{MC,corr}} &= u_X^{\text{MC}} + [(\langle u_X^{\text{data}} \rangle - \langle u_X^{\text{MC}} \rangle)(\Sigma\bar{E}_T)] \\ u_Y^{\text{MC,corr}} &= u_Y^{\text{MC}} + [(\langle u_Y^{\text{data}} \rangle - \langle u_Y^{\text{MC}} \rangle)(\Sigma\bar{E}_T)] \end{aligned} \quad (7.12)$$

2235 The dependence of the mean differences $\langle u_X^{\text{data}} \rangle - \langle u_X^{\text{MC}} \rangle$ and $\langle u_Y^{\text{data}} \rangle - \langle u_Y^{\text{MC}} \rangle$ on $\Sigma\bar{E}_T$ is fitted with a linear
 2236 function. The corrected ϕ distributions are shown in Figure 729. It was shown that the correlation
 2237 between the correction and the magnitude of the recoil is weak and the effect of the correction on
 2238 the measured W spectrum is of per mille level. For this reason no uncertainty was assigned to this
 2239 correction.

2240 7.3.3 Resolution and response corrections

2241 The correction function for $\sigma(u_{\perp})(\Sigma\bar{E}_T, p_T^{\ell\ell})$ is constructed in bins of $p_T^{\ell\ell}$ in the following way:

$$r(\Sigma\bar{E}_T, p_T^{\ell\ell}) = \frac{\sigma(u_{\perp})^{\text{data}}}{\sigma(u_{\perp})^{\text{MC}}}, \quad (7.13)$$

2242 where both $\sigma(u_{\perp})$ functions are obtained as a linear fit to $\sqrt{\Sigma\bar{E}_T}$:

$$\sigma(u_{\perp})(\Sigma\bar{E}_T) = c + d \cdot \sqrt{\Sigma\bar{E}_T}. \quad (7.14)$$

2243 with the following $p_T^{\ell\ell}$ binning:

- 2244 • 5 TeV: $p_T^{\ell\ell} = [0, 3, 4, 6, 7, 9, 11, 13, 16, 20, 26, 40, \infty] \text{ GeV}$
- 2245 • 13 TeV is $p_T^{\ell\ell} = [0, 3, 4, 6, 7, 9, 10, 12, 14, 17, 21, 26, 33, 49, \infty] \text{ GeV}$

2246 Then the correction for the W boson events is performed using the ratio function as a factor:

$$u_{\perp}^{\text{MC,corr}} = u_{\perp}^{\text{MC}} \times r(\Sigma\bar{E}_T, p_T^{\text{true}, V}). \quad (7.15)$$

2247 The correction of the parallel component u_{\parallel} is done as follows:

$$u_{\parallel}^{\text{MC,corr}} = \langle u_{\parallel}^{\text{data}} \rangle + (\langle b^{\text{data}} \rangle - \langle b^{\text{MC}} \rangle) \cdot r_{\parallel} + (u_{\parallel}^{\text{MC}} - \langle u_{\parallel}^{\text{data}} \rangle) \cdot r_{\parallel}. \quad (7.16)$$

2248 Here the resolution correction factor r_{\parallel} is in equation 7.13, but reads as $\sigma(u_{\parallel})^{\text{data}} / \sigma(u_{\perp})^{\text{MC}}$.
 2249 The average $\langle u_{\parallel}^{\text{data}} \rangle$ assumes averaging over all data events in bins of $p_T^{\ell\ell}$ and $\Sigma\bar{E}_T$. The $\Sigma\bar{E}_T$ bins are
 2250 10GeV wide for 5TeV and 20GeV wide for 13TeV. The in each $\Sigma\bar{E}_T$ bin the $p_T^{\ell\ell}$ dependence is fitted with
 2251 a linear function:

$$\langle u_{\parallel}^{\text{data}} \rangle(p_T^{\ell\ell}) = e + f \cdot p_T^{\ell\ell}. \quad (7.17)$$

2252 Similarly the difference of the biases $(\langle b^{\text{data}} \rangle - \langle b^{\text{MC}} \rangle)$ is computed in the same bins of $p_T^{\ell\ell}$ and $\Sigma\bar{E}_T$ and
 2253 fitted in each $\Sigma\bar{E}_T$ bin with a linear function of $p_T^{\ell\ell}$.

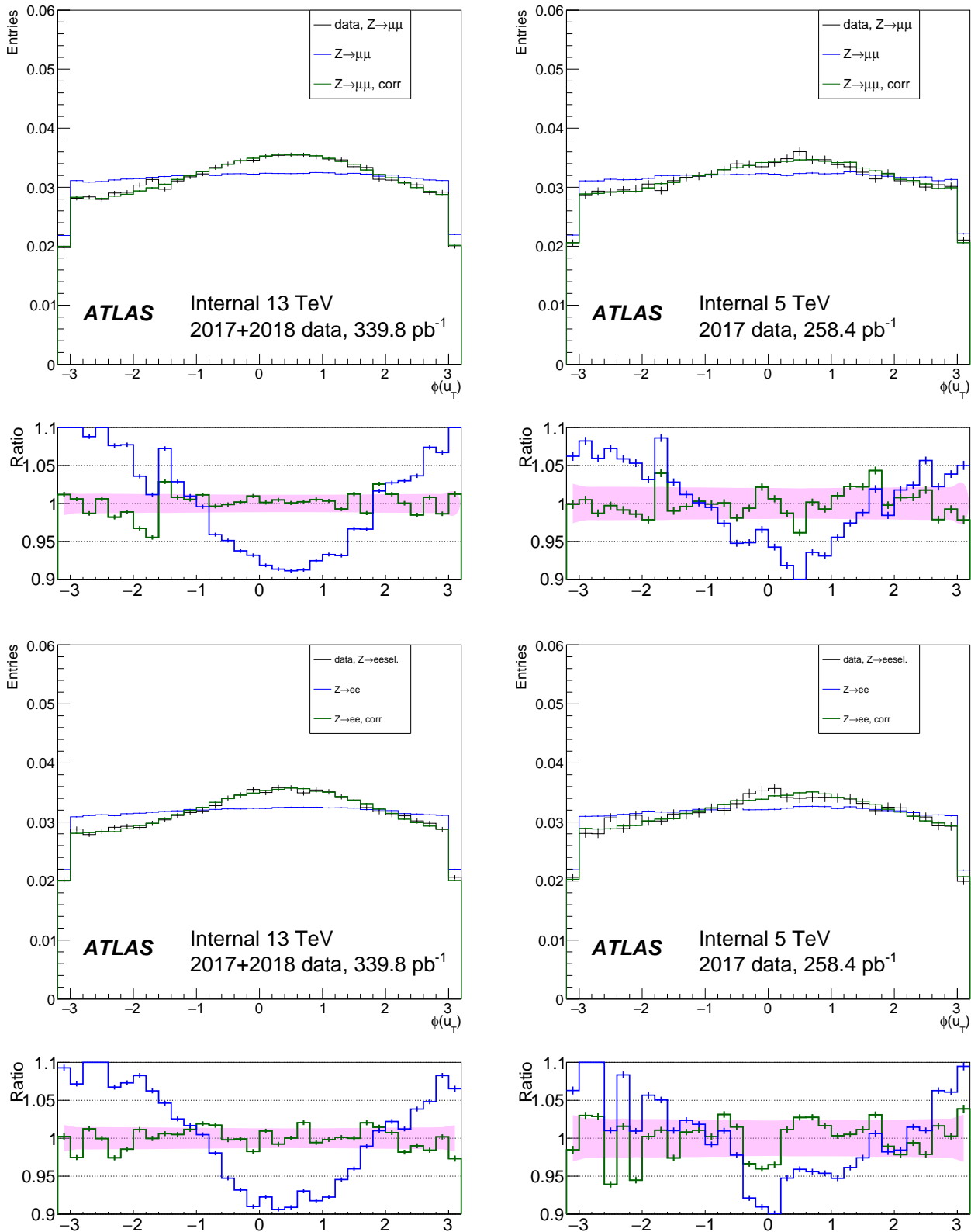


Figure 729: $\phi(u_T)$ at 5 and 13 TeV, for the data and the simulation before and after u_X and u_Y correction, in Z events. The band in the ratio panel is the data statistical uncertainty.

2254 **7.4 Angular coefficients correction**

2255 to be clarified a bit

2256 **Bibliography**

- 2257 [1] Jan Kretzschmar. *Samples and Physics modelling for low pile-up runs taken in 2017 and 2018.*
2258 Tech. rep. ATL-COM-PHYS-2019-075. Geneva: CERN, Feb. 2019. URL: <https://cds.cern.ch/record/2657141>.
- 2260 [2] Morad Aaboud et al. “Electron and photon energy calibration with the ATLAS detector using
2261 2015–2016 LHC proton-proton collision data”. In: *JINST* 14.03 (2019), P03017. doi: 10.1088/
2262 1748-0221/14/03/P03017. arXiv: 1812.03848 [hep-ex].
- 2263 [3] ATLAS Collaboration. “Electron and photon energy calibration with the ATLAS detector using
2264 2015–2016 LHC proton–proton collision data”. In: *JINST* 14 (2019), P03017. doi: 10.1088/1748-
2265 0221/14/03/P03017. arXiv: 1812.03848 [hep-ex].
- 2266 [4] “Electron and photon performance measurements with the ATLAS detector using the 2015–2017
2267 LHC proton-proton collision data”. In: *JINST* 14. arXiv:1908.00005. 12 (Aug. 2019). 31 figures,
2268 3 tables. All figures including auxiliary figures are available at <https://atlas.web.cern.ch/Atlas/GROUPS/PHYSICS/PAPERS/EGAM-2018-01>, P12006. 70 p. doi: 10.1088/1748-0221/14/
2269 12/P12006. URL: <https://cds.cern.ch/record/2684552>.
- 2271 [5] ATLAS Collaboration. “Electron and photon energy calibration with the ATLAS detector using
2272 LHC Run 1 data”. In: *Eur. Phys. J. C* 74 (2014), p. 3071. doi: 10.1140/epjc/s10052-014-3071-4.
2273 arXiv: 1407.5063 [hep-ex].
- 2274 [6] Nansi Andari et al. *Electron and photon energy calibration with the ATLAS detector using 2015–2017*
2275 *LHC proton-proton collision data*. Tech. rep. ATL-COM-PHYS-2018-1720. Geneva: CERN, 2018.
2276 URL: <https://cds.cern.ch/record/2651890>.
- 2277 [7] Morad Aaboud et al. “Electron reconstruction and identification in the ATLAS experiment using
2278 the 2015 and 2016 LHC proton-proton collision data at $\sqrt{s} = 13$ TeV”. In: *Eur. Phys. J. C* 79.8
2279 (2019), p. 639. doi: 10.1140/epjc/s10052-019-7140-6. arXiv: 1902.04655 [physics.ins-det].
- 2281 [8] Georges Aad et al. “Electron and photon performance measurements with the ATLAS detector
2282 using the 2015–2017 LHC proton-proton collision data”. In: *JINST* 14.12 (2019), P12006. doi:
2283 10.1088/1748-0221/14/12/P12006. arXiv: 1908.00005 [hep-ex].
- 2284 [9] *Study of alignment-related systematic effects on the ATLAS Inner Detector tracking*. Tech. rep. ATLAS-
2285 CONF-2012-141. Geneva: CERN, Oct. 2012. URL: <https://cds.cern.ch/record/1483518>.
- 2286 [10] Nicolas Maximilian Koehler et al. *Muon Efficiency Measurements on the Full Run 2 dataset*. Tech.
2287 rep. ATL-COM-PHYS-2019-176. Geneva: CERN, Mar. 2019. URL: <https://cds.cern.ch/record/2665704>.

8

MC samples and selection

“Potentielle citation sans aucun rapport avec le sujet”

— Personne inconnue, contexte à déterminer

8.1 Data and MC samples

The data and MC samples for this study were collected under special beam conditions that ensure low pile-up. The data samples were collected in three runs:

- $\sqrt{s} = 5.02\text{TeV}$ data taken in November 2017, ATLAS data period M, preliminary calibrated luminosity 256.827 pb^{-1} with an uncertainty of $\pm 1.6\%$
- $\sqrt{s} = 13\text{TeV}$ data taken in November 2017, ATLAS data period N, preliminary online luminosity 146.6 pb^{-1}
- $\sqrt{s} = 13\text{TeV}$ data taken in June 2018, ATLAS data period G4+J, preliminary online luminosity 193.2 pb^{-1}

The runs of November 2017 and the run of June 2018 had the same bunch spacing of 25 ns, but a different filling scheme. The two main differences from the high- μ data collection are the following:

- In order to optimize topo-cluster response for the HR lower topo-cluster thresholds were used.
- Single e and μ triggers with significantly lower thresholds and looser identification criteria are run without prescale, most notably `HLT_e15_1hloose_nod0_L1EM12` and `HLT_mu14`.

At the beginning of 5 TeV fills the pile-up reached $\mu/5$, slowly descending to $\mu/1$ by the end of the run. In the case of 13 TeV the luminosity was levelled at $\mu = 2$ in the course of the run. The corresponding distributions for μ and N_{PV} for the 5 TeV and 13 TeV runs are shown in Fig. 81 and Fig. 82.

8.1.1 MC samples and cross-sections

Signal and background processes are modelled using fully simulated and reconstructed using MC samples, specifically tuned for the special run conditions, namely the pileup conditions, lower topo-cluster noise thresholds and adapter trigger menu. No pileup reweighting is performed.

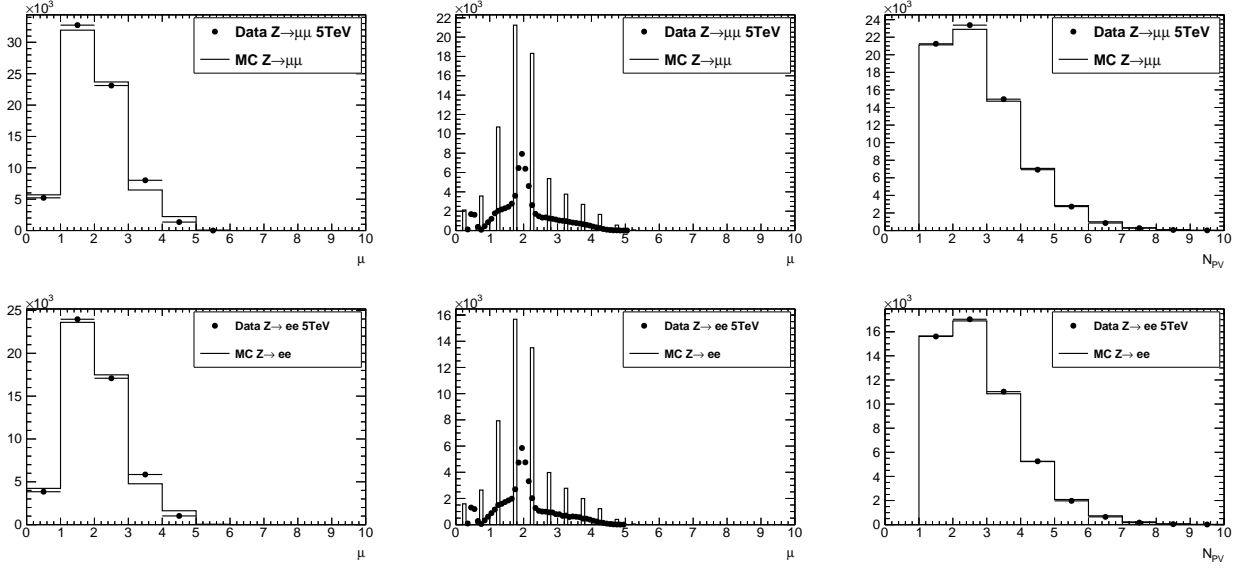


Figure 81: Distributions for the 5 TeV low- μ dataset in a $Z/\gamma^* \rightarrow \mu\mu$ (top row) and a $Z/\gamma^* \rightarrow ee$ (bottom row) selection. The data (points) is compared to $Z/\gamma^* \rightarrow \mu\mu$ or $Z/\gamma^* \rightarrow ee$ signal MC, respectively. The left and middle plots show the actual μ in a coarsely-binned and a finely-binned version. The right plot shows the number of reconstructed primary vertices N_{PV} .

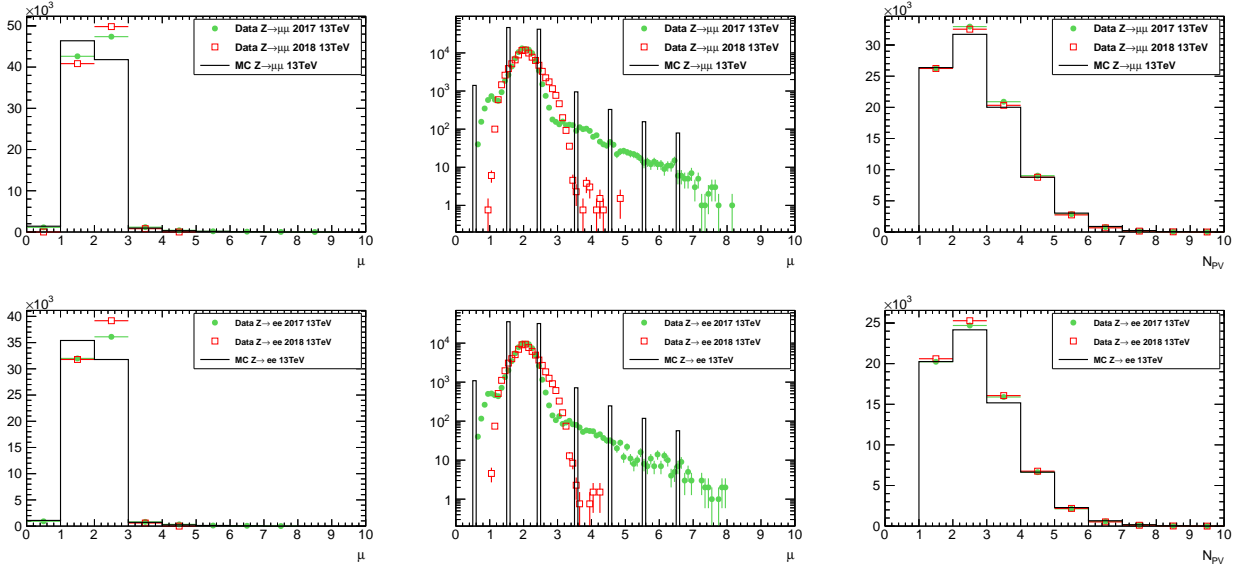


Figure 82: Distributions for the 13 TeV low- μ datasets taken in 2017 and 2018 in a $Z/\gamma^* \rightarrow \mu\mu$ (top row) and a $Z/\gamma^* \rightarrow ee$ (bottom row) selection. The data (points) is compared to $Z/\gamma^* \rightarrow \mu\mu$ or $Z/\gamma^* \rightarrow ee$ signal MC, respectively. All distributions are (roughly) normalised to the same number of selected events in the 2017 dataset. The left and middle plots show the actual μ in a coarsely-binned and a finely-binned version. The right plot shows the number of reconstructed primary vertices N_{PV} .

2314 The information on the simulated samples and their properties is given in Tables 81, 82, 83, 84 [1]. The
2315 predicted event counts are normalized to the cross-sections quoted in the table.
2316 The primary signal event samples for W and Z production are obtained using PowHEG [2, 3, 4, 5] event
2317 generator with CT10 PDF, linked with PYTHIA8 [6] with AZNLO tune [7]. PowHEG+PYTHIA88 samples
2318 are interfaced to PHOTOS++ [8] for final state QED effects simulation.
2319 A set of alternative samples at $\sqrt{s} = 13\text{TeV}$ was prepared with SHERPA2.2.2 [9] using the NNPDF3.0
2320 PDFs and merging $V + 0, 1, 2$ at NLO accuracy with $V + 3, 4$ at LO accuracy with the MEPS@NLO scheme.
2321 A similar set for $\sqrt{s} = 5\text{TeV}$ was prepared with SHERPA2.2.5 with a setup similar to 13 TeV samples.
2322 Pileup is modelled by overlaying simulated soft events over the original hard-scattering event. These
2323 soft events were modelled using PYTHIA8 with NNPDF2.3LO set of PDFs [10] and the A3 tune [11].
2324 The W and Z processes samples are normalized to NNLO calculations performed using the DYTURBO,
2325 an optimised version of DYNNLO [12, 13] using the MMHT2014nnlo PDF set [14]. Corresponding
2326 numerical values were taken from the corresponding ATLAS publications of the 2015 data at 13 TeV [15]
2327 and 5.02 TeV [16] are presented in Table 81 for 13 TeV and Table 84 for 5 TeV. The uncertainties on
2328 those cross-sections arise from the choice of PDF set, from factorization and renormalisation scale
2329 dependence, and the strong coupling constant α_s uncertainty resulting in the total uncertainty estimate
2330 of 5%.

2331 Backgrounds from top-quark pair-production $t\bar{t}$ and single-top production (Wt , t-channel, s-
2332 channel) were generated with PowHEG+PYTHIA8. The 5 TeV $t\bar{t}$ cross section is taken as the top++
2333 prediction observed by CMS [17]. Di-boson combinations VV , $V = W, Z$ are generated with SHERPA in
2334 all decay channels with a requirement of having at least one real lepton in the final state.

2335 8.2 Z vertex reweighting

2336 The 5 TeV MC samples have been generated to be perfectly matched to the data. Although this is not
2337 the case for 13 TeV samples, which can be seen at Fig. 83. It is also seen from these plots that the
2338 2017 and 2018 data were collected at two different runs under different beam conditions. To avoid
2339 possible impact on the acceptance the MC samples were reweighted to the data using $Z \rightarrow ee$ and
2340 $Z \rightarrow \mu\mu$ selections.

2341 8.2.1 Multijet background

2342 The estimate of the multijet background, which contain contributions from fake leptons produced in
2343 semi-leptonic decays of heavy quarks, in-flight pion decays, photon conversions, etc, is done using a
2344 data-driven techniques described in Reference [Xu:2657146]. TO BE ADDED.

Process	Data set	Generator	$\sigma \cdot \text{BR} \cdot \epsilon_{\text{filter}}$ [nb] (th. unc.)	$N_{\text{evt}}^{\text{skim}} [10^6]$	$N_{\text{evt}}^{\text{unskim}} [10^6]$
$W^+ \rightarrow e^+ \nu$	361100	POWHEG+PYTHIA8	11.61 (5%)	40	40
$W^+ \rightarrow \mu^+ \nu$	361101	POWHEG+PYTHIA8	11.61 (5%)	40	40
$W^+ \rightarrow \tau^+ \nu$	361102	POWHEG+PYTHIA8	11.61 (5%)	0.28	5.0
$W^- \rightarrow e^- \bar{\nu}$	361103	POWHEG+PYTHIA8	8.630 (5%)	30	30
$W^- \rightarrow \mu^- \bar{\nu}$	361104	POWHEG+PYTHIA8	8.630 (5%)	29	29
$W^- \rightarrow \tau^- \bar{\nu}$	361105	POWHEG+PYTHIA8	8.630 (5%)	0.24	4.0
$Z \rightarrow ee$	361106	POWHEG+PYTHIA8	1.910×1.03 (5%)	10	10
$Z \rightarrow \mu\mu$	361107	POWHEG+PYTHIA8	1.910×1.025 (5%)	10	10
$Z \rightarrow \tau\tau$	361108	POWHEG+PYTHIA8	1.910×1.025 (5%)	0.12	1.0
$ZZ(q\bar{q}\ell\ell)$	363356	SHERPA 2.2.1	0.01556×0.141 (10%)	0.0064	0.010
$WZ(q\bar{q}\ell\ell)$	363358	SHERPA 2.2.1	0.003433 (10%)	0.0063	0.010
$WW(q\bar{q}\ell\nu)$	363359	SHERPA 2.2.1	0.02472 (10%)	0.0093	0.020
$WW(\ell\nu q\bar{q})$	363360	SHERPA 2.2.1	0.02472 (10%)	0.0093	0.020
$WZ(\ell\nu q\bar{q})$	363489	SHERPA 2.2.1	0.01142 (10%)	0.0047	0.010
$ZZ(4\ell)$	364250	SHERPA 2.2.2	0.001252 (10%)	0.0057	0.010
$WZ(3\ell\nu)$	364253	SHERPA 2.2.2	0.004583 (10%)	0.0062	0.010
$WW(2\ell 2\nu)$	364254	SHERPA 2.2.2	0.01250 (10%)	0.0073	0.010
$WZ(\ell 3\nu)$	364255	SHERPA 2.2.2	0.003235 (10%)	0.0050	0.010
Wt	410013	POWHEG+PYTHIA8	0.03582 (10%)	0.0037	0.010
$W\bar{t}$	410014	POWHEG+PYTHIA8	0.03399 (10%)	0.0037	0.010
$t\bar{t}$ (nominal)	410470	POWHEG+PYTHIA8	0.8318×0.544 (7%)	1.2	2.0
$t(t-\text{chan.}t)$	410642	POWHEG+PYTHIA8	0.03699 (10%)	0.016	0.030
$t(t-\text{chan.}\bar{t})$	410643	POWHEG+PYTHIA8	0.02217 (10%)	0.011	0.020
$t(s-\text{chan.}t)$	410644	POWHEG+PYTHIA8	0.002027 (10%)	0.0050	0.010
$t(s-\text{chan.}\bar{t})$	410645	POWHEG+PYTHIA8	0.001268 (10%)	0.0052	0.010
$t\bar{t}$ (syst.)	410480	POWHEG+PYTHIA8	0.8318×0.438 (7%)	0.85	1.5
$t\bar{t}$ (syst.)	410482	POWHEG+PYTHIA8	0.8318×0.105 (7%)	0.40	0.50
$t\bar{t}$ (syst.)	410557	POWHEG+PYTHIA8	0.8318×0.438 (7%)	0.85	1.5
$t\bar{t}$ (syst.)	410558	POWHEG+PYTHIA8	0.8318×0.105 (7%)	0.40	0.50

Table 81: Monte Carlo samples at $\sqrt{s} = 13\text{TeV}$. Given is a short description of the process, the ATLAS MC data set number (DSID), the names and version numbers of the MC generator(s), the used value of the higher order cross section times any branching and filter efficiencies ($\sigma \cdot \text{BR} \cdot \epsilon_{\text{filter}}$) with the theoretical uncertainty in percent (“th. unc.”), and finally the number of events analysed after skimming at derivation production ($N_{\text{evt}}^{\text{skim}}$) as well as the number of events originally processed and simulated ($N_{\text{evt}}^{\text{unskim}}$). In the case of $Z \rightarrow \ell\ell$ samples, the given $\epsilon_{\text{filter}} > 1$ is related to the fact, that the cross sections were calculated for $66 < m_{\ell\ell} < 116\text{GeV}$, but the generated mass range is larger. The last section of $t\bar{t}$ samples refers to variation samples for systematics studies. The MC equivalent luminosity $N_{\text{evt}}^{\text{unskim}} / (\sigma \cdot \text{BR} \cdot \epsilon_{\text{filter}})$ is generally above 3fb^{-1} for signal and significant backgrounds, the exception are Powheg $W \rightarrow \tau\nu$ and $Z \rightarrow \tau\tau$ samples, that have about 0.45fb^{-1} only.

Process	Data set	Generator	$\sigma \cdot BR \cdot \epsilon_{\text{filter}}$ [nb] (th. unc.)	$N_{\text{evt}}^{\text{skim}} [10^6]$	$N_{\text{evt}}^{\text{unskim}} [10^6]$
$Z \rightarrow \mu\mu$	364100	SHERPA 2.2.1	1.932×0.822 (5%)	8.0	8.0
$Z \rightarrow \mu\mu$	364101	SHERPA 2.2.1	1.933×0.114 (5%)	1.5	1.5
$Z \rightarrow \mu\mu$	364102	SHERPA 2.2.1	1.932×0.0660 (5%)	1.1	1.1
$Z \rightarrow \mu\mu$	364103	SHERPA 2.2.1	0.1063×0.690 (5%)	1.5	1.5
$Z \rightarrow \mu\mu$	364104	SHERPA 2.2.1	0.1062×0.200 (5%)	0.40	0.40
$Z \rightarrow \mu\mu$	364105	SHERPA 2.2.1	0.1063×0.114 (5%)	0.25	0.25
$Z \rightarrow \mu\mu$	364106	SHERPA 2.2.1	0.03889×0.593 (5%)	0.20	0.20
$Z \rightarrow \mu\mu$	364107	SHERPA 2.2.1	0.03885×0.235 (5%)	0.060	0.060
$Z \rightarrow \mu\mu$	364108	SHERPA 2.2.1	0.03889×0.156 (5%)	0.035	0.035
$Z \rightarrow \mu\mu$	364109	SHERPA 2.2.1	0.008310×0.561 (5%)	0.020	0.020
$Z \rightarrow \mu\mu$	364110	SHERPA 2.2.1	0.008310×0.266 (5%)	0.010	0.010
$Z \rightarrow \mu\mu$	364111	SHERPA 2.2.1	0.008320×0.177 (5%)	0.0050	0.0050
$Z \rightarrow \mu\mu$	364112	SHERPA 2.2.1	0.001740 (5%)	0.0050	0.0050
$Z \rightarrow \mu\mu$	364113	SHERPA 2.2.1	0.0001400 (5%)	0.0050	0.0050
$Z \rightarrow ee$	364114	SHERPA 2.2.1	1.933×0.821 (5%)	8.0	8.0
$Z \rightarrow ee$	364115	SHERPA 2.2.1	1.932×0.114 (5%)	1.5	1.5
$Z \rightarrow ee$	364116	SHERPA 2.2.1	1.932×0.0658 (5%)	1.1	1.1
$Z \rightarrow ee$	364117	SHERPA 2.2.1	0.1080×0.694 (5%)	1.5	1.5
$Z \rightarrow ee$	364118	SHERPA 2.2.1	0.1077×0.191 (5%)	0.40	0.40
$Z \rightarrow ee$	364119	SHERPA 2.2.1	0.1078×0.119 (5%)	0.25	0.25
$Z \rightarrow ee$	364120	SHERPA 2.2.1	0.03964×0.616 (5%)	0.20	0.20
$Z \rightarrow ee$	364121	SHERPA 2.2.1	0.03967×0.233 (5%)	0.060	0.060
$Z \rightarrow ee$	364122	SHERPA 2.2.1	0.04068×0.150 (5%)	0.035	0.035
$Z \rightarrow ee$	364123	SHERPA 2.2.1	0.008460×0.569 (5%)	0.020	0.020
$Z \rightarrow ee$	364124	SHERPA 2.2.1	0.008450×0.266 (5%)	0.010	0.010
$Z \rightarrow ee$	364125	SHERPA 2.2.1	0.008470×0.177 (5%)	0.0050	0.0050
$Z \rightarrow ee$	364126	SHERPA 2.2.1	0.001760 (5%)	0.0050	0.0050
$Z \rightarrow ee$	364127	SHERPA 2.2.1	0.0001451 (5%)	0.0050	0.0050

Table 82: Alternative signal $Z \rightarrow \ell\ell$ Monte Carlo samples at $\sqrt{s} = 13\text{TeV}$ produced with SHERPA. General description of the table see Table 81. The samples are split into a long list of orthogonal slices based on “max(pTV,HT)” and filtered further into “b/c/light-jet” subcomponents. For the purpose of this analysis, the number of events in each slice is such that the samples are about 2fb^{-1} each (after application of a penalty factor for negative weight events) and an “inclusive sample” is restored after merging the slices.

Process	Data set	Generator	$\sigma \cdot BR \cdot \epsilon_{\text{filter}}$ [nb] (th. unc.)	$N_{\text{evt}}^{\text{skim}} [10^6]$	$N_{\text{evt}}^{\text{unskim}} [10^6]$
$W \rightarrow \mu\nu$	364156	SHERPA 2.2.1	18.58×0.825 (5%)	31	31
$W \rightarrow \mu\nu$	364157	SHERPA 2.2.1	18.57×0.131 (5%)	8.1	8.1
$W \rightarrow \mu\nu$	364158	SHERPA 2.2.1	18.57×0.0433 (5%)	2.6	2.6
$W \rightarrow \mu\nu$	364159	SHERPA 2.2.1	0.9173×0.674 (5%)	6.3	6.3
$W \rightarrow \mu\nu$	364160	SHERPA 2.2.1	0.9172×0.244 (5%)	2.1	2.1
$W \rightarrow \mu\nu$	364161	SHERPA 2.2.1	0.9163×0.0847 (5%)	0.23	0.23
$W \rightarrow \mu\nu$	364162	SHERPA 2.2.1	0.3296×0.600 (5%)	0.80	0.80
$W \rightarrow \mu\nu$	364163	SHERPA 2.2.1	0.3297×0.293 (5%)	0.27	0.27
$W \rightarrow \mu\nu$	364164	SHERPA 2.2.1	0.3295×0.111 (5%)	0.099	0.099
$W \rightarrow \mu\nu$	364165	SHERPA 2.2.1	0.06993×0.548 (5%)	0.068	0.068
$W \rightarrow \mu\nu$	364166	SHERPA 2.2.1	0.06995×0.320 (5%)	0.034	0.034
$W \rightarrow \mu\nu$	364167	SHERPA 2.2.1	0.06991×0.125 (5%)	0.014	0.014
$W \rightarrow \mu\nu$	364168	SHERPA 2.2.1	0.01456 (5%)	0.020	0.020
$W \rightarrow \mu\nu$	364169	SHERPA 2.2.1	0.001200 (5%)	0.004	0.004
$W \rightarrow e\nu$	364170	SHERPA 2.2.1	18.58×0.825 (5%)	31	31
$W \rightarrow e\nu$	364171	SHERPA 2.2.1	18.57×0.131 (5%)	8.3	8.3
$W \rightarrow e\nu$	364172	SHERPA 2.2.1	18.57×0.0448 (5%)	2.5	2.5
$W \rightarrow e\nu$	364173	SHERPA 2.2.1	0.9168×0.675 (5%)	6.4	6.4
$W \rightarrow e\nu$	364174	SHERPA 2.2.1	0.9176×0.244 (5%)	2.1	2.1
$W \rightarrow e\nu$	364175	SHERPA 2.2.1	0.9173×0.0851 (5%)	0.79	0.79
$W \rightarrow e\nu$	364176	SHERPA 2.2.1	0.3295×0.599 (5%)	0.76	0.76
$W \rightarrow e\nu$	364177	SHERPA 2.2.1	0.3297×0.288 (5%)	0.28	0.28
$W \rightarrow e\nu$	364178	SHERPA 2.2.1	0.3295×0.111 (5%)	0.10	0.10
$W \rightarrow e\nu$	364179	SHERPA 2.2.1	0.06993×0.548 (5%)	0.070	0.070
$W \rightarrow e\nu$	364180	SHERPA 2.2.1	0.06996×0.320 (5%)	0.034	0.034
$W \rightarrow e\nu$	364181	SHERPA 2.2.1	0.06994×0.137 (5%)	0.014	0.014
$W \rightarrow e\nu$	364182	SHERPA 2.2.1	0.01460 (5%)	0.020	0.020
$W \rightarrow e\nu$	364183	SHERPA 2.2.1	0.001200 (5%)	0.0050	0.0050

Table 83: Alternative signal $W \rightarrow \ell\nu$ Monte Carlo samples at $\sqrt{s} = 13\text{TeV}$ produced with SHERPA. See Table 82 for a description of the table. The samples are split into a long list of orthogonal slices based on “max(pTV,HT)” and filtered further into “b/c/light-jet” subcomponents. For the purpose of this analysis, the number of events in each slice is such that the samples are about 1fb^{-1} each (after application of a penalty factor for negative weight events) and an “inclusive sample” is restored after merging the slices.

Process	Data set	Generator	$\sigma \cdot \text{BR} \cdot \epsilon_{\text{filter}}$ [nb] (th. unc.)	$N_{\text{evt}}^{\text{skim}} [10^6]$	$N_{\text{evt}}^{\text{unskim}} [10^6]$
$W^+ \rightarrow e^+ \nu$	361100	POWHEG+PYTHIA8	4.357 (5%)	11	11
$W^+ \rightarrow \mu^+ \nu$	361101	POWHEG+PYTHIA8	4.357 (5%)	11	11
$W^+ \rightarrow \tau^+ \nu$	361102	POWHEG+PYTHIA8	4.357 (5%)	0.065	0.94
$W^- \rightarrow e^- \bar{\nu}$	361103	POWHEG+PYTHIA8	2.902 (5%)	7.0	7.0
$W^- \rightarrow \mu^- \bar{\nu}$	361104	POWHEG+PYTHIA8	2.902 (5%)	7.0	7.0
$W^- \rightarrow \tau^- \bar{\nu}$	361105	POWHEG+PYTHIA8	2.902 (5%)	0.039	0.59
$Z \rightarrow ee$	361106	POWHEG+PYTHIA8	0.6600×1.025 (5%)	6.3	6.3
$Z \rightarrow \mu\mu$	361107	POWHEG+PYTHIA8	0.6600×1.025 (5%)	3.4	3.4
$Z \rightarrow \tau\tau$	361108	POWHEG+PYTHIA8	0.6600×1.025 (5%)	0.039	0.29
$Z \rightarrow ee$	364381	SHERPA 2.2.5	0.6600×1.12 (5%)	5.0	5.0
$Z \rightarrow \mu\mu$	364382	SHERPA 2.2.5	0.6600×1.12 (5%)	5.0	5.0
$Z \rightarrow \tau\tau$	364383	SHERPA 2.2.5	0.6600×1.12 (5%)	1.5	1.5
$W \rightarrow e\nu$	364384	SHERPA 2.2.5	7.259 (5%)	25	25
$W \rightarrow \mu\nu$	364385	SHERPA 2.2.5	7.259 (5%)	25	25
$W \rightarrow \tau\nu$	364386	SHERPA 2.2.5	7.259 (5%)	6.0	6.0
$ZZ(4\ell)$	361063	SHERPA 2.1	0.004624 (10%)	0.017	0.049
$WZ(\ell\ell\ell^-\nu\text{SF})$	361064	SHERPA 2.1	0.0005324 (10%)	0.0073	0.015
$WZ(\ell\ell\ell^-\nu\text{OF})$	361065	SHERPA 2.1	0.001041 (10%)	0.012	0.030
$WZ(\ell\ell\ell^+\nu\text{SF})$	361066	SHERPA 2.1	0.0008433 (10%)	0.010	0.020
$WZ(\ell\ell\ell^+\nu\text{OF})$	361067	SHERPA 2.1	0.001633 (10%)	0.016	0.039
$WW(2\ell 2\nu)$	361068	SHERPA 2.1	0.003356 (10%)	0.068	0.090
$WW(q\bar{q}\ell\nu)$	361091	SHERPA 2.1	0.006059 (10%)	0.078	0.15
$WW(\ell\nu q\bar{q})$	361092	SHERPA 2.1	0.006082 (10%)	0.14	0.26
$WZ(\ell\nu q\bar{q})$	361093	SHERPA 2.1	0.002503 (10%)	0.039	0.075
$WZ(q\bar{q}\ell\ell)$	361094	SHERPA 2.1	0.0007518 (10%)	0.017	0.025
$ZZ(q\bar{q}\ell\ell)$	361096	SHERPA 2.1	0.003789×0.148 (10%)	0.0070	0.010
$t\bar{t}$	410470	POWHEG+PYTHIA8	0.06890×0.544 (7%)	1.8	2.8
$t(s - \text{chan.} t)$	410644	POWHEG+PYTHIA8	0.0005400 (10%)	0.028	0.050
$t(s - \text{chan.} \bar{t})$	410645	POWHEG+PYTHIA8	0.0002751 (10%)	0.028	0.050
Wt	410646	POWHEG+PYTHIA8	0.002990 (10%)	0.018	0.050
$W\bar{t}$	410647	POWHEG+PYTHIA8	0.002983 (10%)	0.019	0.050
$t(t - \text{chan.} t)$	410658	POWHEG+PYTHIA8	0.005414 (10%)	0.028	0.050
$t(t - \text{chan.} \bar{t})$	410659	POWHEG+PYTHIA8	0.002682 (10%)	0.028	0.050

Table 84: Monte Carlo samples at $\sqrt{s} = 5\text{TeV}$. The table follows the same format as Table 81. The MC equivalent luminosity $N_{\text{evt}}^{\text{unskim}} / (\sigma \cdot \text{BR} \cdot \epsilon_{\text{filter}})$ is generally above 2.5fb^{-1} for signal and significant backgrounds, the exception are Powheg $W \rightarrow \tau\nu$ and $Z \rightarrow \tau\tau$ samples, that have about 0.20fb^{-1} and 0.45fb^{-1} only.

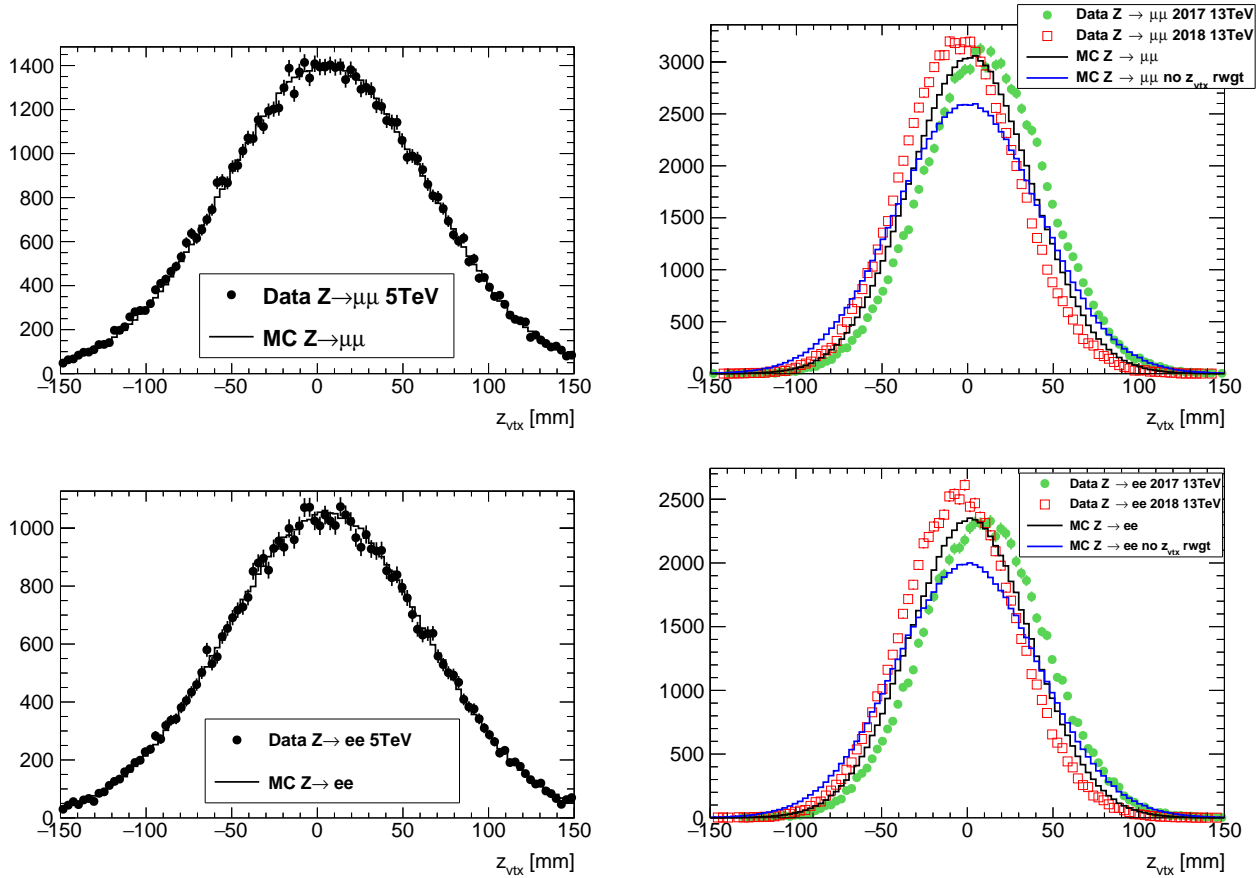


Figure 83: Distributions for the 5 TeV (left) and 13 TeV (right) low- μ dataset(s) in a $Z/\gamma^* \rightarrow \mu\mu$ (top row) and a $Z/\gamma^* \rightarrow ee$ (bottom row) selection. The data (points) is compared to $Z/\gamma^* \rightarrow \mu\mu$ or $Z/\gamma^* \rightarrow ee$ signal MC, respectively. The distributions of the z -position of the primary vertex selected as the hard interaction are compared for the dataset(s) and the MC simulation before (“no z_{vtx} rwgt”, blue, only 13 TeV) and after reweighting (black). For the 13 TeV data the 2017 and 2018 data are shown separately and all distributions are (roughly) normalised to the same number of selected events in the 2017 dataset.

2345 8.3 W analysis event selection and control plots

2346 8.3.1 Event selection

2347 Both in case of 5 and 13 TeV events with $W \rightarrow \ell\nu$ candidate were selected base on a single-lepton
 2348 trigger requirement. The trigger for $W \rightarrow ev$ event candidate HLT_e15_1hloose_nod0_L1EM12 require
 2349 at least one reconstructed electron with E_T larger than 15 GeV passing *loose* identification requirements.
 2350 Candidates for $W \rightarrow \mu\nu$ were triggered by HLT_mu14 trigger requiring one muon with E_T larger than
 2351 14 GeV.

2352 Events are required to contain exactly one lepton (muon or electron) candidate having $p_T > 25\text{GeV}$.

2353 Electrons are required to have $|\eta| < 2.47$ excluding transition region $1.37 < |\eta| < 1.52$. Muons Events
 2354 with additional leptons of the same flavour with transverse momentum greater than 20 GeV satisfying
 2355 some ID criteria are discarded, to better reject the Z background. The ID point is *medium* for the muon
 2356 channel, and *loose* for the electron channel. There is no requirement on the number of leptons with
 2357 different flavour than the channel under study.

2358 To suppress background, in particular from multijet processes, events are required to have E_T^{miss}
 2359 greater than 25 GeV. The W boson transverse mass m_T is demanded to be larger than 50 GeV. This
 2360 transverse mass is defined as follows:

$$m_T = \sqrt{2p_T^\nu p_T^l(1 - \cos \Delta\phi^\nu)} \quad (8.1)$$

2361 The tables 85,87,89,811 contain signal selection event yields for the $W^\pm \rightarrow \ell^\pm \nu$ at $\sqrt{s} = 5$ TeV low- μ
 2362 dataset. Similarly the tables 86,88,810,812 contain the corresponding numbers for the 13 TeV low- μ
 2363 dataset. Table 813 provides a comparison between observed and expected yields. Events denoted as
 2364 $W \rightarrow \ell\nu$ in the tables and the plots contain the sum of background events coming from $W \rightarrow \tau\nu$ and
 2365 other W leptonic decays other than the signal.

Cut	Data	Signal	$W^\pm \rightarrow \ell^\pm \nu$ BG	$Z \rightarrow \ell\ell$	Top	Diboson	Multijet
One electron	1993720	643610 \pm 260	32940 \pm 190	44338 \pm 71	1754.4 \pm 3.9	772.2 \pm 3.7	-
Electron trig matched	1907724	612940 \pm 250	30790 \pm 190	42100 \pm 69	1698.5 \pm 3.8	741.1 \pm 3.6	-
Isolation	1438941	610320 \pm 250	30590 \pm 190	41923 \pm 69	1663.6 \pm 3.8	722.5 \pm 3.6	-
$p_T^e > 25$ GeV	720284	482240 \pm 220	14790 \pm 130	31955 \pm 53	1464.5 \pm 3.5	592.1 \pm 3.2	-
$E_T^{\text{miss}} > 25$ GeV	440605	421510 \pm 210	9650 \pm 100	1336 \pm 20	1223 \pm 3.2	420.8 \pm 2.4	-
$m_T > 50$ GeV	430620	417430 \pm 210	8800 \pm 96	1047 \pm 16	944.3 \pm 2.9	373.5 \pm 2.2	3030 \pm 550

Table 85: Analysis cut flow for $W^+ \rightarrow e^+ \nu$ 5 TeV signal selection. Lepton p_T is required to be over 18 GeV before the final cut.

Cut	Data	Signal	$W^\pm \rightarrow \ell^\pm \nu$ BG	$Z \rightarrow \ell\ell$	Top	Diboson	Multijet
One electron	7915023	1797340 \pm 390	92520 \pm 270	147490 \pm 140	63207 \pm 89	3069 \pm 63	-
Electron trig matched	7840239	1709140 \pm 380	86370 \pm 260	139760 \pm 140	61110 \pm 88	2967 \pm 62	-
Isolation	5413483	1698430 \pm 380	85560 \pm 260	138890 \pm 140	59834 \pm 87	2939 \pm 61	-
$p_T^e > 25$ GeV	2452868	1342200 \pm 330	44450 \pm 190	106270 \pm 110	53811 \pm 82	2565 \pm 58	-
$E_T^{\text{miss}} > 25$ GeV	1275513	1136520 \pm 310	28580 \pm 150	8313 \pm 46	45707 \pm 75	1990 \pm 53	-
$m_T > 50$ GeV	1207776	1117560 \pm 310	24760 \pm 130	6443 \pm 36	34580 \pm 65	1718 \pm 50	28000 \pm 1800

Table 86: Analysis cut flow for $W^+ \rightarrow e^+ \nu$ 13 TeV signal selection. Lepton p_T is required to be over 18 GeV before the final cut.

2366 8.3.2 $\sqrt{s} = 13$ TeV dataset control plots

2367 Control plots for the 13 TeV low- μ dataset are provided here after applying all corrections described
 2368 in section ??, and after applying the selection described above in this section. In each figure, the right(left)-hand column shows distributions for the W^+ (W^-) process. The top (bottom) row shows the
 2369 muon (electron) decay channel. In the ratio panels, the grey band is the total systematic uncertainty,
 2370

Cut	Data	Signal	$W^\pm \rightarrow \ell^\pm \nu$ BG	$Z \rightarrow \ell\ell$	Top	Diboson	Multijet
One muon	2434459	760980 \pm 280	35090 \pm 200	37015 \pm 82	2025.3 \pm 4.1	864.7 \pm 3.7	-
Muon trig matched	2353403	664100 \pm 260	30610 \pm 190	32554 \pm 76	1725.6 \pm 3.8	746.6 \pm 3.4	-
Isolation	1186616	659200 \pm 260	30400 \pm 190	32303 \pm 76	1574.6 \pm 3.7	710.1 \pm 3.3	-
$p_T^\mu > 25\text{GeV}$	632016	508270 \pm 230	13900 \pm 130	22556 \pm 57	1335.3 \pm 3.4	568.2 \pm 2.9	-
$E_T^{\text{miss}} > 25\text{GeV}$	470856	442600 \pm 210	8700 \pm 100	9959 \pm 31	1111.8 \pm 3	424.5 \pm 2.5	-
$m_T > 50\text{GeV}$	457053	438280 \pm 210	7879 \pm 97	9649 \pm 27	879.7 \pm 2.8	381.7 \pm 2.3	720 \pm 190

Table 87: Analysis cut flow for $W^+ \rightarrow \mu^+ \nu$ 5 TeV signal selection. Lepton p_T is required to be over 18 GeV before the final cut.

Cut	Data	Signal	$W^\pm \rightarrow \ell^\pm \nu$ BG	$Z \rightarrow \ell\ell$	Top	Diboson	Multijet
One muon	9570104	2100770 \pm 410	83110 \pm 270	2019400 \pm 2200	71602 \pm 94	3442 \pm 63	-
Muon trig matched	9382783	1840550 \pm 390	72820 \pm 250	1750400 \pm 2000	61519 \pm 87	2956 \pm 59	-
Isolation	3905612	1821750 \pm 380	71780 \pm 250	595700 \pm 1100	56849 \pm 84	2916 \pm 59	-
$p_T^\mu > 25\text{GeV}$	1930655	1393330 \pm 340	34470 \pm 170	170840 \pm 490	49338 \pm 78	2471 \pm 54	-
$E_T^{\text{miss}} > 25\text{GeV}$	1321407	1173860 \pm 310	21450 \pm 140	51090 \pm 180	41956 \pm 72	1930 \pm 49	-
$m_T > 50\text{GeV}$	1244892	1153800 \pm 310	18270 \pm 130	38304 \pm 81	32375 \pm 63	1705 \pm 44	9040 \pm 800

Table 88: Analysis cut flow for $W^+ \rightarrow \mu^+ \nu$ 13 TeV signal selection. Lepton p_T is required to be over 18 GeV before the final cut.

Cut	Data	Signal	$W^\pm \rightarrow \ell^\pm \nu$ BG	$Z \rightarrow \ell\ell$	Top	Diboson	Multijet
One electron	1724472	374900 \pm 200	24150 \pm 160	41995 \pm 70	1590.5 \pm 2.9	684.8 \pm 4	-
Electron trig matched	1645694	359010 \pm 200	22070 \pm 160	39854 \pm 68	1539.9 \pm 2.9	655.7 \pm 3.9	-
Isolation	1176976	357660 \pm 200	21920 \pm 160	39686 \pm 68	1504.6 \pm 2.8	640.7 \pm 3.8	-
$p_T^e > 25\text{GeV}$	529183	302070 \pm 180	11920 \pm 110	30214 \pm 52	1330.8 \pm 2.6	532.9 \pm 3.5	-
$E_T^{\text{miss}} > 25\text{GeV}$	281957	266750 \pm 170	8084 \pm 90	1293 \pm 20	1112.5 \pm 2.4	380 \pm 3	-
$m_T > 50\text{GeV}$	274329	264540 \pm 170	7317 \pm 84	994 \pm 16	855.2 \pm 2.1	338.1 \pm 2.9	2400 \pm 500

Table 89: Analysis cut flow for $W^- \rightarrow e^- \nu$ 5 TeV signal selection. Lepton p_T is required to be over 18 GeV before the final cut.

whilst the brown band adds the MC statistical uncertainty in quadrature on top of it. In regions of the distributions insensitive to the modelling of p_T^W there is generally good agreement between data and predictions. The bulk of the m_T distribution is a typical example of distribution that is mostly insensitive to the modeling of p_T^W . The u_T distribution is an exception, and it can therefore be concluded that the baseline simulation is not modeling p_T^W satisfactorily.

Cut	Data	Signal		$W^\pm \rightarrow \ell^\pm \nu$ BG		$Z \rightarrow \ell\ell$		Top		Diboson	Multijet
One electron	7471742	1323710	\pm 330	78230	\pm 230	140980	\pm 140	61951	\pm 86	3059	\pm 58
Electron trig matched	7402574	1267710	\pm 330	72240	\pm 230	133580	\pm 140	59950	\pm 85	2968	\pm 57
Isolation	4949352	1260540	\pm 330	71550	\pm 230	132740	\pm 140	58689	\pm 84	2937	\pm 57
$p_T^e > 25\text{GeV}$	2113364	1053510	\pm 300	39660	\pm 160	101350	\pm 110	52923	\pm 79	2544	\pm 53
$E_T^{\text{miss}} > 25\text{GeV}$	1008915	900640	\pm 280	25900	\pm 130	7954	\pm 45	45065	\pm 73	1962	\pm 48
$m_T > 50\text{GeV}$	949362	887810	\pm 270	22400	\pm 120	6052	\pm 35	34177	\pm 64	1695	\pm 44
										27400	\pm 2000

Table 810: Analysis cut flow for $W^- \rightarrow e^- \nu$ 13 TeV signal selection. Lepton p_T is required to be over 18 GeV before the final cut.

Cut	Data	Signal		$W^\pm \rightarrow \ell^\pm \nu$ BG		$Z \rightarrow \ell\ell$		Top		Diboson	Multijet
One muon	2075709	440560	\pm 220	22510	\pm 170	34440	\pm 80	1835.6	\pm 3.1	751.5	\pm 3.3
Muon trig matched	2002955	383720	\pm 200	19640	\pm 160	30277	\pm 75	1561.6	\pm 2.9	648	\pm 3.1
Isolation	883078	381010	\pm 200	19450	\pm 160	30046	\pm 74	1411	\pm 2.7	616.9	\pm 2.9
$p_T^\mu > 25\text{GeV}$	426119	314370	\pm 180	9370	\pm 110	20749	\pm 56	1202.1	\pm 2.5	505	\pm 2.5
$E_T^{\text{miss}} > 25\text{GeV}$	298992	276060	\pm 170	5893	\pm 89	8716	\pm 29	1004.2	\pm 2.3	372.6	\pm 2
$m_T > 50\text{GeV}$	287870	273710	\pm 170	5158	\pm 82	8408	\pm 26	788.2	\pm 2	335.6	\pm 1.9
										760	\pm 160

Table 811: Analysis cut flow for $W^- \rightarrow \mu^- \nu$ 5 TeV signal selection. Lepton p_T is required to be over 18 GeV before the final cut.

Cut	Data	Signal		$W^\pm \rightarrow \ell^\pm \nu$ BG		$Z \rightarrow \ell\ell$		Top		Diboson	Multijet
One muon	8773414	1518070	\pm 360	64930	\pm 230	201990	\pm 2200	70580	\pm 90	3230	\pm 60
Muon trig matched	8597493	1322980	\pm 330	56520	\pm 210	1750300	\pm 2000	60579	\pm 84	2806	\pm 56
Isolation	3298569	1310310	\pm 330	55680	\pm 210	593700	\pm 1100	55949	\pm 80	2751	\pm 55
$p_T^\mu > 25\text{GeV}$	1561721	1069770	\pm 300	28230	\pm 150	166810	\pm 490	48544	\pm 75	2362	\pm 52
$E_T^{\text{miss}} > 25\text{GeV}$	1030406	910150	\pm 280	17380	\pm 120	47370	\pm 180	41259	\pm 69	1842	\pm 46
$m_T > 50\text{GeV}$	963568	896850	\pm 270	14710	\pm 110	34572	\pm 80	31772	\pm 61	1598	\pm 43
										9050	\pm 620

Table 812: Analysis cut flow for $W^- \rightarrow \mu^- \nu$ 13 TeV signal selection. Lepton p_T is required to be over 18 GeV before the final cut.

Selection	Observed	Expected
5TeV $W^+ \rightarrow e^+ \nu$	430620	431620 \pm 600
5TeV $W^+ \rightarrow \mu^+ \nu$	457053	457790 \pm 300
5TeV $W^- \rightarrow e^- \nu$	274329	276450 \pm 530
5TeV $W^- \rightarrow \mu^- \nu$	287870	289160 \pm 250
13TeV $W^+ \rightarrow e^+ \nu$	1207776	1213000 \pm 1800
13TeV $W^+ \rightarrow \mu^+ \nu$	1244892	1253490 \pm 870
13TeV $W^- \rightarrow e^- \nu$	949362	979500 \pm 2000
13TeV $W^- \rightarrow \mu^- \nu$	963568	988560 \pm 690

Table 813: Observed and Expected yield comparison for all signal selections.

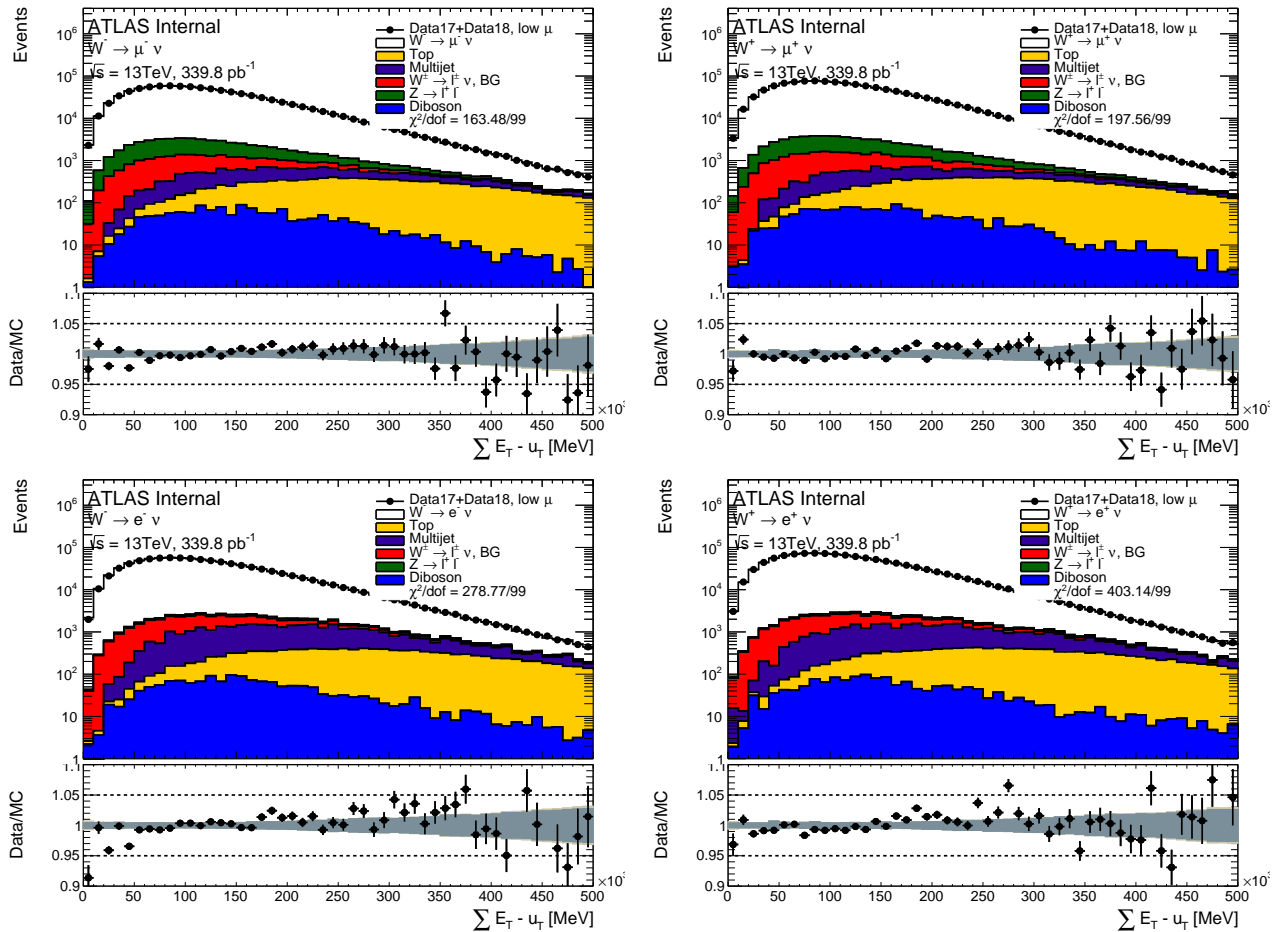


Figure 84: ΣE_T distribution in the muon and electron channel for the $\sqrt{s} = 13 \text{ TeV}$ dataset.

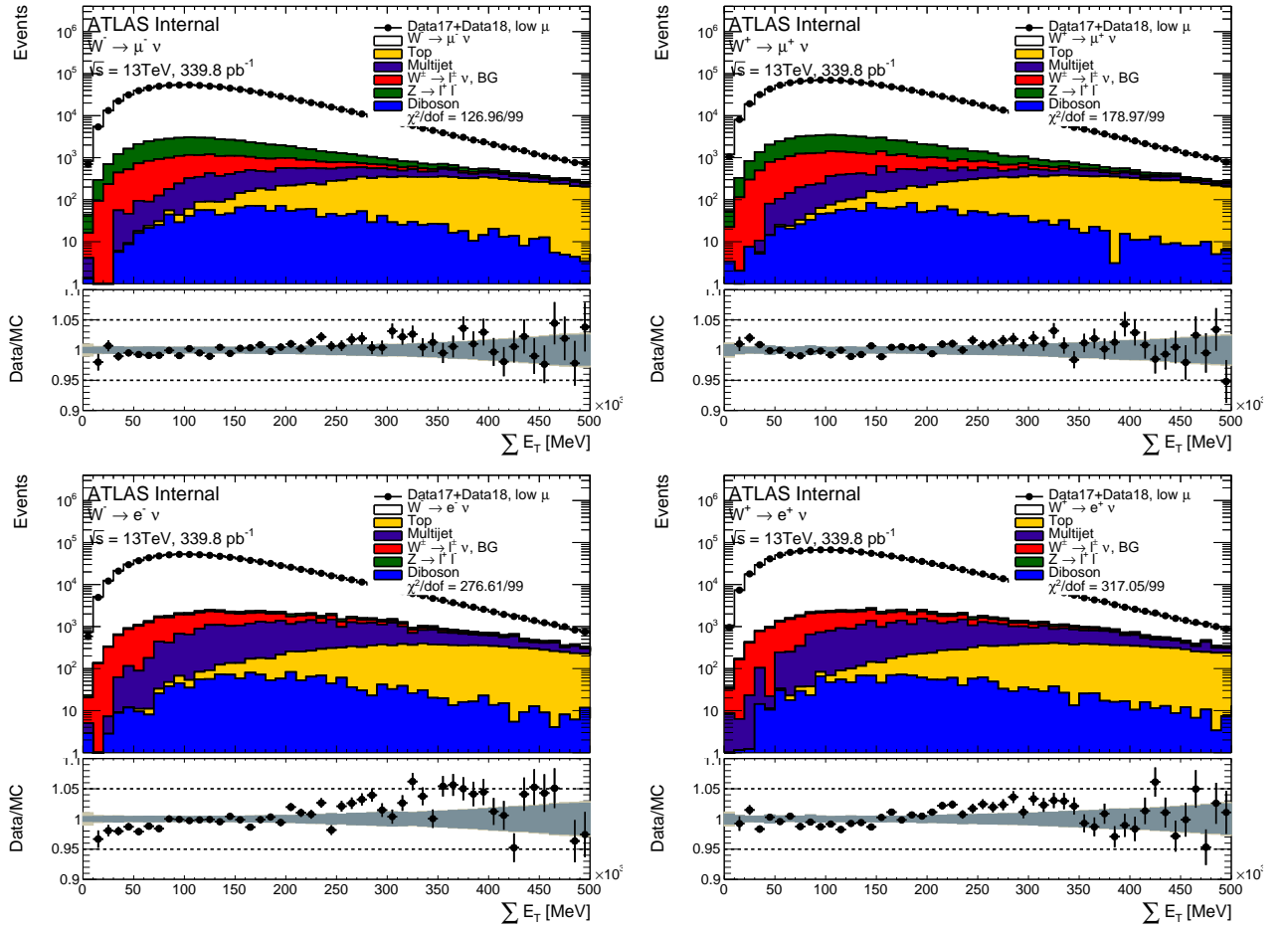


Figure 85: ΣE_T distribution in the muon and electron channel for the $\sqrt{s} = 13$ TeV dataset.

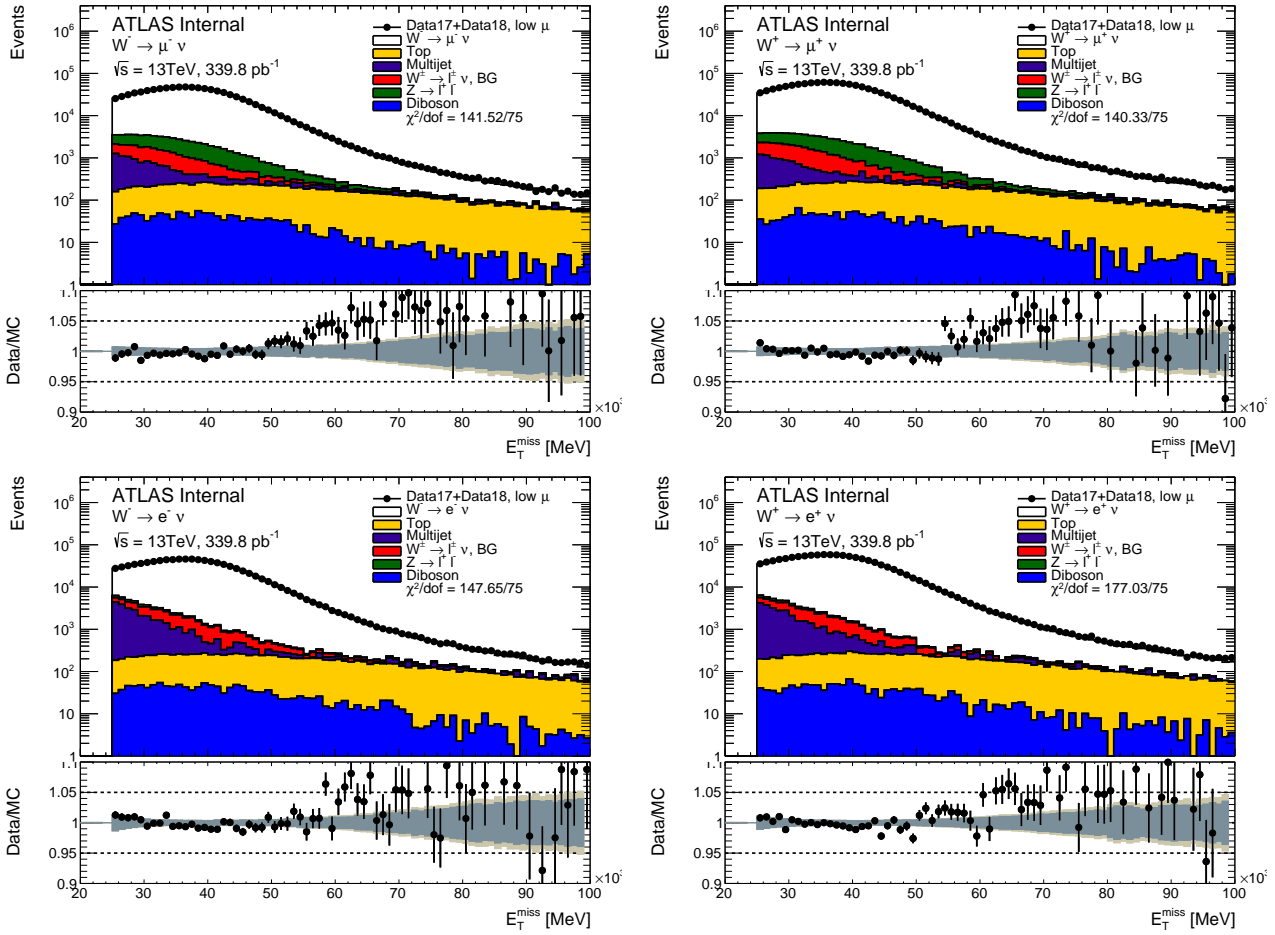


Figure 86: \vec{E}_T^{miss} distribution in the muon and electron channel for the $\sqrt{s} = 13$ TeV dataset.

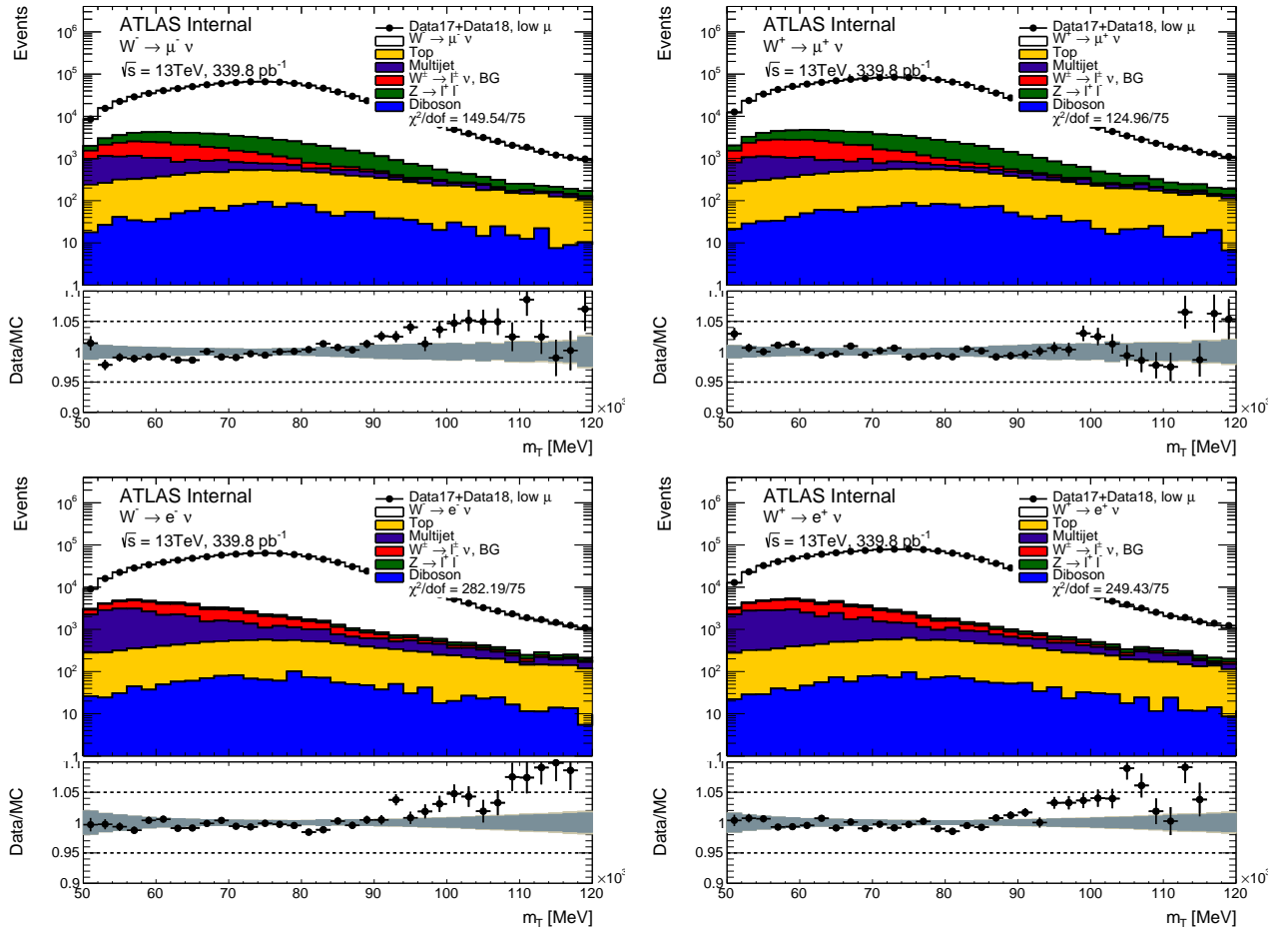


Figure 87: Transverse mass distribution of the W boson in the muon and electron channel for the $\sqrt{s} = 13$ TeV dataset.

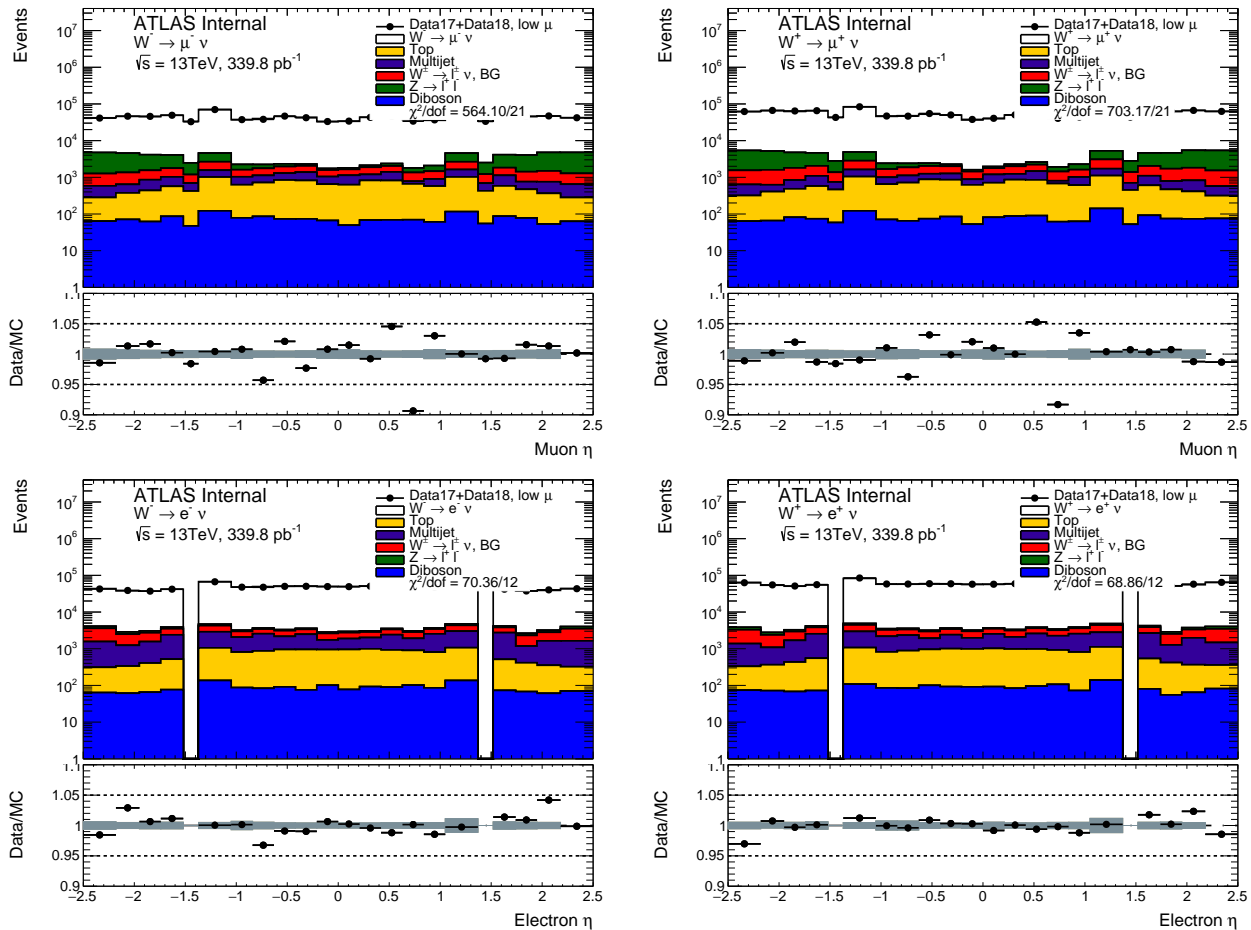


Figure 88: Lepton pseudorapidity distribution in the muon and electron channel for the $\sqrt{s} = 13 \text{ TeV}$ dataset.

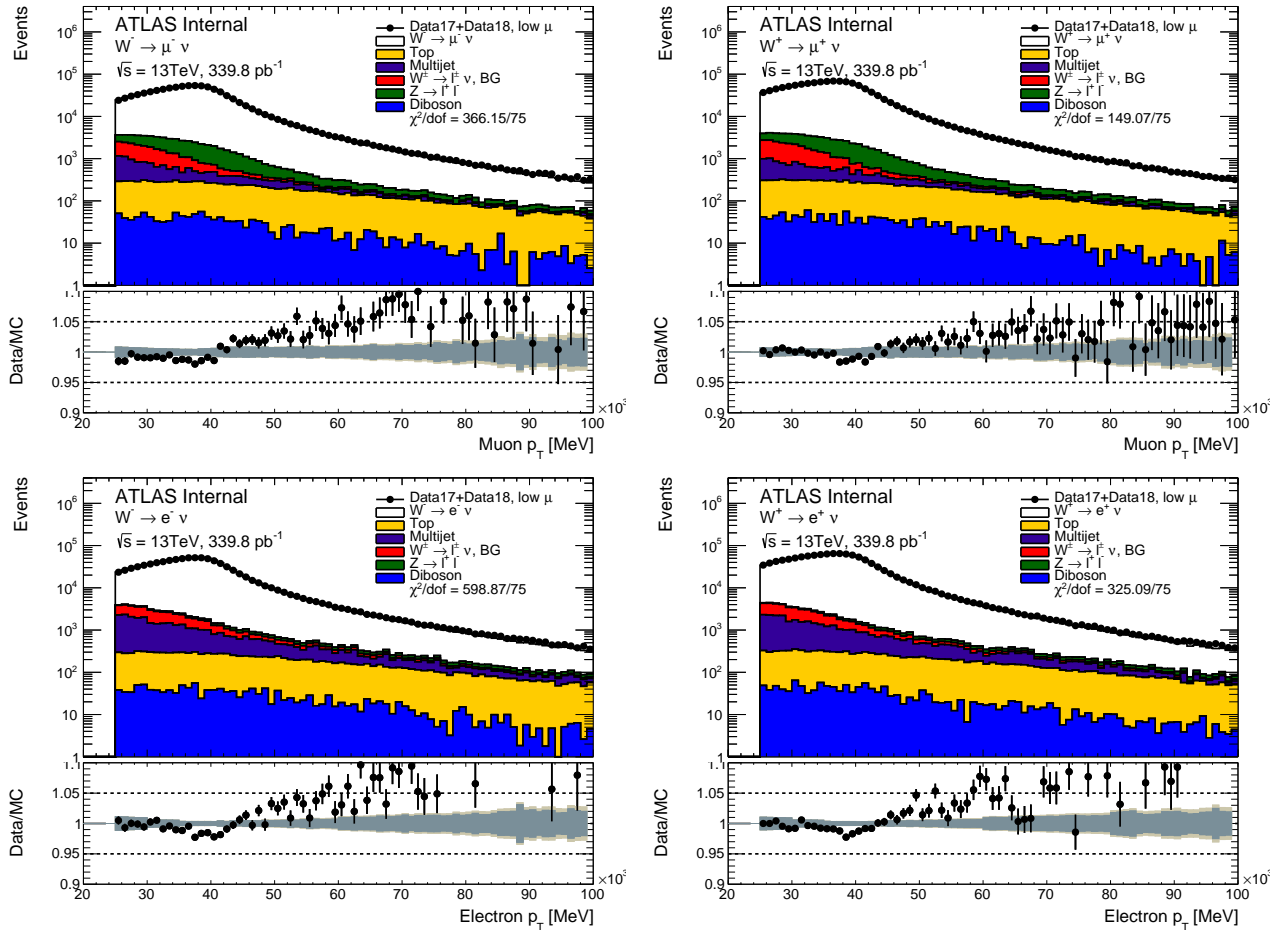


Figure 89: Lepton transverse momentum distribution in the muon and electron channel for the $\sqrt{s} = 13\text{TeV}$ dataset.

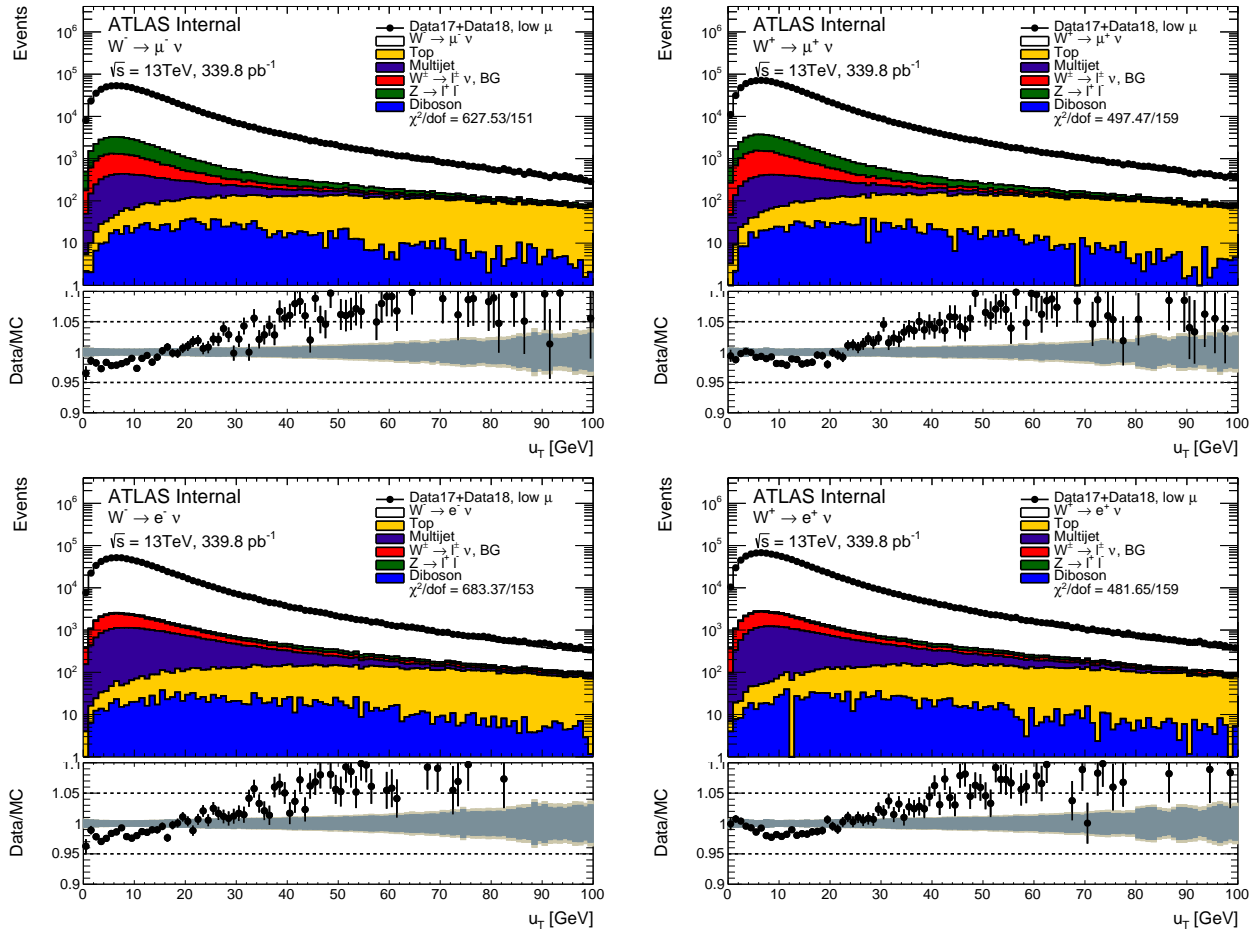


Figure 810: W transverse momentum distribution in the muon and electron channel for the $\sqrt{s} = 13\text{TeV}$ dataset.

2376 **8.3.3 $\sqrt{s} = 5$ TeV dataset control plots**

2377 Control plots for the 5 TeV low- μ dataset are provided here after applying all corrections described
 2378 in section ??, and after applying the selection described above in this section. In each figure, the
 2379 right(left)-hand column shows distributions for the W^+ (W^-) process. The top (bottom) row shows the
 2380 muon (electron) decay channel. In the ratio panels, the grey band is the total systematic uncertainty,
 2381 whilst the brown band adds the MC statistical uncertainty in quadrature on top of it. In regions of
 2382 the distributions insensitive to the modelling of p_T^W there is generally good agreement between data
 2383 and predictions. The bulk of the m_T distribution is a typical example of distribution that is mostly
 2384 insensitive to the modeling of p_T^W . Compared to the 13 TeV situation, the u_T distribution seems to
 2385 indicate that the baseline simulation models p_T^W more satisfactorily.

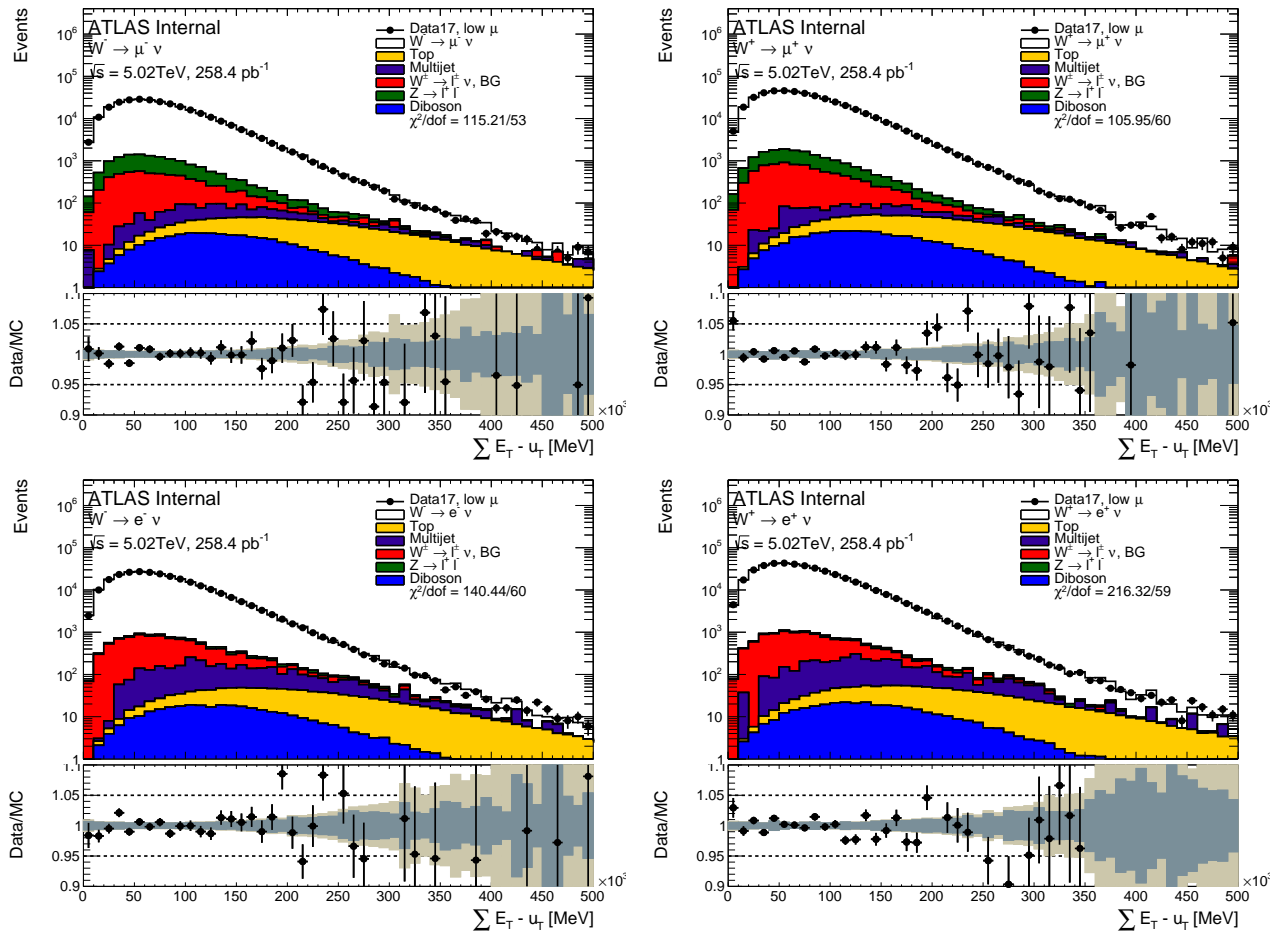


Figure 811: ΣE_T distribution in the muon and electron channel for the $\sqrt{s} = 5$ TeV dataset.

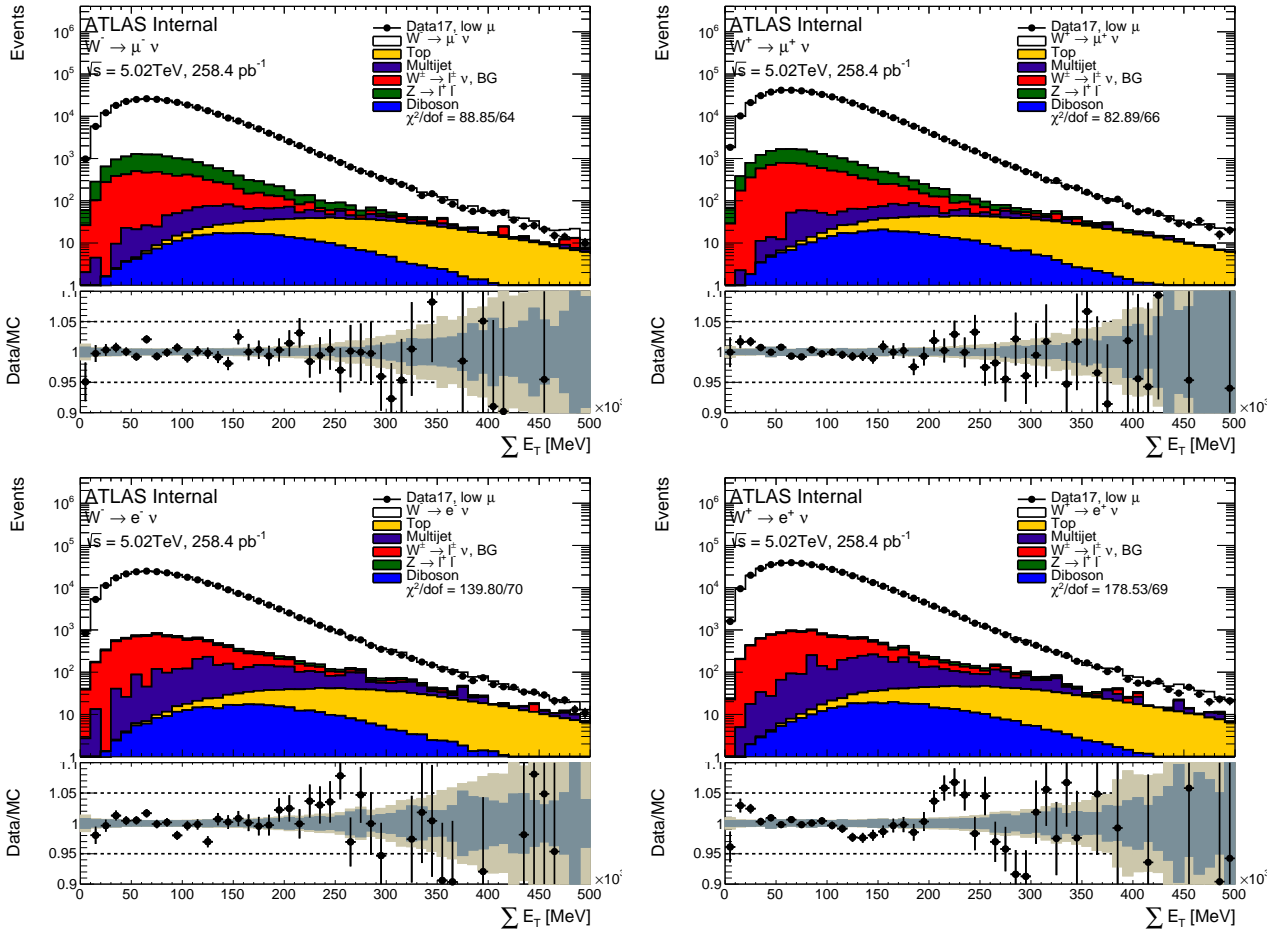


Figure 812: ΣE_T distribution in the muon and electron channel for the $\sqrt{s} = 5$ TeV dataset.

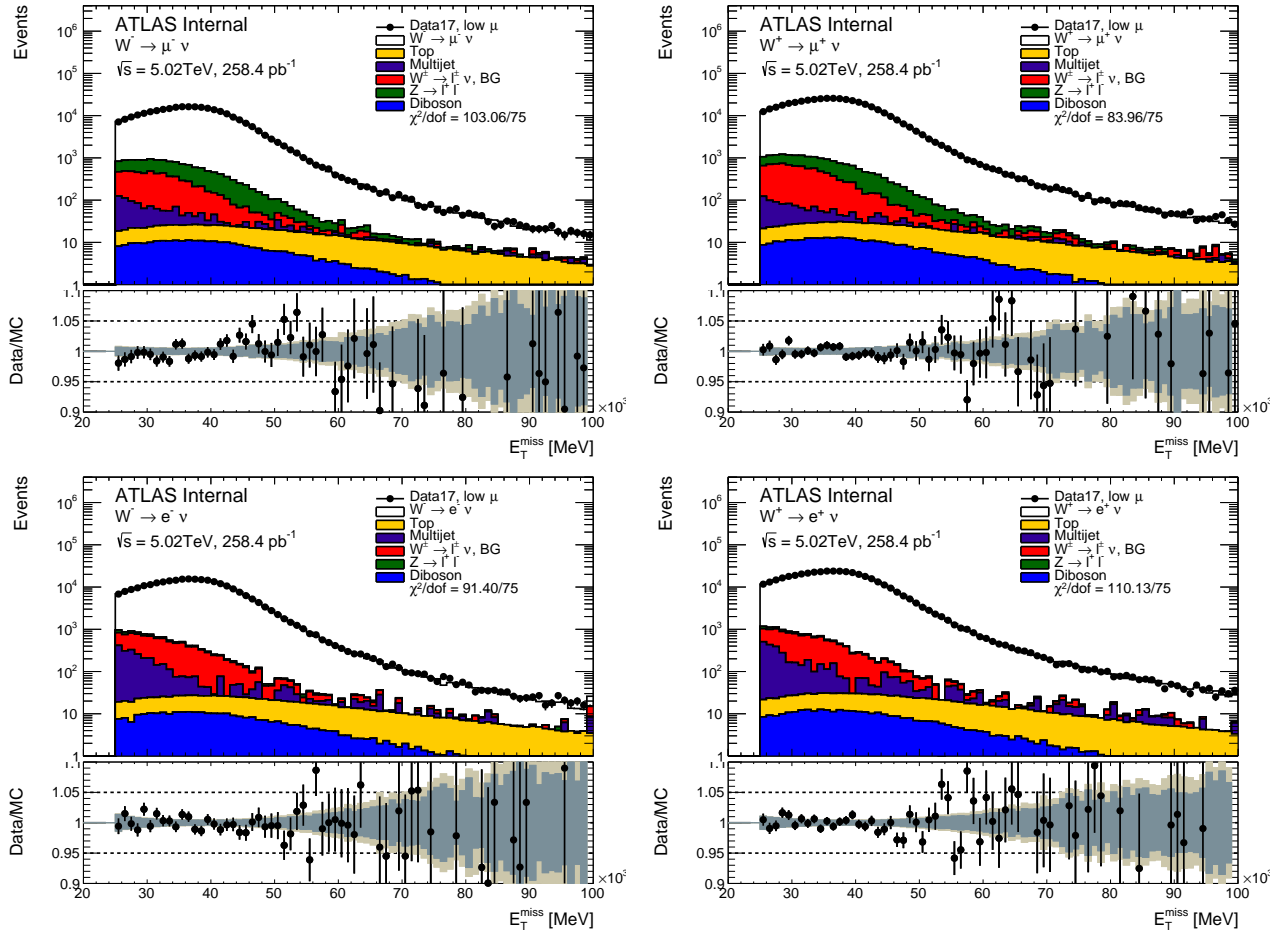


Figure 813: \vec{E}_T^{miss} distribution in the muon and electron channel for the $\sqrt{s} = 5$ TeV dataset.

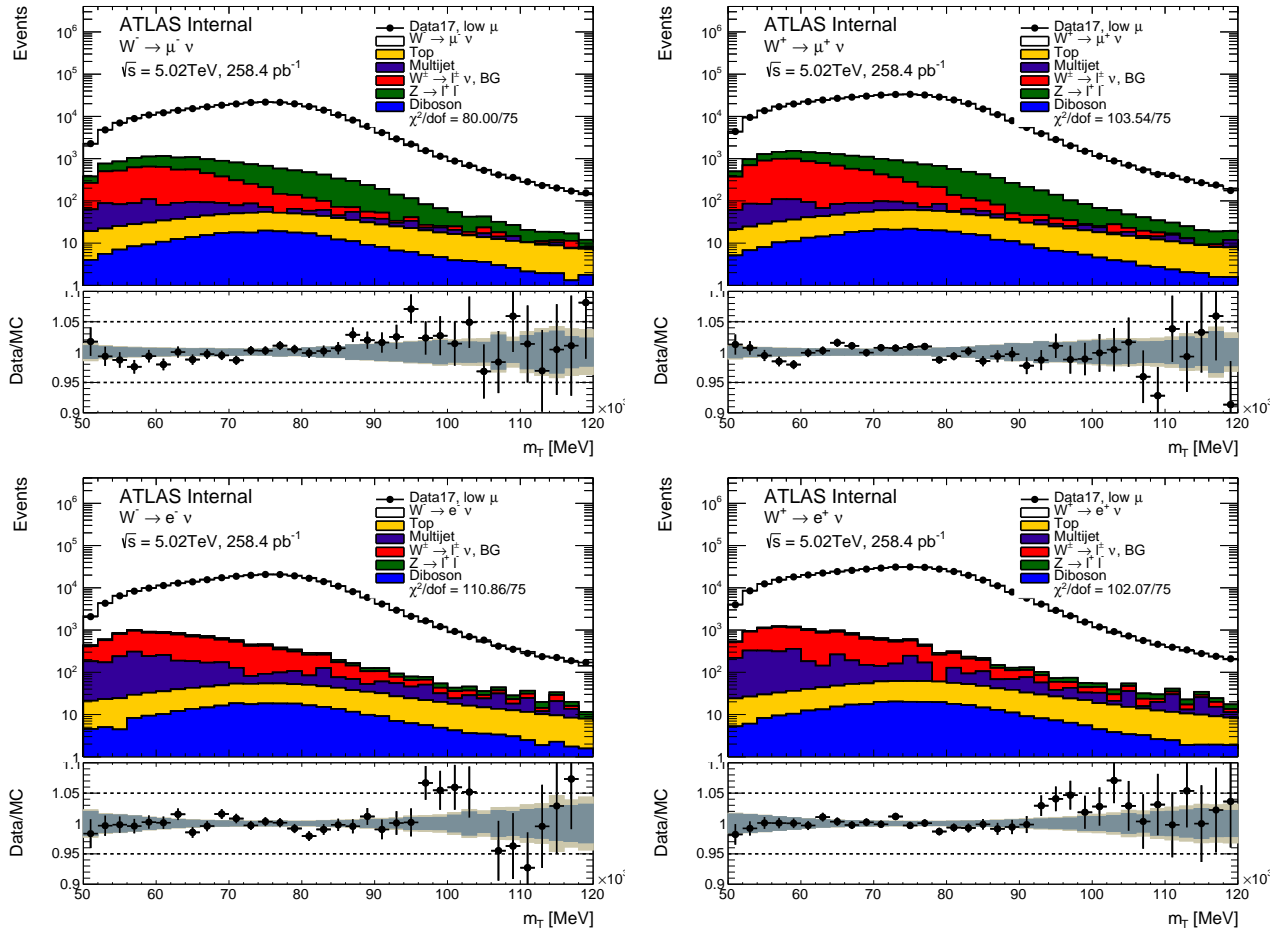


Figure 814: Transverse mass distribution of the W boson in the muon and electron channel for the $\sqrt{s} = 5$ TeV dataset.

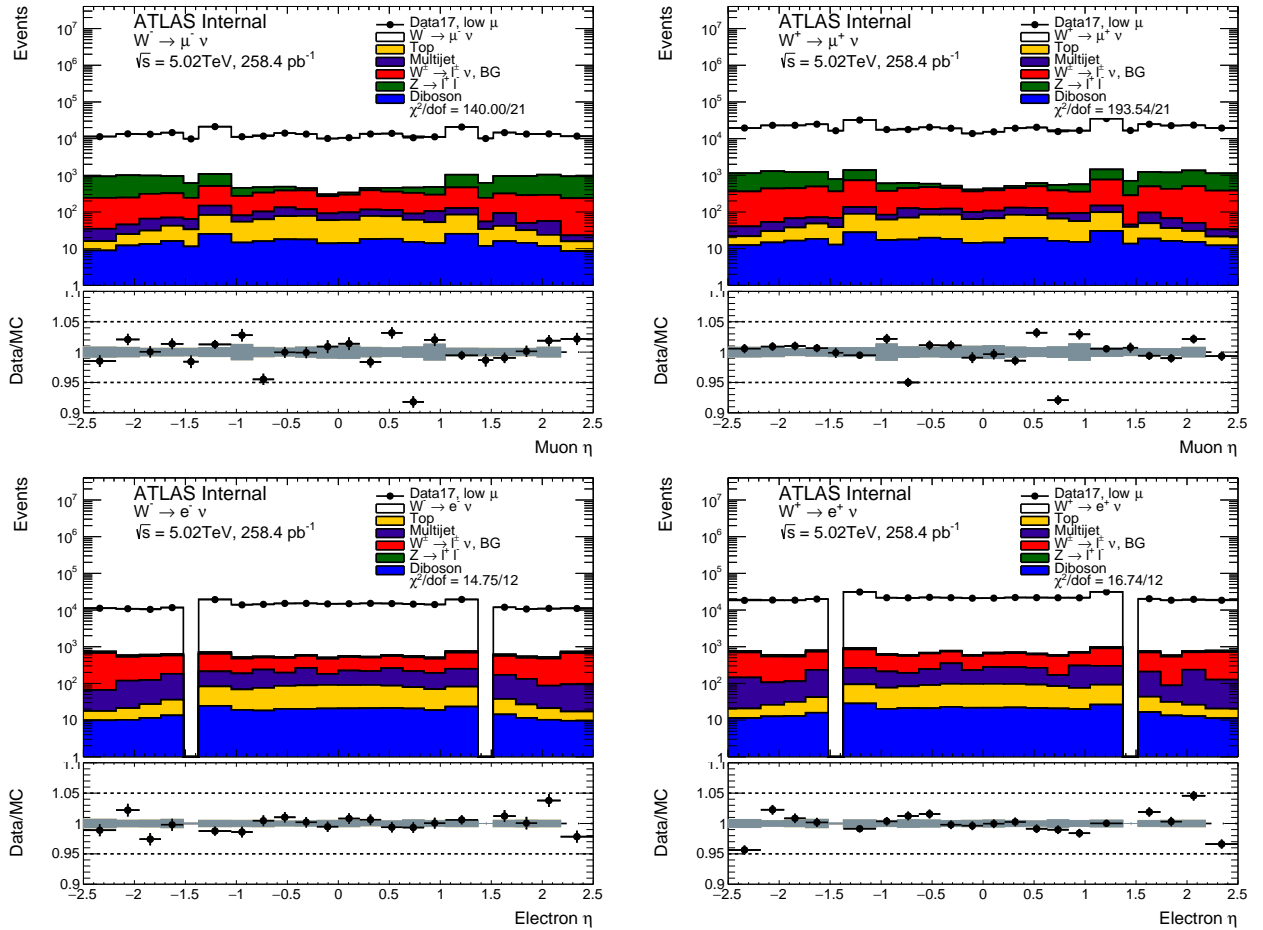


Figure 815: Lepton pseudorapidity distribution in the muon and electron channel for the $\sqrt{s} = 5\text{ TeV}$ dataset.

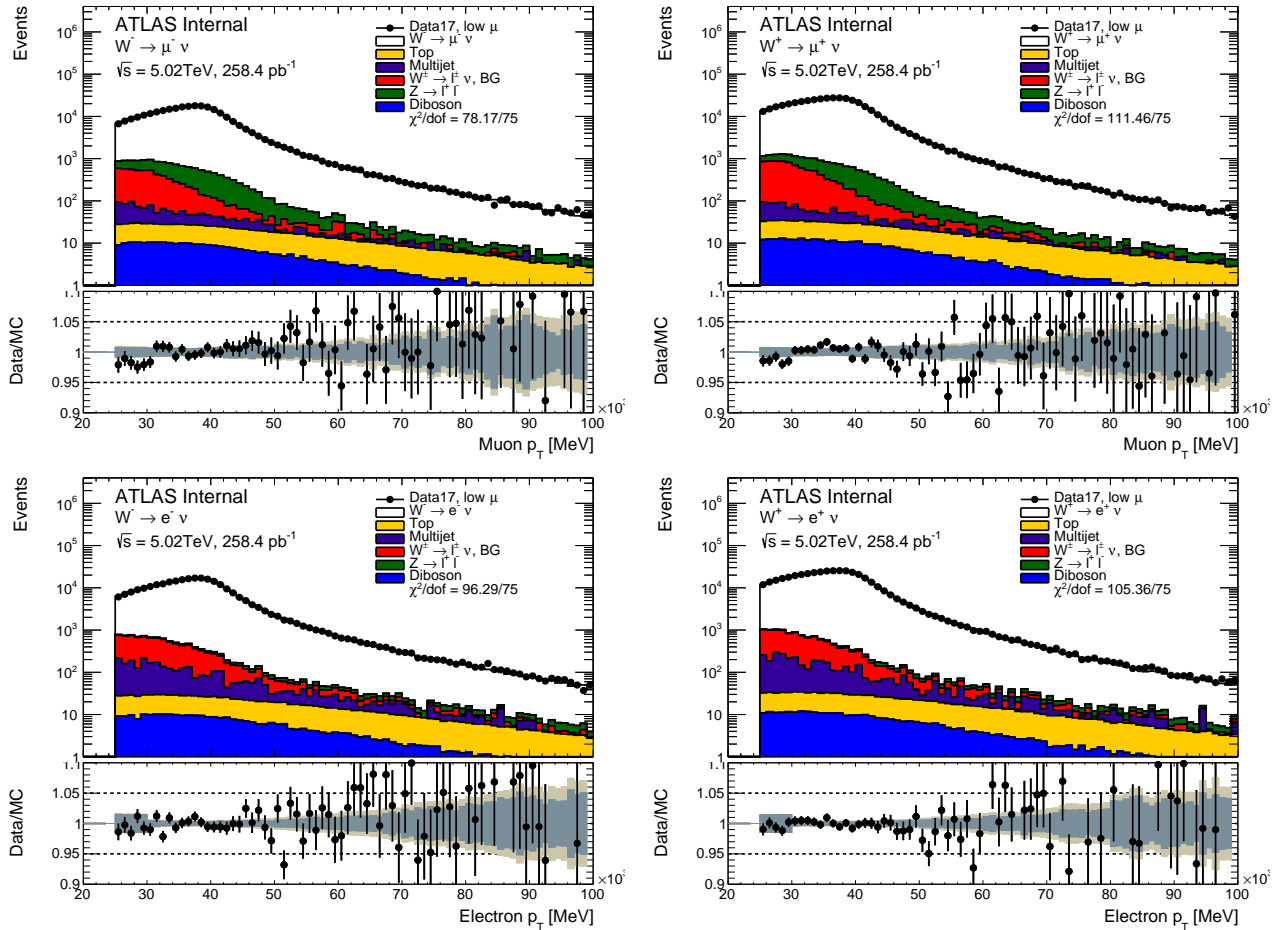


Figure 816: Lepton transverse momentum distribution in the muon and electron channel for the $\sqrt{s} = 5$ TeV dataset.

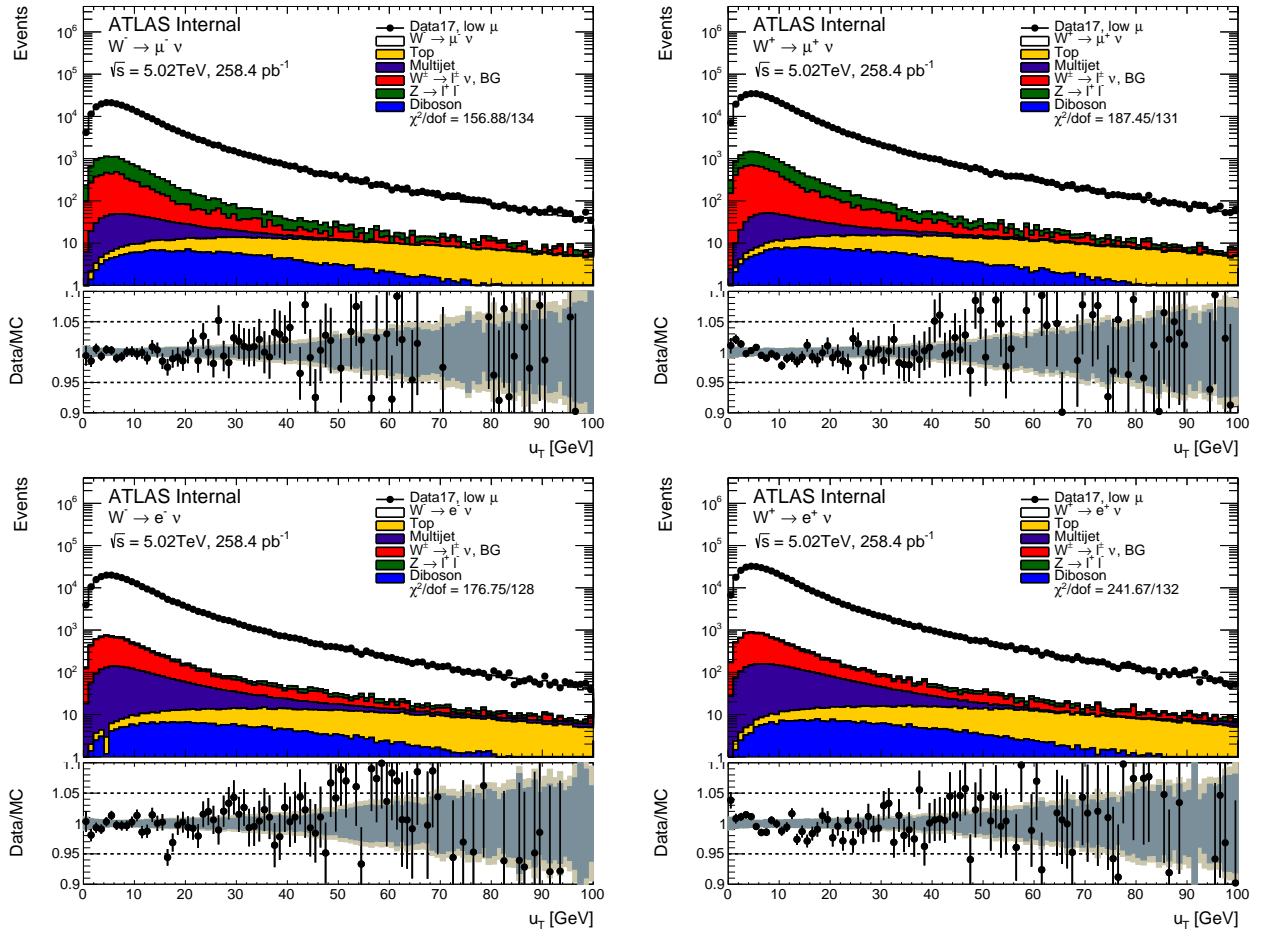


Figure 817: W transverse momentum distribution in the muon and electron channel for the $\sqrt{s} = 5$ TeV dataset.

2386 **Bibliography**

- 2387 [1] Jan Kretzschmar. *Samples and Physics modelling for low pile-up runs taken in 2017 and 2018.*
2388 Tech. rep. ATL-COM-PHYS-2019-075. Geneva: CERN, Feb. 2019. URL: <https://cds.cern.ch/record/2657141>.
- 2390 [2] Paolo Nason. “A New method for combining NLO QCD with shower Monte Carlo algorithms”.
2391 In: *JHEP* 11 (2004), p. 040. doi: 10.1088/1126-6708/2004/11/040. arXiv: hep-ph/0409146.
- 2392 [3] Stefano Frixione, Paolo Nason, and Carlo Oleari. “Matching NLO QCD computations with Parton
2393 Shower simulations: the POWHEG method”. In: *JHEP* 11 (2007), p. 070. doi: 10.1088/1126-
2394 6708/2007/11/070. arXiv: 0709.2092 [hep-ph].
- 2395 [4] Simone Alioli et al. “NLO vector-boson production matched with shower in POWHEG”. In: *JHEP*
2396 0807 (2008), p. 060. doi: 10.1088/1126-6708/2008/07/060. arXiv: 0805.4802 [hep-ph].
- 2397 [5] Simone Alioli et al. “A general framework for implementing NLO calculations in shower Monte
2398 Carlo programs: the POWHEG BOX”. In: *JHEP* 06 (2010), p. 043. doi: 10.1007/JHEP06(2010)043.
2399 arXiv: 1002.2581 [hep-ph].
- 2400 [6] T. Sjöstrand, S. Mrenna, and P. Skands. “Brief Introduction to PYTHIA 8.1”. In: *Comput. Phys.
2401 Comm.* 178 (2008), p. 85. doi: 10.1016/j.cpc.2008.01.036. arXiv: 0710.3820v1 [hep-ph].
- 2402 [7] ATLAS Collaboration. “Measurement of the Z/γ^* boson transverse momentum distribution in
2403 pp collisions at $\sqrt{s} = 7\text{ TeV}$ with the ATLAS detector”. In: *JHEP* 09 (2014), p. 145. doi: 10.1007/
2404 JHEP09(2014)145. arXiv: 1406.3660 [hep-ex].
- 2405 [8] Piotr Gonolka and Zbigniew Was. “PHOTOS Monte Carlo: A Precision tool for QED corrections
2406 in Z and W decays”. In: *Eur. Phys. J.* C45 (2006), pp. 97–107. doi: 10.1140/epjc/s2005-02396-4.
2407 arXiv: hep-ph/0506026.
- 2408 [9] Stefan Höche et al. “NLO matrix elements and truncated showers”. In: *JHEP* 1108 (2011), p. 123.
2409 doi: 10.1007/JHEP08(2011)123. arXiv: 1009.1127 [hep-ph].
- 2410 [10] Richard D. Ball et al. “Parton distributions with LHC data”. In: *Nucl. Phys. B* 867 (2013), p. 244.
2411 doi: 10.1016/j.nuclphysb.2012.10.003. arXiv: 1207.1303 [hep-ph].
- 2412 [11] ATLAS Collaboration. *The Pythia 8 A3 tune description of ATLAS minimum bias and inelastic
2413 measurements incorporating the Donnachie–Landshoff diffractive model.* ATL-PHYS-PUB-2016-017.
2414 2016. URL: <https://cds.cern.ch/record/2206965>.
- 2415 [12] S. Catani and M. Grazzini. “An NNLO subtraction formalism in hadron collisions and its
2416 application to Higgs boson production at the LHC”. In: *Phys. Rev. Lett.* 98 (2007), p. 222002. doi:
2417 10.1103/PhysRevLett.98.222002. arXiv: hep-ph/0703012 [hep-ph].
- 2418 [13] S. Catani et al. “Vector boson production at hadron colliders: A Fully exclusive QCD calculation
2419 at NNLO”. In: *Phys. Rev. Lett.* 103 (2009), p. 082001. doi: 10.1103/PhysRevLett.103.082001.
2420 arXiv: 0903.2120 [hep-ph].

- 2421 [14] L.A. Harland-Lang, A. D. Martin, P. Motylinski, R. S. Thorne. “Parton distributions in the LHC
2422 era: MMHT 2014 PDFs”. In: *Eur. Phys. J. C* 75.5 (2015), p. 204. doi: 10.1140/epjc/s10052-015-
2423 3397-6. arXiv: 1412.3989 [hep-ph].
- 2424 [15] ATLAS Collaboration. “Measurement of W^\pm and Z-boson production cross sections in pp col-
2425 lisions at $\sqrt{s} = 13\text{TeV}$ with the ATLAS detector”. In: *Phys. Lett. B* 759 (2016), p. 601. doi:
2426 10.1016/j.physletb.2016.06.023. arXiv: 1603.09222 [hep-ex].
- 2427 [16] ATLAS Collaboration. “Measurements of W and Z boson production in pp collisions at $\sqrt{s} =$
2428 5.02TeV with the ATLAS detector”. In: *Eur. Phys. J. C* 79 (2019), p. 128. doi: 10.1140/epjc/
2429 s10052-019-6622-x. arXiv: 1810.08424 [hep-ex].
- 2430 [17] CMS Colaboration. “Measurement of the inclusive $t\bar{t}$ cross section in pp collisions at $\sqrt{s} = 5.02$
2431 TeV using final states with at least one charged lepton”. In: *JHEP* 03 (2018), p. 115. doi: 10.1007/
2432 JHEP03(2018)115. arXiv: 1711.03143 [hep-ex].

9

W boson pT spectrum

2433

2434

2435 “*Potentielle citation sans aucun rapport avec le sujet*”

2436 — Personne inconnue, *contexte à déterminer*

2437 9.1 Unfolding

2438 The measured W p_T spectrum is subject to various detector effects (finite resolution and acceptance,
2439 reconstruction efficiency, etc.) that distort the true underlying spectrum. Mathematically, the unfolding
2440 problem is an integral equation of the following form:

$$\int K(x, y) \cdot f(x) dx = g(y), \quad (9.1)$$

2441 where we seek the function $f(x)$ assuming that $g(y)$ and the kernel $K(x, y)$ are known [1]. The function
2442 $g(y)$ is convoluted (or folded) with the kernel hence the name of the problem. In experimental physics
2443 it is more common to use binned distributions instead of continuous functions:

$$\sum_i \mathbf{R}_{ij} \cdot \mathbf{T}_i + \mathbf{B}_j = \mathbf{D}_j, \quad (9.2)$$

2444 with \mathbf{D} , \mathbf{T} and \mathbf{B} being vectors that represent detector-level (measured), truth and background dis-
2445 tributions respectively; each vector has n components that represent the bins in the corresponding
2446 distribution. The response matrix \mathbf{R} represents bin-to-bin migrations caused by the detector effects.
2447 The response matrix is usually obtained through MC simulation, along with the corrections for the
2448 fiducial volume acceptance and efficiency. Each event is simulated on the truth and reconstructed
2449 levels, this means that element R_{il} of the migration matrix contains events that pass both reconstruction
2450 and truth cuts (R&T) and would go to bin i of the truth distribution and to bin j of the reconstructed
2451 distribution. Detector acceptance for bin i is defined as the ratio $A_i = \sum_j R_{ij}/T_i$. Similarly the recon-
2452 struction efficiency for bin j is defined as the ratio $\epsilon_j = \sum_i R_{ij}/D_j$. The underlying distribution estimate
2453 is presented in the following way:

$$\sum_i \mathbf{V}_{ij} \cdot (\mathbf{D}_i - \mathbf{B}_i) = \mathbf{U}_j, \quad (9.3)$$

2454 where U vector provides the underlying distribution estimate and V is the unfolding transformation
2455 matrix.

2456 There exist a diverse variety of methods to obtain the unfolding transformation. In the current analysis

2457 a Bayesian iterative method is used [2], [3]. The method allows to obtain the unfolding transformation
 2458 provided that the response matrix, acceptance and efficiency corrections are known and the number of
 2459 iterations is given. The number of iterations as well as the unfolded distribution binning are adjusted
 2460 in order to minimize the unfolding bias and keep the uncertainty below the designated level.

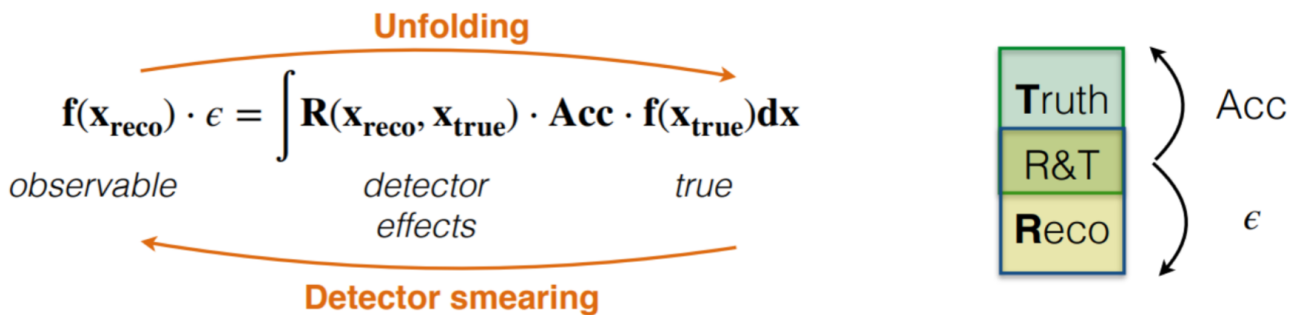


Figure 91: Schematic description of the unfolding procedure.

2461 9.2 Uncertainties propagation

2462 The detector-level uncertainties breakdown for the p_T distribution are presented here. Uncertainties
 2463 breakdown for the rest of the observables are listed in Appendix A.
 2464 These uncertainties now have to be propagated to the unfolded level.

2465 9.2.1 Statistical uncertainty propagation using Bootstrap method

2466 Bootstrap is a computer-based method of dataset parameters estimate and propagation using the
 2467 analysis distribution resampling. In particular bootstrapping used for the propagation of statistical
 2468 uncertainties.

2469 Both data and MC-simulated datasets have limited number of events, hence the statistical uncertainties
 2470 due to fluctuations. In order to estimate the statistical uncertainty a number of pseudo-data sets is
 2471 generated for both data and MC where each event is assigned a random weight w :

$$w = \mathcal{P}(n, 1), \quad (9.4)$$

2472 where n is a random number generated with Poisson distribution with mean $\lambda = 1$, value $\mathcal{P}(n, 1)$ is a
 2473 Poissonian probability of observing n events while expecting an average of 1 event.
 2474 The bootstrapping defined in this way allows to take into account the correlated effect of statistical
 2475 fluctuations across all observables and distributions in the analysis. For the determination of statistical
 2476 uncertainty of the unfolded spectrum 400 bootstrap samples were generated. In both data and MC

²⁴⁷⁷ cases the statistical uncertainty is estimated by composing the covariant matrix C_{kl}^{stat} :

$$C_{kl}^{stat} = \frac{1}{N_{bs}-1} \sum_{\alpha=1}^{N_{bs}} (U_k^\alpha - \langle U_k \rangle)(U_l^\alpha - \langle U_l \rangle), \quad (9.5)$$

where N_{bs} is the number of the Bootstrap toys used, vector U stands for the varied underlying distribution, $\langle U_k \rangle$ is the average underlying distribution. However, the variation is performed in a different way for Data and MC:

$$U_j^{\alpha, (MC)} = V_{ij}^\alpha \sum_i (D_i - B_i),$$

$$U_j^{\alpha, (Data)} = V_{ij} \sum_i (D_i^\alpha - B_i).$$

²⁴⁷⁸ In the MC case it is the response matrix V^α to be varied (α index corresponds to the variation number),
²⁴⁷⁹ whereas in Data the toys are obtained by varying the measured distribution D_i^α . The statistical
²⁴⁸⁰ uncertainty for both cases is defined as:

$$\delta U_k = \sqrt{C_{kk}^{stat}}. \quad (9.6)$$

²⁴⁸¹ 9.2.2 Systematic uncertainty propagation

Systematic uncertainties are broken down into a number of uncorrelated uncertainty sources, which include signal and background modelling uncertainties, calibration and efficiency uncertainties, physics modelling uncertainties. The systematic variations used for uncertainty estimate on the detector level are propagated to the level of underlying distribution in two different ways. For the background uncertainties:

$$U_j^a = V_{ij} \sum_i (D_i - B_i^a),$$

total background estimate B_i^a is varied in luminosity and cross-section of every back-ground (index a numbers the sources of uncertainty). For other sources of systematic uncertainty:

$$U_j^a = V_{ij}^a \sum_i (D_i - B_i),$$

response matrix variation is created. The corresponding covariance matrix is defined as:

$$C_{kj}^a = \delta U_k^a \delta U_l^a,$$

²⁴⁸² where the deltas are $\delta U_k^a = U_k^a - U_k^{Nom}$. The total covariance matrix is calculated as a sum:

$$C_{kl}^{tot} = C_{kl}^{stat, Data} + C_{kl}^{stat, MC} + \sum_a C_{kl}^a. \quad (9.7)$$

2483 **9.2.3 Unfolded uncertainty breakdown**

2484 Figures 92, 94, contain the systematic uncertainties breakdown for electron and muon channels for
 2485 the reconstructed level distributions for 5 and 13 TeV. Similarly figures 93, 95 contain unfolded-level
 2486 uncertainties.

2487 At the detector level the designated level of uncertainty of below 1% is preserved up to 25 GeV for 5
 2488 TeV datasets and up to 50 GeV for 13 TeV samples in every channel. An increased role of background
 2489 uncertainty is observed at 13 TeV due to the significantly higher cross-sections of diboson and top-
 2490 antitop backgrounds. The scale and hierarchy of uncertainties are preserved at the unfolded level.

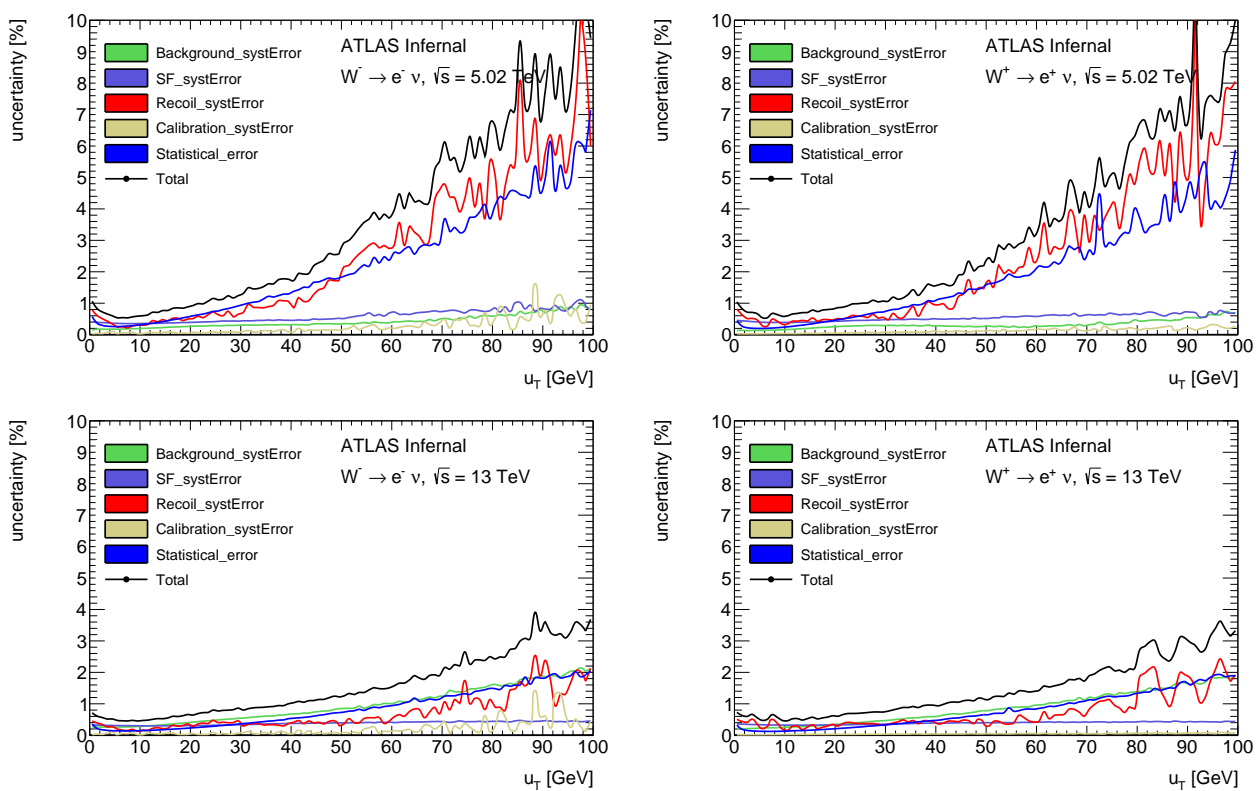


Figure 92: Breakdown of systematic uncertainties for 5 (a,b) and 13 (c,d) TeV in the electron channel at the reconstructed level

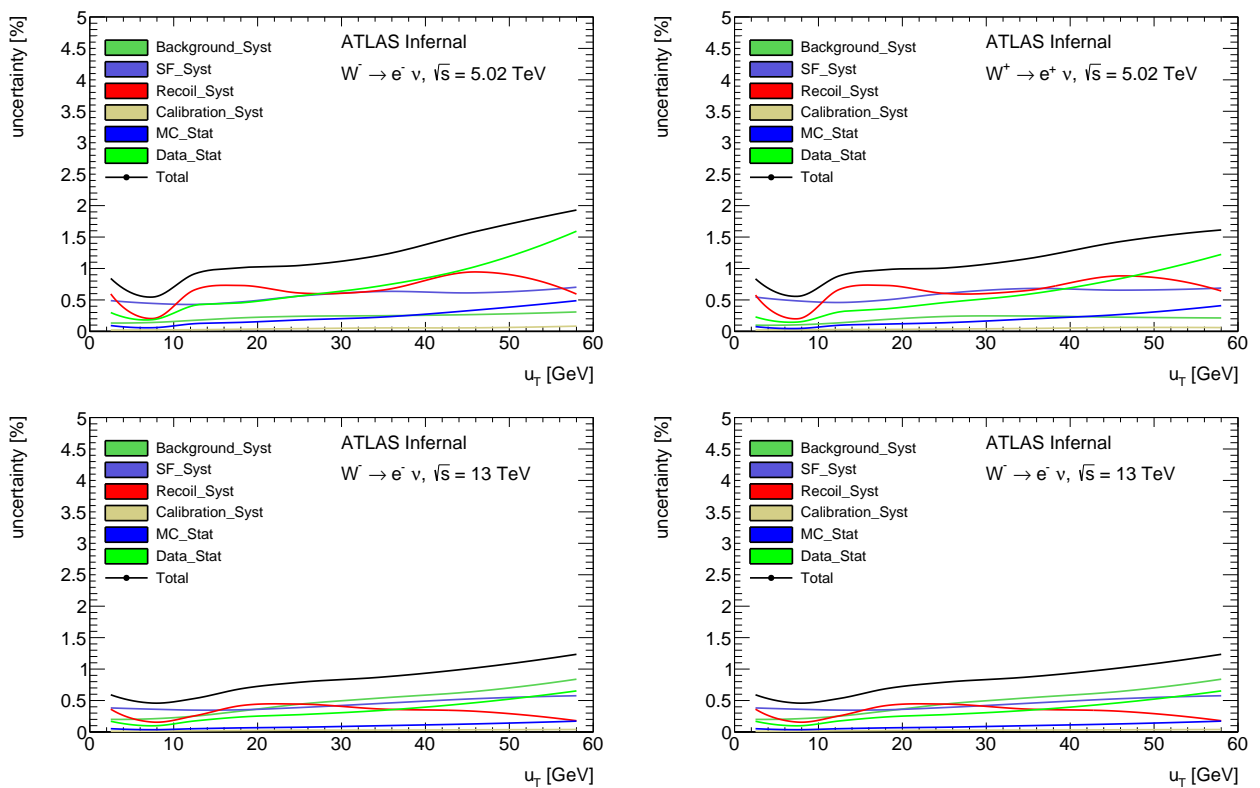


Figure 93: Breakdown of systematic uncertainties for 5 (a,b) and 13 TeV (c,d) in the electron channel at the unfolded level

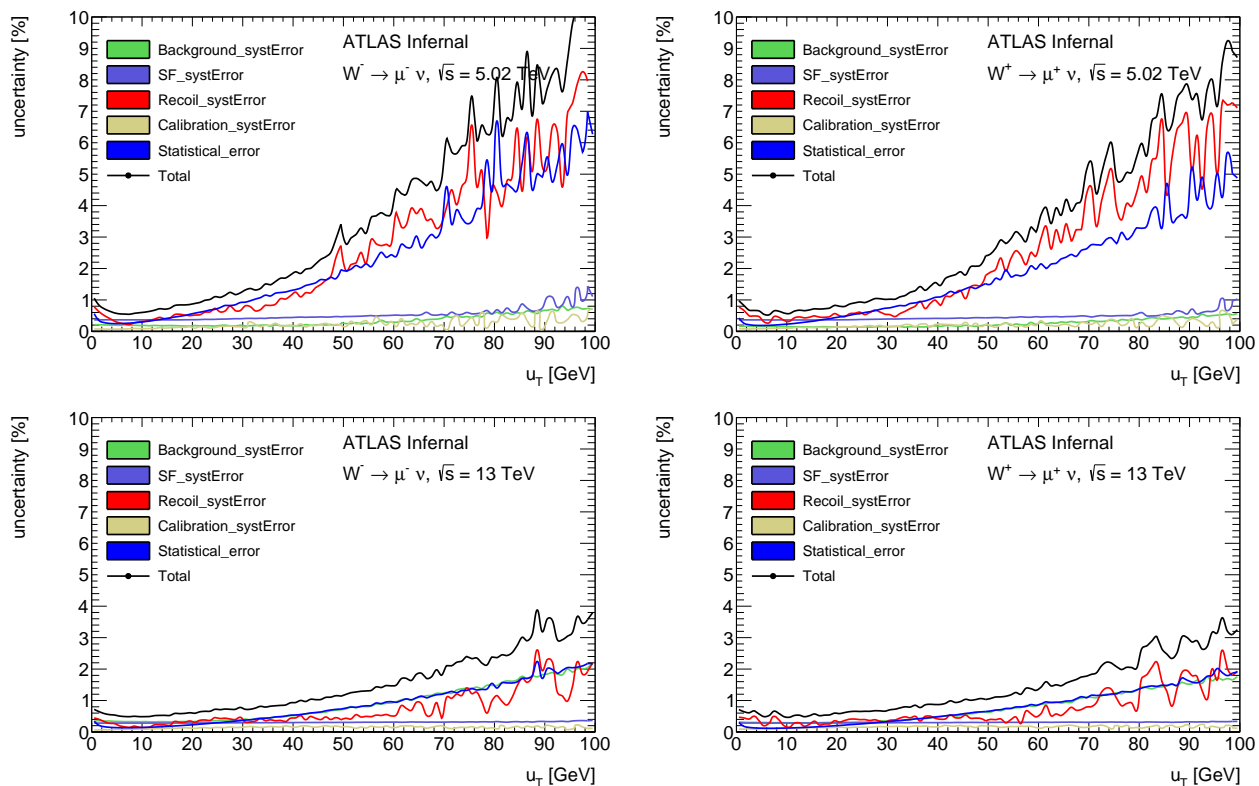


Figure 94: Breakdown of systematic uncertainties for 5 (a,b) and 13 (c,d) TeV in the muon channel at the reconstructed level

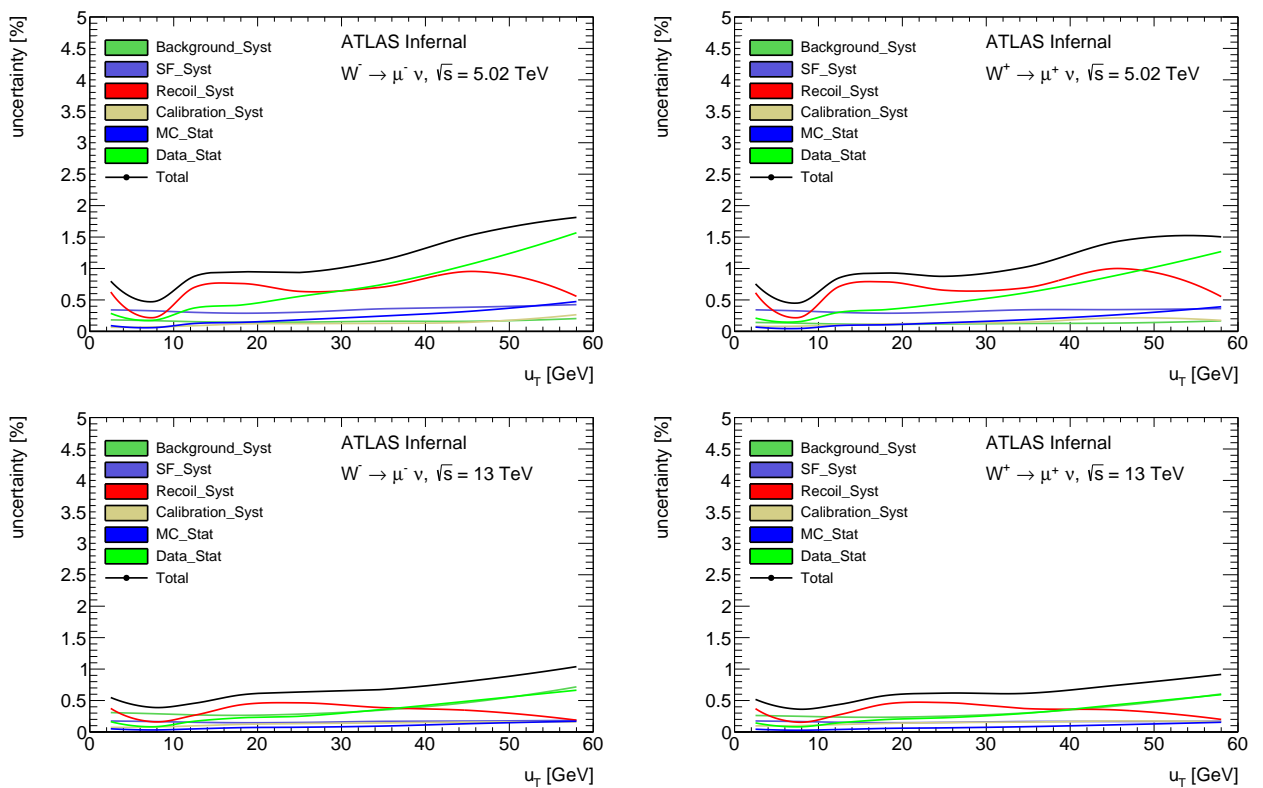


Figure 95: Breakdown of systematic uncertainties for 5 (a,b) and 13 TeV (c,d) in the muon channel at the unfolded level

2491 **9.3 Unfolding bias**

2492 One of the uncertainties associated with unfolding usage is called unfolding bias and may arise because
2493 the procedure relies on the MC simulation of the distribution, which is used as a prior hypothesis for
2494 the Bayesian algorithm. Possible discrepancies between the modelled and true distribution lead to
2495 erroneous bin-to-bin migrations and can lead to distortions of the spectrum.

2496 In order to estimate the bias induced by the unfolding procedure it is necessary to quantify how much
2497 the unfolded result is impacted by the assumed MC distribution. A set of samples with a different
2498 distribution at the truth level though compatible at the detector level is generated.

2499

2500 The truth distribution is reweighted until a good agreement between the data and MC is reached at
2501 the reconstruction level. The agreement is estimated in the kinematic region of $u_T < 100\text{GeV}$ using the
2502 χ^2 criterion. The truth reweighting procedure is applied to MC samples with a different distribution:
2503 PYTHIA8, Sherpa and DYRES were used. Fig. demonstrates the initial difference in the distributions.

2504

2505 The results are presented on fig 96 for 5 GeV bins and 3 unfolding iterations. The obtained bias is
2506 close to the precision goal of the measurement ($\sim 1\%$) for the 5 TeV dataset. The 13 TeV dataset shows
2507 a larger bias, which can be explained by a larger discrepancy between data and Monte-Carlo. Worse
2508 resolution in 13 TeV suggests a necessity to try a broader binning comparing to 5 GeV.

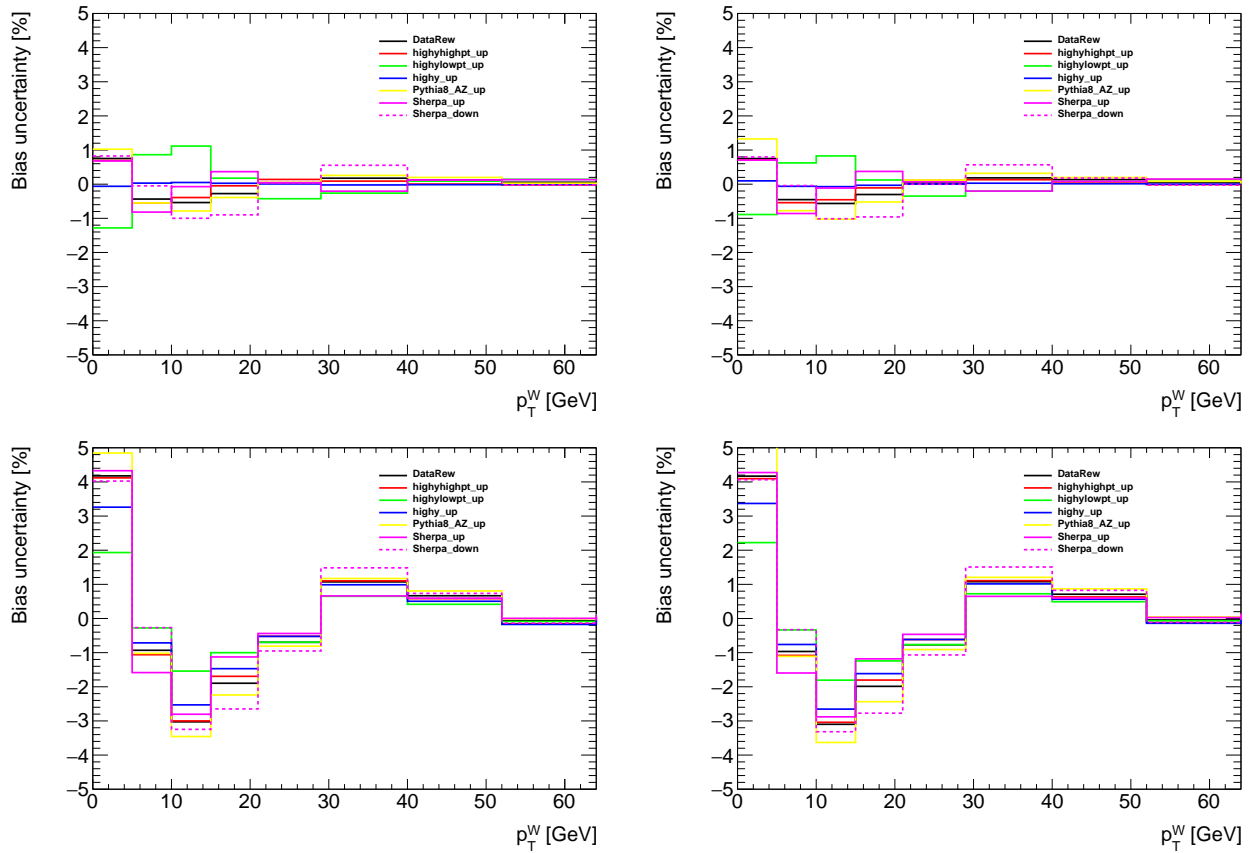


Figure 96: Unfolding bias on p_T^W in the electron channel after 3 iterations, for W^- (left) and W^+ (right), at 5 TeV (top) and 13 TeV (bottom).

2509

9.4 Results

2510 The comparison of unfolded spectrum to different theoretical predictions is presented at Figure 97 for
 2511 electron channel and at 98 for the muon channel. The estimated experimental uncertainties raise from
 2512 1% at low p_T^W to about 5% (2%) at $p_T^W = 100$ GeV, at 5 TeV (13 TeV).

2513 The predictions are generated using Powheg AZNLO, Pythia AZ, Sherpa and DYRES. Powheg and
 2514 Pythia agree with the data to a similar extent. A softer spectrum is predicted by Sherpa, while DYRES
 2515 is on the opposite side compared to the data. The observed behaviour holds for both energies, both
 2516 charges and both decay channels.

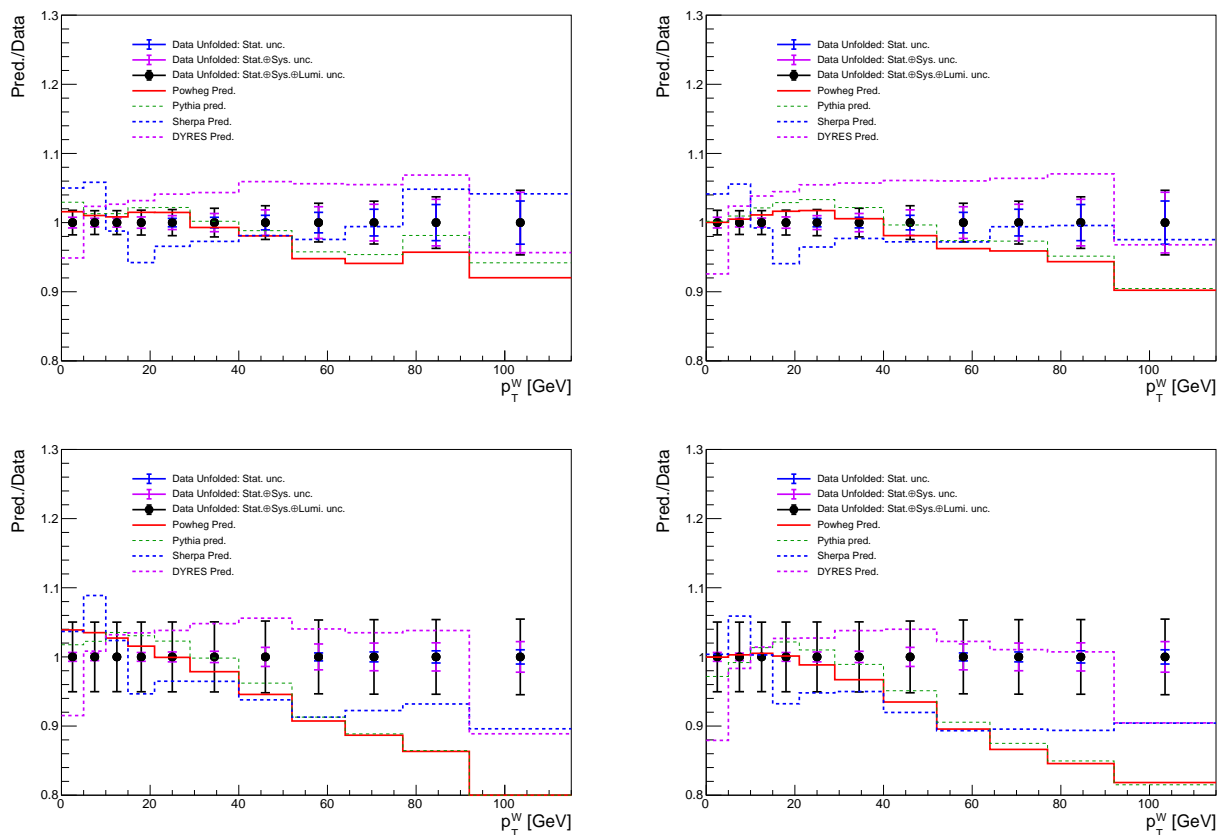


Figure 97: Unfolded measurement results in the W^- (left) and W^+ (right) electron channels, at 5 TeV (top) and 13 TeV (bottom).

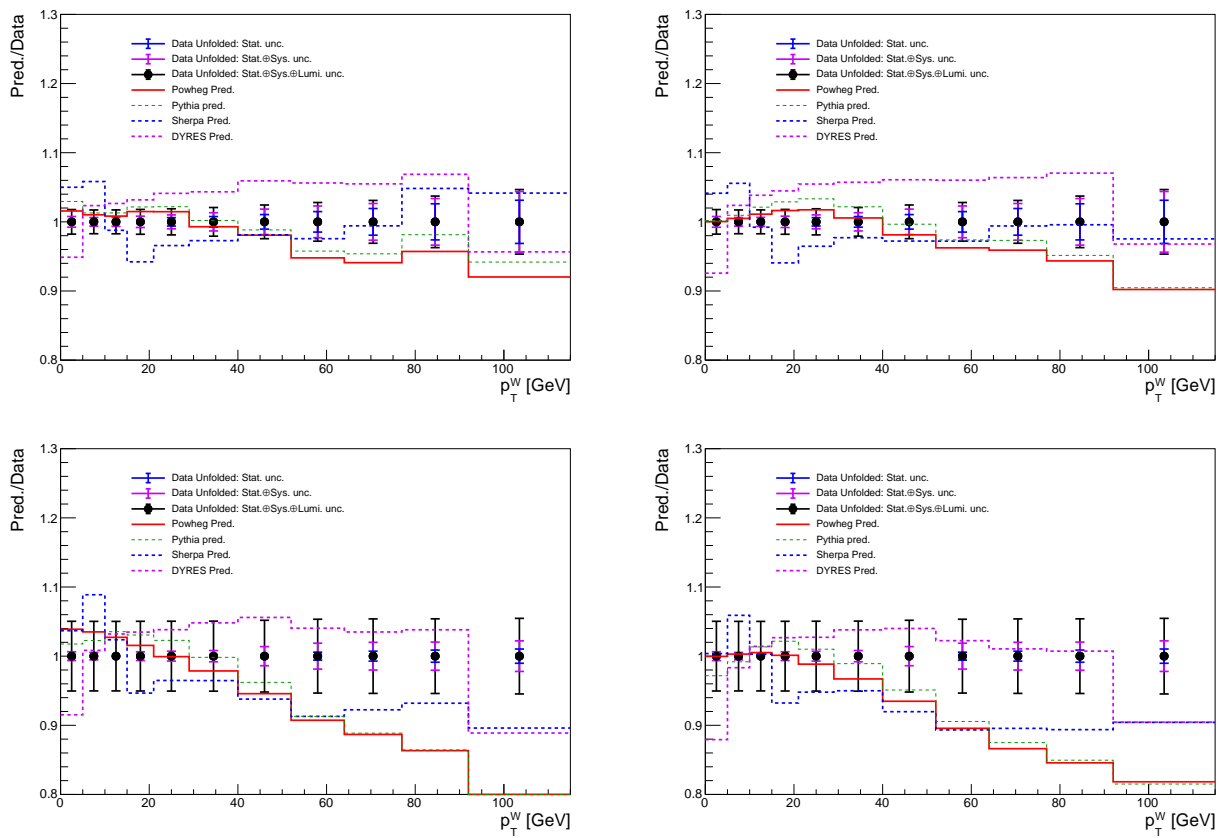


Figure 98: Unfolded measurement results in the W^- (left) and W^+ (right) muon channels, at 5 TeV (top) and 13 TeV (bottom).

2517 Bibliography

- 2518 [1] Stefan Schmitt. “Data Unfolding Methods in High Energy Physics”. In: *EPJ Web Conf.* 137 (2017).
2519 Ed. by Y. Foka, N. Brambilla, and V. Kovalenko, p. 11008. doi: 10.1051/epjconf/201713711008.
2520 arXiv: 1611.01927 [physics.data-an].
- 2521 [2] G. D’Agostini. “A multidimensional unfolding method based on Bayes’ theorem”. In: *Nuclear
2522 Instruments and Methods in Physics Research Section A: Accelerators, Spectrometers, Detectors and
2523 Associated Equipment* 362.2 (1995), pp. 487–498. issn: 0168-9002. doi: [https://doi.org/10.1016/0168-9002\(95\)00274-X](https://doi.org/10.1016/0168-9002(95)00274-X). url: <http://www.sciencedirect.com/science/article/pii/016890029500274X>.
- 2524 [3] G. D’Agostini. “Improved iterative Bayesian unfolding”. In: *Alliance Workshop on Unfolding and
2525 Data Correction*. Oct. 2010. arXiv: 1010.0632 [physics.data-an].

2528

2529

Hadronic recoil regression with deep neural networks

2530 In the recent years a significant progress was achieved in the field of big datasets analysis. There is a
2531 number of principles available for solving a wide variety of tasks. In this thesis a DNN was used for
2532 the regression of the 2-component hadronic recoil vector.

2533 10.1 Deep neural networks

2534 Normally a machine learning problem has a number of ingredients: a dataset \mathbf{X} , a set of parameters
2535 θ , a model $g(\theta)$ and a loss function $C(\mathbf{X})$ that tells us how well the model $g(\theta)$ describes the dataset.
2536 Finding the values of θ that would minimize the loss function we fit the model.

2537 10.1.1 Gradient descent optimization

2538 One of the most powerful and used class of methods in minimizing the loss function is called the
2539 *gradient descent*, [1] especially its sub-class, the stochastic gradient descent (SGD) [2], [3]. One of its
2540 modifications called ADAM [4] was used as an optimization algorithm in the work presented in this
2541 thesis.

2542 Let's assume that a loss function $E(\theta)$ may be estimated as a sum over n data points:

$$E(\theta) = \sum_{i=1}^n e_i(x_i, \theta). \quad (10.1)$$

2543 In the simplest case of the gradient descent (GD) algorithm we start looking for the values of parameters
2544 θ such that the sum of functions $\sum_{i=1}^n e_i$ is minimal. We start with a certain value θ_0 and then iteratively
2545 perform the following:

$$\begin{aligned} v_t &= \eta_t \nabla_{\theta} E(\theta_t), \\ \theta_{t+1} &= \theta_t - v_t, \end{aligned} \quad (10.2)$$

2546 where $\nabla_{\theta} E(\theta_t)$ is the gradient of $E(\theta)$ with respect to θ ; factor η_t is called the *learning rate* and defines
2547 the length of the step in the direction of θ performed with every iteration. Balancing learning rate
2548 is very important for learning process and convergence. A value too low can make the convergence
2549 "stuck" in the local minimum, it also increases the number of iterations. Picking a very high learning

2550 rate we risk to miss the minimum so the algorithm would never converge to a minimum. Also, if the
 2551 number of data points n is high, calculating the gradient is a costly task in terms of CPU time.
 2552 Some of the problems accompanying the use of GD are dealt with by using its modification - the SGD.
 2553 The idea is the following: instead of using all the available data points n at each iteration of the GD, we
 2554 split the data into k *minibatches*, each having M data points, such that $k = n/M$. Normally the size of
 2555 the batch is few hundreds of data points, to provide a certain degree of variance and incorporating
 2556 stochasticity. The transition to SGD algorithm is done in the following way:

$$\nabla_{\theta} E(\theta) = \sum_{i=1}^n \nabla_{\theta} e_i(x_i, \theta) \rightarrow \sum_{i \in B_l} \nabla_{\theta} e_i(x_i, \theta), \quad (10.3)$$

2557 where B_l is a set of data points belonging to a minibatch $l \in 1, \dots, n/M$. Now every next iteration of θ
 2558 parameters update is performed over a different batch, consecutively running over all the batches:

$$\begin{aligned} \nabla_{\theta} E^{EM}(\theta) &= \sum_{i \in B_l} \nabla_{\theta} e_i(x_i, \theta), \\ v_t &= \eta_t \nabla_{\theta} E^{EM}(\theta_t), \\ \theta_{t+1} &= \theta_t - v_t. \end{aligned} \quad (10.4)$$

2559 A full iteration over all the n/M batches is called an *epoch*. Now stochasticity prevents the gradient
 2560 algorithm from getting stuck in a local minimum. Also computing the gradient over fewer data point
 2561 notably decreases the CPU time spent.
 2562 The algorithm may be further improved, adding a "memory", that is to say making every next step t
 2563 dependent on the direction of the previous step $t-1$:

$$\begin{aligned} v_t &= \gamma v_{t-1} + \eta_t \nabla_{\theta} E^{EM}(\theta_t), \\ \theta_{t+1} &= \theta_t - v_t. \end{aligned} \quad (10.5)$$

2564 Thanks to analogy from physics the parameter γ is called a *momentum*, having $0 \leq \gamma \leq 1$ [5], [6].
 2565 This parameter provides a certain "inertia" in the change of the direction of the gradient descent.
 2566 Introduction of the momentum helps for quicker convergence in the case of a slow but steady change
 2567 of a certain parameter during the gradient descent.
 2568 The convergence of the GD may be significantly improved if the learning rate could be different in
 2569 different directions, depending on the landscape of the parameter space θ : the steeper the gradient
 2570 in a certain direction - the smaller the corresponding step. The optimal step could be estimated by
 2571 obtaining the *Hessian matrix* in the vicinity of a point θ_0 , providing a description of the local curvature
 2572 in a multidimensional space. Although calculating Hessian matrix is complicated and slow-converging
 2573 process [7]. However, a number of methods use the second moment of the gradient to efficiently
 2574 estimate the optimal learning rate. One of such methods is called ADAM (ADAptive Momentum) [4],

2575 its iterative relations are the following:

$$\begin{aligned}
 g_t &= \nabla_{\theta} E(\theta_t) \\
 m_t &= \beta_1 m_{t-1} + (1 - \beta_1) g_t \\
 s_t &= \beta_2 s_{t-1} + (1 - \beta_2) g_t^2 \\
 \hat{m}_t &= \frac{m_t}{1 - (\beta_1)^t} \\
 \hat{s}_t &= \frac{s_t}{1 - (\beta_2)^t} \\
 \theta_{t+1} &= \theta_t - \eta_t \frac{\hat{m}_t}{\sqrt{\hat{s}_t} + \epsilon}.
 \end{aligned} \tag{10.6}$$

2576 Here the parameters β_1 and β_2 set the memory lifetime for the first and second moment; η is the learning
 2577 rate and ϵ is a small regularization constant keeping the denominators from vanishing. Like in other
 2578 cases of the SGD here the iterations are performed batch-wise. Parameter s_t is linked to the variance of
 2579 the gradient size. This basically means that the learning rate is proportional to the first momentum of
 2580 the gradient and inverse proportional to its standard deviation.

2581 10.1.2 DNN structure and training

2582 A neural network is composed of single neurons, also called nodes, arranged in layers. The first layer is
 2583 called the input layer, the last one is called the output layer; all the layers in between are named hidden
 2584 layers (see Fig. 101).

2585 A single node i takes a vector of k input features $\mathbf{x} = (x_1, x_2, \dots, x_k)$ and produces a scalar input $a_i(\mathbf{x})$.
 2586 Function a_i may have a different form, although it normally can be decomposed into two steps. The
 2587 first step is a linear transformation of the inputs into a scalar value assigning each input a weight:

$$z^i = w_k^i \cdot x_k + b^i, \tag{10.7}$$

2588 where $\mathbf{w}^i = (w_1^i, w_2^i, \dots, w_k^i)$ is a set of k weights assigned to corresponding inputs. The weights \mathbf{w}^i are
 2589 specific to a neuron i , as well as the scalar bias b^i . The next step is where the non-linear function σ_i
 2590 comes into play: we can express the output function $a_i(\mathbf{x})$ as follows:

$$a_i(\mathbf{x}) = \sigma_i(z^i). \tag{10.8}$$

2591 There exists a number of options for the non-linear function σ ; in current thesis a tanh is used. When
 2592 the neurons are arranged in layers in a feed-forward neural network - the outputs from neurons of
 2593 the previous layer serve as inputs for the succeeding layers neurons. The universal approximation
 2594 theorem states, that a neural network with a single hidden layer can approximate any continuous
 2595 multiparametric function with arbitrary accuracy [8], [9]. However, in practice it is easier to reach the
 2596 possible precision having more hidden layers.

2597 So in terms of a DNN fitting the model means tuning the weights and biases (\mathbf{w}^i, b^i) in such a way
 2598 that a loss function applied to the new dataset would be minimal. It is reached through iterative
 2599 process called *training*, that involves the GD with an algorithm called *backpropagation* [10]. The
 2600 backpropagation algorithm allows to calculate the gradients and adjust the corresponding parameters

2601 in a very computation-efficient way.

Let us assume that there are L layers in the network $l = 1, \dots, L$, that w_{jk}^l and b_j^l are the weight of an

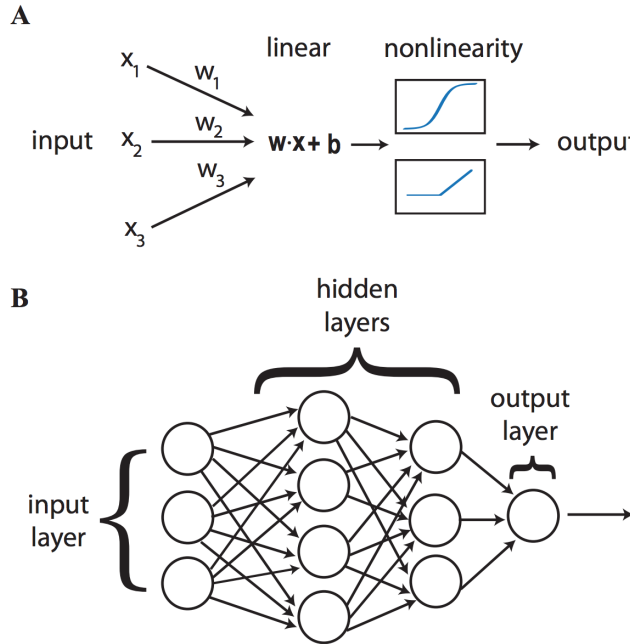


Figure 101: A: The nodes perform a linear transformation of the inputs, then apply a non-linear activation function. B: The architecture of a deep neural network: neurons are arranged into layers [11].

2602

2603 input parameter k and the bias for node k in layer l respectively. The layered structure of the neural
2604 network ensures that the inputs for the nodes in layer l depend only on the outputs of the nodes from
2605 layer $l - 1$, hence:

$$a_j^l = \sigma \left(\sum_k w_{jk}^l a_k^{l-1} + b_j^l \right) = \sigma(z_j^l), \quad (10.9)$$

2606 where the linear weighted sum is denoted as:

$$\sigma(z_j^l) = \sum_k w_{jk}^l a_k^{l-1} + b_j^l. \quad (10.10)$$

2607 The cost function E is computed from the output of the neural network, so it directly depends only on
2608 the values of a_j^L . Let us define the error Δ_j^L of the j -th node in the output (L -th) layer as a change in the
2609 cost function with respect to the weighted output of the last layer:

$$\Delta_j^L = \frac{\partial E}{\partial z_j^L}. \quad (10.11)$$

2610 At the same time the loss depends indirectly on all the preceding layers, so keeping in mind eq. 10.9
2611 we can define the error of an arbitrary node j in arbitrary layer l as the change in the cost function E
2612 with respect to the weighted input z_j^l :

$$\Delta_j^l = \frac{\partial E}{\partial z_j^l} = \frac{\partial E}{\partial a_j^l} \sigma'(z_j^l), \quad (10.12)$$

2613 where $\sigma'(z_j^l)$ is the derivative of the non-linear activation function σ with respect to its input at z_j^l . But
 2614 on the other hand we can also interpret the error function Δ_j^L in terms of bias partial derivatives:

$$\Delta_j^l = \frac{\partial E}{\partial z_j^l} = \frac{\partial E}{\partial b_j^l} \frac{\partial b_j^l}{\partial z_j^l} = \frac{\partial E}{\partial b_j^l} \cdot \mathbf{1}. \quad (10.13)$$

2615 So starting from the output layer we can compute the error in any layer l , provided we know it for the
 2616 subsequent layer $l+1$:

$$\begin{aligned} \Delta_j^l &= \frac{\partial E}{\partial z_j^l} = \sum_k \frac{\partial E}{\partial z_j^{l+1}} \frac{\partial z_j^{l+1}}{\partial z_j^l} = \\ &= \sum_k \Delta_j^l \frac{\partial z_j^{l+1}}{\partial z_j^l} \left(\sum_k \Delta_j^l w_{kj}^{l+1} \right) \sigma'(z_j^l). \end{aligned} \quad (10.14)$$

2617 And finally we can get the gradient of the cost function E with respect to a weight of an arbitrary
 2618 neuron:

$$\frac{\partial E}{\partial w_{jk}^l} = \frac{\partial E}{\partial z_j^l} \frac{\partial z_j^l}{\partial w_{jk}^l} = \Delta_j^l a_k^{l-1}. \quad (10.15)$$

2619 Using these four equations (10.11, 10.13, 10.14, 10.15) it is possible to "backpropagate" the error back
 2620 from the output layer and once we can compute the gradient - we know how we should tune the
 2621 weights and biases in order to minimize the loss function.

2622 10.1.3 Batch normalization

2623 Batch normalization is a regularization scheme that helps to improve the speed and stability of the
 2624 DNN training. The main idea behind the method is to prevent an *internal covariant shift* - a change in
 2625 the distribution of network activations due to the change in network parameters during training by
 2626 means of normalization of the parameters transferred from layer l to layer $l+1$ [12]. So let us consider
 2627 a layer l that has d inputs $\mathbf{x} = (x^1, x^2, \dots, x^d)$, then for every x^k we perform the following transformation:

$$\hat{x}^k = \frac{x^k - E[x^k]}{\sqrt{Var[x^k]}}, \quad (10.16)$$

2628 where $E[x^k]$ and $Var[x^k]$ are the expectation and variance of the parameter x , calculated over the
 2629 training dataset, respectively. Although we have to be sure that we preserve the non-linearity of the
 2630 activation function output. In order to do this the two additional parameters are introduced:

$$y^k = \gamma \hat{x}^k + \beta^k, \quad (10.17)$$

2631 where the parameters γ and β are trained just like the rest of the network parameters. Practically
 2632 if the training is performed within the mini-batch scheme with batch size $B = x_1, \dots, x_m$ the batch
 2633 normalization layer is inserted between the DNN layers the transformations for the input x are the

2634 following:

$$\begin{aligned}
 \frac{1}{m} \sum_{i=1}^m x_i &\rightarrow \mu_B \\
 \frac{1}{m} \sum_{i=1}^m (x_i - \mu_B)^2 &\rightarrow \sigma_B^2 \\
 \frac{x_i - \mu_B}{\sqrt{\sigma_B^2 + \epsilon}} &\rightarrow \hat{x}_i \\
 \gamma \hat{x}_i + \beta &\rightarrow y_i \equiv BN_{\gamma, \beta}(x_i),
 \end{aligned} \tag{10.18}$$

2635 where ϵ is a small regularization constant.

2636 10.2 HR regression

2637 Considering that hadronic recoil is an observable what uses many inputs from ID, EMC and HC it is
2638 reasonable to expect improvement of the result using modern MultiVariate Analysis (MVA) techniques.

2639 10.2.1 Input features and model

2640 Training, testing and validation was performed using the MC sample $W^+ \rightarrow \mu\nu$ at 13 TeV with the same
2641 selection. From the 3625136 events that have passed the selection 2 275 902 were used for training and
2642 1 349 234 for testing the performance. Below is the list of 38 input features:

- 2643 • **Hadronic recoil** is possible in a number of definitions. As it was described before, the HR may be
2644 defined using exclusively charged PFO, exclusively neutral PFO or both. All three definitions are
2645 included to the input features in the with two Cartesian components for each definition, making
2646 6 input features.
- 2647 • **Transverse energy sum** $\sum E_T$ is also defined in three similar ways, adding three input features.
- 2648 • Cartesian components of the two leading jets momenta in the transverse plane. The jets were
2649 demanded to have $p_T > 20$ GeV. If one or both jets don't make the cut or there is less than two jets
2650 in the event - the corresponding features were assigned zero value.
- 2651 • Cartesian components of the five leading Neutral Particle Flow Objects (nPFOs) and five leading
2652 Charged Particle Flow Objects (cPFOs) momenta in the transverse plane.
- 2653 • Number of primary vertices in the event.
- 2654 • Pile-up value μ .
- 2655 • Total number of jets in the event.
- 2656 • Total number of nPFOs and cPFOs in the event.

2657 All input features were pre-processed using the StandardScaler module from Scikit Learn package [13].
 2658 The model contains 3 dense layers with 256 neurons each, alternated with batch normalization layers
 2659 (see Fig. 102). Using batch normalization layers has allowed to reduce the training time by the factor of 10. The model has used Adam optimizer with learning step 0.001 and batch size of 4000 data points.

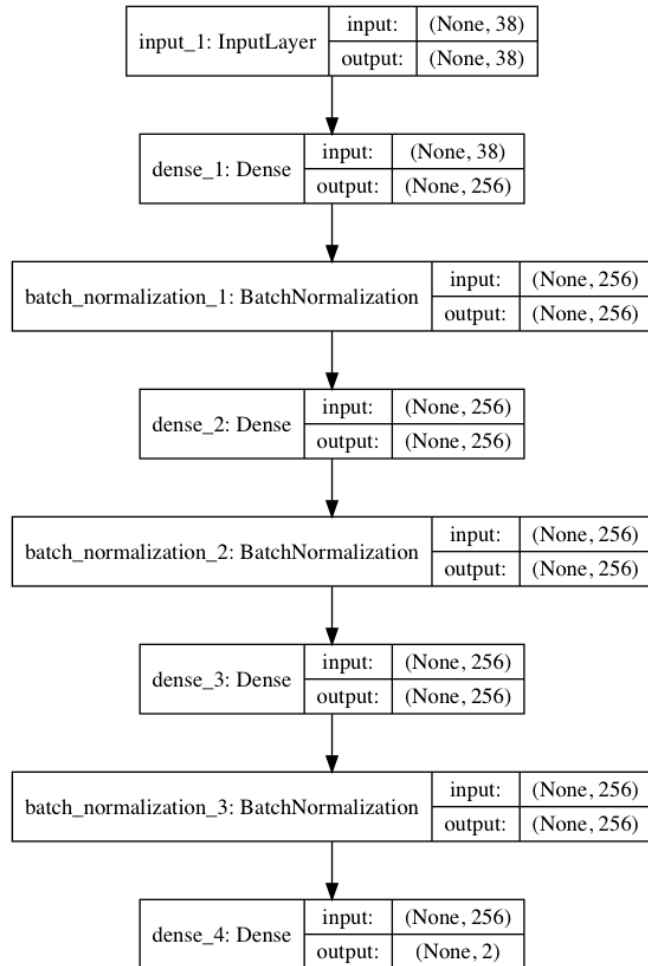


Figure 102: A model of the DNN used in the analysis.

2660
 2661 Twenty percent of events were used for validation. The two target values were Cartesian components
 2662 of the truth HR vector.

2663 10.2.2 Kinematic distributions

2664 The results presented here demonstrate the regression plots obtained with the trained DNN. They
 2665 include the plots from the test sample of $W^+ \rightarrow \mu\nu$ at 13 TeV, as well as plots from.

2666 10.3 Technical details

2667 **Bibliography**

- 2668 [1] Yann LeCun et al. "Gradient-based learning applied to document recognition". In: *Proceedings of*
2669 *the IEEE*. 1998, pp. 2278–2324.
- 2670 [2] Léon Bottou. "Stochastic Gradient Descent Tricks". In: vol. 7700. Jan. 2012, pp. 421–436. doi:
2671 10.1007/978-3-642-35289-8_25.
- 2672 [3] David E. Rumelhart, Geoffrey E. Hinton, and Ronald J. Williams. "Learning representations by
2673 back-propagating errors". In: *Nature* 323 (1986), pp. 533–536.
- 2674 [4] Diederik P. Kingma and Jimmy Ba. *Adam: A Method for Stochastic Optimization*. cite arxiv:1412.6980Com-
2675 ment: Published as a conference paper at the 3rd International Conference for Learning Repre-
2676 sentations, San Diego, 2015. 2014. url: <http://arxiv.org/abs/1412.6980>.
- 2677 [5] Yu Nesterov. "A method of solving a convex programming problem with convergence rate
2678 $O(1/k^2)$ ". In: vol. 27. Jan. 1983, pp. 372–376.
- 2679 [6] Boris Polyak. "Some methods of speeding up the convergence of iteration methods". In: *Ussr*
2680 *Computational Mathematics and Mathematical Physics* 4 (Dec. 1964), pp. 1–17. doi: 10.1016/0041-
2681 5553(64)90137-5.
- 2682 [7] Yann LeCun et al. "Efficient BackProp". In: *Neural Networks: Tricks of the Trade*. Ed. by Genevieve
2683 B. Orr and Klaus-Robert Müller. Berlin, Heidelberg: Springer Berlin Heidelberg, 1998, pp. 9–50.
2684 ISBN: 978-3-540-49430-0. doi: 10.1007/3-540-49430-8_2. url: https://doi.org/10.1007/3-540-49430-8_2.
- 2686 [8] Kurt and Hornik. "Approximation capabilities of multilayer feedforward networks". In: *Neural*
2687 *Networks* 4.2 (1991), pp. 251–257. doi: 10.1016/0893-6080(91)90009-T. url: <http://www.sciencedirect.com/science/article/pii/089360809190009T>.
- 2689 [9] G. Cybenko. "Approximation by superpositions of a sigmoidal function". In: *Mathematics of*
2690 *Control, Signals and Systems* 2.4 (Dec. 1989), pp. 303–314. issn: 1435-568X. doi: 10.1007/BF02551274. url: <https://doi.org/10.1007/BF02551274>.
- 2692 [10] D. E. Rumelhart and D. Zipser. "Feature Discovery by Competitive Learning". In: *Parallel Dis-*
2693 *tributed Processing*. MIT Press, 1986, pp. 151–193.
- 2694 [11] Pankaj Mehta et al. "A high-bias, low-variance introduction to Machine Learning for physicists".
2695 In: *Phys. Rept.* 810 (2019), pp. 1–124. doi: 10.1016/j.physrep.2019.03.001. arXiv: 1803.08823
2696 [[physics.comp-ph](#)].
- 2697 [12] Sergey Ioffe and Christian Szegedy. "Batch Normalization: Accelerating Deep Network Training
2698 by Reducing Internal Covariate Shift". In: *Proceedings of the 32nd International Conference on*
2699 *International Conference on Machine Learning - Volume 37*. ICML15. Lille, France: JMLR.org, 2015,
2700 pp. 448–456.

- 2701 [13] F. Pedregosa et al. “Scikit-learn: Machine Learning in Python”. In: *Journal of Machine Learning*
2702 *Research* 12 (2011), pp. 2825–2830.

2703

2704

11 Appendix A

2705 "Potentielle citation sans aucun rapport avec le sujet"

2706 — Personne inconnue, contexte à déterminer

2707 11.1 Experimental uncertainties of main observables

Mesure de la masse du boson W avec le détecteur ATLAS au LHC

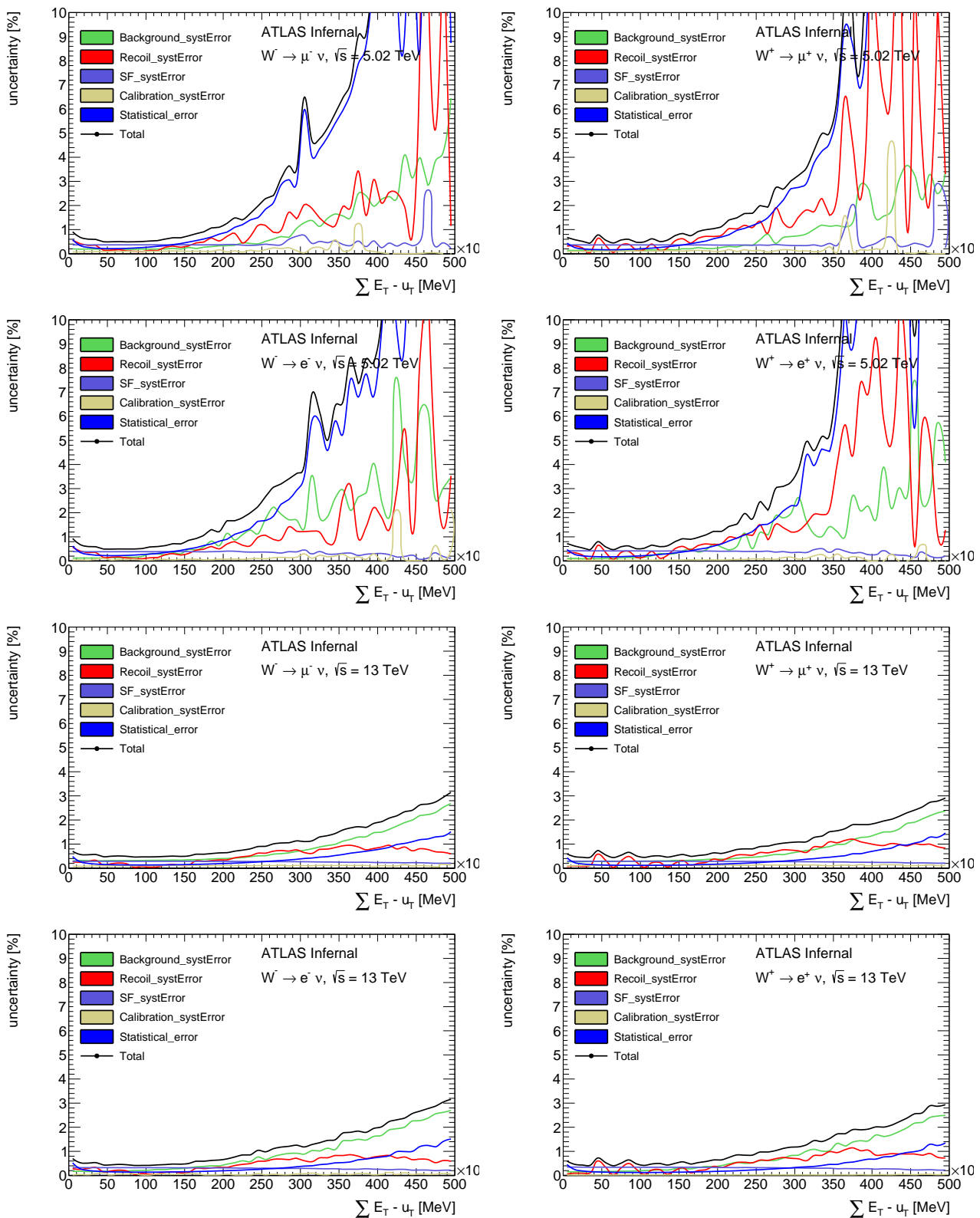


Figure 111: ΣE_T systematic error breakdown in the muon and electron channel for the $\sqrt{s} = 5 \text{ TeV}$ and $\sqrt{s} = 13 \text{ TeV}$ datasets.

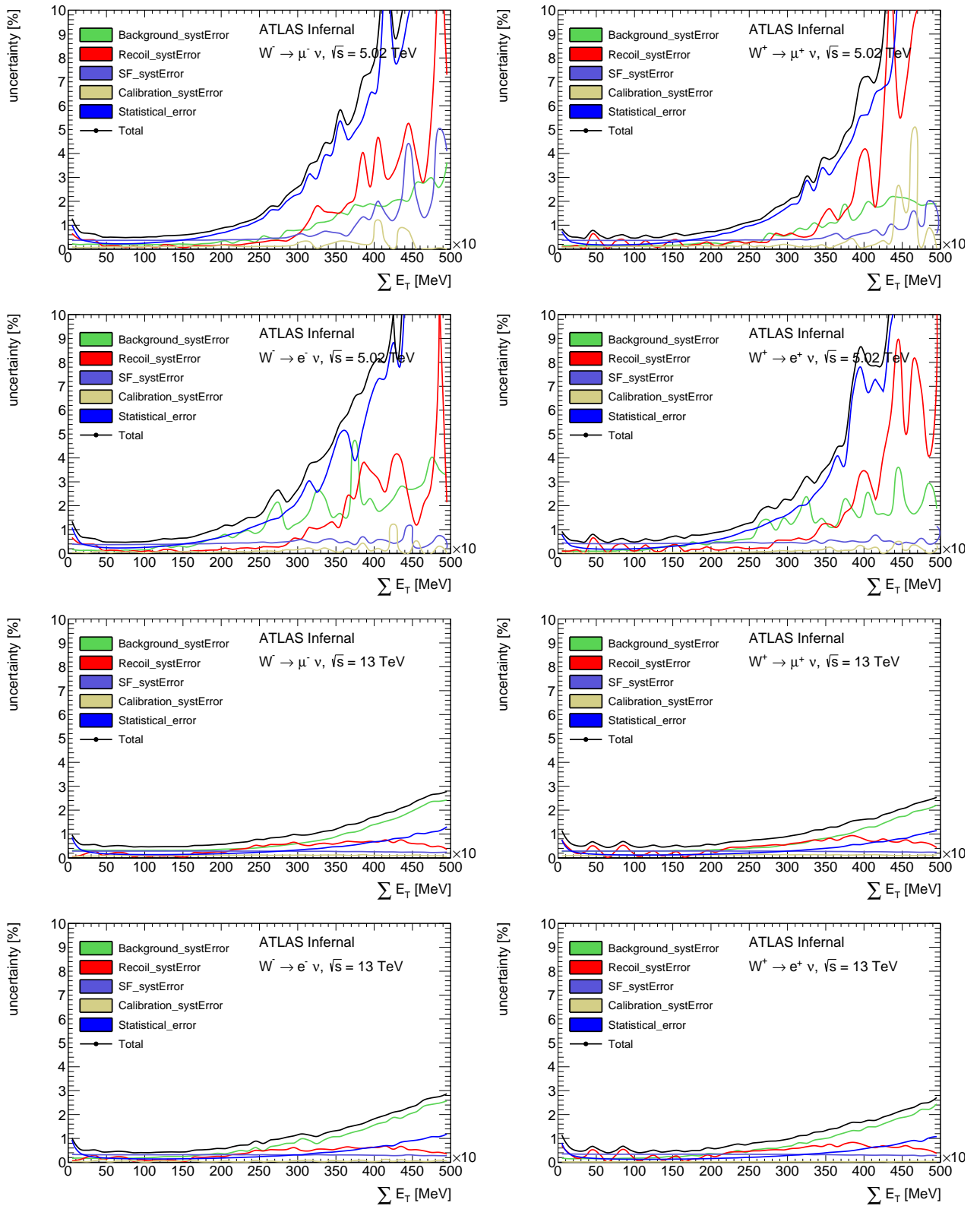


Figure 112: ΣE_T systematic error breakdown in the muon and electron channel for the $\sqrt{s} = 5\text{ TeV}$ and $\sqrt{s} = 13\text{ TeV}$ datasets.

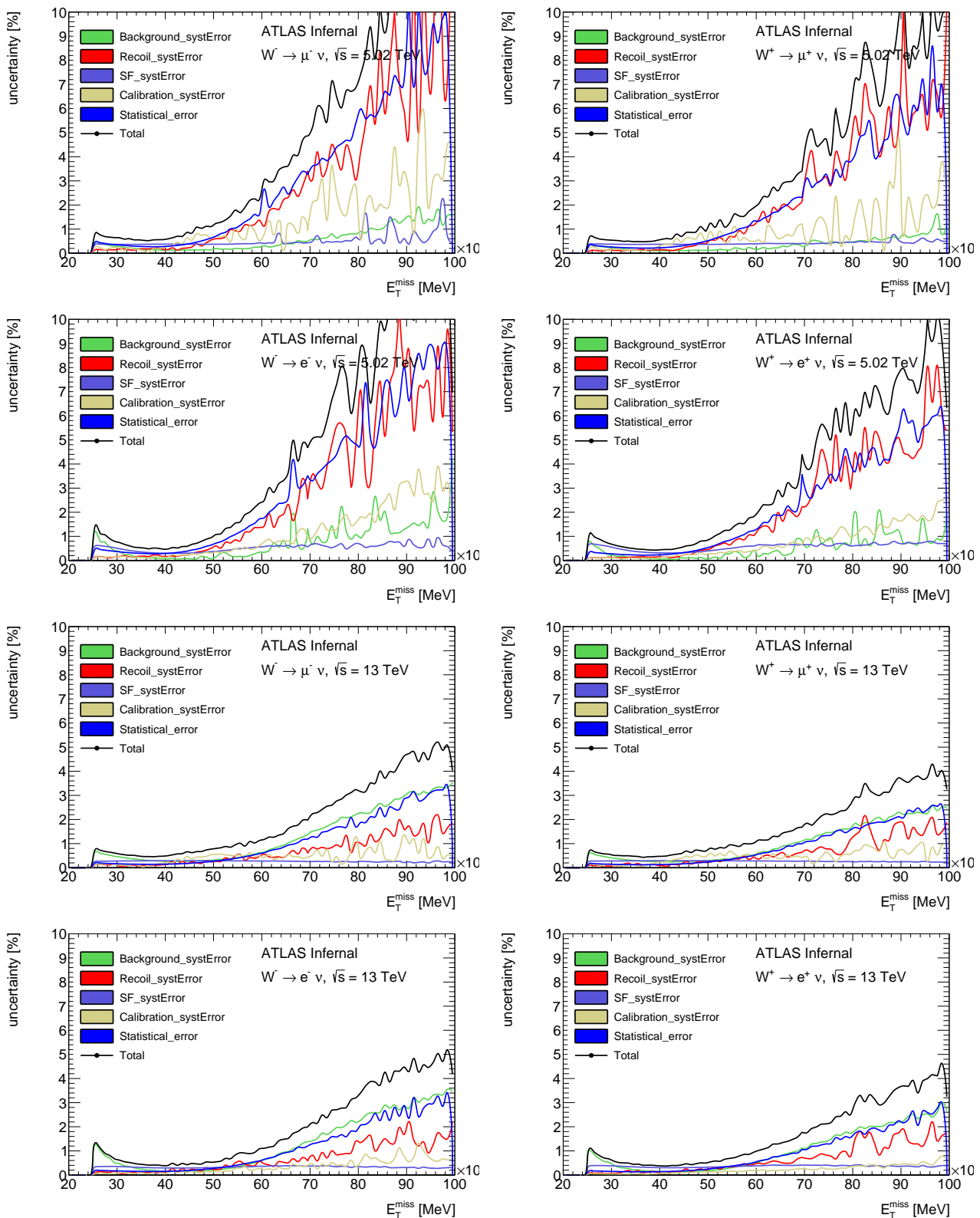


Figure 113: \vec{E}_T^{miss} systematic error breakdown in the muon and electron channel for the $\sqrt{s} = 5 \text{ TeV}$ and $\sqrt{s} = 13 \text{ TeV}$ datasets.

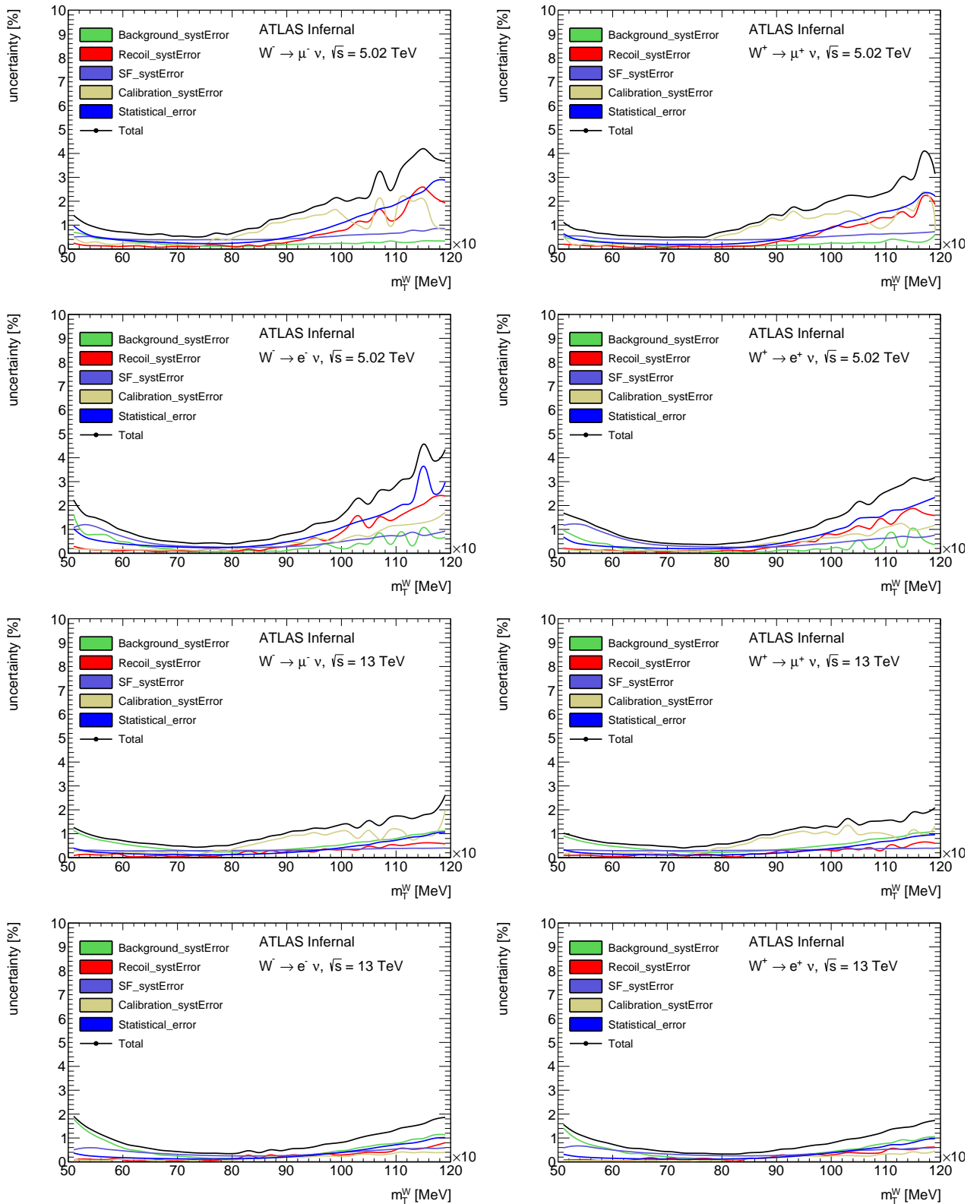


Figure 114: Transverse mass systematic error breakdown of the W boson in the muon and electron channel for the $\sqrt{s} = 5$ TeV and $\sqrt{s} = 13$ TeV datasets.

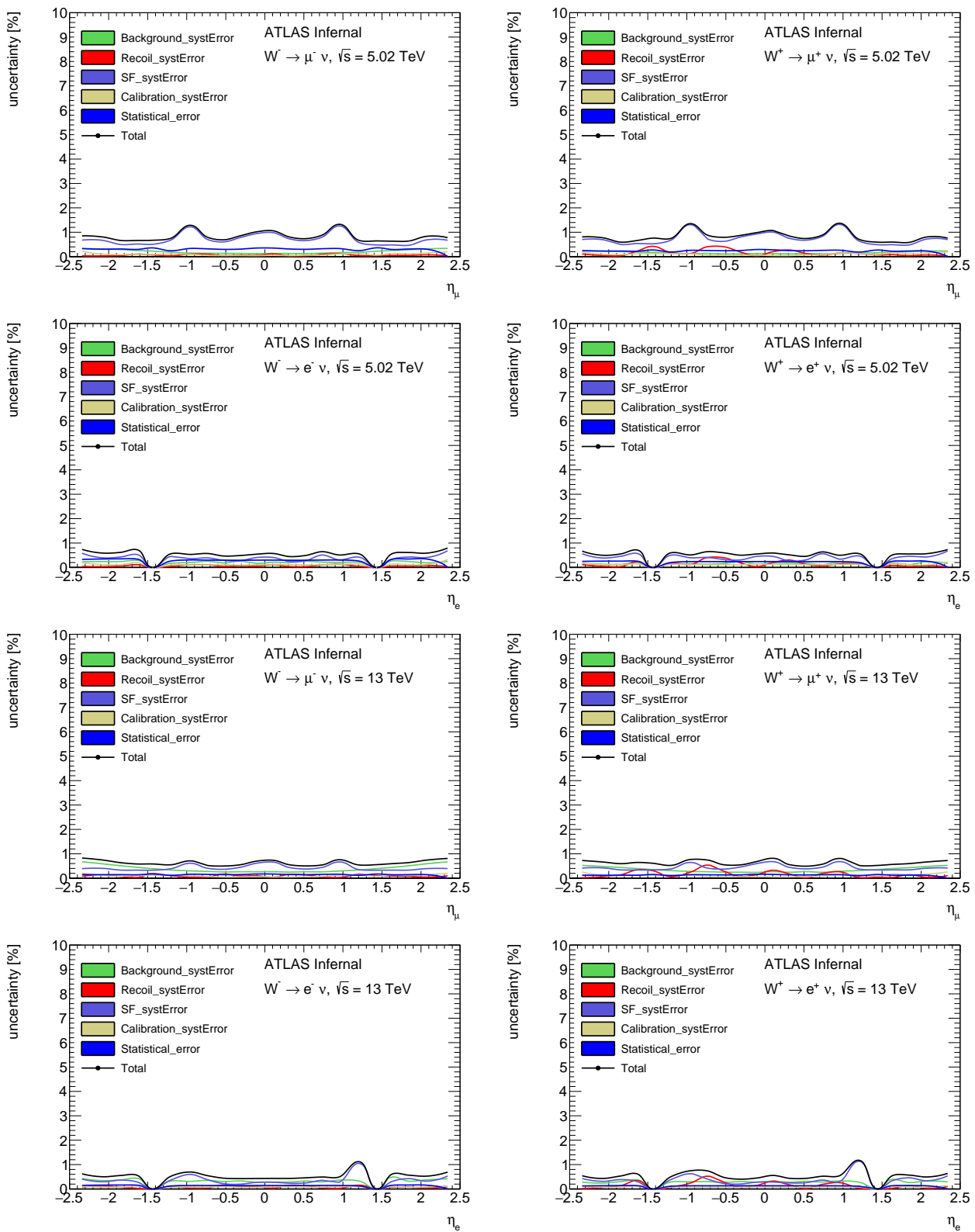


Figure 115: Lepton pseudorapidity systematic error breakdown in the muon and electron channel for the $\sqrt{s} = 5 \text{ TeV}$ and $\sqrt{s} = 13 \text{ TeV}$ datasets.

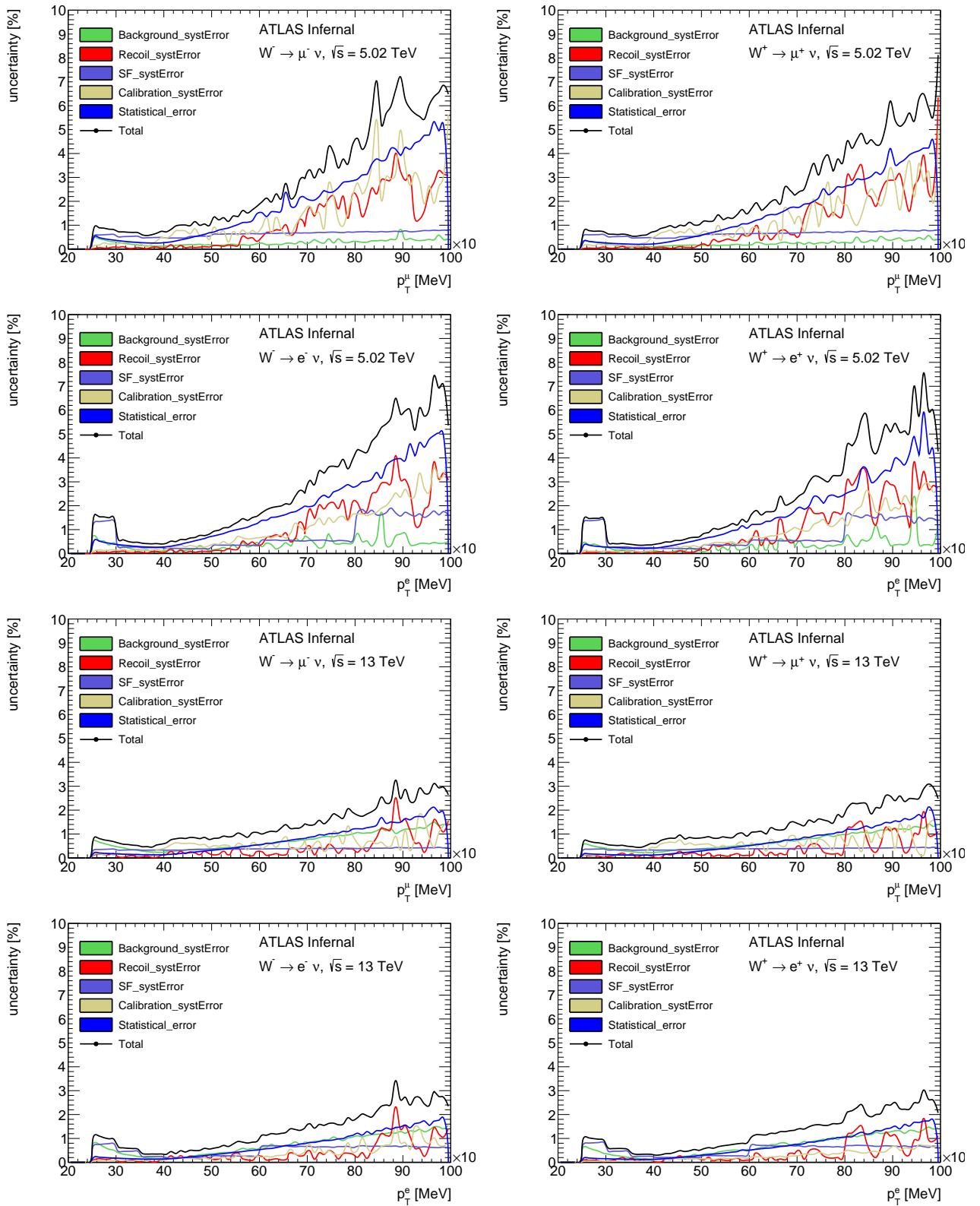


Figure 116: Lepton transverse systematic error breakdown distribution in the muon and electron channel for the $\sqrt{s} = 5 \text{ TeV}$ and $\sqrt{s} = 13 \text{ TeV}$ datasets.

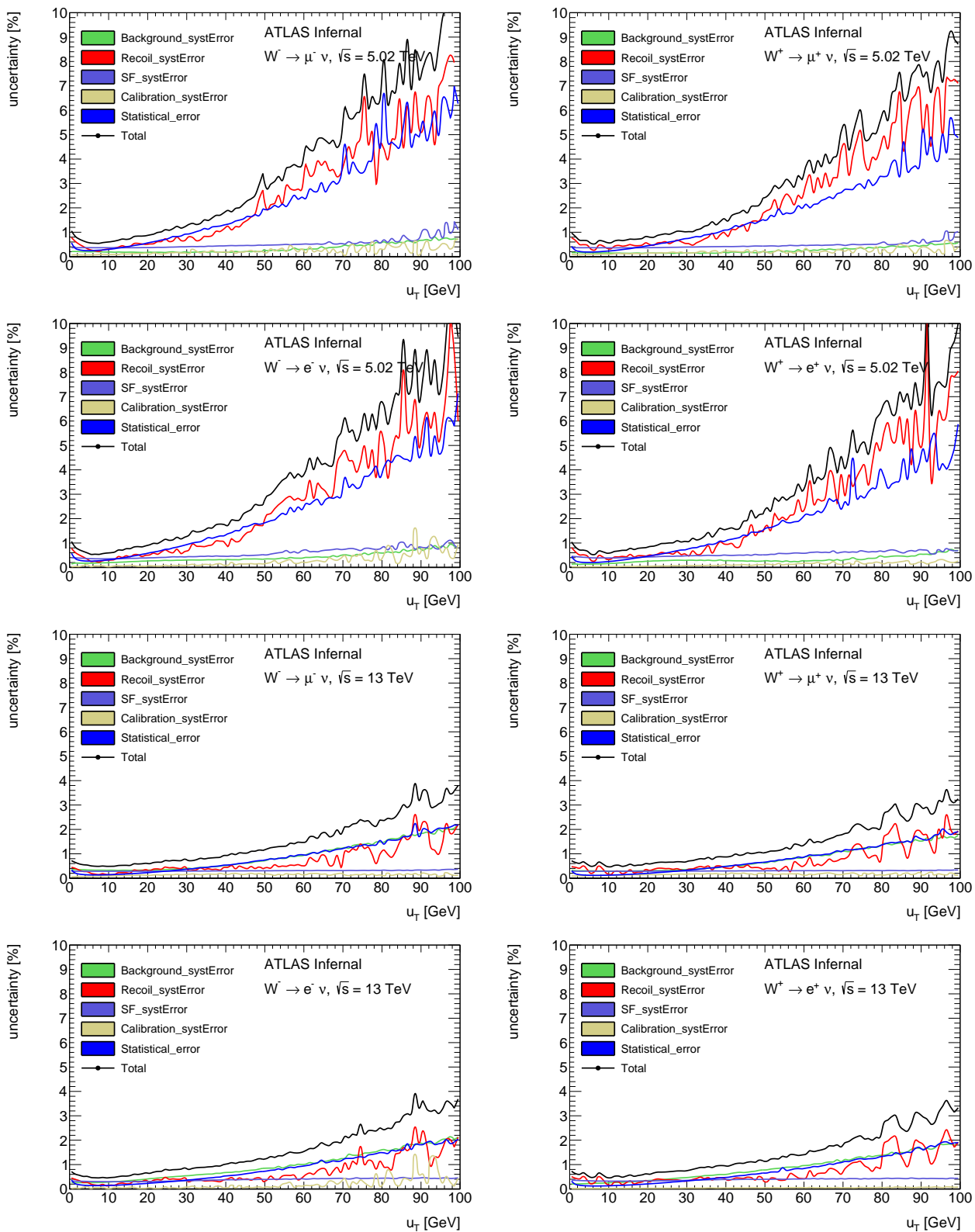


Figure 117: W transverse momentum systematic error breakdown in the muon and electron channel for the $\sqrt{s} = 5$ TeV and $\sqrt{s} = 13$ TeV datasets.